UNIVERSIDAD NACIONAL AUTÓNOMA DE MÉXICO
PROGRAMA DE POSGRADO EN ASTROFÍSICA

Instituto de Radioastronomía y Astrofísica

THE EVOLUTION OF THE INNER REGIONS OF PROTOPLANETARY DISKS

TESIS QUE PARA OPTAR POR EL GRADO DE
DOCTOR EN CIENCIAS (ASTROFÍSICA)

PRESENTA
EZEQUIEL MANZO MARTÍNEZ

TUTORES
DRA. SUSANA LIZANO SOBERÓN, INSTITUTO DE
RADIOASTRONOMÍA Y ASTROFÍSICA
DRA. NURIA CALVET, UNIVERSIDAD DE MICHIGAN

MORELIA, MICHOACÁN (AGOSTO 2020)

Dedicado a mi familia, y a aquellos que se fueron instalando también en mi corazón.

Agradecimientos

Esta tesis es el producto de un lapso de tiempo donde mi dedicación, atención y objetivos estuvieron enfocados en llevar a cabo este proyecto.

Aprovecho la oportunidad para agradecer el apoyo obtenido a través del proyecto PAPIIT-UNAM IN101418 y del proyecto CONACyT 23863.

Contents

List of Figures

List of Tables

Abstract

Protoplanetary disks surrounding low-mass, pre-main sequence stars are natural byproducts of the star formation process and the sites where new planetary systems emerge. Different studies and observations have revealed that these disks show evidence of evolution, probably due to different stages of the planet formation process they undergo. In addition, it has been observed that the number of disk-bearing stars in several stellar groups, ranging from 1 to 13 Myr, decreases with age, suggesting a timescale of evolution of $\sim 5-7$ Myr. It has also been found that both the amount of gas from the disk being accreted onto the central star, and the median mid and near-IR emission in disks of a given population, decrease as the age of the population increases; both aspects are indicative of evolutionary processes affecting both the gas and the dust components. Additionally, since the process of planet formation occurs within the disks, their innermost regions are of particular interest, since it is in those regions where terrestrial planets form.

Here, using near and mid-IR observations, we study the evolution of the inner few astronomical units of protoplanetary disks around low-mass stars. We consider nearby stellar groups with ages spanning from 1 to 11 Myr, distributed into four age bins. Combining PANSTARRS photometry with spectral types we derive the reddening ($A_{\rm V}$) consistently for each star, which we use (1) to measure the excess emission above the photosphere with a new indicator of IR excess and (2) to estimate the mass accretion rate ($\dot{M}$) from the equivalent width of the Hα line. Using the observed decay of $\dot{M}$ with age as a constraint to fix the viscosity parameter of viscous evolutionary models, we use the statistical method known as Approximate Bayesian Modeling to infer the dust properties that produce the observed decrease of the IR excess with age, in the range between 4.5 μm and 24 μm. In addition, we also use the observed decay of $\dot{M}$ as a prior when we perform the Approximate Bayesian Modeling. We calculate an extensive grid of irradiated accretion disk models, including a two-layered wall to emulate a curved dust inner edge, and obtain the vertical structure similar to the surface density predicted by viscous evolution.

We find that the median dust depletion, that is, the dust-to-gas mass ratio in the disk upper layers relative to the standard insterstellar medium value ($\epsilon \sim 0.01$), is $\epsilon \sim 3 \times 10^{-3}$ at 1.5 Myr, consistent with previous studies, and it decreases to $\epsilon \sim 3 \times 10^{-4}$ by 7.5 Myr, which suggests a high degree of settling of the disks in the stellar populations. In addition, we include photoevaporation in a simple model of the disk evolution and find that a photoevaporative wind mass-loss rate ranging from $\sim 1 - 3 \times 10^{-9}\, M_{\odot} yr^{-1}$ agrees reasonably well with the decrease of the disk fraction with age, as well as with the decrease of the fraction of accretors with age. Finally, we use mean models, obtained using the median parameters found at the different age bins, to study the H_2O and CO snowlines, and show that they are curved surfaces and not vertical fronts; we also find that their location at the midplane migrates inwards towards the star as the disk evolves. This study represents a comprehensive statistical study of *evolved* disks at different evolutionary stages, focused on their innermost regions; it shows that, in addition to the substructure in the dust component of the disks, revealed by recent ALMA observations, there is a common overall evolution of the bulk disk matter, the mass accretion rate, and the degree of dust settling.

Resumen

Los discos protoplanetarios alrededor de estrellas jóvenes de baja masa, en pre-secuencia principal, se forman como consecuencia natural del proceso de formación estelar y son los lugares donde nuevos sistemas planetarios emergen. Distintos estudios y observaciones han revelado que estos discos muestran evidencias de evolución, probablemente debido a las diferentes etapas del proceso de formación de planetas que ocurre dentro de ellos. Adicionalmente, se ha observado que el número de estrellas con discos en varios grupos estelares, con edades entre 1 y 13 millones de años, decae con la edad, lo cual sugiere una escala de evolución de los discos de $\sim 5 - 7$ millones de años. También se ha encontrado que, tanto la cantidad de gas en el disco que es acretada por la estrella central, como la mediana de la emisión en el cercano y mediano IR en discos de una población estelar dada, decaen conforme la edad de la población estelar aumenta; ambos aspectos indican procesos evolutivos que afectan tanto la componente de polvo como la de gas. Por otro lado, como el proceso de formación de planetas ocurre dentro de los discos, las regiones más internas de éstos son de interés particular, pues es en esas regiones donde se forman los planetas tipo terrestres.

En este trabajo estudiamos la evolución de las regiones internas (las primeras unidades astronómicas) de discos protoplanetarios alrededor de estrellas de baja masa, usando observaciones en el cercano y mediano IR. Incluimos grupos estelares cercanos, con edades que abarcan de 1 a 11 millones de años, los cuales agrupamos en cuatro bines de edad. Combinando datos fotométricos de PANSTARRS con tipos espectrales, calculamos el enrojecimiento (A_{V}) de manera consistente para cada estrella, el cual usamos para (1) medir el exceso de emisión sobre la fotósfera, usando un indicador nuevo del exceso IR, y (2) para determinar la tasa de acreción de masa ($\dot{M}$) por medio del ancho equivalente de la línea de Hα. Usamos el decaimiento observado de $\dot{M}$ con la edad como una restricción para obtener el parámetro

de viscosidad de modelos evolutivos viscosos, y usamos el método estadístico conocido como Modelado Bayesiano Aproximado para determinar las propiedades del polvo que producen el decaimiento observado del exceso IR con la edad, en el intervalo de longitudes de onda entre 4.5 μm y 24 μm. Adicionalmente, usamos el decaimiento observado de $\dot{M}$ como *prior* en el método Modelado Bayesiano Aproximado. Además, calculamos una red extensa de modelos de discos de acreción irradiados, que incluyen una pared de polvo de dos capas para simular una pared interna del disco curvada, y obtenemos una estructura vertical del disco que es similar a la densidad superficial predicha por la evolución viscosa.

Encontramos que la mediana del *dust depletion* (agotamiento de polvo), es decir, el cociente de masa de polvo a gas en las capas superiores del disco, relativo al valor estándar del medio interestelar ($\epsilon \sim 0.01$), es $\epsilon \sim 3 \times 10^{-3}$ a 1.5 millones de años, lo cual es consistente con resultados de estudios previos, y decrece hasta $\epsilon \sim 3 \times 10^{-4}$ hacia los 7.5 millones de años, lo cual sugiere un alto grado de asentamiento de los discos en las poblaciones estelares estudiadas. Adicionalmente, incluimos la fotoevaporación en un modelo simple de evolución del disco y encontramos que una tasa de pérdida de masa en un viento fotoevaporativo del orden de $\sim 1 - 3 \times 10^{-9}\, M_{\odot} yr^{-1}$ ajusta relativamente bien el decaimiento de la fracción de discos, así como de la fracción de acretores, con la edad. Finalmente, utilizamos modelos promedio, obtenidos usando la mediana de los parámetros encontrados en nuestro estudio en los diferentes bines de edad, para estudiar las *snowlines* (líneas de nieve) de H_2O y CO, y mostramos que éstas son superficies curvadas hacia la estrella cerca del plano medio, y no frentes verticales. Además, encontramos que su ubicación en el plano medio del disco va migrando hacia la estrella central conforme el disco evoluciona. Este trabajo representa un estudio estadístico exhaustivo de discos *evolucionados* en distintas etapas evolutivas, enfocado en sus regiones mś internas; el estudio muestra que, además de la subestructura observada en la componente de polvo de los discos, revelada por observaciones recientes de ALMA, existe una evolución general en común del disco, la tasa de acreción de masa y el grado de asentamiento del polvo.

1

Introduction

1.1 Disk formation around young stars

The star formation process involves various forces and physical phenomena, for instance magnetic fields, gravity, turbulence, gas thermal pressure, among others; all of them competing with each other simultaneously. It begins with the gravitational collapse of dense cores inside molecular clouds, which are large structures of gas and dust, inside which stars form. These cores are the densest regions within the clouds, and low-mass cores have typical densities between $\sim 10^3$ and $10^5\,\mathrm{cm}^{-3}$, temperatures ranging $\sim 10-30\,\mathrm{K}$, and sizes of a few $\sim 0.01-0.1\,\mathrm{pc}$ (André et al., 2014, and references therein); the median observed masses of cores are $\sim 10\,M_\odot$ (e.g. Hartmann, 2009, and references therein).

Once gravity overcomes the internal pressure and the magnetic forces, the core becomes gravitationally unstable and collapses. During the collapse, an accretion disk surrounding the protostar is formed as a consequence of the conservation of angular momentum of the initially rotating core. These circumstellar disks, composed of gas and dust, surround the pre-main sequence (PMS) stars during their first million years (Shu, Adams & Lizano, 1987), they are responsible for increasing the mass of the central star, and they are the sites where new planetary systems are born (Williams & Cieza, 2011; Testi, 2014). These accretion disks are also known as protoplanetary disks, highlighting their potential to form planets.

1.2 Young stellar objects

Since the electromagnetic radiation represents the only source of information of the physical state of the disks, a useful tool that has allowed the study of disks, in particular of the properties of the dust component, is the spectral energy distribution (SED) (see Figure 1.1), which shows the received energy flux as a function of wavelength or frequency. Young stars surrounded by protoplanetary disks exhibit excess flux over the stellar photosphere from the infrared to millimeter wavelengths due to emission of dust particles; thus, the SED of the system is directly related to the structure and the physical conditions of the dusty component of the protoplanetary disk (D'Alessio et al., 1998, 2001, 2006). The young stellar objects (YSOs) can be classified according to their mass into:

- **Herbig Ae/Be stars (HAe/Be):** A and B stars with emission lines, and stellar masses $2\,M_{\odot} \lesssim M_{*} \lesssim 8\,M_{\odot}$. Their photospheric temperatures are $\gtrsim 10000$ K.
- **T Tauri stars (TTSs):** These stars show strong emission lines and have stellar masses $0.08\,M_{\odot} \lesssim M_{*} \lesssim 2\,M_{\odot}$. Their photospheric temperatures range $\sim 3700 - 4700$ K. Based on the strength of their lines (see §1.6), these stars were originally classified as (Herbig & Bell, 1988):
    1. **Classical T Tauri stars (CTTSs):** They were defined as stars with equivalent widths of H$\alpha \gtrsim 10\,\text{Å}$. They also show excess in lines and continua above the intrinsic photospheric fluxes, thus they should be accreting material from the disk.

2. **Weak T Tauri stars (WTTSs):** These objects have equivalent widths of H$\alpha < 10\,$Å. It is thought that these stars are not accreting mass from the disk.
3. **Intermediate Mass T Tauri stars (IMTTSs):** They have spectral types ranging from early K to late F, with masses $1\,M_{\odot} \lesssim M_{*} \lesssim 5\,M_{\odot}$, which are similar to the masses of Herbig Ae stars. These stars are thought to be the predecesors of Herbig Ae stars.

- **Young brown dwarfs (YBDs):** These are objects with stellar masses $M_{*} \lesssim 0.08\,M_{\odot}$ and their core will never reach high enough temperatures to burn Hydrogen, although they burn Deuterium and Lithium for a short period of time. Their photospheric temperatures are $\lesssim$ 3700 K.

Later,White & Basri (2003) and Barrado y Navascués & Martín (2003) found that the equivalent width of the Hα line is a function of the spectral type, and thus, the initial criterion of 10 Å (Herbig & Bell, 1988) used to separate the CTTSs and the WTTSs evolved. More recently, taking into account not only the dependence of the equivalent width of Hα on the spectral type, but also the variability of Hα, Briceño et al. (2019) identified the **CTTS-WTTS (C/W)**: these stars have equivalent widths of Hα between that of a CTTS and WTTS, and they may correspond to stars evolving from an active period of accretion (CTTS) to a non accreting phase (WTTS).

As an illustration, in Figure 1.1 we show the SED of the CTTS BP Tau, located in the Taurus region. This Figure shows the typical SED of a disk-bearing star accreting material from the disk. It can be seen that, in addition to the stellar photosphere (dashed line) there is an excess of emission at longer wavelengths (IR, millimeter), produced by dust particles in the disk; additionally the UV excess comes from the material being accreted onto the star (Hartmann, Herczeg & Calvet, 2016, and references therein). The modeling of the SEDs allows us to interpret the observations and infer the physical properties of the dust (e.g. Calvet et al., 2002, 2005; D'Alessio et al., 2005, 2006; Espaillat et al., 2007, 2012; Maucó et al., 2016; Grant et al., 2018).

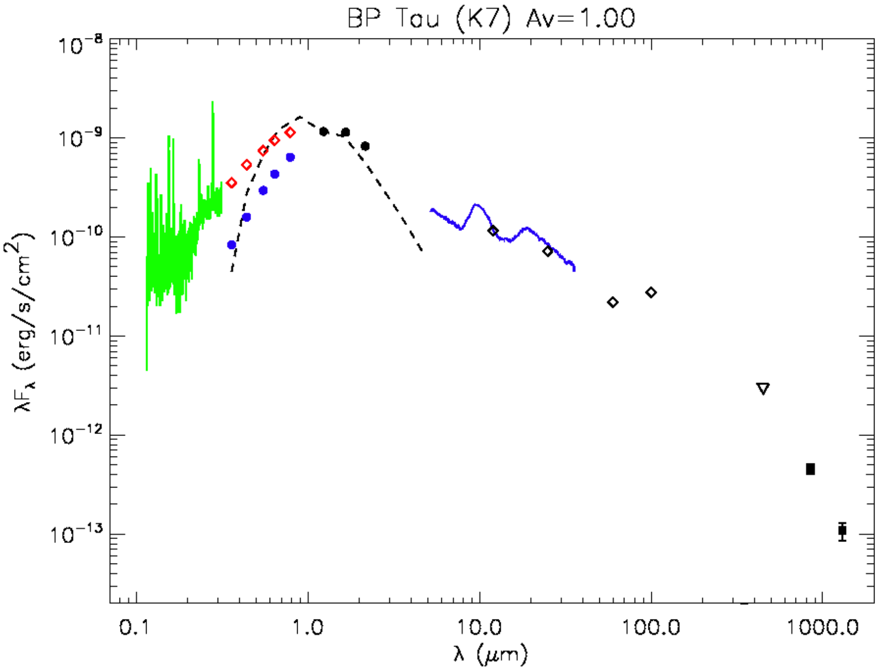

Figure 1.1: SED of BP Tau. Different components are shown: the stellar photosphere (black dashed line), UV data (green) and IRS spectra (blue line). Solid circles come from the direct observations, while the data corrected by reddening is shown with empty circles. Figure taken from Calvet & D'Alessio (2011). The references for the data can be found in Calvet & D'Alessio (2011).

There is another classification scheme of YSOs, which is independent and not equivalent to the above mentioned scheme, based on the IR slope of their SEDs, in the range $2.2\,\mu m - 25\,\mu m$, defined as (Lada, 1987)

$$\alpha_{IR} = \frac{\log(\lambda_2 F_{\lambda_2}) - \log(\lambda_1 F_{\lambda_1})}{\log(\lambda_2) - \log(\lambda_1)}, \tag{1.1}$$

which is represented by the following groups:

- **Class I:** these objects have positive slopes and correspond to objects surrounded by a dusty envelope. Their IR excess becomes stronger for longer wavelengths.

- **Class II:** these objects have negative slopes, but not as steep as the Rayleigh-Jeans limit for stellar photospheres $\lambda F_\lambda \propto \lambda^{-3}$. Their IR slopes range $-1.3 < \alpha_{IR} < 0$, thus the IR excess decreases for longer wavelengths.
- **Class III:** these objects have photospheric slopes $\alpha_{IR} \sim -3$. They are thought to have dissipated their innermost disk.

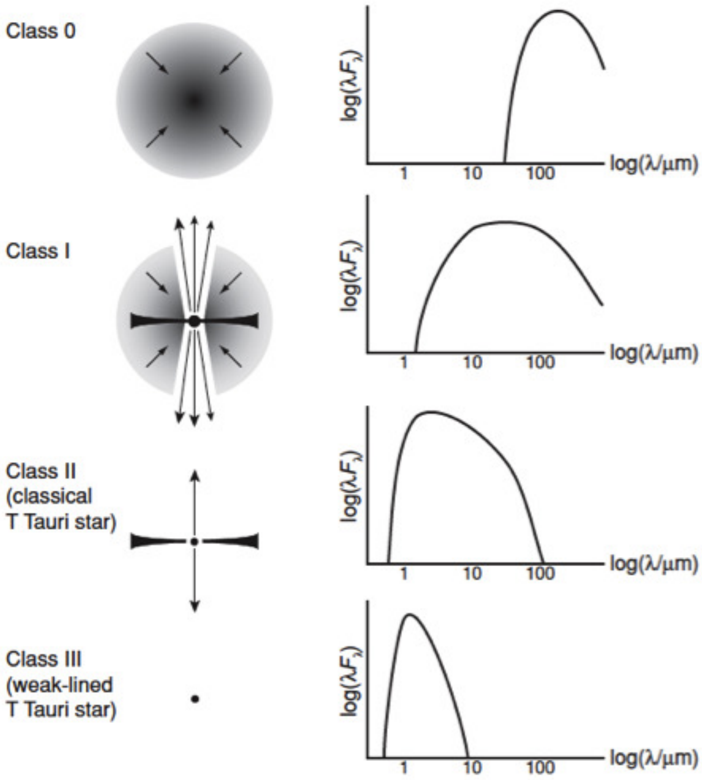

Figure 1.2: Classification scheme of YSOs based on their IR slope. Figure taken from Armitage (2010).

Andre et al. (1993) identified **Class 0** objects, which show very weak IR emission, reaching their peak at sub-millimetric wavelengths. Later it was proposed that this classification scheme was indicative of a sequence of evolution (cf. Figure 1.2) where a protostar is a Class 0/Class I object embedded in a collapsing envelope of gas and dust. Once the density of the envelope drops and is dissipated by a stellar/disk wind and/or a jet, the accretion disk becomes visible in the SED, dominating the emission from the IR to the mm; this stage corresponds to a Class II object. At a later stage of evolution, the disk is dissipated by various mechanisms (e.g. photoevaporation and/or the formation of planets in the inner regions), and the stellar photosphere becomes the main component dominating the SED in the IR, as a Class III object. In the last decade this simple scheme has evolved; for instance the discovery of pre-transitional disks (PTDs) (see §1.4) - disks with deficit of emission in the near-IR and excess at longer wavelengths - suggests that there is a wider variety of disks that may undergo different pathways of evolution, which have not been entirely understood.

1.3 The H-R diagram

The Hertzsprung-Russell (H-R) diagram is a plot of the luminosity versus the effective temperature of a group of stars. During their evolution, the stars occupy different regions on the H-R diagram, depending on their age and mass. The central star is the main source of irradiation of the disk, affecting its structure, thus it is important to know its properties. Additionally, detailed numerical models used to make comparisons with observations use the stellar properties as input parameters. The physical properties of young stars can be obtained in the H-R diagram using evolutionary tracks of stellar evolution models (e.g. Baraffe et al., 1998; Siess, Dufour & Forestini, 2000; Tognelli et al., 2011). Given the spectral type of the star, the extinction $A_{\rm V}$, the flux at an optical band, and the distance d, one can obtain the effective temperature $T_{\rm eff}$ and stellar luminosity L_*. With these properties a double interpolation can be performed using a set of evolutionary tracks to find the

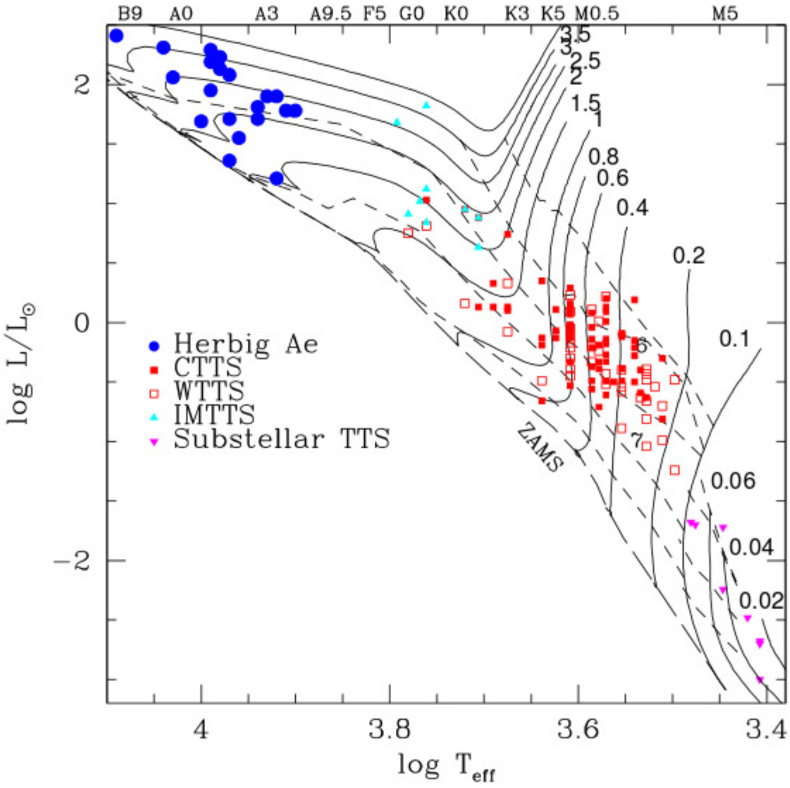

Figure 1.3: Location of a sample of YSOs in a H-R diagram: Herbig Ae/Be stars (HAe/Be) (blue solid dots), Classical T Tauri stars (CTTSs) (red solid squares), Weak T Tauri stars (WTTSs) (red empty squares), Intermediate Mass T Tauri stars (IMTTSs) (cyan solid triangles), and substellar objects (substellar TTSs) (pink solid triangles). Also shown is the Zero Age Main Sequence (ZAMS), as well as evolutionary tracks for stars of different masses (solid lines) as indicated in the labels, and isochrones for: 0.3, 1, 3, 10 , and 30 Myr (from top to bottom). Figure taken from Calvet & D'Alessio (2011).

stellar mass M_*, radius R_*, and age (see §2.2).

Figure 1.3 shows the location of a sample of YSOs in a H-R diagram. In this diagram we show the evolutionary tracks for different stellar masses indicated in the labels (solid lines) from Siess, Dufour & Forestini (2000); young stars of a given mass move along these lines during their life. The isochrones from Baraffe et al. (1998) (constant age lines) are shown with dashed lines. In the pre-main sequence phase, low-mass stars have convective interiors, and obtain their energy from gravitational contraction, while some might undergo fusion reactions of Deuterium and Lithium for a short period of time. The presence of these elements is revealed in the spectra of TTSs, and is used as a youth tracer (e.g. Briceño et al., 1997, 2019). As shown in Figure 1.3, TTSs evolve along Hayashi lines, reducing their radius at almost constant $T_{\rm eff}$, thus, decreasing their luminosity.

1.4 Dust continuum and photometry

The dust in the disk is the main source of opacity, although it represents only $\sim 0.01\%$ of the disk mass, thus, in order to understand and reproduce observations coming from dust emission (e.g. photometric data and continuum images) it is important to know the dust properties (see §3.2.4). The dust component is subject to many physical processes such as radial drift, vertical settling, and diffusion of large particles (Dullemond & Dominik, 2004; D'Alessio et al., 2006; Alexander & Armitage, 2007; Hughes & Armitage, 2010; Birnstiel et al., 2012; Bitsch et al., 2015); simultaneously, the dust grains coagulate, they fragment, and are affected by the presence of dust traps and vortexes in the disk (Brauer et al., 2007; Birnstiel et al., 2010, 2012; Ali-Dib et al., 2014; Andrews et al., 2018; Testi, 2014, and references therein). The sum of these processes induces the formation of planetesimals and influences the final location of the forming planets in the disk.

Accretion disks surrounding young, low-mass pre-main sequence stars have been extensively studied over the last three decades, thanks to the advent of photometric data, as well as the first images of disks, revealed by interferometric observations using the Very Large Array (VLA) (Rodríguez et al., 1992, 1994).

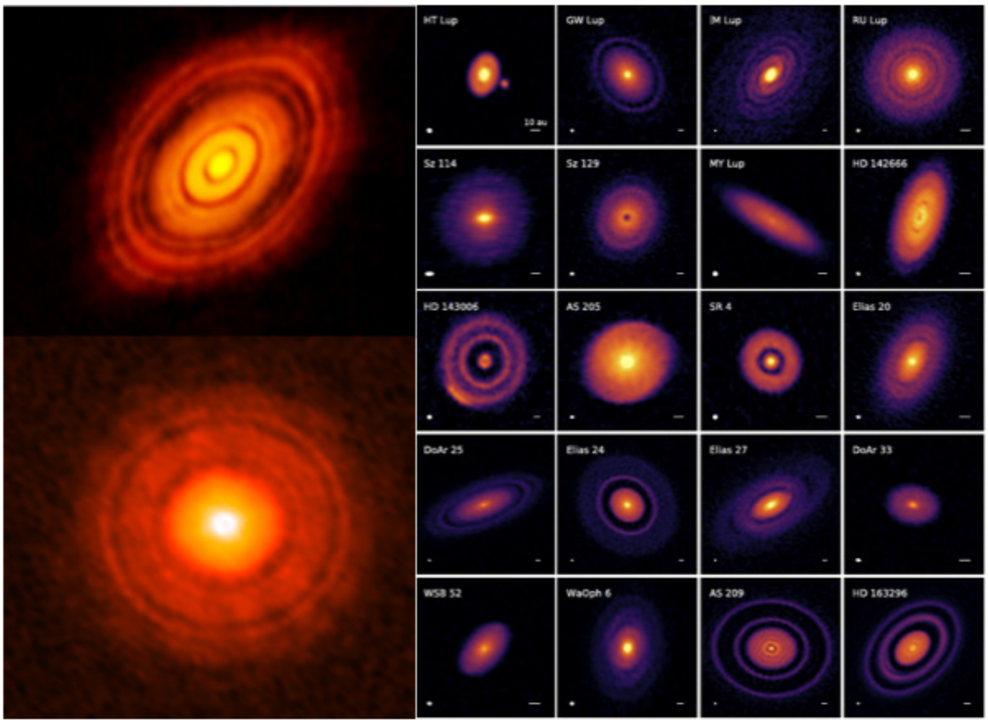

Figure 1.4: 1.3 mm ALMA dust continuum image of HL Tau (upper left) from ALMA partnership (2015), 870 mm ALMA image of TW Hya (lower left) from Andrews et al. (2016), and 1.25 mm continuum emission from the disks in the DSHARP sample (right half) from Andrews et al. (2018).

Since then, and encouraged by the quick development of sophisticated numerical models to calculate the detailed physical structure and emission of disks (e.g. D'Alessio et al., 1998, 2006; Alexander & Armitage, 2007; Birnstiel et al., 2012; Bitsch et al., 2015), their study has substantially grown, currently being one of the most active in the field. The growing amount of observational data has not only allowed researchers to directly measure some of the disks' properties, but also to provide constraints to the models, leading to a better understanding of the physical processes that favor the formation of planetesimals and, eventually, rocky and giant planets. Using instruments such as the Sub-Millimeter Array (SMA), the Very Large Array (VLA), and in more recent years the Atacama Large Millimeter Array (ALMA), disk images have been obtained with amazing detail using dust thermal emission, e.g., the disks around HL Tau and TW Hya (ALMA partnership, 2015; Andrews et al., 2016), as well as disks' surveys (Andrews et al., 2018), which have revealed that disks have substructure such as gaps, spiral arms and dust asymmetries (cf. Figure 1.4).

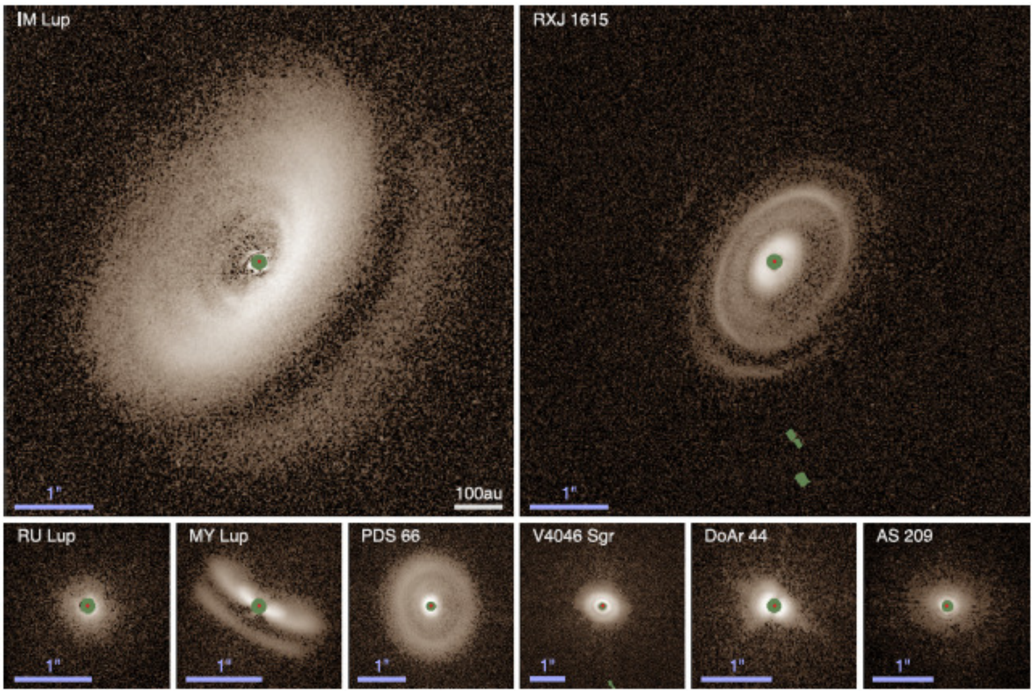

Figure 1.5: VLT SPHERE/DARTIS images of disks in Lupus, obtained using polarimetric differential imaging in the H band. The green zones are the areas obscured by the coronagraph or bad pixels, while the red dots represent the positions of the stars. Figure and details can be found in Avenhaus et al. (2018).

Detailed studies about the dust distribution and the properties of the dust grains have been carried out, using ALMA and VLA observations; in particular these studies suggest not only grain growth, but also that the properties of the dust grains change at different disk radii, e.g., in the ~ 1 Myr old disk around HL Tau (Carrasco-González et al., 2016; Liu et al., 2017; Carrasco-González et al., 2019). It has also been suggested that dust settling towards the midplane is present in HL Tau, with large (1 cm) dust grains located in the midplane, and small (100 μm) grains in the disk atmosphere (Tapia et al., 2019).

In addition, the photometric data from various instruments (e.g. *Spitzer* IRAC and MIPS 24, WISE, Herschel PACS) and the detailed modeling of these data, have contributed to a better understanding of the dust properties and also to identify new types of disks, such as transitional disks (TDs) and pre-transitional disks (Espaillat et al., 2007, 2010, see §1.7). In parallel, infrared spectra obtained with instruments such as the *Spitzer* IRS have allowed precise determinations of the dust composition in disks, revealing different levels of dust processing and mineralogy (e.g. Oliveira et al., 2011; McClure et al., 2012). Complementary, using disk models to fit millimeter photometry (e.g. ALMA, SMA, SCUBA) in the SEDs, disk masses estimates have been obtained (e.g. Williams et al., 2013; Cieza et al., 2015; Maucó et al., 2016). More recently, Very Large Telescope (VLT) observations of T Tauri disks in the Lupus region, using SPHERE/IRDIS polarimetric differential imaging (Avenhaus et al., 2018), have shown impressive three-dimensional disk structures, tracing the scattered light on their surfaces (cf. Figure 1.5). The different observations complement each other, and they illustrate how the development of instruments and telescopes allows us to get direct images and data with a high level of detail.

Studies of large samples of disk-bearing stars in several stellar groups and clusters of different ages also provide information about the evolution of the disks' bulk matter. These studies have revealed observational trends that may also indicate evolution signatures in the disks and help to constrain the disks' lifetimes. In particular, it has been found that the median strength of

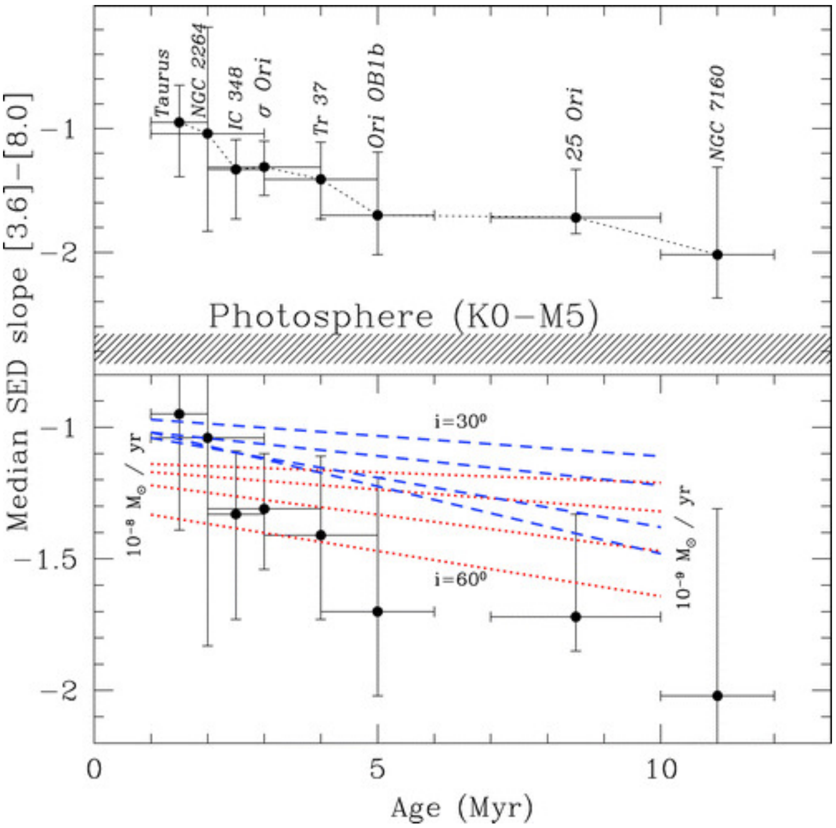

Figure 1.6: Median SED slope in the IRAC spectral range versus ages of various stellar groups. Distinct lines represent different degrees of settling, showing flatter slopes for models with smaller degree of settling. Models with an inclination angle i, between the disk rotation axis and the line of sight, are shown in blue ($i = 30^{\mathrm{o}}$) and red ($i = 60^{\mathrm{o}}$). Figure from Hernández et al. (2007a).

the near-infrared excess in disks of a given population decreases as the age of the population increases (Hernández et al., 2007b; Luhman et al., 2010), as shown in Figure 1.6. As mentioned before, the IR excess arises from hot and warm dust in the disk, as opposed to the colder dust, which is traced by (sub)millimeter observations. The observed decrease of the strength of the excess in the SEDs may be consistent with the decrease of total disk mass with time resulting from viscous evolution (see §3.1). Alternatively, the decay of emission may require dust evolution, such as growth and settling towards the midplane (Weidenschilling, 1997; Dullemond & Dominik, 2004; Birnstiel et al., 2009, 2010, 2011). Despite recent progress, details of the processes leading to the decrease of dust emission with age are still uncertain.

1.5 Mass accretion rates, molecular lines, and snowlines

In addition to the dust component, the gas component of the disks has also been a subject of study. The mass accretion rate ($\dot{M}$) is a measure of the amount of disk material that falls onto the star per unit time, thus, it provides information about the gas content. During the period of accretion, a fraction of the gas in the disk ends up falling onto the star, which increases its mass, and releases accretion energy in the process. This accretion energy appears as a continuum excess that veils the photospheric lines and dominates in the UV continuum and in emission lines (Calvet & Gullbring, 1998; Hartmann, Herczeg & Calvet, 2016). Measurements of mass accretion rates indicate that stars are accreting material at different rates. It has also been found that the mass accretion rate decreases with age (Hartmann et al., 1998; Hartmann, Herczeg & Calvet, 2016, and references therein), which is consistent with the viscous evolution of self-similar disks (Lynden Bell & Pringle, 1974; Hartmann et al., 1998).

Various studies indicate that $\dot{M}$ decreases with age (cf. Figure 1.7), suggesting that the gas component evolves alongside the dust component. Figure 1.7 shows the mass accretion rate versus stellar age, obtained using different methods (Balmer continumm, photometric U-band measurements, and from emission lines), for a sample of stars with masses ranging $0.3 - 1\,M_{\odot}$. This Figure shows a clear decreasing trend with age; while the dispersion present in the data might be due to the uncertainties in the different methods used to determine $\dot{M}$, as well as in age determinations and/or the stellar properties.

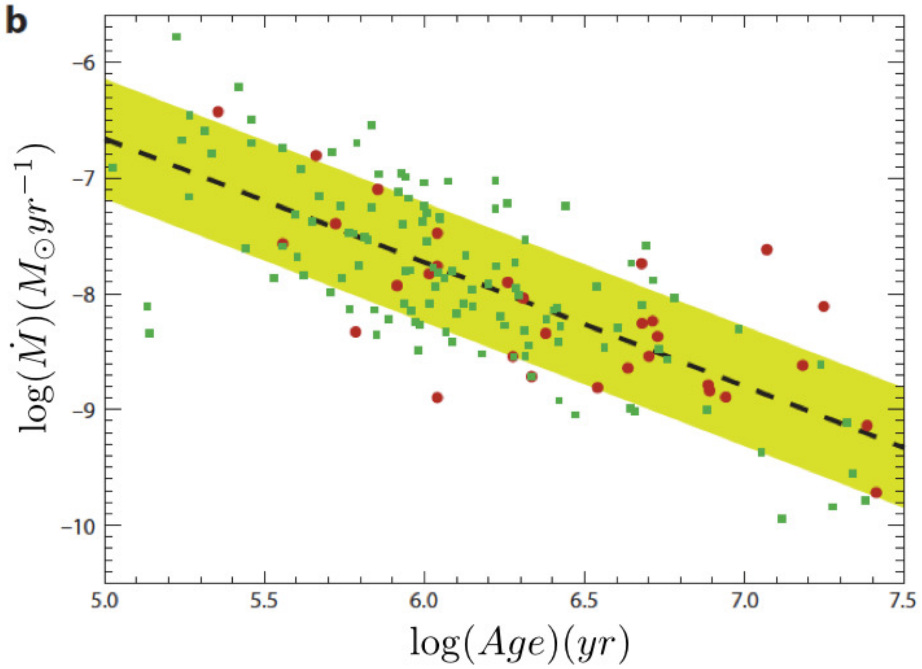

Figure 1.7: Mass accretion rates versus stellar age obtained from two methods: spectroscopic measurements of the Balmer continuum (red circles) and from emission lines (green squares). The line and the shaded region show the best linear fit and 1σ scatter, respectively. Only mass accretion rates for stars with $0.3 - 1\,M_\odot$ are shown. Figure taken from Hartmann, Herczeg & Calvet (2016).

The gas component of the disk contains atoms, molecular ions, and molecules of different species. The line mm/sub-mm emission from some of these molecules has been detected, for instance CO and its isotopologues, as well as CS, HCN, N_2H^+, DCO^+, among others (e.g. Öberg et al., 2011; Qi et al., 2011, 2013; Ali-Dib et al., 2014; Madhusudhan et al., 2014; Qi et al., 2015; Cieza et al., 2016). These observations can be used to estimate disk masses, but not all of the molecules are useful for this purpose; since CO emission is optically thick it is not a good tracer of the disk mass, however the CO isotopologues can be used instead. The different molecules can be frozen-out, photo-dissociated and/or subject to other physical conditions, depending on their location in the disk. In addition, molecular line emission can be used to obtain the kinematics of the system, however, the rotation profile of the disk, and determination of the mass of the star, can be more easily achieved in the most massive, brightest disks, as well as in disks located close by, like TW Hya. Currently, ALMA does not have the sensitivity to detect the emission from fainter disks, at the highest angular resolution configuration.

The gas species that sublimate at relatively low temperatures ($\lesssim 150$ K) are known as *volatiles*. These volatiles seem to play a major role in the process of planet formation, giving rise to an active chemistry that influences the composition of the planets' atmospheres during their formation process (Madhusudhan et al., 2011; Öberg et al., 2011; Pontoppidan et al., 2014, and references therein). Emission of molecular lines arises from transitions of different molecules such as CO, H_2O, N_2H^+, ^{13}CO, DCO^+; and these transitions can be used as tracers of the gas component throughout the disk. Measurements and determinations of the gas spatial distribution in disks allow the detection of *snowlines*. The disk radius where a certain volatile reaches its sublimation temperature is called a snowline or condensation front. Outside the snowline the volatiles are frozen, adhered to the surface of dust grains, and inside the snowline they remain in the gas phase. In the last decade, studying the location of different snowlines has gained attention, in particular to explain the chemical composition of some exoplanetary atmospheres, since it depends directly on the available molecules in the surrounding regions of the planets, during their formation process (Öberg et al., 2011; Ali-Dib et al., 2014; Madhusudhan et al., 2014). It has also been suggested that an enhancement of dust growth can occur near the location of different condensation fronts, favoring the accumulation of millimeter and decimeter grains, which might eventually form planetesimals (Zhang et al., 2015; Okuzumi et al., 2016).

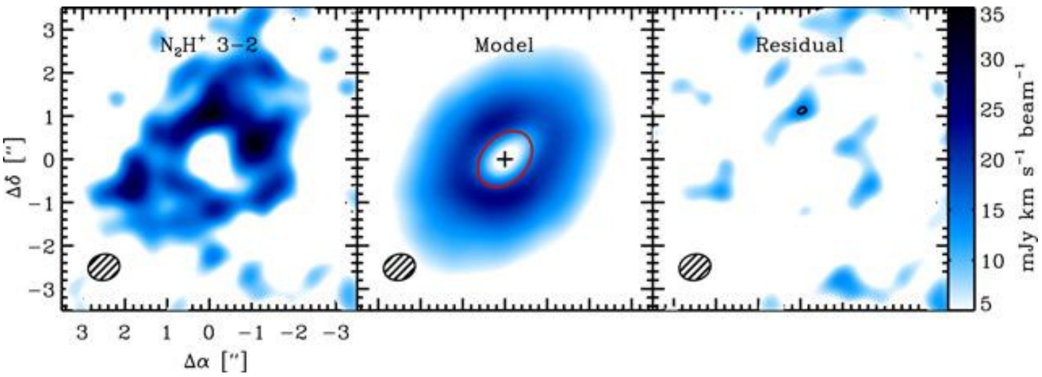

Figure 1.8: N_2H^+ J=3-2 observations for the disk around HD163296 (left panel), synthetic observations of a model (central panel), and residuals (right panel). The red ellipse indicates the N_2H^+ inner radius at 90 au. Figure taken from Qi et al. (2015).

Some authors have found that the shape and location of the different snowlines are influenced by changes in the gas surface density (Piso et al., 2015; Krijt et al., 2016; Powell et al., 2017). Molecules such as CO and its isotopologues have been observed and measured (Qi et al., 2011, 2013, 2015), e.g. Figure 1.8, and while the H_2O snowline is far more difficult to detect and study because it is located very close to the star, they are both important to understand their influence in the dust component of the disk, the chemical abundances in exoplanetary atmospheres, and also the composition of the planets and asteroids in the Solar System. A more general overview about the different theoretical and observational aspects of snowlines can be found in Pontoppidan et al. (2014).

1.6 Magnetospheric accretion

The magnetospheric accretion represents the most accepted scenario for transferring matter onto the star from the disk (see Figure 1.9). The star's magnetosphere truncates the gaseous inner disk and matter moving towards the star couples to the magnetic field forming the accretion columns, along the magnetic field lines.

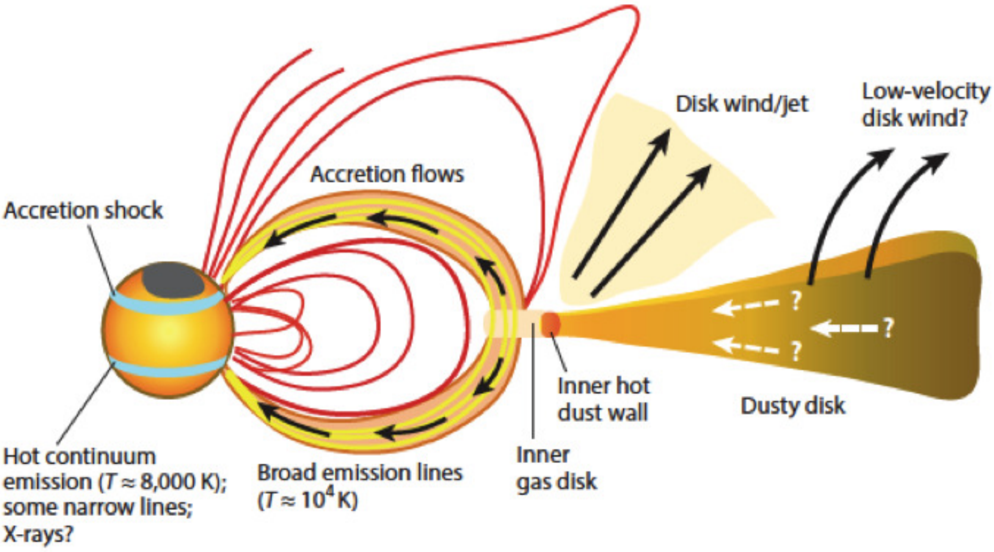

Figure 1.9: Schematic representation of an accretion disk around a pre-main sequence star. The disk emits at IR, sub-mm and mm wavelengths. A fraction the disk material falls onto the star producing accretion shocks on the stellar surface. The gaseous disk is truncated by the stellar magnetosphere, while the dust sublimation radius is located outside the magnetospheric radius $R_{\rm mag}$. The material being accreted emits broad emission lines as it falls onto the star, and produces a hot continuum when it reaches the stellar surface. Figure taken from Hartmann, Herczeg & Calvet (2016).

This scenario explains not only the presence of some observed emission-line profiles, but also the UV and optical flux excesses in CTTSs (cf. Figure 1.10). These fluxes are thought to originate when the material crashes on the stellar surface, forming the accretion shocks, where the excess of kinetic energy dissipates (Hartmann, Herczeg & Calvet, 2016, and references therein).

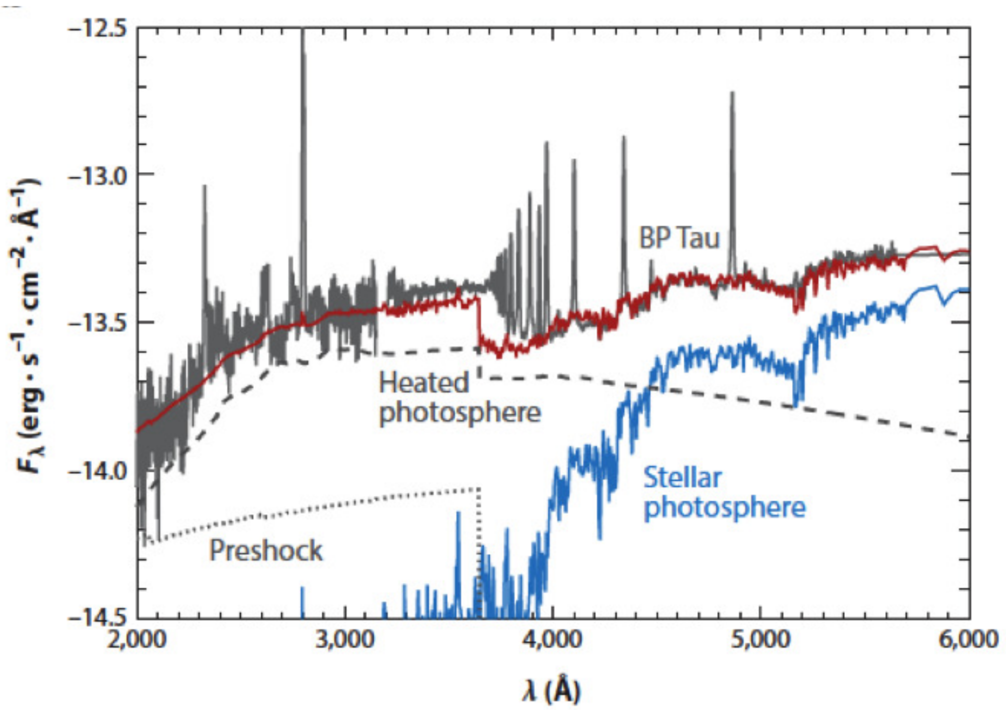

Figure 1.10: SED of BP Tau (gray line) and the stellar photosphere (blue line). Also shown is an accretion shock model (red line) with two components: the heated photosphere (dashed line) and the pre-shock region (dotted line). Figure taken from Hartmann, Herczeg & Calvet (2016).

Figure 1.10 shows the SED of the CTTS BP Tau (gray line), where the contribution from the stellar photosphere is shown in blue. An accretion shock model (red line) gives a good fit to the SED, taking into account the contribution from the pre-shock region and the heated photosphere, which correspond to the dotted and dashed lines, respectively (Hartmann, Herczeg & Calvet, 2016).

It is thought that disk instabilities are responsible for episodic events of active accretion, in which the star shows a significant increase in $\dot{M}$ of several orders of magnitude, which later decreases in a period of time of decades or centuries. These objects have been designated as FU Ori objects (Hartmann & Kenyon, 1996). Another type of object with a less variable accretion are the EXor outbursts, which are interpreted as objects that increase up to 100 times their accretion rates in a period of months to a few years (e.g. Herbig, 1977, 1989). Although FU Ori and EXor outbursts are prototypical objects that show a significant variability in accretion, it is important to mention that variable accretion is a widespread phenomenon among YSOs.

1.7 Disk fraction and evolution

Studies of disks in populations ranging from $\sim$ 1 to 11 Myr indicate that the number of disk-bearing stars decreases with age, from a frequency of ~ 70 % at 1 Myr to $< 10\%$ by 10 Myr (Hernández et al., 2007a, 2008; Briceño et al., 2019). The frequency of stars accreting mass from their disk also decreases with age, in proportions similar, but not equal, to the frequency of inner disks estimated from dust emission (Fedele et al., 2010; Briceño et al., 2019). This suggests a timescale of evolution of $\lesssim$ 10 Myr, in which a young gas-and-dust rich disk can form an entire planetary system. Figure 1.11 shows the disk fraction and the accretors fraction, i.e., the number of disk-bearing stars and accretors, relative to the total number of stars of several stellar groups, versus the age of the groups, that range from 1 to 13 Myr. The drop in the frequency is more steep in the first 5 Myr, and then it flattens out, indicating that most of the inner disks disappear very fast ($\sim$ 5 Myr).

On the other hand, disk censuses using broad band photometric SEDs indicate that the decrease of IR emission leading to the evolution from optically thick full primordial disks to optically thin debris disks follows at least two evolutionary pathways (Hernández et al., 2007b; Merín et al., 2010; Cieza et al., 2007; Williams & Cieza, 2011). One is represented by the *evolved*

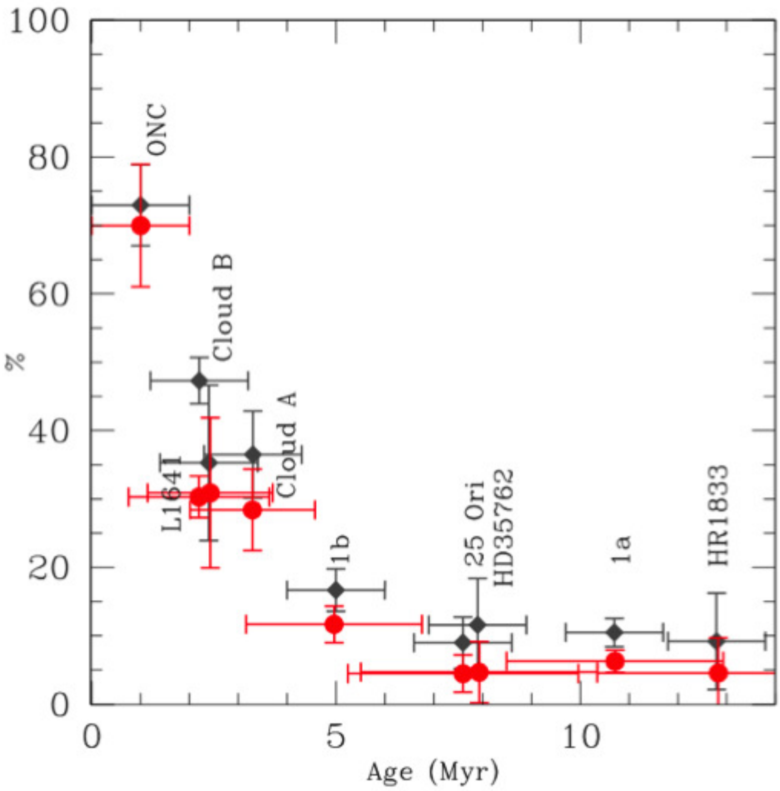

Figure 1.11: Disk fraction (gray diamonds) and accretors fraction (red solid circles) as a function of age for various stellar groups, from Hernández et al. (2007b) and Briceño et al. (2019).

disks in which the flux at all bands decreases with age (Hernández et al., 2008; Luhman et al., 2010), suggesting a gradual depletion of dust at all disk radii (Merín et al., 2010). These disks are known as evolved (used in this thesis), "anemic", "homologously depleted", and "homogeneously draining" (Lada et al., 2006; Currie et al., 2009; Koepferl et al., 2013) in which no large inner cavities are detectable in their SEDs. An alternative pathway of disk evolution comes from observations of inner disk zones cleared of small dust, which appear as flux deficits in the near-IR in the *transitional disks* (TDs; Strom et al., 1989; Calvet et al., 2002, 2005; D'Alessio et al., 2005). Observationally, classical transitional disks have been defined as protoplanetary disks with little or no near-IR excess ($\lambda \lesssim 10\mu m$) and significant excess comparable to the median of Taurus (Maucó et al., 2016; Furlan et al., 2006) at longer wavelengths. Several explanations have been given for opening holes in the inner disk: dynamical clearing by planets, photoevaporation and viscous evolution, dust grain growth, differential dust drift, dead zones and condensations fronts (Zhu et al., 2011, 2012; Espaillat et al., 2014; Owen, 2016; Alexander et al., 2014; Chiang & Murray Clay, 2007; Dullemond & Dominik, 2005; Birnstiel et al., 2012; Pinilla et al., 2016; Zhang et al., 2015). The *pre-transitional disks* (PTDs; Espaillat et al., 2007, 2010), those with an optically thick inner ring inside their large cavities, may correspond to a phase of evolution previous to transitional disks in which the innermost disk has not yet completely dissipated. The most accepted explanation is that the large gaps are due to the presence of planets, which have already been found in the cleared regions of pre-transitional disks (Keppler, 2019; Haffert et al., 2019).

Figure 1.12 shows a simple scheme of the different stages of the star formation process for low-mass stars ($M_* \lesssim 2\,M_\odot$). A rotating dense core (panel *a*) collapses, forming a Class 0/Class I object (see §1.2), i.e., a young star-disk system embedded in a dusty/gaseous envelope (panel *b*), which eventually is destroyed by a jet and/or a strong stellar wind, characteristic of these young stars, revealing the accretion disk feeding the star in the magnetospheric accretion scenario (panel *c*). At a later stage, a pre-transitional disk is formed; these disks are characterized by having gaps devoid of dust possibly due to planets forming inside those regions (panel *d*); once the inner disk is completely dissipated, the protoplanetary disk shows a large inner hole (tens of au), probably with planets inside the hole, forming a transitional disk (panel *e*). In the last stages, the system evolves towards a debris disk (panel *f*), a gas-poor disk in which the dust component has almost entirely coagulated into major rocky bodies to, eventually, form a new planetary system (panel *g*). As an illustration, Figure 1.13 shows artistic images of disks at different evolutionary stages: a full disk (upper left), a pre-transitional disk (upper

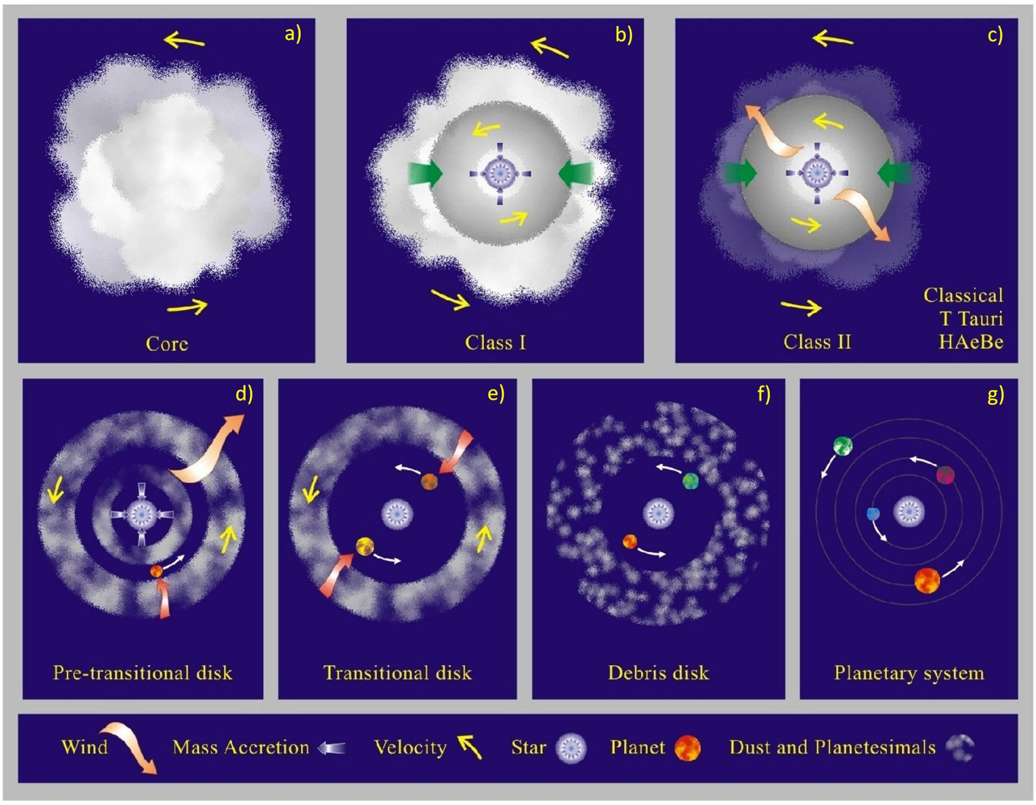

Figure 1.12: Different stages of the star formation process of low-mass stars, with $M \lesssim 2M_\odot$. Credits: Alberto García "el artista".

right), a transitional disk (lower left), and a debris disk (lower right).

As discussed in §1.4, ALMA high angular resolution observations at submillimetric wavelengths have shown that dust substructure is ubiquitous in protoplanetary disks, with multiple rings and spiral arms detected in numerous disks (ALMA partnership, 2015; Andrews et al., 2016, 2018); transitional disks and pre-transitional disks are extremes cases in which the dust structures are also apparent in the SEDs. Several interpretations have been suggested for these structures. For instance, large dust particles get trapped at the edges of gaps opened by forming planets, resulting in bright rings (Zhang et al., 2018). Alternatively, the gaps could be due to changes in the

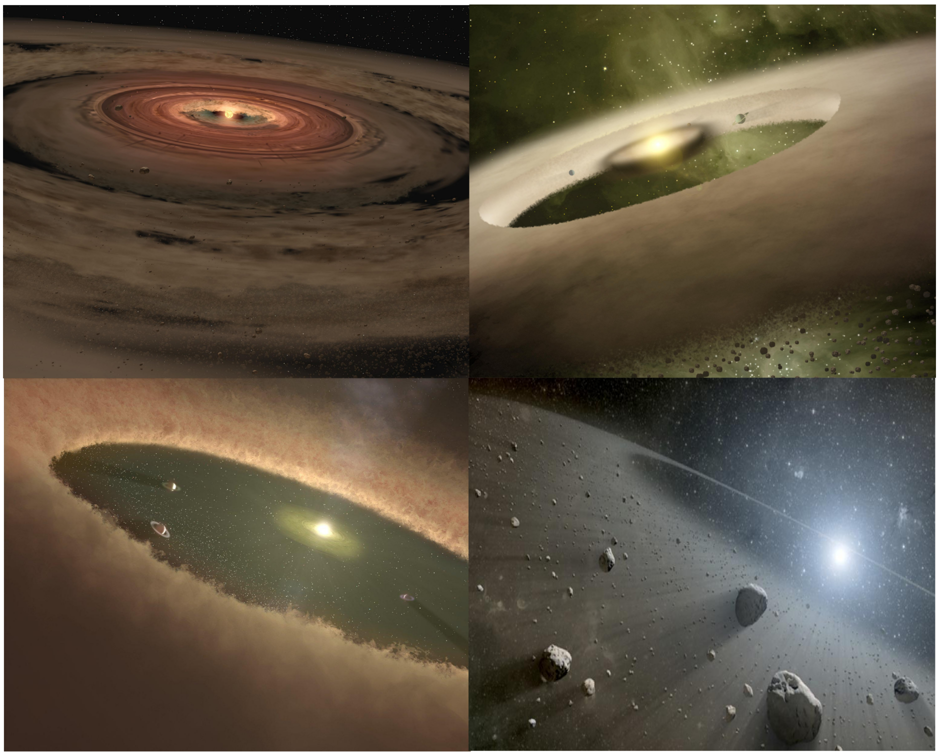

Figure 1.13: Artist's conceptions of disks at different stages of evolution. Show are a full disk (upper left), a pre-transitional disk (upper right), a transitional disk (lower left), and a debris disk (lower right). Images taken from https://www.spitzer.caltech.edu, www.universetoday.com, nexsci.caltech.edu, and www.irs.uni-stuttgart.de.

dust properties, as happens in sublimation fronts (Zhang et al., 2015). In any event, observations of disk structures are biased towards the bright and largest disks, as well as the closest (Andrews et al., 2018; Long et al., 2018, 2019), as discussed in §1.5. On the other hand, except for the TDs, disks with detected structure share the same location in near and mid-IR color-color diagrams as many unresolved disks (cf. IRAC colors in Hartmann et al., 2005), which might suggest a common overall evolution, at least in the inner regions.

1.8 Thesis objectives

Several studies give different estimates for the relative numbers of (pre) transitional and evolved disks in populations of different ages. Part of these differences arises because the criteria to define a transitional or an evolved disk are far from homogeneous (Williams & Cieza, 2011). In this work we use the observational definition of transitional disk as given above, which physically corresponds to disks with inner holes of tens of au (Espaillat et al., 2012, 2014). These disks represent <10-20% of the total disk population in young stellar clusters (Muzerolle et al., 2010). Our focus in this work will be the rest of the disks, which encompass the "weak" and "warm" excess disks of Muzerolle et al. (2010), the "primordial ultra-settled" and the "homogeneous draining" of Koepferl et al. (2013) and Ercolano et al. (2015), the "anemic" of Currie et al. (2009), and the "evolved" of Hernández et al. (2008) and Luhman et al. (2010).

For the development of this thesis we carry out a new disk census, including well known, nearby, young stellar groups studied using *Spitzer* IRAC photometry (3.6, 4.5, 5.8, and 8 μm; Fazio et al., 2004) and the 24 μm MIPS photometry (Rieke et al., 2004). In general, we also use optical PANSTARRS data (Chambers et al., 2016) to trace the stellar photosphere of the disk-bearing stars. The groups included in this work have ages between 1 and 11 Myr, the critical age range where significant disk evolution takes place (Hernández et al., 2007a). We study the evolution of dust using a new indicator of the flux excess over the photosphere in the near and mid-IR, between 4.5 μm and 24 μm. We also use the D'Alessio Irradiated Accretion Disk (DIAD) models (D'Alessio et al., 1998, 1999, 2001, 2005, 2006) to infer the state of the dust at a given age using Approximate Bayesian Computation, which is a statistical method that uses the models to find the mean distributions of different disk parameters, by reproducing disks' near and mid-IR observables. In addition, in contrast to previous works, we also include the decrease of the observed mass accretion rate with age as an additional constraint in the evolution. In particular, we focus on indicators of dust settling at two size scales, at ~ 0.1 au and at ~ 10 au, to explore the degree of inner disk settling.

The structure of this thesis is the following. In Chapter 2, we present the general properties of the stellar populations studied in this work, calculate the stellar properties and disks excesses, as well as mass accretion rates, and discuss how they change as the age increases. In Chapter 3 we describe the viscous evolution of disks, detail the disk models that we use to interpret the observations and the approximations we adopt. In Chapter 4 we explain our model grid and the statistical method used to reproduce the observed data. In Chapter 5 we present the results inferred from using these models to interpret the disk evolution indicators, discuss our results, and put them in context of what is known from previous studies. Finally, in Chapter 6 we summarize and present the conclusions.

2

Observed disk evolution

In this Chapter we describe the general properties of the stellar groups included in this work (§2.1) and explain how we obtain stellar luminosities and stellar masses, as well as the extinction for all the stars in the sample (§2.2). Then we introduce a new indicator of IR excess in the near and mid-IR: the disk color excess (see §2.3), which we use to trace the evolution of the dust component of the disk. Additionally, we describe how the stellar groups are distributed into four age bins to make a study with good statistical significance (§2.4). In addition, we show the observational trends we find, which suggest clear signatures of disk evolution in the different groups (§2.5). Finally, we describe how we determine mass accretion rates homogeneously and show the corresponding results (§2.6), finding a decreasing trend for $\dot{M}$ with age, as revealed by previous studies.

2.1 Sample of stellar populations

Studies of disk-bearing stars in various stellar populations spanning a wide age interval allow us to understand the physical processes the disks are undergoing, producing the observed evidences of evolution not only seen in the dust component, but also related to the gas content. It is important to perform statistical studies in order to quantify and constrain the physical parameters of the disks, that are responsible for producing these evolution signatures (cf. Figures 1.6, 1.7, and 1.11). Detailed models of the structure and emission of disks are often used to reproduce the observed data (SEDs, IR slopes, dust continuum images, molecular line emission), providing powerful tools to characterize the physical properties of the disks (e.g. D'Alessio et al., 1998, 1999, 2005; Calvet et al., 2005; D'Alessio et al., 2006; Espaillat et al., 2007, 2010; McClure et al., 2013; Grant et al., 2018).

The purpose of this thesis is to make a comprehensive statistical study of the evolution of disks around T Tauri stars, motivated by the large amount of observed signatures of evolution. The importance of statistical studies lies in the fact that they give us insights on the global picture concerning how disks evolve, from optically thick full disks to optically thin structures, and eventually into a planetary system similar to ours. The sample we use consists of nearby ($\lesssim$ 500 pc), young ($\sim$ 1 to 11 Myr old) stellar clusters/groups with previously reported *Spitzer* photometry, as well as available spectroscopic information for most of the stars reported in each stellar group. The stellar clusters/groups included in this work are the following (see Table 2.1): the Orion Nebula Cluster (ONC), Taurus, the IC 348 cluster, the σ Orionis cluster (σ Ori), the λ Orionis cluster (λ Ori), the Orion OB1b subassociation (Ori OB1b), the Upper Scorpius subassociation (UpSco), the γ Velorum cluster (γ Vel), and the Orion OB1a subassociation (Ori OB1a), which includes the stellar aggregate 25 Ori and the recently identified aggregates HD 35762 and HR 1833 (Briceño et al., 2019). For each cluster/group, we compiled stars in the spectral range K0-M6, which have temperatures ranging $2600\,\mathrm{K} \lesssim T_{\mathrm{eff}} \lesssim 5030$ K. One of the main objectives of this thesis is to study the evolution of the dust component of the disk (§2.5), hence, we selected stars in the above mentioned clusters/populations, with additonal IRAC photometry in all four bands ([3,6], [4.5], [5.8], and [8.0]). At this point of the selection, the sample contains diskless stars as well as disk-bearing stars. In

§2.3 we describe the methodology followed to separate the disk-bearing stars from the rest, in each stellar group.

Table 2.1: Stellar groups

Group	Mean distance pc	Age Myr	Disk fraction %	References	Initial Sample	Disk-bearing stars	Accretors sample	Age bin
ONC	400	1-3	73 ± 5.9	4,7,4	508	305	228	1
Taurus	130-200	1-2	63.6 ± 5.1	8,9,*	137	87	16	1
IC 348	320	2-3	47 ± 12	10,1,1	163	59		2
σ Ori	400	3	36 ± 4	11,2,2	185	73	40	2
λ Ori	400	4-6	18.5 ± 4	12,3,3	142	24		3
Ori OB1b	400	4-5	13-17	4,17,6	278	45	59	3
Upper Sco	146	5-11	25 ± 0.02	13,14,9	59	19		3
γ Vel	345	7.5	5-7	15,16,5	125	14		4
Ori OB1a	350-360	6-13	6-10	4,4,6	189	13	77	4

References: (1) Lada et al. (2006), (2) Hernández et al. (2007a), (3) Hernández et al. (2010), (4) Briceño et al. (2019), (5) Hernández et al. (2008), (6) Hernández et al. (2007b), (7) Hillenbrand et al. (2013), (8) Galli et al. (2019), (9) Luhman & Mamajek (2012), (10) Ortiz-León et al. (2018), (11) Pérez-Blanco et al. (2018), (12) Kounkel et al. (2018), (13) Galli et al. (2018), (14) David et al. (2019), (15) Franciosini et al. (2018), (16) Jeffries et al. (2017), (17) Maucó et al. (2018). *Using the data from Luhman et al. (2010) we estimate a disk fraction of 63.7 ± 5.1 in Taurus.
Column "Initial sample" refers to the number of K0-M6 stars initially compiled (diskless and disk-bearing stars) with IRAC and PANSTARRS photometry in each stellar group. Column "Disk-bearing stars" refers to the number of stars with near-IR excess above the photosphere, separated according to §2.3, which correspond to the sample used to study the dust component of the disks. Column "Accretors sample" refers to the CTTSs/CWTTSs sample, described in §2.6 used to study the evolution of $\dot{M}$.

Another important objective of this thesis is to study the mass accretion rates of the disks (§2.6). For this purpose, we use a different sample from the one used to study the dust component. In this case we selected previously confirmed TTSs with existing measurements of the equivalent width of the Hα line (EW Hα), measured using the SpTClass tool (Hernández et al., 2004; Hernández et al., 2017), and with GAIA DR2 parallaxes with relative errors $\lesssim 20\%$, regardless of whether or not they have IRAC photometry. This means that some stars in this sample, used to calculate mass accretion rates, additionally have IRAC photometry and thus they also belong to the sample used to study the dust component. However there are stars which do not have IRAC photometry, while having the necessary information to determine the corresponding mass accretion rate. As a consequence, there are stars in this sample of accretors, which do not belong to the sample used to study the dust component using color excesses and, accordingly, there are stars with color excesses for which $\dot{M}$ could not be determined.

One relevant aspect of this work, related to the sample selection, is that we keep our sample as homogeneous as possible, trying to minimize the presence of inconsistencies in the treatment of the data and/or determinations of parameters. For instance, using different methods, optical colors, and evolutionary tracks to determine mass accretion rates, extinctions, and stellar properties, respectively, introduces dispersion in the data, which we would like to minimize. Following this idea, we use the color $[g - i]$ from PANSTARRS (Chambers et al., 2016) to estimate homogeneously visual extinctions for the samples of TTSs (see §2.2). Thus we also require that the TTSs have g and i magnitudes reported by PANSTARRS [1]. Table 2.1 shows the general properties of the stellar populations included in this work, which were compiled from the literature, except for the last four columns. Based on both the stellar ages and disk frequencies previously reported, as an independent indicative of the age, we grouped the stellar population into four age bins (see last column of Table 2.1).

2.1.1 Orion Nebula Cluster sample

The ONC is a very young stellar cluster ($\sim 1 - 3$ Myr; Hillenbrand, 1997; Hillenbrand et al., 2013; Da Rio et al., 2010; Megeath et al., 2016) with a mean distance of $\sim$ 400 pc (Briceño et al., 2019, using GAIA DR2 data). Also Briceño et al. (2019) estimate a disk frequency of $\sim 73 \pm 5.9\%$. The initial sample of TTSs includes 782 stars with spectral types, equivalent widths

---

[1] Except for the γ Velorum cluster, which was not observed by the PANSTARRS survey.

of Li1 λ6708 Å (EW LiI), and EW Hα obtained from the analysis of low-resolution spectra observed with the fiber-fed multi-object Hectospec instrument mounted on the 6.5 m. Telescope of the MMT Observatory (Hernández et al., 2020a in prep.). We also include 127 TTSs with spectral types, EW LiI, and EW Hα reported by Briceño et al. (2019). Spectral types, EW LiI, and EW Hα were obtained using the SpTClass code (Hernández et al., 2017), an IRAF/IDL code based on the methods described in Hernández et al. (2004). We complete the initial sample adding 86 TTSs and 48 TTSs with spectral types reported by Hillenbrand (1997) and Hillenbrand et al. (2013), respectively. Out of 1036 TTSs in the initial sample, 500 TTSs have IRAC/MIPS photometry reported by Megeath et al. (2012). We also include 170 additional TTSs with IRAC/MIPS photometry provided by Tom Megeath (private communication) which were not included in Megeath et al. (2012). Finally, out of 670 TTSs with IRAC/MIPS photometry, we select 508 K0-M6 TTSs with g and i magnitudes from PANSTARRS .

2.1.2 Taurus complex sample

Taurus is one of the best studied and closest star-forming molecular cloud complexes, with an estimated age of $\sim 1-2$ Myr (Luhman et al., 2010; Furlan et al., 2011). Using data from Luhman et al. (2010) we estimate a disk frequency of this complex of $\sim$ 63.7 ± 5.1% for K0-M6 stars. Based on distances provided by GAIA DR2 and Very Long Baseline Interferometry (VLBI) observations, Galli et al. (2019) show that the Taurus star forming complex includes several molecular clouds located at different distances (from $\sim$130 pc to $\sim$200 pc). Based mostly on the work of Hartmann et al. (2005) and Luhman et al. (2010), Esplin et al. (2014) compiled 414 members of Taurus with IRAC/MIPS photometry. From this sample, we selected 260 TTSs with measurements in all the photometric bands of IRAC and with spectral types ranging from K0 to M6. In some cases, stars identified as binary stars have spectral types for the two components (e.g. M1+M7); in this case we select the spectral type of the brighter component (e.g. M1). Out of 260 TTSs, 137 TTSs have g and i photometry from PANSTARRS. On the other hand, in order to study the mass accretion rates, a sample of 100 TTSs with optical low resolution spectra available from the FAST Public Archive [2] was selected. We have measured EW Hα in this thesis for this sample using the SpTClass tool (Hernández et al., 2017).

2.1.3 IC 348 cluster sample

IC 348 is a nearby and compact young cluster ($\sim$ 2-3 Myr) located in the Perseus OB2 star forming region (Lada et al., 2006; Herbst, 2008). Combining trigonometric parallaxes from Very Long Baseline Array (VLBA) observations and GAIA DR2 parallaxes, Ortiz-León et al. (2018) estimate a distance of ∼320 pc for this cluster. Lada et al. (2006) estimated a disk frequency of $\sim 47 \pm 12\%$ and provide spectral types and IRAC/MIPS photometry for 307 stars in the IC 348 cluster. From this set, we selected 220 stars with spectral types ranging from K0 to M6 and with photometric measurements in all IRAC bands. Out of 220 TTSs, 163 TTSs have PANSTARRS g and i magnitudes.

2.1.4 σ Ori cluster sample

σ Ori is a young ($\sim$ 3 Myr) and relatively populous stellar cluster located in the Orion OB1b sub association and with a disk frequency of $\sim 36 \pm 4\%$ (Hernández et al., 2007a). Using GAIA DR2 parallaxes, Pérez-Blanco et al. (2018) estimate a mean distance of ∼400 pc. We have selected 221 TTSs with spectral types ranging from K0 to M6, EW LiI, and EW Hα obtained by Hernández et al. (2014) using the SpTClass tool and with photometric measurements in all IRAC bands (Hernández et al., 2007a). From this sam-

---

[2] http://tdc-www.harvard.edu/cgi-bin/arc/fsearch

ple, 185 TTSs have PANSTARRS g and i magnitudes.

2.1.5 λ Ori cluster sample

λ Ori is a young (∼4-6 Myr) and relatively populous stellar group with an overall disk frequency for M type stars of $\sim 18.5 \pm 4\%$ (Hernández et al., 2010). Combining spectroscopic and astrometric data from APOGEE-2 and GAIA DR2, Kounkel et al. (2018) reported an average distance of ∼400 pc for this stellar cluster. Spectral types were compiled from Bayo et al. (2011) and Sacco et al. (2008). We also add stars with effective temperatures reported by Bayo et al. (2008) and Bayo et al. (2011). Those effective temperatures were converted to spectral types using Table 6 from Pecaut & Mamajek (2013). From this compilation we have selected 181 TTSs with spectral types ranging from K0 to M6 and with photometric measurements in all IRAC bands (Hernández et al., 2010). From this sample, we select 142 TTSs with PANSTARRS g and i magnitudes.

2.1.6 Ori OB1b region sample

Briceño et al. (2019) report EW LiI and EW Hα for 551 TTSs with spectral types ranging from K0 to M6 located in this subassociation. Based on GAIA DR2 parallaxes and the PMS models of Siess, Dufour & Forestini (2000), Briceño et al. (2019) adopted a distance of 400 pc and a stellar age of ∼5 Myr. The disk frequency in Ori OB1b is $\sim 13-17\%$ (Hernández et al., 2007b; Briceño et al., 2019). Out of 551 TTSs, 104 and 213 TTSs have photometric measurements in all IRAC bands provided by Hernández et al. (2007b) and Hernández et al. (2020b in prep.), respectively. From this sample, we select 278 TTSs with PANSTARRS g and i magnitudes.

2.1.7 Upper Scorpius region sample

Upper Sco is the youngest stellar population of the Scorpius-Centaurus OB association, which is the nearest region of recent massive star formation (Preibisch & Mamajek, 2008). Based on the GAIA first data release, Galli et al. (2018) estimate a mean distance of ∼146 pc. Stellar ages estimated for Upper Scorpius range from ∼5 (Preibisch et al., 2002) to 11 Myr (Pecaut et al., 2012) and recently, using eclipsing binaries, David et al. (2019) estimate an age of 5-7 Myr. Out of 306 stars in Luhman & Mamajek (2012) with spectral types ranging from K0 to M6, 74 stars have protoplanetary disks. The disk frequency reported by Luhman & Mamajek (2012) is $\sim 25 \pm 0.02\%$ for Upper Scorpius. Out of 306 K and M stars, 90 stars have photometric measurements in all IRAC bands. Finally, out of 90 stars, we select 59 stars with PANSTARRS g and i magnitudes.

2.1.8 γ Velorum cluster sample

γ Vel is a young stellar cluster with a central binary system consisting of an O7.5 star and a Wolf-Rayet star (WC8; Hernández et al., 2008). Based on GAIA DR2 observations, Franciosini et al. (2018) estimate a distance of ∼345 pc. The stellar age of the γ Velorum cluster can range from 5 Myr to 20 Myr, with an age of 7.5± 1 Myr inferred from the color-magnitude diagram (Jeffries et al., 2017). The disk frequency of the cluster is $\sim 5-7\%$ (Hernández et al., 2008). Out of 557 stars with optical photometry (V, $\mathrm{I_c}$) and IRAC photometry in all bands (Hernández et al., 2008), we compile 125 stars with effective temperatures lower than 5000 K (e.g. spectral type K0 or later; Pecaut & Mamajek, 2013) reported by Spina et al. (2014), Frasca et al. (2015) or Smiljanic et al. (2016). From the sample of 125 stars, 11 do not have reported spectral types or effective temperature, thus we estimate their stellar mass using the $[\mathrm{V}-\mathrm{I_c}]$ versus stellar mass relation from Prisinzano et al. (2016), then we estimate their effective temperature from the relation $T_{\rm eff} = 1005.78\ M_* + 3042.1$ (Frasca et al., 2015), which is valid for $0.1\,M_\odot \lesssim M_* \lesssim 2.5\,M_\odot$. Since γ Vel is out of the area coverage of the PANSTARRS survey, we estimate visual extinction using the $[\mathrm{V}-\mathrm{I_c}]$ color instead of the $[g-i]$ color (see §2.2).

2.1.9 Ori OB1a region sample

Briceño et al. (2019) report EW LiI and EW Hα for 1211 TTSs with spectral types ranging from K0 to M6 located in this sub-association. This sample includes 807 TTSs located in the dispersed population of Ori OB1a, and 404 TTSs members of the stellar groups 25 Ori, HR 1833, and HD 35762. Since some TTSs of the dispersed population of Ori OB1a are located close to other younger stellar groups, we rejected 100 TTSs located near the λ Ori star forming region (DEC$> 4^{\rm o}$) or near the Ori OB1b subassociation (DEC$< -2^{\rm o}$). Based on GAIA DR2 parallaxes and the PMS models of Siess, Dufour & Forestini (2000), Briceño et al. (2019) adopted a distance of 350-360 pc with a stellar age range of $\sim$9-14 Myr. The disk frequency for the Orion OB1a subassociation is $\sim 6-10\%$ (Hernández et al., 2007b; Briceño et al., 2019). Out of 1211 TTSs, 121 and 93 TTSs have photometric measurements in all IRAC bands, reported in Hernández et al. (2007b) and Hernández et al. (2020b in prep.), respectively. From this sample, we select 189 TTSs with PANSTARRS g and i magnitudes.

In Appendix A we show the information related to the sample of stars used to study the dust component, when each selection criteria is applied (cf. Table A.1). In addition, we show the corresponding information for the sample of stars used to study the mass accretion rates (cf. Table A.2) in §2.6. These tables summarize the information described above, related to the sample selection in each stellar group.

2.2 Visual extinctions, stellar luminosities, and stellar masses

The extinction A_λ is a measure of the absorption and dispersion of light in the interstellar medium (ISM) and it has a dependence on wavelength: as the wavelength increases, the extinction decreases, since the ISM dust is more efficient at absorbing short-wavelength radiation (UV, optical, IR; cf. Figure 3.4). In general, we calculate the extinction $A_{\rm V}$ for each star in our sample, using the $[g - i]$ color from PANSTARRS. One of the advantages of using PANSTARRS photometry is that this survey was performed several times per filter, over a four-year time span, which addresses the effects of variability when using the reported mean magnitude. The intrinsic photospheric color $[g - i]_{\rm o}$ was added to Table 6 from Pecaut & Mamajek (2013), using the following relation between the color $[{\rm V} - {\rm I_c}]$ and the PANSTARRS color $[g - i]$:

$$[g - i] = 0.475(\pm0.019) + 0.751(\pm0.007)\,[{\rm V} - {\rm I_c}]. \tag{2.1}$$

The relation (2.1) was obtained using a sample of confirmed TTSs with both $[{\rm V} - {\rm I_c}]$ color reported by Briceño et al. (2019) and $[g - i]$ color from PANSTARRS. We use Table 6 from Pecaut & Mamajek (2013) to interpolate the spectral types, and obtain the effective temperature $T_{\rm eff}$, the bolometric correction for the J band (BC$_J$), and the intrinsic color $[g - i]_{\rm o}$. The extinction $A_{\rm V}$ is estimated from the $[g - i]$ color with the relation:

$$A_{\rm V} = \frac{[g - i] - [g - i]_{\rm o}}{A_g/A_{\rm V} - A_i/A_{\rm V}}, \tag{2.2}$$

using the standard interstellar reddening law ($R_{\rm V}$=3.1) and relations from Cardelli, Clayton & Mathis (1989), with a central wavelength of 0.481 μm and 0.752 μm for the g and i band, respectively (Tonry et al., 2012). The PANSTARRS survey does not cover the region of the sky of γ Vel, thus, the extinction $A_{\rm V}$ for this stellar cluster is estimated from the color $[{\rm V} - {\rm I_c}]$ and the standard interstellar reddening law, and the relation from Cardelli, Clayton & Mathis (1989), with a central wavelength of 0.79 μm for the $\mathrm{I_c}$ filter. The intrinsic color $[\mathrm{V}-\mathrm{I_c}]_\mathrm{o}$ was estimated by interpolating the effective temperature in Table 6 from Pecaut & Mamajek (2013). Figure 2.1 shows a comparison between the extinction A_V derived from the PANSTARRS $[g-i]$ color and A_V obtained from the color $[\mathrm{V}-\mathrm{I_c}]$; this comparison is performed using a sample of CTTSs in OB1b and OB1a, from Briceño et al. (2019). The dispersion in the plot is due to the photometric and spectroscopic uncertainties, as well as the photometric intrinsic variability of young stars.

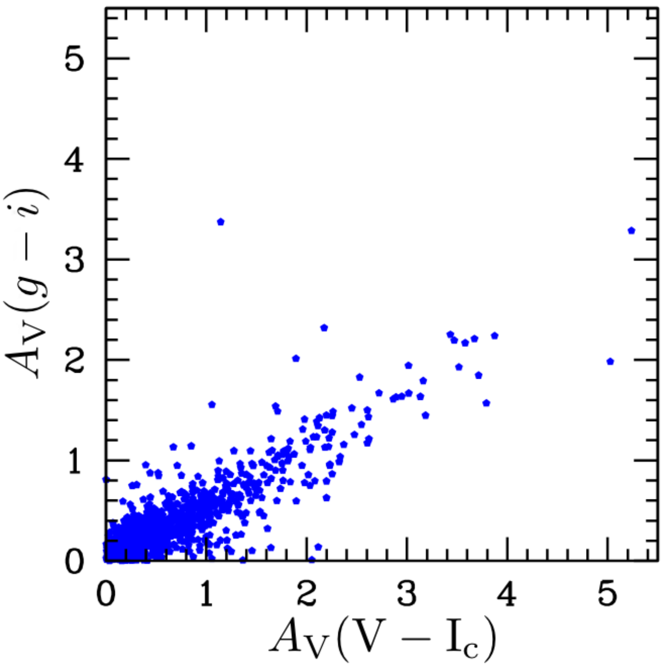

Figure 2.1: A_V derived from the PANSTARRS $[g-i]$ color vs A_V derived from the color $[\mathrm{V}-\mathrm{I_c}]$, for a sample of T Tauri stars in OB1a and OB1b from Briceño et al. (2019).

The stellar luminosities (L_*) were calculated for TTSs with uncertainties in parallaxes below 20% (Gaia Collaboration et al., 2018), thus, distances can be calculated as the inverse of the parallaxes (Bailer-Jones, 2015). For stars with uncertainties in parallaxes $\gtrsim 20\%$, the use of a prior assumption is necessary, and the inverse relation between the parallax and the distance is not valid (Bailer-Jones, 2015). We decided not to use stars with Bayesian distances, since our sample consists of stars that belong to different stellar populations/clusters; assuming a unique prior in the Bayesian determination of distances may introduce additional uncertainties in the data. From the sample that contains diskless and disk-bearing stars, $\sim 20\%$ have parallaxes with relative errors $> 20\%$. We derive the absolute bolometric magnitude from the absolute J magnitude and the bolometric correction BC_J using Table 6 from Pecaut & Mamajek (2013). The 2MASS J magnitudes (Cutri et al., 2003) were corrected for extinction using the derived $A_{\rm V}$ from PANSTARRS and the standard reddening law. Finally, the luminosities are obtained using the value $M_{bol} = 4.74$ for the Sun.

The stellar mass (M_*) is obtained by performing a double interpolation of the effective temperature $T_{\rm eff}$ and the luminosity L_* in the H-R diagram, using the evolutionary tracks from the PMS models of Siess, Dufour & Forestini (2000). From the sample of stars that contains diskless as well as disk-bearing stars, the stellar masses of some stars ($\sim 16\%$) could not be determined, since their luminosities and/or effective temperatures fall out of the range of these stellar evolutionary models.

2.3 Disk color excess

As discussed in §1.4, some authors have used near and mid-IR slopes (e.g. Hernández et al., 2007a) to study the evolution of the dust in the disk, and they have found that the median slope in the IRAC spectral range of different stellar groups decreases with stellar age (Figure 1.6), arguing that the decreasing mass accretion rates with age and the presence of dust settling might explain the decay in the IR slopes. Motivated by these studies, we introduce a new indicator of disk infrared excesses to gauge the global dust evolution: the *disk color excess* (hereafter DCE), in order to understand and quantify the evolution of the dust in the disks.

Unlike other indicators of IR excess previously used, this indicator takes into account not only the extinction correction of infrared colors used as disk tracers, but also the photospheric contribution. The J band is used as anchor of the colors to measure the infrared excesses over the photosphere because this band is representative of the stellar photosphere of TTSs, since it is less contaminated by infrared excesses produced by the dust component in the disk, or by excess emission from accretion shocks than other optical-red bands. For each star in each population described in §2.1, we define the DCE for each *Spitzer* color $[J-\lambda_{IR}]$ as follows:

$$\mathrm{DCE}_{J-\lambda_{IR}} = [J-\lambda_{IR}]_{\mathrm{obs}} - [J-\lambda_{IR}]_{\mathrm{o}} - \left(\frac{A_J}{A_{\mathrm{V}}} - \frac{A_{\lambda_{IR}}}{A_{\mathrm{V}}}\right) \times A_{\mathrm{V}}, \tag{2.3}$$

where λ_{IR} represents the *Spitzer* IRAC/MIPS magnitudes [3.6], [4.5], [5.8], [8.0], and [24], while $[J-\lambda_{IR}]_{\mathrm{o}}$ represents the intrinsic *Spitzer* photospheric colors, which depend on the stars' spectral types. In Equation (2.3), the term $[J-\lambda_{IR}]_{\mathrm{obs}}-(A_J-A_{\lambda_{IR}})$ is the correction by interstellar extinction to the observed *Spitzer* color $[J-\lambda_{IR}]_{\mathrm{obs}}$; then we subtract the intrinsic photospheric color $[J-\lambda_{IR}]_{\mathrm{o}}$ to the color corrected by extinction. The selective extinctions, $A_{3.6}/A_{\mathrm{V}}$=0.048, $A_{4.5}/A_{\mathrm{V}}$=0.035, $A_{5.8}/A_{\mathrm{V}}$=0.024, $A_{8.0}/A_{\mathrm{V}}$=0.031, and A_{24}/A_{V}=0.015, are estimated interpolating the central wavelengths of each filter using Table 21.6 from Allen's Astrophysical Quantities (Cox, 2000) assuming a standard interstellar law. The photospheric *Spitzer* colors, $[J-3.6]_{\mathrm{o}}$, $[J-4.5]_{\mathrm{o}}$, $[J-5.8]_{\mathrm{o}}$, $[J-8.0]_{\mathrm{o}}$, and $[J-24]_{\mathrm{o}}$ are estimated by interpolating the spectral types in Table 13 from Luhman et al. (2010), which contains colors for stars with spectral types later than K4. For K-type stars earlier than K4, we assume the photospheric *Spitzer* colors of a K4 star. This approximation is in agreement within 1% with empirical photospheric colors in the spectral type range K0-K4 that will be available in a forthcoming paper by Luhman

& Esplin (2020). At each age bin, the observational sample contains at most 3 K0-K4 stars (cf. Figure 2.4), thus, the estimated *Spitzer* colors are not affected, since the total sample used in each age bin is much larger than the number of K0-K4 stars.

For each stellar cluster/group in the sample described in §2.1, we separate the disk-bearing stars from the diskless stars using the distributions of DCE$_{J-[5.8]}$ and DCE$_{J-[8.0]}$, by setting a photospheric limit above which the disk-bearing stars are located. As an illustration, Figure 2.2 shows these distributions for Taurus. The corresponding distributions for the rest of the stellar groups were also built. We estimate the photospheric region by fitting a Gaussian function (green dashed line) to the DCE distributions around the photospheric values (e.g. DCE$\sim$0). We apply the 3σ-clipping method, which consists of calculating the center value (C_G) and the standard deviation (σ_G) of the Gaussian function and redoing the Gaussian fitting for stars within the range $C_G - 3 \times \sigma_G <$ DCE $< C_G + 3 \times \sigma_G$. This process is repeated until the values for the center and σ of the Gaussian function converge. In our populations, these values converge in less than four iterations. The final value of $C_g + 3 \times \sigma_G$ is used to set the limit that separates disk-bearing stars from those with photospheric values. In order to avoid stars in our sample at evolutionary stages earlier than Class II objects (e.g Class 0, Class I objects), the upper limits for disk-bearing stars are set by estimating the DCEs associated to a flat SED (DCE$_{J-[5.8]}$=4.28; DCE$_{J-[8.0]}$=5.30). Thus, our disk-bearing stars sample consists of those stars with DCEs values, in [5.8] and [8.0], between the photospheric limit and the flat SED limit. In other words, a star is classified as a disk-bearing star if it shows excess above the photospheric limit in the DCE$_{J-[5.8]}$ and in the DCE$_{J-[8.0]}$, simultaneously; also, these excesses should be lower than the flat SED limit mentioned above. The number of TTSs selected as disk-bearing stars in each stellar population is indicated in Table 2.1 (column 7).

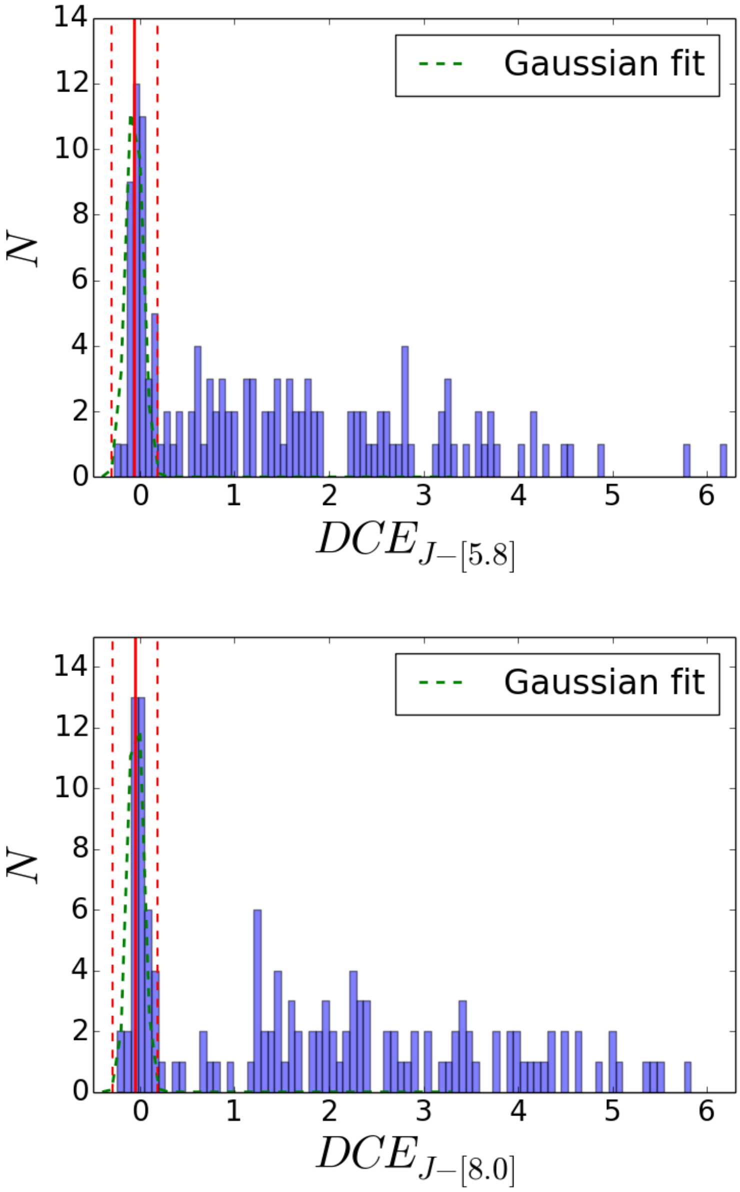

Figure 2.2: DCE$_{J-[5.8]}$ distribution (upper panel) and DCE$_{J-[8.0]}$ distribution (lower panel) for stars in the Taurus sample. The green line is the Gaussian fit to the distribution of DCEs and red lines are the center value of the Gaussian (solid line) and the 3σ limits (dashed lines).

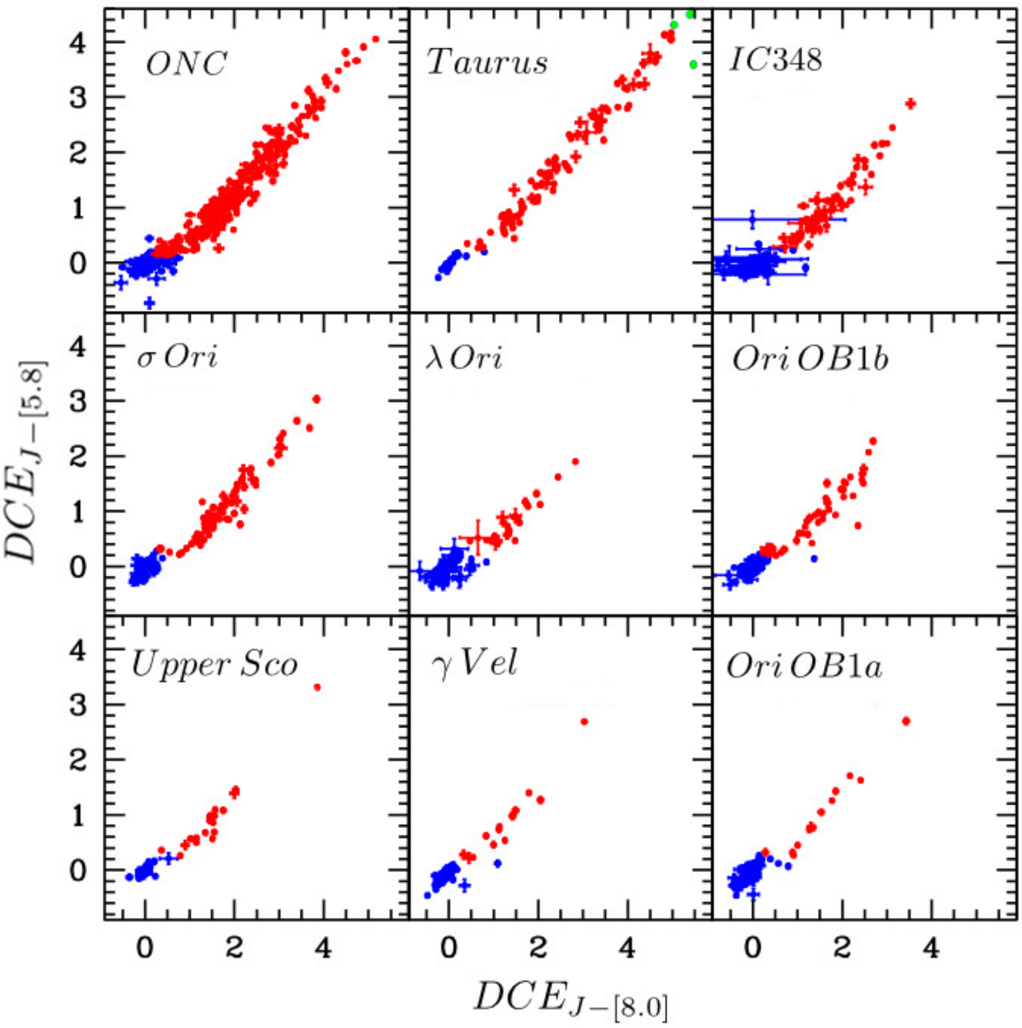

Figure 2.3: $\mathrm{DCE}_{J-[5.8]}$ versus $\mathrm{DCE}_{J-[8.0]}$ diagrams for all stellar groups. Red dots correspond to the stars with excess at $5.8\,\mu m$ and $8\,\mu m$ and blue dots are stars without excess. The green points in the Taurus panel are objects in earlier stages than Class II objects.

In Figure 2.3 we show the $\mathrm{DCE}_{J-[5.8]}$ versus the $\mathrm{DCE}_{J-[8.0]}$ for the stellar clusters/groups described in section 2.1, highlighting in red the disk-bearing sample selected to study the global evolution of the dusty component of the disks. In the Taurus panel, the green points in the upper right corner correspond to stars in earlier evolutionary stages than Class II objects. Following Equation (2.3) we calculate, besides the DCEs$_{J-[5.8]}$ and DCE$_{J-[8.0]}$, the rest of the DCEs (J-[3.6], J-[4.5], and J-[24]) for the disk-bearing sample. Notice that, since the MIPS photometry is less deep than the IRAC observations, and the MIPS sky coverage can be slightly different from the IRAC coverage, there are some disk-bearing stars that do not have an estimation of the DCE$_{J-[24]}$. This bias affects mainly the disk-bearing stars with the smallest values of DCE$_{J-[5.8]}$ and DCE$_{J-[8.0]}$; this means that the MIPS observations are biased towards the brightest objects in the mid-IR, which should be the youngest and/or most massive disks. As an illustration, Figure 2.4 shows the distribution of spectral types for all the disks-bearing stars in our sample (purple), as well as for the stars with MIPS 24 detections (pink) in all age bins (see §2.4). It can be seen that the main difference in these distributions is observed for stars with the latest spectral types.

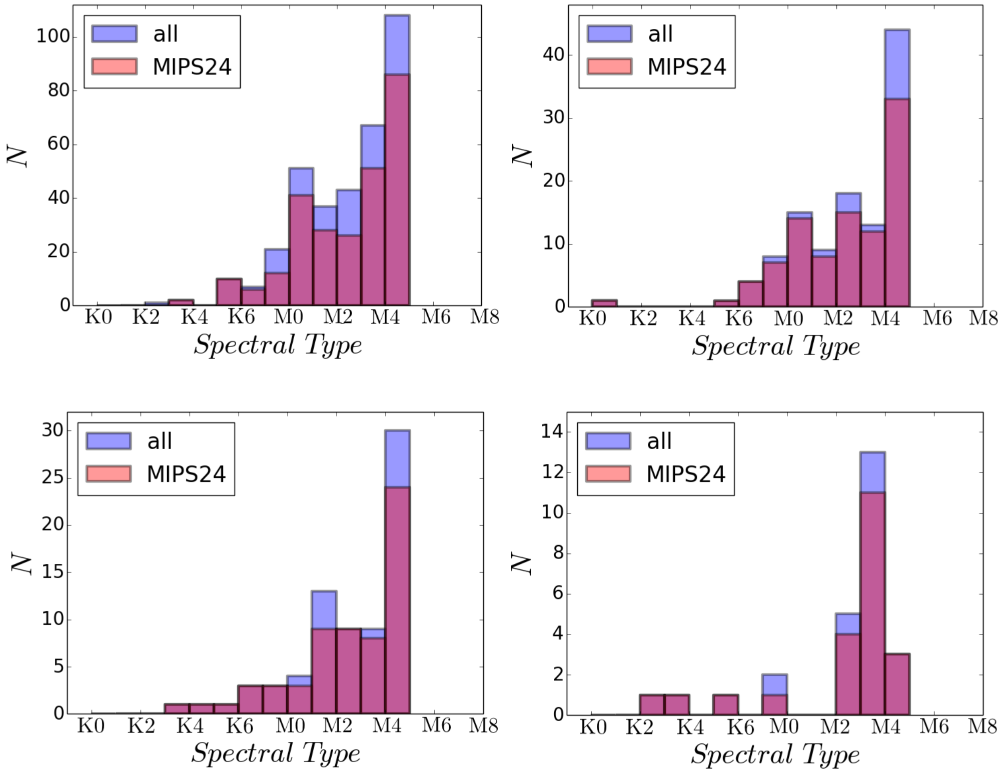

Figure 2.4: Distribution of spectral types at 1.5 Myr (bin 1, upper left), 3 Myr (bin 2, upper right), 4.5 Myr (bin 3, lower left), and 7.5 Myr (bin 4, lower right). Bin 1, 2, 3, and 4 correspond to 1-2, 2-3, 3-5, and 5-11 Myr, respectively. The purple distribution comes from all the stars in our sample, while the pink one corresponds to stars with MIPS 24 detections.

2.4 Separation into age bins

Since the purpose of this work is to make a study with good statistical significance, we grouped the disk-bearing sample selected in each stellar population into 4 groups or age bins. This allows us to have a representative sample of disks at each age bin. The criteria taken into account to group the disk-bearing sample into the four age bins is based on two aspects: (1) their nominal age taken from literature estimates, which are obtained by fitting one isochrone to the location of all the stars of a given stellar group in the H-R diagram, and (2) their disk fraction (see column 4 in Table 2.1), which also provides an additional indicator of the age of the stellar groups. Following both criteria, we separate the populations into the following age bins:

- Bin 1 : ONC and Taurus
- Bin 2 : IC 348 and σ-Ori
- Bin 3 : λ-Ori, Ori OB1b, and Upper Sco
- Bin 4 : γ Vel and Ori OB1a

Table 2.1 shows general properties of all stellar populations described in §2.1 and the age bin we assigned to them. We defined the following ages of the bins: 1.5 Myr (bin 1), 3 Myr (bin 2), 4.5 Myr (bin 3), and 7.5 Myr (bin 4). For bin 1, 1.5 Myr represents a typical intermediate value for the mean age of the stars in the ONC (1 Myr) and Taurus (2 Myr); for bin 2 we used 3 Myr since it agrees with most literature mean age estimates for IC 348 (3 Myr) and σ-Ori (3 Myr); for bin 3 we used 4.5 Myr as an intermediate value of the mean ages of λ-Ori (4-6 Myr), Ori OB1b (4-6 Myr), and Upper Scorpius (5-7 Myr), noticing that bin 3 is mostly dominated by the stars in λ-Ori and Ori OB1b; for bin 4 we used 7.5 Myr as an intermediate value between the mean ages of γ Vel (7 Myr), and the groups that were included as members of the sample for OB1a: 25 Ori, HD 35762, and HR 1833, which range from 6 to 11 Myr. There has been a lot of discussion in the literature about the age of Upper Scorpius, however we assigned this stellar population to the third age bin, in agreement with its disk fraction, and with the age (5-7 Myr) recently determined by David et al. (2019), although some authors suggest it is older ($\sim$ 11 Myr, Pecaut et al., 2012; Song et al., 2012).

In order to test the goodness of our assemblage of age bins, we plot in Figure 2.5 the median of the stellar luminosity estimated following the method described in §2.2, versus the age of each bin. It can be seen that the median of the stellar luminosity decreases with age, which is in agreement with expectations from stellar evolution of low-mass stars, since most stars in each bin are late K and M, as shown in Figure 2.4 and, thus, they are evolving along Hayashi tracks, decreasing their luminosity at approximately constant effective temperature (cf. Figure 1.3). Statistically, the quartiles are large enough to be considered constant with age, however a general tendency is observed as the age increases.

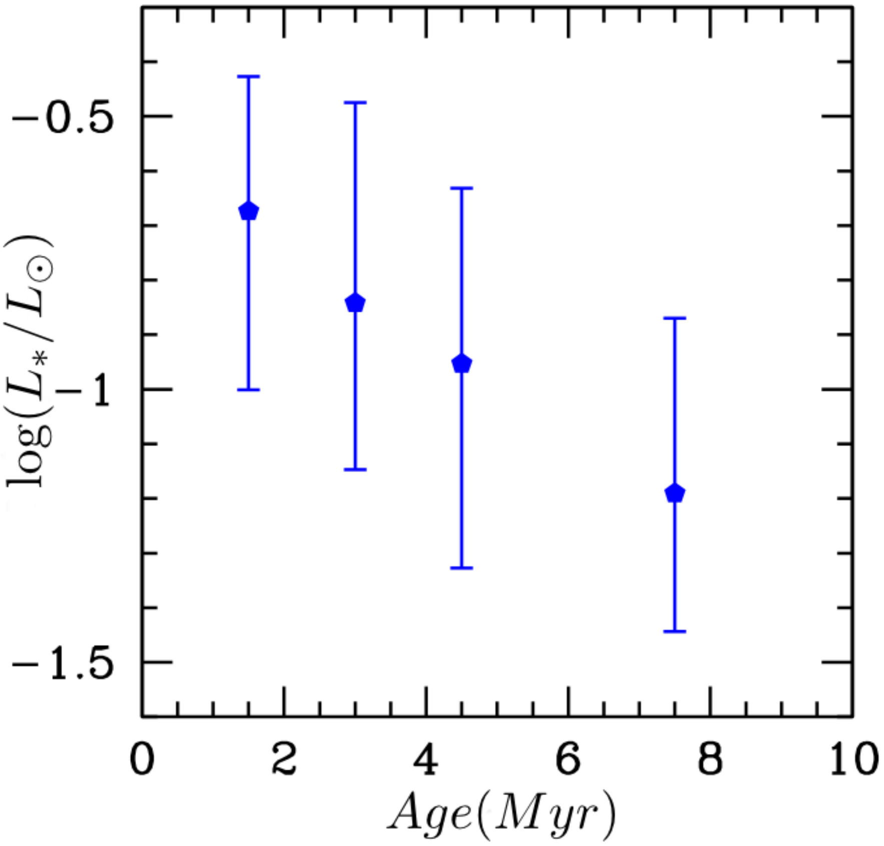

Figure 2.5: Median of the stellar luminosity (blue pentagons) for the stars in each age bin versus the age of the bin. The vertical bars represent the second and third quartiles, where 50 % of the data lie.

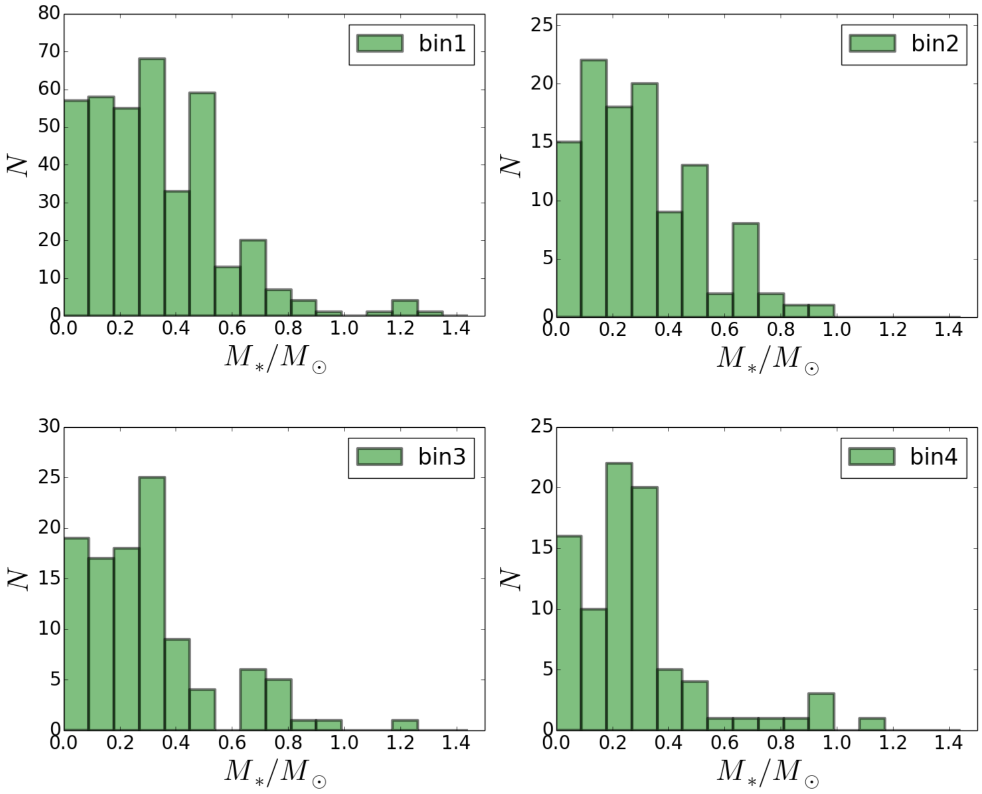

Figure 2.6: Distribution of stellar masses in all bins.

We built the distributions of stellar masses per age bin, in which the mass was obtained by interpolating the stellar luminosity and effective temperature in the H-R diagram, using the evolutionary tracks from Siess, Dufour & Forestini (2000). Nuria Calvet provided the Fortran routine that performs a double linear interpolation that we used. In the distributions shown in Figure 2.6, we include both the stars with determinations of mass accretion rates (with and without IRAC photometry) (see §2.6) as well as the stars with IRAC data for which $\dot{M}$ could not be determined (DCEs sample), discussed in §2.3. We find that the mean value of the observed stellar masses in all age bins is $\sim 0.3\,M_\odot$ (see Table 2.2), thus, this value will be adopted as representative of the stellar mass in our model grid (see §4.1); this is in agreement with the peak of the initial mass function in 25 Ori, discussed in Suárez et al. (2019). The distributions of stellar masses show a concentration of stars towards the lowest masses ($\lesssim 0.5\,M_{\odot}$).

Table 2.2: Observed stellar masses

bin	Mean ($M_{*}/M_{\odot}$)	σ
1	0.33	0.24
2	0.30	0.20
3	0.29	0.22
4	0.28	0.22

2.5 The evolution of the disk color excess

With the DCEs obtained using Equation (2.3) for our disk-bearing stars sample, we build histograms for the observed DCEs in the IRAC and MIPS 24 bands, which are shown in Figure 2.7. The first thing to notice is that the "tails" located at the right end of the distributions (e.g. $\mathrm{DCE}_{J-[4.5]} \gtrsim 2$) in the youngest bin, disappear as the age of the bin increases (from top to bottom), while the position of the peak of the distributions remains approximately in the same position: $\sim$ 0.4, 0.5, and 1.8 for the IRAC disk color excesses J-[4.5], J-[5.8], and J-[8.0], respectively. In the case of the color excess $\mathrm{DCE}_{J-[24]}$, the peak moves towards smaller values with age, from $\sim$ 4.5 at bin 1, to $\sim$ 3.5 at bin 4; also the tail at the right end of the distribution disappears. We also plot the median value of these DCEs distributions (which is shown in Figure 2.8) as function of age; the error bars are the quartiles, which indicate the range where 50% of the disk-bearing stars are located. There is a decreasing trend of the median DCEs with age, which is more rapid during the first 5 Myr. Notice that the central star irradiates directly the disk, in particular the innermost regions, hence the emission at 4.5 μm arises from radii which are located inside those radii from which the emission at 8 μm arises (cf. Figure 5.4). The steeper decay of emission at shorter wavelengths (e.g. the upper left panel in Figure 2.8) than the more gradual decay at longer wavelengths (e.g. the lower right panel in Figure 2.8) indicates a more rapid evolution of the innermost radii (traced by the DCE$_{J-[4.5]}$) during the first 5 Myr, than the disk material from which the flux at 24 μm arises (traced by the DCE$_{J-[24]}$).

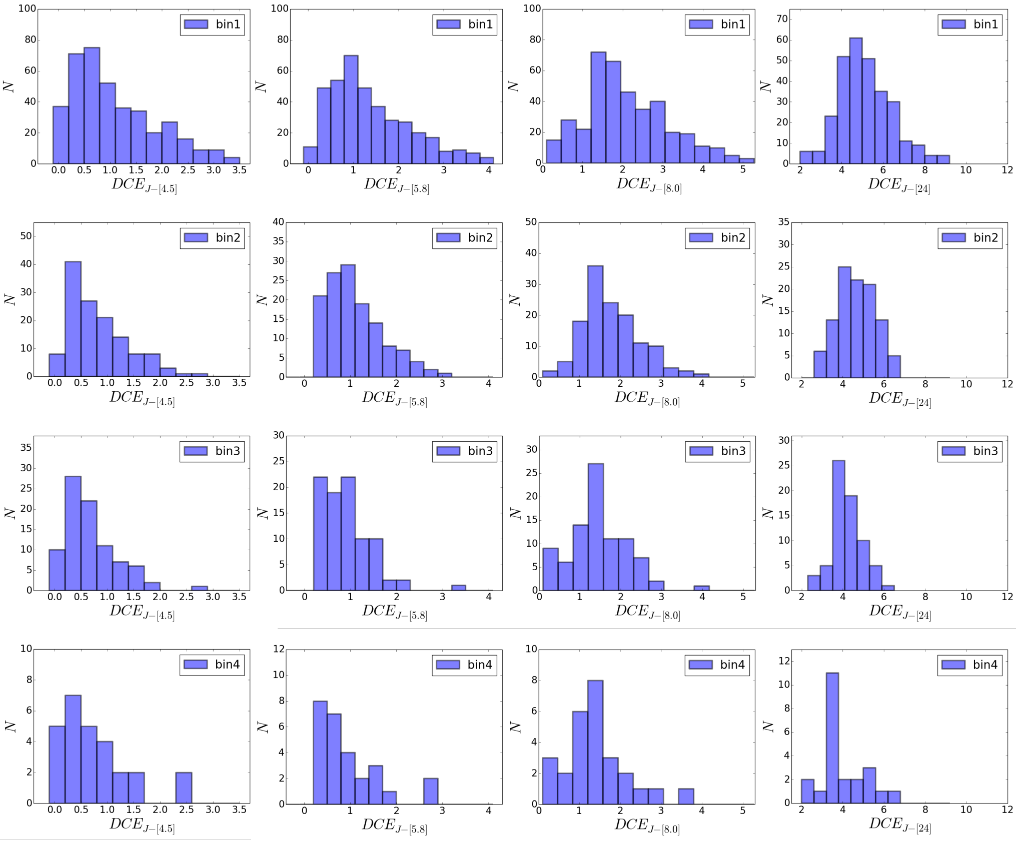

Figure 2.7: DCE distributions for: J-[4.5](first column), J-[5.8](second column), J-[8.0](third colum) and J-[24](fourth column). The age of the bins: 1.5, 3, 4.5, and 7.5 Myr, increases from top to bottom.

Additionally, a two-sample KS-test was performed on the different DCE distributions for all the age bins. The KS-test determines the probability,

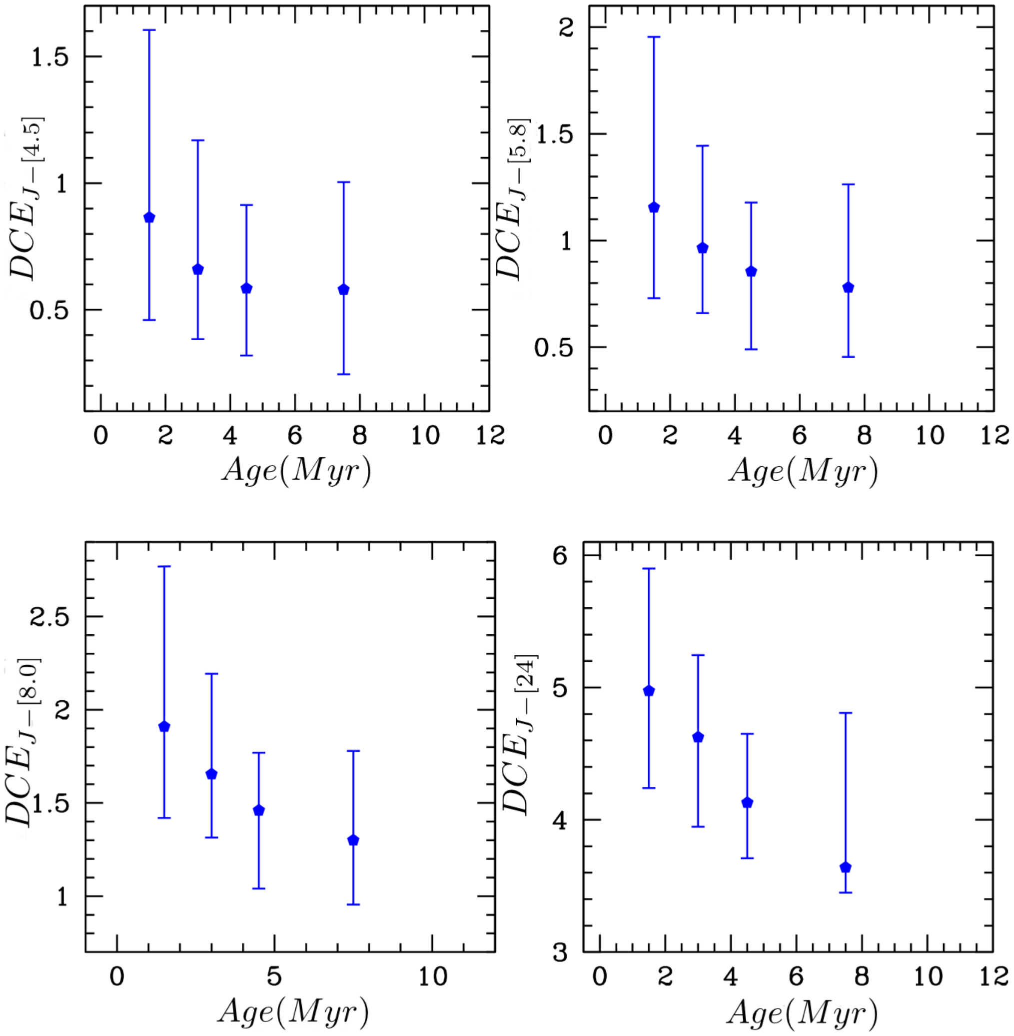

Figure 2.8: Evolution of the median disk excess for: *a*) $J-[4.5]$ (upper left), *b*) $J-[5.8]$ (upper right), *c*) $J-[8.0]$ (lower left), and *d*) $J-[24]$ (lower right). The blue pentagons correspond to the median of each distribution for each age bin and the bars are the quartiles, which indicate the range where 50% of the stars with excess are located.

given by the p-value, that the two cumulative distributions to be compared are drawn from the same sample. We find the p-values reported in Table 2.3. The low p-value between bin 1 and bin 2 (p-value <6%) indicates different DCE distributions, which suggests significant dust evolution between these two bins. In contrast, the KS-test high p-value in bin 3 and bin 4 (p-value>90%) indicates no difference between the DCE distributions (cf. Table 2.3), suggesting little or no dust evolution between these older bins.

Table 2.3: KS-test p-values

bins	$\mathrm{DCE}_{J-[4.5]}$	$\mathrm{DCE}_{J-[5.8]}$	$\mathrm{DCE}_{J-[8.0]}$	$\mathrm{DCE}_{J-[24]}$
1-2	0.04	0.05	0.06	0.06
2-3	0.45	0.23	0.43	0.17
3-4	0.99	0.99	0.99	0.91

Notice that the distance to each star is not used to calculate the observed DCEs, however, an additional constraint to add to our observational sample would be to only include stars with GAIA DR2 parallaxes with relative errors $< 20\%$, and with coherent parallaxes and proper motions, that is, within $3\times\sigma$ from the median value. We call this sample the restricted sample. As a test, we calculated the DCE distributions for this restricted sample, and plotted the median DCEs, which are shown in Figure 2.9. We obtained the same evolutionary trends in the different DCEs, but in this case the uncertainties are larger, given by a wider interval between the second and third quartiles of the distributions, in particular for the oldest bins. Given this result, and since the purpose of this work is to make a statistical study of a sample of T Tauri stars as representative as possible, and with good significance, we decided to work with the initial sample without further constraints in proper motions and/or parallaxes. In any case, the stars in our observational sample have previous membership confirmation for each stellar group.

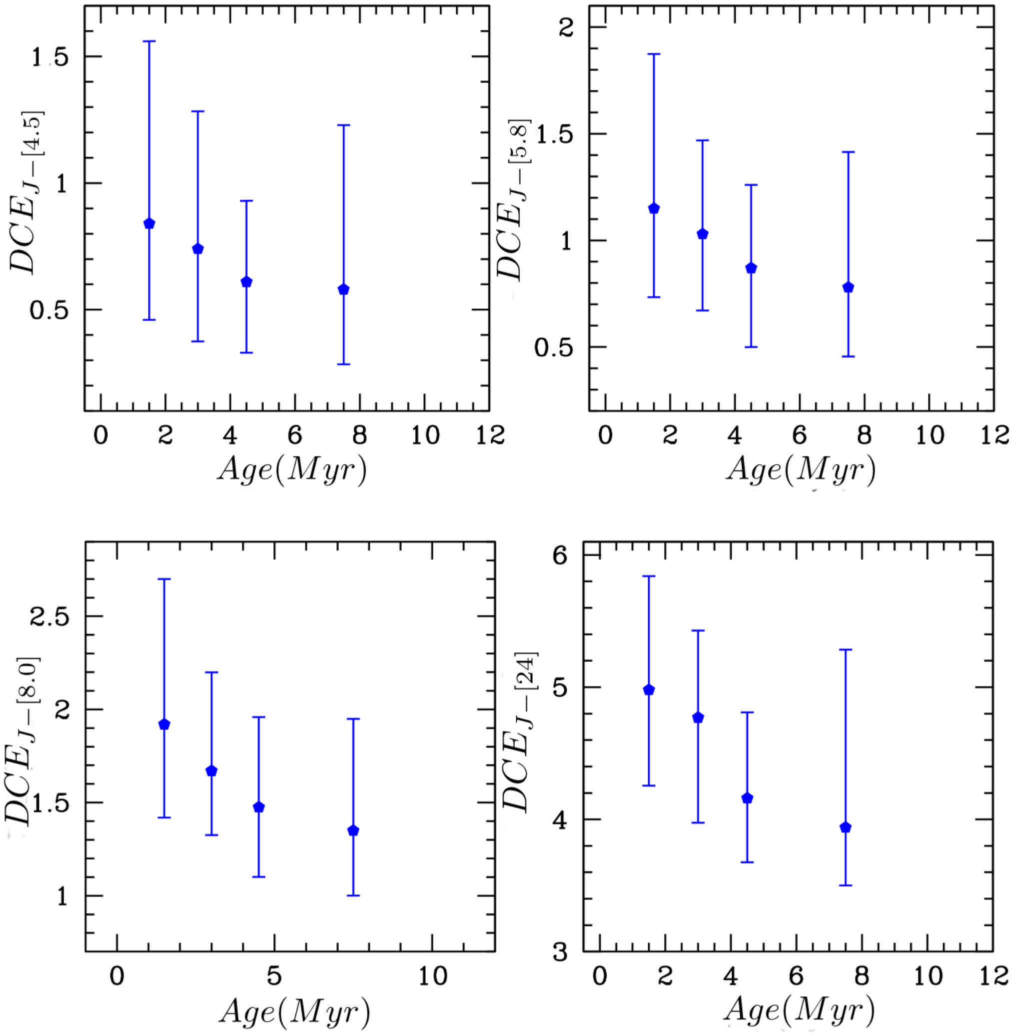

Figure 2.9: Evolution of the median disk excess for: $a)\, J - [4.5]$ (upper left), $b)\, J - [5.8]$ (upper right), $c)\, J - [8.0]$ (lower left), and $d)\, J - [24]$ (lower right). The blue pentagons correspond to the median of each distribution for each age bin and the bars are the quartiles, which indicate the range where 50% of the stars with excess are located. The data correspond to the sample with good GAIA DR2 distances, as well as with coherent parallaxes (see text for details).

2.6 Gas evolution: mass accretion rates

The mass accretion rate $\dot{M}$ measures the amount of disk material that falls onto the star per unit time and, therefore, it is an indicator of the amount of gas in the inner disk. The youngest disks have a larger gas reservoir and, as discussed in §3.1, viscous evolution is responsible of a redistribution of angular momentum in the disk, allowing a fraction of the disk material to move towards smaller radii and eventually fall onto the star; as a consequence the disk expands, decreasing its surface density, since angular momentum is conserved. It is thought that an anomalous viscosity is responsible for the redistribution of angular momentum within the disk, since it should be more efficient than the typical molecular viscosity, in order to explain the observed disk lifetimes.

Different studies have shown that the mass accretion rate decreases with age (cf. Hartmann, Herczeg & Calvet, 2016), which is expected from viscous evolution, since at the early stages the disk is fairly massive. Extensive determinations of mass accretion rates in different star forming regions have been carried out by many authors (Hartmann, Herczeg & Calvet, 2016, and references therein), however they have used different methods to measure the rates (cf. §1.5). In this thesis we use our large sample of stellar groups at different ages to re-determine the evolution of $\dot{M}$ in a homogeneous way, using the EW of the Hα line. We decided to use this method since we have EW Hα measurements compiled from the literature, or determined by us, for a large samples of disks at each age bin. This allows us to apply the same method for determining $\dot{M}$, keeping the sample as homogeneous as possible.

The EW Hα used to determine $\dot{M}$ in our samples was estimated using the SpTClass tool (Hernández et al., 2007b, 2014, 2017). This estimation can be a good proxy to study the global evolution of the gas component of protoplanetary disks in YSOs (Ingleby et al., 2011; Alcalá et al., 2014; Maucó et al., 2016; Fairlamb et al., 2017). As discussed in §2.1, the sample used to determine $\dot{M}$ includes some TTSs with measurements of EW Hα without IRAC photometry, and thus it is different from the sample analyzed in §2.5. Additionally, the stars in this sample have GAIA DR2 parallaxes, with uncertainties below 20%. Following the classification scheme from Briceño et al. (2019), we determine $\dot{M}$ for Classical TTSs (CTTSs) and for TTSs with EW Hα intermediate between that of a CTTS and WTTSs (CWTTSs, see §1.2), and thus, we have included the following samples of CTTSs and CWTTSs (hereafter accretors), which have stellar masses estimated following the proceedure discussed in §2.2:

- *Bin 1*: We have included 228 accretors located in the ONC (§2.1.1) and 16 accretors located in Taurus (§2.1.2). Out of 244 accretors, 163 and 14 stars also belong to the sample used to study the dust in §2.5, in the ONC and in Taurus, respectively.

- *Bin 2*: We have included 40 accretors located in the σ Ori cluster (§2.1.4). Out of 40 accretors, 36 stars also belong to the sample used to study the dust in §2.5.

- *Bin 3*: We have included 59 accretors located in Orion OB1b (§2.1.6). Out of 59 accretors, 19 stars also belong to the sample used to study the dust in §2.5.

- *Bin 4*: We have included 77 accretors located in Orion OB1a. (§2.1.9). Out of 77 accretors, 9 stars also belong to the sample used to study the dust in §2.5.

The $\dot{M}$ was estimated from the Hα line luminosity ($L_{\mathrm{H}\alpha}$) using the relation

$$L_{\mathrm{H}\alpha} = 4\pi\, d^2 \times (\mathrm{EW\,H}\alpha) \times F_{cont}, \tag{2.4}$$

where d is the distance calculated as the inverse of the GAIA DR2 parallaxes. The continuum flux at 0.6563 μm (F_{cont}) was estimated as follows. We calculated the V and $\mathrm{I_c}$ magnitudes of each object from the intrinsic $[\mathrm{V}-\mathrm{I_c}]$ and $[\mathrm{V}-\mathrm{J}]$ colors from Table 6 of Pecaut & Mamajek (2013) and the J magnitude corrected by extinction. The V and $\mathrm{I_c}$ magnitudes were converted to fluxes using the respective zero points for each filter, and F_{cont} was obtained by interpolating between these fluxes at 0.6563 μm. The accretion luminosity, L_{acc}, was computed using Equation (10) from Ingleby et al. (2013)

$$\log(L_{\mathrm{acc}}) = 1.0(\pm0.2)\log(L_{\mathrm{H}\alpha}) + 1.3(\pm0.7), \tag{2.5}$$

and the mass accretion rate for each star was then obtained from the accretion luminosity using the relation

$$L_{\mathrm{acc}} = \frac{GM_*\dot{M}}{R_*}, \tag{2.6}$$

where we used the derived stellar mass and radius estimated from the effective temperature and the stellar luminosity in §2.2.

Table 2.4: Sample for mass accretion rates

Group	Age Myr	Stars with $\dot{M}$	Median $\log(\dot{M})$ $M_\odot yr^{-1}$	σ	Age bin
ONC+Taurus	1-3	244	-8.49	0.50	1
σ Ori	3	40	-8.60	0.32	2
Ori OB1b	4-5	59	-9.19	0.43	3
Ori OB1a	6-13	77	-9.29	0.50	4

Table 2.4 shows the groups for which the mass accretion rates were determined, their age, the median of $\log(\dot{M})$, and the standard deviation σ, including the stars with and without IRAC photometry.

In Table B.1 (cf. Appendix B) we show all the stars with $\dot{M}$ shown in Table 2.4, as well as the stars used in the determination of the different DCEs (§2.5) without EW Hα. Notice that the errors associated with the different DCEs in Table B.1 are underestimated, since they do not include the uncertainties from the determination of spectral types, intrinsic colors or extinctions. We cannot include the propagated uncertainties, since most of the references from which the spectral types of effective temperatures were taken do not include such errors in the published data. It must be mentioned, however, that these underestimated errors do not affect our results, since we do not use them in any way as a weight to determine the disk parameters.

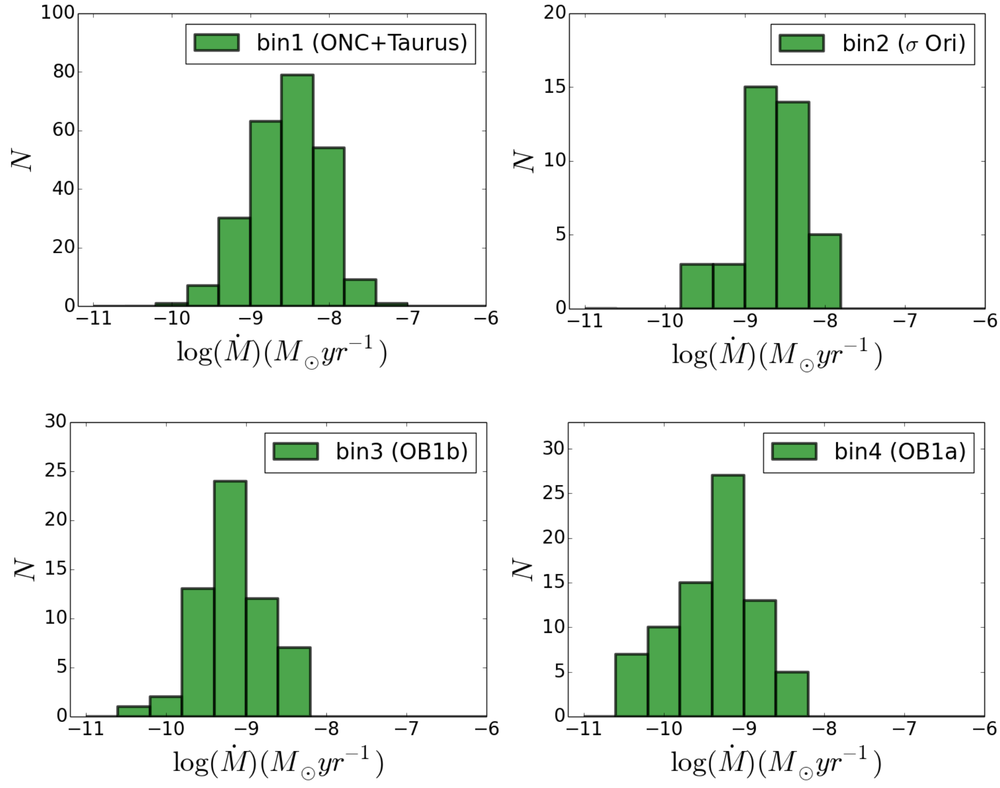

Figure 2.10: Mass accretion rates distributions calculated in this work, for the different age bins.

Figure 2.10 shows the distribution of mass accretion rates, built for each age bin. It can be seen that the distributions, and their peaks, move towards lower values as the age of the clusters/groups increases. Figure 2.10 confirms what has been previously discussed and found in other works (Hartmann, Herczeg & Calvet, 2016, and references therein). Recall that the mass accretion rates in this work are determined self-consistently, using the luminosity of the Hα line, for each star in the stellar groups. This is important because our results are not affected by any bias that might be introduced when different methods are used.

In Figure 2.11 we plot the median of the mass accretion rates versus the age bin. The vertical bars are the quartiles, which show where 50% of the data of each age bin lie. There is a clear trend of decreasing accretion rates with age, as previously found. The median seems to fall more rapidly during the first 5 Myr, and then the decrease flattens out. A similar behavior is observed in the evolution of the medians of the different DCEs (see Figure 2.8). Recently, Manara et al. (2020) measured mass accretion rates of 36 targets in upper Scorpius, and compare their results with previous mass accretion rate estimations in Lupus and Chamaeleon I (Manara et al., 2016; Alcalá et al., 2014); they find that the median $\dot{M}$ in the three regions does not decay with time, in contrast with our results. Instead, they argue that models of disks with dust evolution, and in which the accretion is driven by magnetohydrodynamic winds, can explain their observations. Notice that our sample is significantly larger than the one used by Manara et al. (2020), and that we consider a wider age interval in our study of mass accretion rates, which might explain the discrepancies in both results.

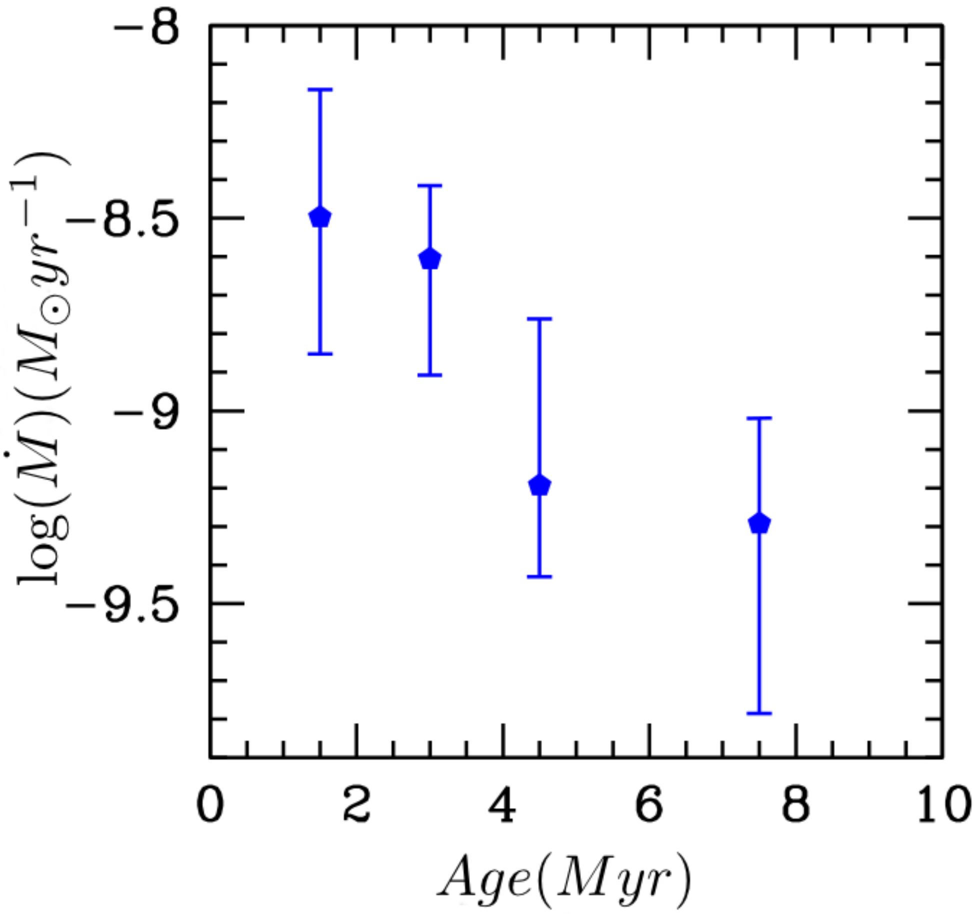

Figure 2.11: Median of the mass accretion rates for the different age bins. The blue bars are the quartiles, which show where 50% of the data of each age bin lie.

3

Evolutionary models

In this chapter we describe the equations governing the viscous evolution of protoplanetary disks. In §3.1 we discuss the similarity solution from Lynden Bell & Pringle (1974) for the radial evolution of the surface density, used in this thesis, to explain the decay of $\dot{M}$ we find in §2.6. In addition, we explore the range of values for the parameter space given by the initial disk mass $M_d(0)$, the characteristic radius R_1, and value of the α viscosity parameter, that best fit the observed decay of $\dot{M}$. Finally, in §3.2 we describe in detail the D'Alessio models used here to build an extensive grid of irradiated accretion disk models, their assumptions, and the different ingredients taken into account to calculate their structure and emission.

3.1 Viscously evolving disks

We now explain the equations for viscous evolution of disks. The characteristic timescale of viscous evolution $t_s \sim R/v_R$, can be written as

$$t_s \sim R^2/\nu, \tag{3.1}$$

where ν is the viscosity coefficient and v_R is the radial accretion velocity of a gas parcel of the disk. Equation (3.1) can be interpreted as the timescale in which a perturbation in the disk density, of size $\sim R$ would vanish due to the diffusion of particles in the gas. Alternatively, it can be interpreted as the characteristic timescale in which a gas element, with velocity v_R, would travel a distance R. If the molecular viscosity was the driving agent in the disks' evolution, instead of a viscosity of turbulent origin (anomalous viscosity), the viscous timescales would be of $\sim 10^{11}$ Myr, which are ~ 10 orders of magnitude greater than the observed disks' lifetimes (cf. the disk fraction and the accretors fraction in Figure 1.11). This is why it has been proposed that the viscosity that operates in the disks, driving their evolution, has a turbulent origin, however, the specific details of this viscosity are not entirely understood.

The evolution of the radial surface density Σ of a Keplerian disk is given by (Lynden Bell & Pringle, 1974)

$$\frac{\partial \Sigma}{\partial t} = \frac{3}{R}\frac{\partial}{\partial R}\left[R^{1/2}\frac{\partial}{\partial R}(R^{1/2}\nu\Sigma)\right], \tag{3.2}$$

where ν is the viscosity coefficient. For the case of a power-law radial dependence of the viscosity coefficient $\nu \propto R^{\gamma}$, Equation (3.2) has a similarity solution for Σ as a function of time, given by (Lynden Bell & Pringle, 1974; Hartmann et al., 1998)

$$\Sigma(R,t) = \frac{C}{3\pi\nu_1 r^{\gamma}}\mathbb{T}^{\frac{(5/2-\gamma)}{(2-\gamma)}} \exp\left[\frac{-r^{(2-\gamma)}}{\mathbb{T}}\right], \tag{3.3}$$

where

$$r = \frac{R}{R_1}, \qquad\qquad \nu = \nu_1\left(\frac{R}{R_1}\right)^{\gamma}. \tag{3.4}$$

In Equations (3.3) and (3.4), R_1 is a characteristic radius and C is a constant. In addition, a non-dimensional time is defined such that

$$\mathbb{T} = \frac{t}{t_s} + 1, \tag{3.5}$$

where the viscous timescale t_s is given by

$$t_s = \frac{1}{3(2-\gamma)^2}\frac{R_1^2}{\nu_1}. \tag{3.6}$$

Equation (3.3) tells us that the surface density Σ is given by the product of two terms; the former is a power-law of the radius $r^{-\gamma}$, while the latter is an exponential function $\exp\left[\frac{-r^{(2-\gamma)}}{\mathbb{T}}\right]$, which dominates at large radii. For smaller radii than some critical radius $R_{\rm c}$, the surface density decreases as a power-law of the radius, and for larger radii than $R_{\rm c}$ the surface density falls-off exponentially. The physical interpretation is that the anomalous viscosity in the disk induces a redistribution of angular momentum. This effect allows the loss of angular momentum of a fraction of the disk material, which eventually falls onto the star. Another fraction of the disk material gains angular momentum, and moves toward larger radii; this causes the disk to expand and develop this outer region in which the surface density falls-off exponentially.

Given the similarity solution in Equation (3.3), the mass accretion rate can be written as

$$\dot{M}(R,t) = C\mathbb{T}^{(5/2-\gamma)/(2-\gamma)} \exp\left(-\frac{r^{2-\gamma}}{\mathbb{T}}\right)\left[1-\frac{2(2-\gamma)r^{2-\gamma}}{\mathbb{T}}\right]. \tag{3.7}$$

The true origin of the viscosity that operates in the disks remains unclear, however, the magneto-rotational instability (Balbus & Hawley, 1991) is the favorite candidate, responsible for producing the viscous dissipation and tranfer of angular momentum in the disks. The physical interpretation of this instability is the following: if a magnetic field line connects two disk anulii, the one that is closest to the star moves with a higher angular velocity than the other ring, since they are both rotating with Keplerian velocities; as a consequence, the magnetic field line will be stretched. Since the intensity of the magnetic field is not strong enough to force the disk to rotate as a rigid body, it will simultaneously make the outer ring rotate faster and the inner ring rotate slower than their respective Keplerian angular velocities. In the process, a net transfer of angular momentum occurs from the inner ring to the outer ring, along the magnetic field line. This is an unstable process, since the inner ring loses angular momentum and moves to inner radii, while the outer ring gains angular momentum and moves to outer radii, stretching the magnetic field line even more. This transfer of angular momentum between different disk anulii produces an effective turbulent viscosity.

Usually, the α prescription for the viscosity is used (Shakura & Sunyaev, 1973)

$$\nu = \alpha c_s H, \tag{3.8}$$

where $c_s = (kT/\mu m_H)^{1/2}$ is the sound speed, k is the Boltzmann constant, T is the temperature, $\mu = 2.34$ is the mean molecular weight, m_H is the hydrogen mass, and $H = c_s/\Omega_K(R)$ is the gas scale height, where $\Omega_K(R) = (GM_*/R^3)^{1/2}$ is the Keplerian angular velocity, G is the gravitational constant, M_* is the stellar mass, and α is a free parameter related with the efficiency of the viscosity. Equation (3.8) can be re-written as

$$\nu \propto \alpha T_{\rm c} R^{3/2}, \tag{3.9}$$

in which $T_{\rm c}$ is the disk midplane temperature as a function of R. If α is assumed to be constant throughout the disk, and also if the midplane temperature is a power-law of the radius $T_{\rm c} \propto R^{-q}$, the viscosity coefficient ν has also a power-law dependence on radius, with exponent

$$\gamma = \frac{3}{2} - q. \qquad (\alpha\,\text{constant}) \tag{3.10}$$

Accretion disk models have shown that irradiation from the central star dominates the heating in the disk upper layers (e.g. D'Alessio et al., 1998) for $R >> R_*$, and $T_{\rm c} \propto R^{-1/2}$, thus $\gamma = 1$. In Hartmann et al. (1998) the analysis and comparison with observations is made for $\gamma = 1$, in which case the surface density Σ becomes

$$\Sigma(R,t) = \frac{M_d(0)}{2\pi R_1^2}\frac{1}{r\mathbb{T}^{3/2}}\exp\left[-\frac{r}{\mathbb{T}}\right]. \tag{3.11}$$

The mass accretion rate as a function of R and t is

$$\dot{M}(R,t) = \frac{M_d(0)}{2t_s}\frac{1}{\mathbb{T}^{3/2}}\left(1-\frac{2r}{\mathbb{T}}\right)\exp\left[-\frac{r}{\mathbb{T}}\right], \tag{3.12}$$

with

$$t_s = \frac{1}{3}\frac{R_1^2}{\nu_1}, \tag{3.13}$$

and at $R = 0$, Equation (3.12) becomes

$$\dot{M}(0,t) = \frac{M_d(0)}{2t_s}\frac{1}{\mathbb{T}^{3/2}}. \tag{3.14}$$

Finally, the disk mass is given by

$$M_d(R,t) = \frac{M_d(0)}{\mathbb{T}^{1/2}}\left(1-\exp\left[-\frac{r}{\mathbb{T}}\right]\right). \tag{3.15}$$

In Equations (3.11), (3.12), (3.13), (3.14), and (3.15), $M_d(0)$ is the initial disk mass, R_1 is a characteristic radius, inside which 60% of the original disk mass is located, t_s is the characteristic viscous timescale at R_1, and ν_1 is the viscosity at R_1. Notice that the similarity solutions for the evolution of the disk surface density depend only on (1) the initial disk mass $M_d(0)$ and (2) the characteristic radius R_1, given a fixed value of the α parameter in the viscosity prescription (Equation 3.8).

As discussed above, in the Shakura & Sunyaev (1973) prescription, the viscosity is given by Equation (3.8). Since the viscosity increases linearly with radius $\nu \propto R$, the similarity solution can be applied (cf. Hartmann et al., 1998). In this work we assume that Equation (3.11) holds for the evolution of the disk surface density distribution.

Using the α viscosity prescription (Equation 3.8) and Equation (3.14), the mass accretion rate onto the star can be written as

$$\dot{M}(0,t) = \frac{3\alpha}{2(GM_*R_1)^{1/2}} \frac{kT_1}{\mu m_H} \frac{M_d(0)}{\mathbb{T}^{3/2}}, \tag{3.16}$$

for a temperature profile $T = T_1(R/R_1)^{-1/2}$, such that the viscous time is

$$t_s = \frac{(GM_*R_1)^{1/2}}{3\alpha} \frac{\mu m_H}{kT_1}. \tag{3.17}$$

For a given initial disk mass $M_d(0)$ and a characteristic radius R_1, and for a star of mass M_*, Equation (3.16) gives the predicted evolution of the mass accretion rate onto the star for these evolutionary models. Since for the stellar groups discussed in §2.1, $t >> t_s$, one obtains

$$\dot{M}(0,t) = \frac{(GM_*R_1)^{1/4}}{2\,(3\alpha)^{1/2}} \left(\frac{\mu m_H}{kT_1}\right)^{1/2} \frac{M_d(0)}{t^{3/2}}. \tag{3.18}$$

We adopt the approximation $T_1 = T_{d2}(100\,\mathrm{au}/R_1)^{1/2}$, with $T_{d2} = 10$ K, a typical temperature at 100 AU (c.f. D'Alessio et al., 1998, 2001). Then, the mass accretion rate can be written as

$$\begin{aligned} \frac{\dot{M}(0,t)}{M_\odot\,\mathrm{yr}^{-1}} &= 1.39 \times 10^{-8} \left(\frac{\alpha}{0.01}\right)^{-1/2} \left(\frac{M_*}{M_\odot}\right)^{1/4} \left(\frac{R_1}{\mathrm{AU}}\right)^{1/2} \\ &\times \left(\frac{T_{d2}}{10K}\right)^{-1/2} \left(\frac{M_d(0)}{M_\odot}\right) \left(\frac{t}{\mathrm{Myr}}\right)^{-3/2}. \end{aligned} \tag{3.19}$$

In the fiducial model of Hartmann et al. (1998), the parameters $M_d(0)$ and R_1 were set to 0.1 $M_\odot$ and 10 au, respectively, and calculations were shown for $M_* = 0.5\,M_\odot$. In this thesis, we will use the values for α, $M_d(0)$, R_1, and M_*, that are consistent with our observational samples and the observed decay of mass accretion rate with age (cf. Figure 2.11).

As mentioned before, the purpose of this thesis is to use the disk models discussed in §3.2, in order to explore the disk parameters that reproduce the observed DCEs distributions shown in §2.5. For this purpose, we built a grid of disk models for each age bin. The models use the properties of the central star as input parameters thus, at each age bin, we need to use stellar properties that are representative of the stars in that bin. We adopt a stellar mass $M_* = 0.3\,M_\odot$, which corresponds to the mean stellar mass from our samples (see §2.4 and Table 2.2), as representative of the stellar masses in the different age bins, and given the mass of the star, we obtained the stellar luminosity and effective temperature.

As discussed above, the similarity solution for Σ depends on the disk mass $M_d(0)$, the characteristic radius R_1, and α, thus, the evolution of the surface density will be given by the values adopted for these parameters which, in principle, are not known *a priori*. There is a lot of discussion in the literature concerning disk masses and the values of α in the viscosity prescription, but no definitive consensus have been achieved yet (Guilloteau et al., 2011; Mulders & Dominik, 2012; Flaherty et al., 2018; Mohanty et al., 2018; Dutrey et al., 2014; Turner et al., 2014, and references therein).

In order to provide values of these parameters that are consistent with observed data, we fit the observed decay of the mass accretion rate with age shown in Figure 2.11, using Equation (3.19) and find the triads of values $(R_1, M_d(0), \alpha)$ that provide the best χ^2 fit to the data, using the relation

$$\chi^2 = \sum_{i=1}^{4} \frac{(\dot{M}_{\mathrm{obs}_i} - \dot{M}_{\mathrm{vis}_i})^2}{\sigma_i^2}, \tag{3.20}$$

where $\dot{M}_{\mathrm{obs}_i}$ are the median mass accretion rates shown in Table 2.4 and Figure 2.11, $\dot{M}_{\mathrm{vis}_i}$ are the mass accretion rates obtained using Equation (3.19), and the standard deviation σ of the distributions of mass accretion rates was calculated using the median absolute deviation (MAD) of the observational data, assuming Gaussian distributions, with the relation $\sigma = 1.4826 \times \mathrm{MAD}$.

Figure 3.1 shows the goodness of the fits, as indicated by the value of χ^2, for a range of values of R_1 and $M_d(0)$, and for three values of α: 0.01, 0.001, and 0.0001.

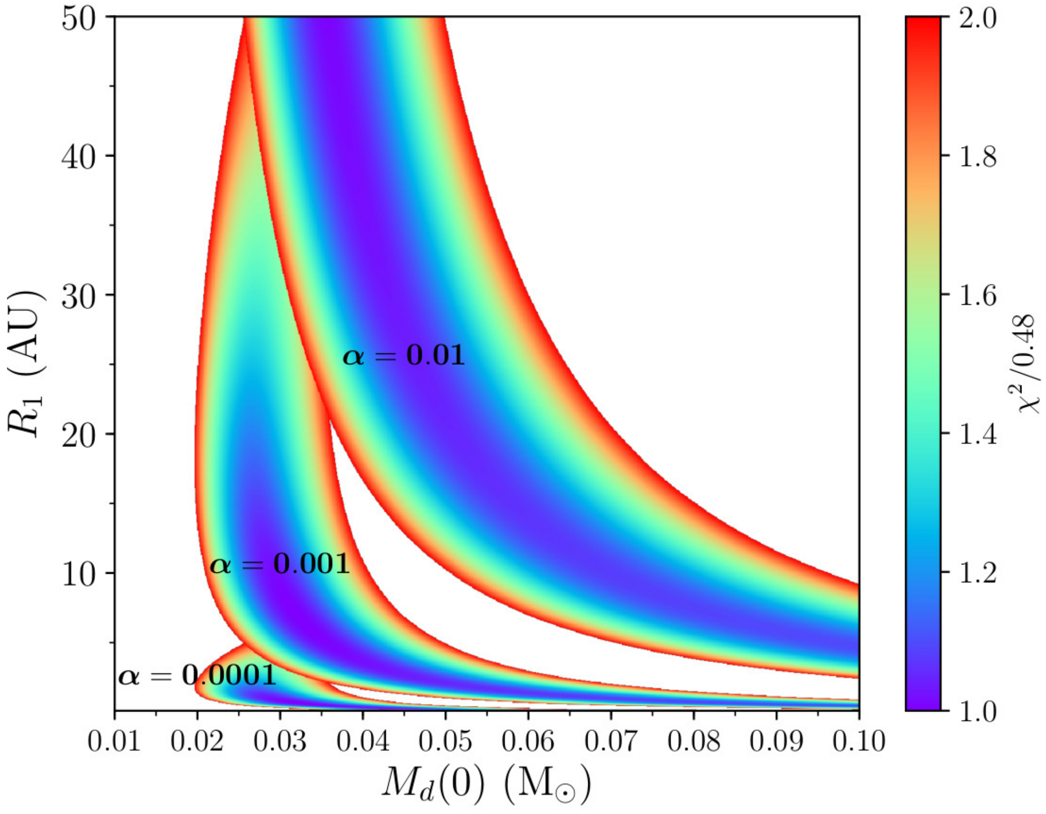

Figure 3.1: Normalized $\chi^2/0.48$ for the fits to the observed decay of mass accretion rate with age in Figure 2.11 from different combinations of the evolutionary parameters R_1 and $M_d(0)$, and the viscosity parameter α. Each color map region corresponds to a different value of α, indicated in the label. The values are normalized to the global minimum as indicated in the scale.

The lowest value of $M_d(0)$ among the best fitting models for α=0.001 is about 0.03 $M_\odot$, or about twice the minimum solar nebula (MMSN). According to Andrews & Williams (2005), the mean value of the disk mass for disks in the 1-2 Myr old Taurus association is 0.005 $M_\odot$, so in principle the mean initial disk mass could be lower than 0.03 $M_\odot$. However, Andrews &

Williams (2005) note that the formation of giant planets requires disk masses of a few MMSN. In addition, models with $\alpha \lesssim 0.001$ predict very low values of R_1, less than 5 au. In contrast, a recent large ALMA disks' survey in Orion finds that Class 0 and Class I objects have mean dust disk radii of ~ 45 au and ~ 37 au, respectively (Tobin et al., 2020). These objects are representative of the initial stages of viscous evolution, which argues against very low values of the radius R_1. The fits for $\alpha = 0.0001$ yield unrealistically small values of R_1 and $M_d(0)$.

On the other hand, for $\alpha = 0.01$, Figure 3.1 shows that values of R_1 ranging from ~ 5 au to radii even larger than 50 au, with $0.03\, M_\odot \lesssim M_d(0) \lesssim 0.1\, M_\odot$, give reasonable fits to the observed data (cf. Figure 3.2). The observed mean values of the dust disks' radii for Class 0 and Class I objects from Tobin et al. (2020), suggest that the characteristic radius R_1 is larger than the values inferred from the analysis for $\alpha = 0.001$ and 0.0001. To be consistent with these considerations, we adopt models with $\alpha = 0.01$.

Figure 3.2 shows the median values of the mass accretion rate distributions at each age bin (also shown in Figure 2.11 and Table 2.4), and the error bars indicate the standard deviation of the distributions. The red shaded area in Figure 3.2 corresponds to the mass accretion rates predicted by triads of values $(R_1, M_d(0), \alpha)$ which have normalized $\chi^2/0.48 \leq 2$ in Figure 3.1, and the green solid line shows the theoretical mass accretion rate for one of these triads, $M_d(0) = 0.07\, M_\odot$, $R_1 = 10$ au (e.g. Hartmann et al., 1998), and α=0.01. It must be noticed that different triads $(R_1, M_d(0), \alpha)$ can also provide a good match to the observed data, and the goodness of the fits is determined by their χ^2 value, shown in Figure 3.1. Our analysis suggests that the observed decay of $\dot{M}$ with age is consistent with viscous evolution of the gas in the disk, for these evolutionary models.

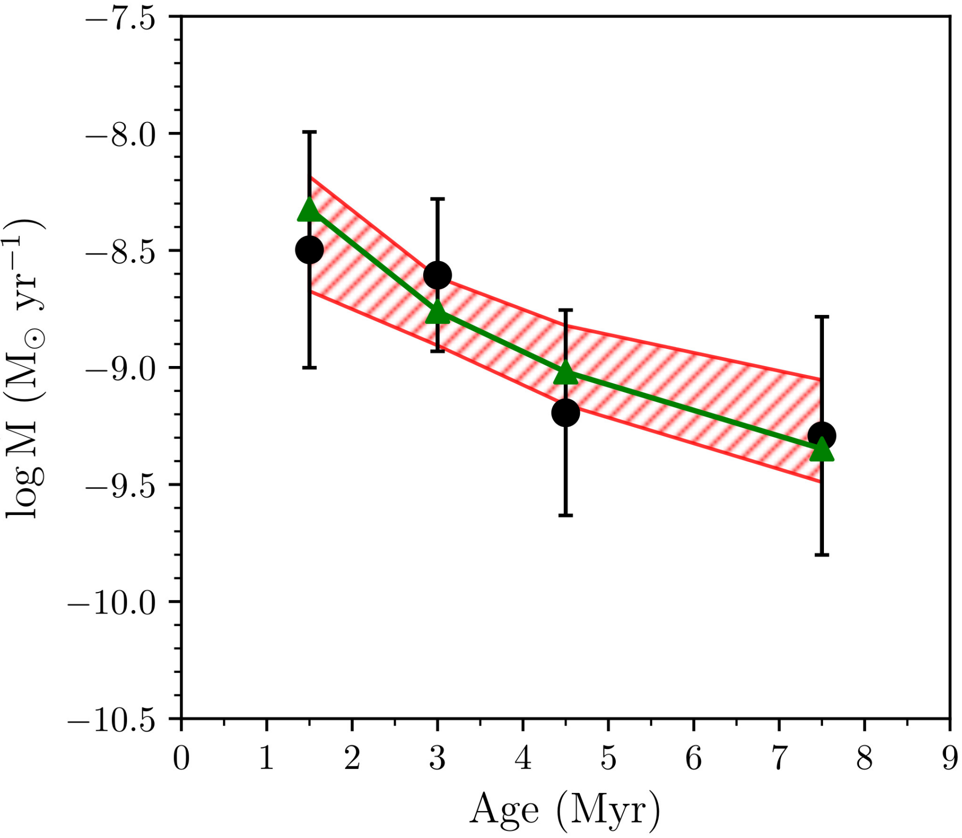

Figure 3.2: Median mass accretion rates as a function of age (black points), where the error bars correspond to the standard deviation of the distributions at each age. The solid green line shows the theoretical mass accretion rate for $M_d(0) = 0.07\,M_\odot$, $R_1 = 10$ au, and α=0.01. The red region corresponds to models with $\chi^2/0.48 \leq 2$ in Figure 3.1.

3.2 The D'Alessio models

Given the observed signatures of evolution discussed in §2.5, §2.6, and §3.1, we aim to calculate the emission of disks for which the radial distribution of surface density is given by Equation (3.11) at each one of the age bins for which we have obtained color excesses and, thus, compare the models to the observations. To do so, we need to calculate the vertical structure of the disk, namely, we need to solve the disk structure equations to obtain the radial and vertical distribution of the temperature and volumetric density, which result in the given $\Sigma(R,t)$. For this purpose, we use the irradiated disk models developed by D’Alessio (1996); D’Alessio et al. (1998, 1999, 2001, 2006), adopting several approximations to adapt these models to the Lynden Bell & Pringle (1974) models.

3.2.1 Assumptions

The D’Alessio models are models of irradiated accretion disks in steady state, and they assume that the disk is steady, geometrically thin and axially symmetric. The basic assumptions of these models are: (1) the dust and gas are assumed to be thermally coupled, i.e., they follow the same temperature distribution, (2) the disk is heated by absorption of stellar and accretion shock radiation as well as viscous dissipation, (3) the energy is transported by radiation, convection, and a turbulent flux, and (4) the disk is cooled by dust thermal emission.

We will adopt the α prescription to represent the viscosity (Shakura & Sunyaev, 1973), with the sound speed evaluated at the midplane temperature T_c. In this prescription, the uncertainties as to the origin and efficiency of the viscosity are included in the α parameter, with the constraint that $\alpha < 1$, and in this thesis we adopt $\alpha = 0.01$ (cf. §3.1). As discussed in §3.1, with the α prescription, the viscosity only increases linearly with radius, as assumed in the Lynden Bell & Pringle (1974) similarity solution, if the temperature depends on radius as $T \propto R^{-1/2}$ (Hartmann et al., 1998), which only happens approximately in more realistic physical situations (cf. D’Alessio et al., 2001, 2006).

3.2.2 Vertical structure equations

We now describe the equations that are solved in order to obtain the disk vertical and radial structure.

Hydrostatic equilibrium

$$\frac{dP_{\mathrm{g}}}{dz} = -\rho g_z - \frac{dP_{\mathrm{rad}}}{dz}. \tag{3.21}$$

This equation describes the vertical gradient of the gas thermal pressure. Since the disk is in vertical hydrostatic equilibrium, the sum of all the vertical components of the forces equals zero, thus, the disk is not expanding nor contracting in the vertical direction. Here the forces involved are: the gas thermal pressure gradient (dP_{g}/dz), the vertical component of the stellar gravity ($-\rho g_z$), and the radiation pressure gradient (dP_{rad}/dz). Both pressure gradients (gas and radiation) act in the opposite direction to the vertical component of the stellar gravity $-\rho g_z$. The term dP_{rad}/dz might be important in disks with the highest mass accretion rates or in low density regions. The disk's self-gravity is neglected, since for $M_d \lesssim 1/3\, M_*$, the disk is gravitationally stable (Shu et al., 1990).

Viscous heating

$$\frac{dF}{dz} = \Gamma_{\mathrm{vis}} + \Gamma_{\mathrm{ion}}. \tag{3.22}$$

This is an equation for the energy rate per unit volume, locally generated by viscous dissipation and ionization by energetic particles at each height, and it describes how the total flux $F = F_{\mathrm{vis}} + F_{\mathrm{ion}}$ changes in the vertical direction; $\Gamma_{\mathrm{vis}} = (9/4)\alpha P_g \Omega_K$ is the heating rate per unit volume due to viscous dissipation and $\Gamma_{\mathrm{ion}} = n_{_{\mathrm{H2}}}[\Delta Q_{\mathrm{cos}}\zeta_{\mathrm{cos}} \exp^{-\Sigma/\lambda} + \Delta Q_{\mathrm{rad}}\zeta_{\mathrm{rad}}]$ is the heating rate per unit volume due to ionization from energetic particles (cosmic rays and ^{26}Al). In these expressions, α is the free parameter of the prescription adopted for the viscosity coefficient, $n_{_{\mathrm{H2}}}$ is the number density of Hydrogen molecules, $\lambda = 96\,\mathrm{gr\,cm^{-2}}$ is the attenuation surface density scale of cosmic rays, $\Delta Q_{\rm cos} \sim 20\,\mathrm{eV}$ and $\Delta Q_{\rm rad} \sim 10\,\mathrm{eV}$ (Goldsmith & Langer, 1978) are the energies released in heating in each cosmic ray ionization and in radioactive decay ionization, respectively, and $\zeta_{\rm cos} = 1 \times 10^{-7}\mathrm{seg}^{-1}$ (Nakano & Umebayashi, 1986) and $\zeta_{\rm rad}(^{26}\mathrm{Al}) = 5.2 \times 10^{-19}\mathrm{seg}^{-1}$ (Stepinski, 1992) are the ionization rates due to cosmic rays and radioactive decay, respectively.

Energy transport by radiation

$$\frac{dF_{\rm rad}}{dz} = \Lambda_{\rm d} - \Gamma_{\rm d} - \Gamma_{\rm irr}, \tag{3.23}$$

$$\frac{dJ_{\rm d}}{dz} = -3\rho\chi_R \frac{(F_{\rm rad} - F_{\rm s} - F_{\rm i})}{4\pi}. \tag{3.24}$$

These are equations for the derivative of the total radiative flux $dF_{\rm rad}/dz$ and for the derivative of the mean intensity $dJ_{\rm d}/dz$ of the disk radiation field, integrated in wavelength. They describe how the effective stellar radiation penetrates in the disk, a fraction being truly absorbed while another fraction is being scattered. The fraction that is truly absorbed is taken into account as a local heating source of the disk. The energy rate per unit area transported by radiation is given by the direct effective stellar flux $F_{\rm i}$, the diffuse stellar flux $F_{\rm s}$, and the disk radiative flux $F_{\rm d}$, so that $F_{\rm rad} = F_{\rm i} + F_{\rm s} + F_{\rm d}$.

The gradient of the total radiative flux $dF_{\rm rad}/dz$ is given by the contribution of three energy rates per unit volume (Equation 3.23): the disk's radiative cooling rate por unit volume ($\Lambda_{\rm d} = 4\pi\rho\kappa_P\sigma T^4/\pi$), the heating rate per unit volume due to the disk's own radiation ($\Gamma_{\rm d} = 4\pi\rho\kappa_P J_{\rm d}$), and the heating rate per unit volume due to the radiation from the star ($\Gamma_{\rm irr} = 4\pi\rho\kappa_P^*(J_{\rm s} + J_{\rm i})$). In these expresions, ρ is the disk mass volumetric density, κ_P is the Planck mean opacity (see. §3.2.4) evaluated at the local temperature, σ is the Steffan-Boltzmann constant, T is the disk local temperature, κ_P^* is the Planck mean opacity evaluated at the temperature of the star T_*, while $J_{\rm i}$ and $J_{\rm s}$ are the mean intensities of the direct stellar flux and the diffuse stellar flux, respectively. The gradient of the disk mean intensity $J_{\rm d}$ in the vertical direction is given by Equation (3.24), where χ_R is the Rosseland mean opacity (see. §3.2.4).

Turbulent and/or convective energy transport

$$\frac{dT}{dz} = -\nabla(F_{\rm rad}, F, T, P_{\rm g})\frac{T}{P_{\rm g}}\rho g_z. \tag{3.25}$$

This is an equation for the temperature gradient in the vertical direction, given a turbulent flux of energy that depends on the α viscosity parameter. The Schwarzschild criterion for convective stability is verified at each height, and when the disk becomes unstable against convection, this mechanism is included in the energy transport.

When the vertical structure of the disk is calculated, some of the boundary conditions are known at the disk midplane, while others are known at the disk surface, which has an unknown height z_∞. The disk surface, defined as the height at which the thermal pressure reaches a small arbitrary value P_∞, is obtained as an *eigenvalue* of the problem. At each radius, the vertical structure equations are integrated subject to the following boundary conditions (cf. D'Alessio, 1996; D'Alessio et al., 1998): at $z = z_\infty$, $P = P_\infty = 10^{-9}{\rm din\,cm^{-2}}$. The calculation starts from the guessed z_∞ upper boundary (see §3.2.3), estimating the unknown conditions in the upper boundary, then the code iterates until the conditions at the lower boundary, which are known *a priori* are satisfied. The total flux produced by viscous dissipation at $z = z_\infty$ is $F_{\rm vis}(z_\infty)$ and the net flux produced by energetic particles ionization is at $z = z_\infty$ is $F_{\rm ion}(z_\infty)$, thus the total energy flux is given by

$$F = F_{\rm rad} = (F_{\rm vis} + F_{\rm ion})|_{z_\infty}. \tag{3.26}$$

The turbulent and convective fluxes are zero since, by definition, the turbulent and/or convective elements (eddies) cannot get out from the disk surface. The effective stellar flux intercepted by the disk surface at z_∞ is $F_{\rm irr}$. This flux is reprocessed by the disk and emerges from its surface at a wavelength range characteristic of the disk temperature. From the steady state assumption, the incident stellar flux is equal to the emergent reprocessed stellar flux, both integrated in frequency. As a consequence, the net flux associated with the effective stellar irradiation is zero at z_∞ and it does not contribute to Equation (3.26). All the energy flux emerging from the surface of the disk is transported by radiation, i.e., $F_{\rm rad}(z_\infty) = F(z_\infty)$. Finally, the disk mean intensity at z_∞ is

$$J_{\rm d}(z_\infty) = J_\infty = \frac{1}{2\pi}(F_{\rm vis} + F_{\rm ion} + F_{\rm irr} - F_{\rm s})|_{z_\infty}. \tag{3.27}$$

At $z = 0$, $F = F_{\rm rad} = 0$, i.e., at the disk midplane ($z = 0$), all the energy fluxes are zero, due to the reflection symmetry.

3.2.3 Solving the vertical structure equations

The D'Alessio code for the structure and emission of a disk starts with the calculation of the structure of a non-irradiated accretion disk, purely heated by viscous dissipation, as a first guess. Given this first solution, the surface at which the optical depth to the effective stellar radiation equals one is found. This surface, known as the irradiation surface $z_{\rm s}$, allows one to calculate how much of the effective stellar flux is intercepted by the disk, and also the impinging angle of the radiation in the disk's atmosphere. Then, the disk structure is calculated adding the effective stellar radiation intercepted by the disk as an additional heating mechanism. Since the disk is more heated in the presence of irradiation, its temperature increases with respect to the purely viscous case. This changes the disk's density distribution through Equation (3.21) (hydrostatic equilibrium), which yields a new disk structure with an irradiation surface different to that from the initial solution. The new irradiation surface is calculated for the new disk structure, as well as the new irradiation flux and impinging angle. Finally, the new irradiated disk structure is computed. This procedure is repeated until a new disk structure is computed self-consistently with the effective stellar irradiation included in the calculation of the temperature, when the code converges and satisfies the boundary conditions.

Once the disk structure is obtained, in the D'Alessio models the surface density Σ is obtained by integrating the volumetric density $\rho(R, z)$ in the vertical direction, and corresponds to the column density of a steady disk, which lacks the exponential fall-off at large radii (cf. Equation 3.11). Since we cannot impose *a priori* the radial surface density of the disk in the model, following Qi et al. (2011) we modified the α parameter so that

$$\alpha = \alpha_0 e^{R/R_\mathrm{t}}, \tag{3.28}$$

where R_t is the critical radius outside which the exponential fall-off becomes important and α_0 is the value of α at $R << R_\mathrm{t}$. The critical radius is given by $R_\mathrm{t} = R_1 \mathbb{T}$ (Equation 3.11). For $t >> t_s$, this is

$$\begin{aligned} R_\mathrm{t} &= 1.37 \times 10^2 \mathrm{AU} \left(\frac{T_{d2}}{10\,\mathrm{K}}\right) \left(\frac{M_*}{0.30\,M_\odot}\right)^{-1/2} \\ &\left(\frac{\alpha_1}{0.01}\right) \left(\frac{t}{\mathrm{Myr}}\right), \end{aligned} \tag{3.29}$$

where α_1 is the parameter used in the viscosity ν_1, at R_1 (see §3.1). As stated in Qi et al. (2011), this modification adds an exponential taper to the radial distribution of the surface density, and does not reproduce the predicted behavior of the mass flow at large radii, but the effect on the observables is negligible, since irradiation dominates over viscous heating at these large radii.

The main input parameters for the D'Alessio models are the stellar mass M_*, the stellar radius R_*, and effective temperature T_eff, the mass accretion rate $\dot{M}$ and viscosity parameter α, the dust composition, size distribution, and spatial distribution in the disk. To be consistent with the surface density distribution resultant from viscous evolution calculations at a given age bin (Equation 3.11), the model uses as further input the transition radius $R_{\rm t}$, Equation (3.29), with $\alpha = 0.01$. In addition, we use the evolutionary models of Siess, Dufour & Forestini (2000) for a star of mass 0.30 $M_\odot$ (§2.2 and §3.1) to obtain the stellar luminosity and effective temperature at each age bin (see Table 4.1).

In the models, the disks are irradiated by the star and the accretion shocks on the stellar surface. The shocks are formed when disk material falls onto the star, creating hot spots on the surface, with a characteristic temperature of $\sim$ 8000 K (Hartmann, Herczeg & Calvet, 2016, and references therein). The total luminosity irradiating the disk is then $L_{\rm t} = L_* + L_{\rm shock}$, where we adopt $L_{\rm shock} = L_{\rm acc}$ (cf. Equation 2.6). From now on we refer to the radiation of the star plus the radiation from the accretion shocks, as the effective stellar radiation.

3.2.4 Dust properties and settling

The dust is the main source of opacity in protoplanetary disks. The opacity χ_ν describes the capacity of a medium to absorb and scatter radiation of a given frequency ν, and has units of cross-section per unit mass. The opacity is the sum of the true absorption coefficient κ_ν and the scattering coefficient σ_ν. The true absorption includes the processes of absorption that transform the energy of the radiation field into thermal energy, i.e., the photons are destroyed, while in the scattering processes the impinging radiation bounces when hitting the medium, and no photons are destroyed, thus, the photons retain their original wavelength.

The optical depth along a ray $\vec{s}$, is defined as

$$\tau_\nu = \int_{s_1}^{s_2} \chi_\nu \rho ds, \tag{3.30}$$

and it describes the extinction, that is, the absorption and scattering along the ray, between s_1 and s_2. The optical depth is a non-dimensional quantity and its physical interpretation can be explained as the distance $= s_2 - s_1$, in units of the mean free path of a photon of frequency ν.

The dust is the main absorption and scattering component of the incident stellar and accretion shocks radiation, and the dust species used in the models are silicates and graphite, with abundances typical of the ISM (Draine & Lee, 1984). We assume a power law size distribution $n(a) \propto a^{-p}$, with an exponent of 3.5, where the sizes of dust grains range between a minimum radius $a_{\rm min} = 0.005\,\mu m$ and a maximum radius $a_{\rm max}$. The vertical dust settling is included in the models by assuming two populations of dust grains with different values of $a_{\rm max}$: the disk upper layers contain small atmospheric sub-micron grains, while the large grains that have settled are concentrated towards the midplane (D'Alessio et al., 2006).

The maximum grain size for the upper layers is $a_{\rm max} = 0.25\,\mu m$, while $a_{\rm max} = 1\,{\rm mm}$ in the midplane (D'Alessio et al., 2006). Both populations have different dust-to-gas mass ratios, ζ and, since the midplane region contains the mass of the dust grains that have settled from the upper layers, the corresponding $\zeta_{\rm big}$ is larger than the standard value $\zeta_{\rm std}$=0.01 (Draine & Lee, 1984). Accordingly, in the surface layers $\zeta_{\rm small}$ is smaller than the standard value. The distribution of the large grains population extends to a height $z_{\rm big}(R)$ and in this thesis we adopt $z_{\rm big}(R) = H$, where H is the scale height at the local temperature. The degree of dust settling is quantified using the following parameter (D'Alessio et al., 2006)

$$\epsilon = \frac{\zeta_{\rm small}}{\zeta_{\rm std}}. \tag{3.31}$$

The values for $\zeta_{\rm big}/\zeta_{\rm std}$ are computed using Equation (A5) from D'Alessio et al. (2006). Figure 3.3 shows the cross-section of a disk, illustrating the treatment used here for the dust settling. In the absence of settling ($\zeta_{\rm small} = \zeta_{\rm std}$ and $\zeta_{\rm big} = \zeta_{\rm std}$) the small and the large grains are mixed, and equally populate the upper layers and the midplane; in contrast, when settling is present ($\zeta_{\rm small} < \zeta_{\rm std}$ and $\zeta_{\rm big} > \zeta_{\rm std}$), the upper layer contain small grains, while the largest grains concentrate toward the midplane.

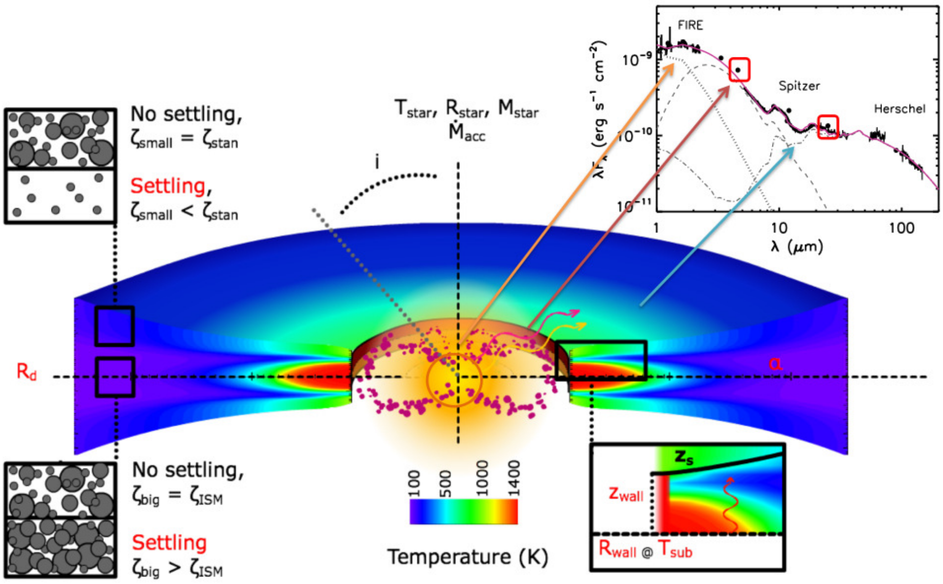

Figure 3.3: Cross-section of a disk, illustrating the dust settling. Image credits: Melissa McClure.

As discussed in §3.2.3 and in §3.2.6, the disk structure is calculated self-consistently by solving the vertical structure equations in an iterative scheme (D'Alessio et al., 1998), and the radiative transfer is done using mean opacities calculated in two wavelength regions, the "stellar" and the "local" temperature regions (Calvet et al., 1991; D'Alessio et al., 1998). We now explain the mean opacities used to obtain the disk structure.

The Rosseland mean opacity is a harmonic mean defined by

$$\chi_R^{-1} = \frac{\int_0^\infty (1/\chi_\nu)(dB_\nu/dT)d\nu}{\int_0^\infty (dB_\nu/dT)d\nu}, \tag{3.32}$$

where B_ν is the Planck function. This is a frequency averaged opacity, characteristic of the disk's radiation, and it is a measure of how "transparent" a medium is to the incoming radiation. The Rosseland mean optical depth is defined as

$$\tau_R(z,R) = \int_z^{z(R)} \chi_R(T,\rho)\rho(z,R)dz, \tag{3.33}$$

where $z(R)$ depends on the radius.

The Planck mean opacity is defined by

$$\kappa_P = \frac{\int_0^\infty \kappa_\nu B_\nu d\nu}{\int_0^\infty B_\nu d\nu}. \tag{3.34}$$

The true absorption of the radiation in the stellar range of frequencies is described by a mean Planck type opacity κ_P^*, evaluating the true absoprtion coefficient at the local pressure and temperature, while the Planck function is evaluated at the stellar temperature.

The mean opacities are computed from the monochromatic opacities of each dust species. The equations for the energy transport (cf. §3.2.2) are integrated in frequency and allow us to calculate the disk structure avoiding the problem of solving the radiative transfer within the disk for each wavelength. The “stellar” mean opacities are the average of opacities calculated at the stellar and shock temperatures, weighted by the corresponding luminosity.

Figure 3.4 shows the monochromatic absorption coefficient as a function of wavelength for a mix of silicates and graphite. The green line corresponds to the distribution of dust grains with $a_{\max} = 0.25\,\mu m$ and the red line corresponds to the distribution of dust grains with $a_{\max} = 1\,\mathrm{mm}$. Both populations

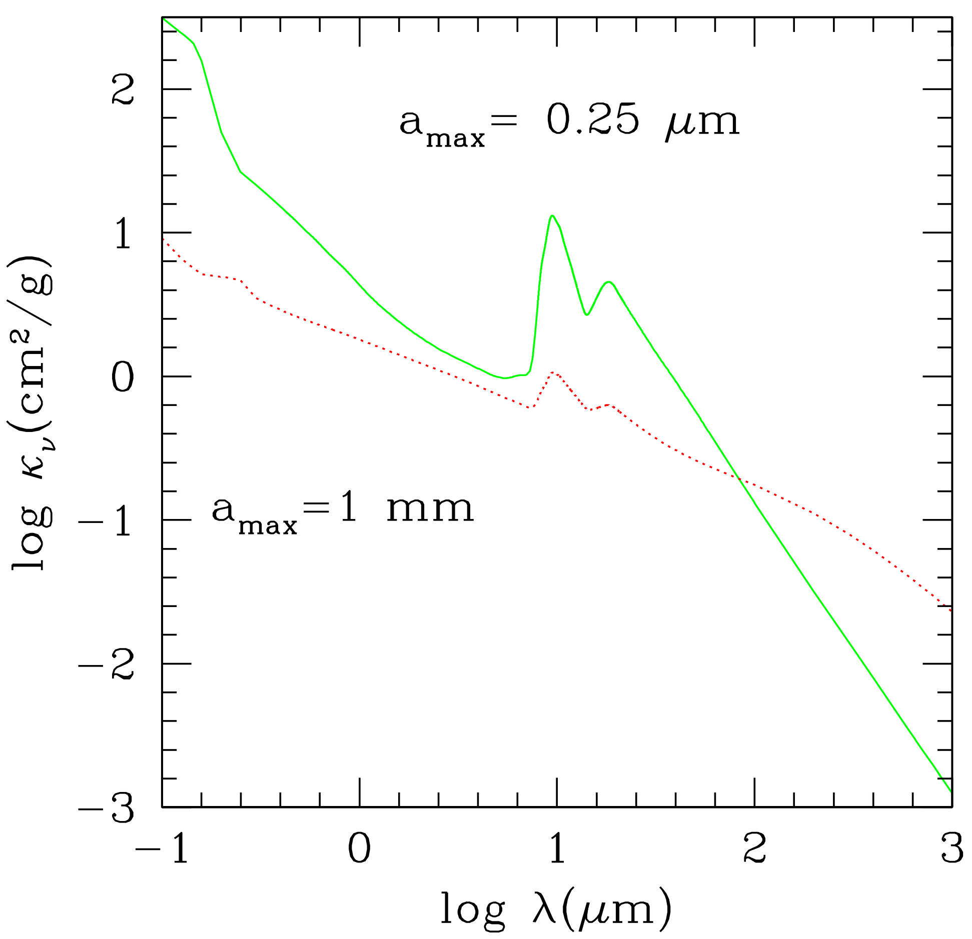

Figure 3.4: Monochromatic absorption coefficient as a function of wavelength for two distributions of dust grains: (1) with $a_{\mathrm{max}} = 0.25\ \mu m$ (green) and (2) with $a_{\mathrm{max}} = 1$ mm (red); both with $a_{\mathrm{min}} = 0.005\,\mu m$. The calculation corresponds to the mix of silicates and graphite used in this work, and with a size distribution with exponent $p = 3.5$.

have a minimum grain size $a_{\mathrm{min}} = 0.005\,\mu m$ and their size distributions were computed for an exponent $p = 3.5$. Notice that increasing the maximum size of the dust grains, given a fixed disk mass, decreases the number of sub

μm grains, which are more efficient absorbing the radiation in the shortest wavelengths (UV, optical), however the absorption coefficient increases for wavelengths larger than the millimeter. The silicate features at 10 μm and 18 μm become weaker when the abundance of large grains increases since, as the grains are larger, they become gray absorbers, i.e., they absorb equally all wavelengths of the radiation.

3.2.5 The wall

The most important contributor to the overall disk emission in the near-IR is the disk region at the dust destruction radius (Isella & Natta, 2005; D'Alessio et al., 2005; Dullemond & Monnier, 2010), which we name "the wall", and it is the disk inner border. For radii smaller than the wall radius, the temperature reaches values above the silicates sublimation temperature ($\sim$ 1500 K), and we assume that dust does not exist. In the literature, the wall is generally assumed to be vertical and irradiated frontally by the central star, but several studies have shown that the wall may instead be curved (Isella & Natta, 2005; Tannirkulam et al., 2008; McClure et al., 2013). Figure 3.5 shows an illustration of the curved dust wall. This kind of shape for the wall is expected because the larger dust grains settle towards the disk midplane. Since the micron-sized atmospheric grains are more efficient absorbing radiation at wavelengths characteristic of the effective stellar radiation, the larger grains can survive closer to the star. In addition, the dust sublimation temperature decreases with density as discussed in Pollack et al. (1994).

McClure et al. (2013) modeled the SED and near-IR spectra of four T Tauri stars in the Taurus region, and found that a treatment of the wall that accounts for its curvature allows for a much better fit to the spectra than a vertical wall. Following McClure et al. (2013) we mimic the curvature of the wall as a two-layered wall. The lower layer contains larger (1 μm) hotter grains (1500 K), while the upper layer contains sub-micron (0.25 μm), cooler

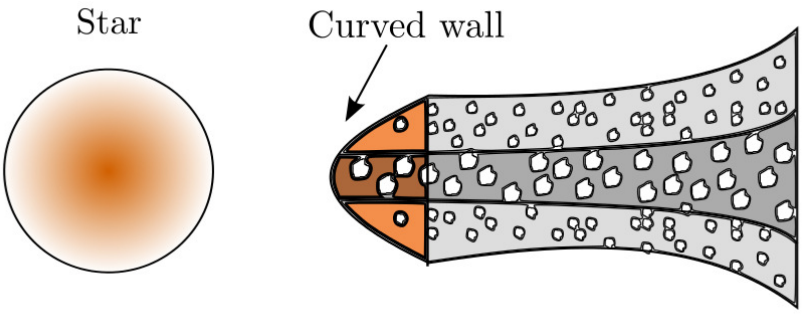

Figure 3.5: Illustration of the curved dust wall. The larger dust grains at the midplane can survive closer to the star than the smaller atmospheric grains.

(1000 K) grains. The radius of each layer, R_{in_1} and R_{in_2} for the lower and upper wall, respectively, is set by the total luminosity, L_t, and the respective dust properties, using the relation $R_{in_i} \propto (L_* + L_\mathrm{acc})^{1/2}(T_{w_i})^{-2}$, where T_{w_i} is the sublimation temperature of the dust grains in the lower ($i = 1$) and the upper ($i = 2$) wall, respectively. Both layers are frontally illuminated with a normal impinging angle. The calculation of the emission from each layer follows the treatment of D'Alessio et al. (2005).

3.2.6 Disk emission

Once the disk structure is calculated, that is $T(R, z)$ and $\rho(R, z)$ (see §3.2.2 & §3.2.3), using mean opacities computed from a set of monochormatic opacities (§3.2.4), the emission from the disk can be obtained. The main input parameters are the disk inclination angle i, which is the angle between the line of sight of the observer and the disk's rotation axis, and the outer disk radius R_d. The SED is calculated using a grid of beams parallel to the line of sight, which go across and fully cover the projection of the disk on the plane of the sky (see Figure 3.6). Then, the radiative transfer equation

$$\mu \frac{dI_\nu}{d\tau_\nu} = I_\nu - S_\nu \tag{3.35}$$

is integrated for a given wavelength, in a ray-by-ray solution including thermal emission from the dust and a single scattering of stellar radiation (D'Alessio et al., 1998, 2006). In Equation (3.35), I_ν is the specific intensity of the radiation field, τ_ν is the optical depth, $\mu = \cos(i)$, and $S_\nu = \eta_\nu / \chi_\nu$ is the source function, where η_ν is the emissivity and χ_ν is the opacity. By repeating this procedure for a wide range of wavelengths, the SED is obtained.

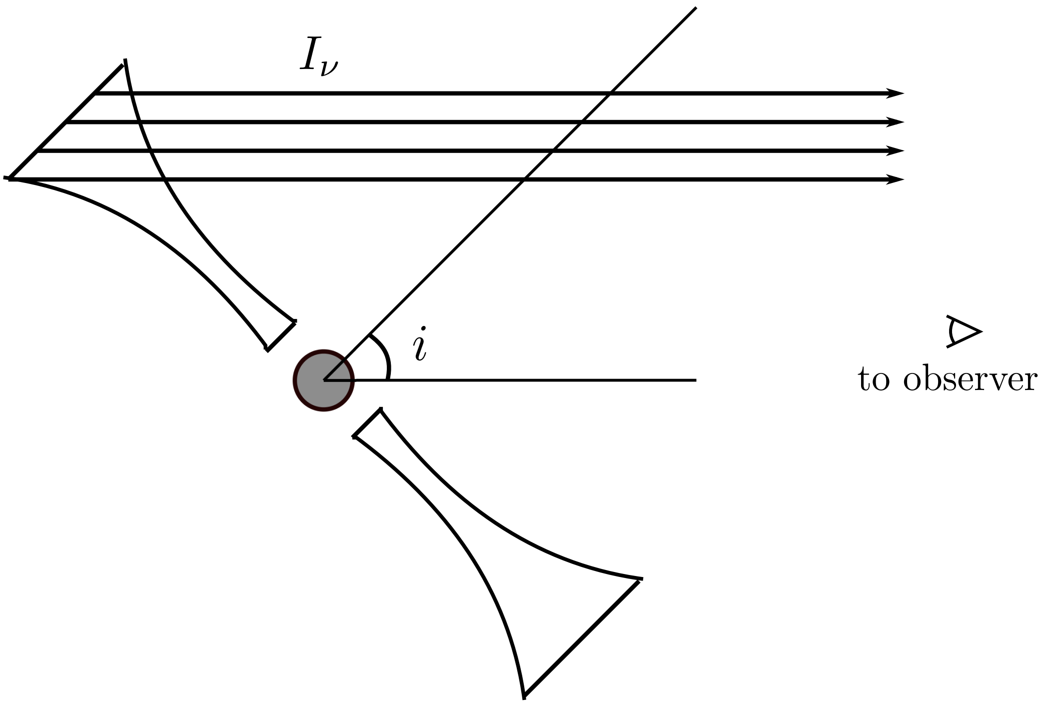

Figure 3.6: Illustration of the disk rotation's axis with respect to the line of sight, given by the angle i. The synthetic SED is obtained by solving the radiative transfer equation along beams that cover the projection of the disk in the plane of the sky.

The total SED is constructed as the sum of the emission from the disk, the wall, the star, and the accretion shock. We assume the shock emits as a blackbody with $T = 8000$ K and emitting area $f 4\pi R_*^2$. The filling factor f is then calculated by the condition that the shock luminosity is the accretion luminosity.

4

Comparison with observations

In this Chapter we explain how we build the grids of disk models for each age bin, and the statistical method applied in order to reproduce the observed DCE distributions. In §4.1 we give details about the construction of the model grid, the parameters we varied, and the different contributions to the synthetic SEDs of the models. In §4.3 we introduce the method of Approximate Bayesian Computation, which we use to find the distributions of the disk parameters that reproduce the observed decay of the different DCEs with age, shown in §2.5.

4.1 Construction of the model grid

Using the methods described in §3.2, we computed a grid of disk models for each age bin, since the stellar properties change during the timescale of disks' evolution and, thus, the corresponding characteristic central star must be used at each bin.

Concerning the gas content, the models were calculated using the following mass accretion rates: $2 \times 10^{-8}, 1 \times 10^{-8}, 5 \times 10^{-9}, 1 \times 10^{-9}$ and $5 \times 10^{-10} M_{\odot} yr^{-1}$, which represent a comprehensive range of the measured accretion rates in T Tauri disks around low-mass stars.

Related to the dust component, in particular the wall (see §3.2.5), for simplicity, we only considered cases where the upper and the lower parts of the two-layered wall at the dust destruction radius have the same ratio

$$\frac{z_{\rm wall}}{H} = \frac{z_{\rm wall_1}}{H_1} = \frac{z_{\rm wall_2}}{H_2}, \tag{4.1}$$

where H_1 and H_2 are the gas scale heights $H_1 \propto T_{w_1}^{1/2} R_{in_1}^{3/2} M_*^{-1/2}$ and $H_2 \propto T_{w_2}^{1/2} R_{in_2}^{3/2} M_*^{-1/2}$, at the lower and upper wall, respectively. As mentioned before, we assume that the dust in the lower and upper wall sublimates at $T_{w_1} = 1500$ K (with $a_{\rm max} = 1\,\mu m$) and $T_{w_2} = 1000$ K (with $a_{\rm max} = 0.25\,\mu m$), respectively, recalling that the largest grains can survive closer to the star. We run models with values for $z_{\rm wall}/H$ from 0.1 to 4, in steps of 0.8 . The total physical height of this two-layered wall is then

$$Z_{\rm wall}(au) = \left(\frac{z_{\rm wall}}{H}\right)(H_1 + H_2). \tag{4.2}$$

where H_1 and H_2 are expressed in astronomical units. We also varied the settling parameter ϵ (see §3.2.4 and Figure 3.3), from 1 to 0.0001, and the cosine of the inclination $\cos(i)$, from 0 to 1. For each age bin we run 1350 disk models, thus, the total number of models calculated, taking into account the four bins, is 5400. Since we are neither including nor modeling data beyond $24\,\mu m$, the disk outer radius $R_{\rm disk}$ is chosen arbitrarily, with the only constraint that it is located beyond the critical radius $R_{\rm t}$ (Equation 3.29). We use these parameters to compute disk models following the treatment discussed in §3.2, and build their synthetic SEDs and DCEs (see Figures 4.1 and 4.2). In Table 4.1 we show the values for R_*, $T_{\rm eff}$, L_*, and $R_{\rm disk}$, adopted in each age bin to compute the model grid.

Table 4.1: Parameters of the models

Age Myr	R_* $R_\odot$	$T_{\rm eff}$ K	L_* $L_\odot$	$R_{\rm disk}$ au
1.5	1.71	3360	0.38	230
3	1.25	3385	0.21	410
4.5	0.97	3416	0.13	660
7.5	0.79	3451	0.09	1080

As previously mentioned, the pre-main sequence star is also evolving during the characteristic timescales of the disk's evolution, hence, we take into account the changes in the stellar properties during its evolution. The star is contracting along Hayashi tracks in the H-R diagram (cf. Figure 1.3), at almost constant $T_{\rm eff}$, while decreasing its luminosity. This means that the effective stellar irradiation intercepted by the disk does not remain constant in time. As a consequence the resulting density and temperature distributions in the disk structure are affected. As mentioned in §3.2.3, and to be consistent with the determination of the stellar masses of our observational sample (cf. §2.2), we use the stellar models from Siess, Dufour & Forestini (2000), to obtain the stellar properties, using the evolutionary track of a $0.3\,M_\odot$ star, which is the mean value obtained from the distribution of stellar masses in all age bins (cf. §2.2).

To compute the DCEs of the models in the IRAC and MIPS 24 bands, given the synthetic SEDs, we calculate their fluxes and magnitudes in the 2MASS, IRAC, and MIPS 24 bands, using the corresponding transmission profiles of the filters. Using the J band and the IRAC and MIPS 24 bands, we then built the corresponding synthetic colors. We also obtain the values for the photospheric magnitudes and photospheric colors of the models, and calculate the corresponding DCEs, by subtracting the models' photospheric colors from the colors obtained from the complete synthetic SED of the model. We calculate the DCEs for the colors J-[4.5], J-[5.8], J-[8.0], and

J-[24].

Figure 4.1 shows the SEDs for two of our models (§3.2.6), with stellar parameters from bin 1, for two values of the wall height: $z_{\rm wall}/H$ =0.8 (left panel) and $z_{\rm wall}/H$ =3 (right panel). We show in different colors the contribution of each component, and indicate with solid red circles the 2MASS, IRAC, and MIPS 24 fluxes; the red squares indicate the fluxes at 4.5 μm and at 24 μm.

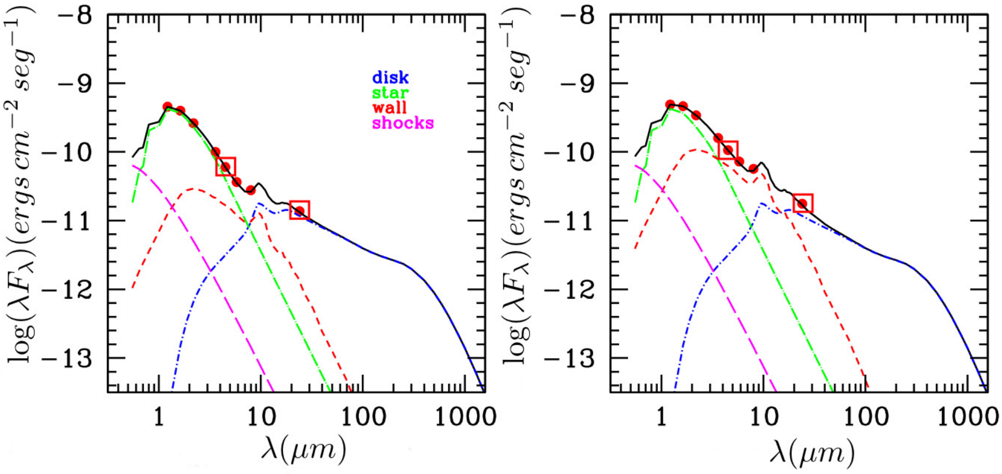

Figure 4.1: SEDs of disk models from bin 1, with ϵ=0.0001, $z_{\rm wall}/H$=0.8 (left) and $z_{\rm wall}/H$=3 (right), with $\dot{M} = 1.0 \times 10^{-8}\, M_\odot/yr$. Each line represents a different component: the star (green dashed), the wall (red short-dashed), the accretion shocks (pink long-dashed), the disk (blue dot-dashed), and the total (black solid). The red points correspond to the 2MASS, IRAC, and MIPS 24 fluxes; the red squares indicate the flux at 4.5 μm and at 24 μm. The inclination is $\cos(i) = 0.5$.

It can be seen that at 24 μm the flux is dominated by the disk contribution, and thus, the excess at 24 μm can be used to estimate the degree of dust settling in the disk, quantified by the parameter ϵ (§3.2.4), which measures the dust depletion in the disk upper layers (D'Alessio et al., 2006).

The emission at 4.5 μm is better traced by the wall, which dominates the near-IR emission.

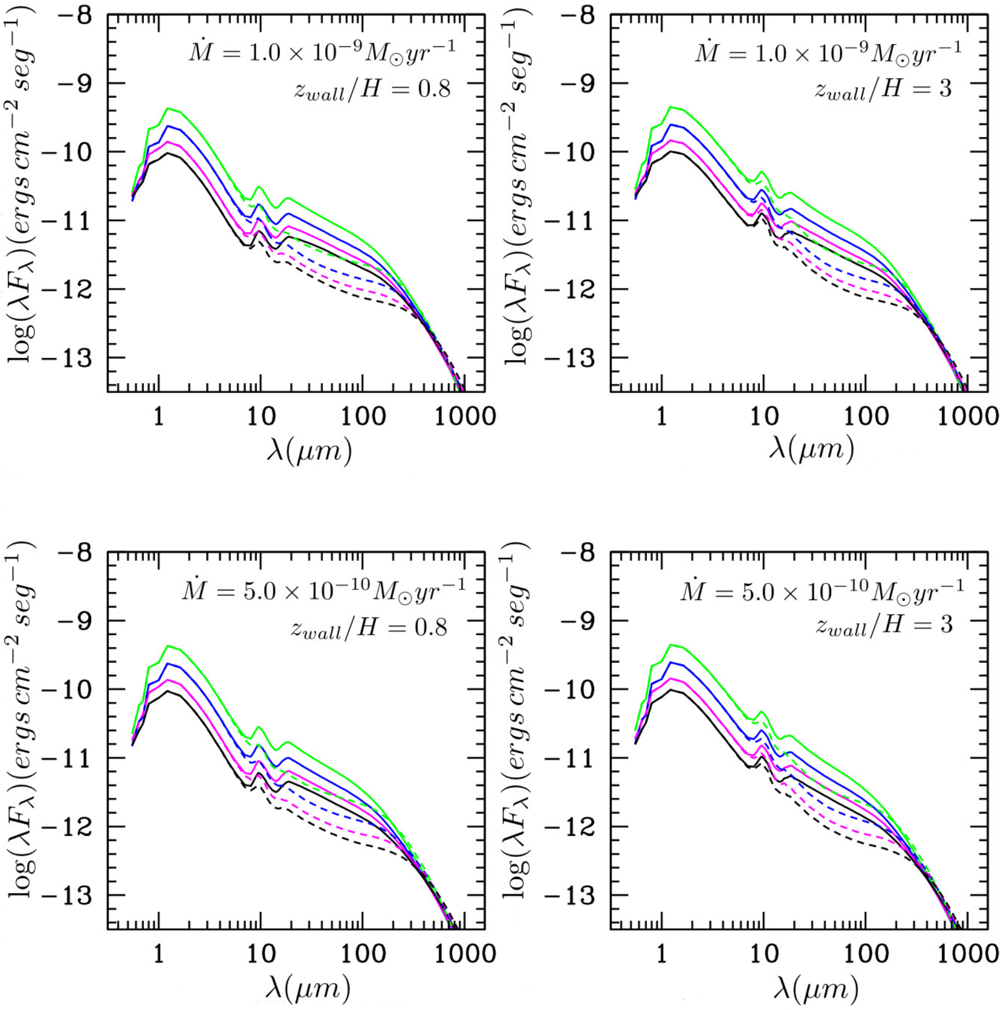

Figure 4.2: SEDs of disk models for different age bins: bin 1 (green), bin 2 (blue), bin 3 (magenta), and bin 4 (black), with $\dot{M} = 1.0 \times 10^{-9}\ M_{\odot}/yr$ (upper panels) and $\dot{M} = 5.0 \times 10^{-10}\ M_{\odot}/yr$ (lower panels). Two values of ϵ are shown: 0.01 (solid lines) and 0.0001 (dashed lines). The left and right panels correspond to models with $z_{\rm wall}/H$=0.8 and $z_{\rm wall}/H$=3, respectively. The inclination is $\cos(i) = 0.5$.

In order to illustrate the effects of varying the mass accretion rate, the ϵ parameter, and the height of the wall $z_{\rm wall}/H$, at each age bin, we show in Figure 4.2 the SEDs of disk models with $z_{\rm wall}/H$=0.8 (left panels) and $z_{\rm wall}/H$=3 (right panels), for bin 1 (green), bin 2 (blue), bin 3 (magenta), and bin 4 (black). In the upper and lower panels we show models with $\dot{M} = 1.0 \times 10^{-9}\, M_{\odot}/yr$ and $\dot{M} = 5.0 \times 10^{-10}\, M_{\odot}/yr$, respectively; additionally, two values of the parameter ϵ are indicated with different lines: 0.01 (solid lines) and 0.0001 (dashed lines).

Various effects can be seen in Figure 4.2. The first effect is that for a given $\dot{M}$ and $z_{\rm wall}/H$, the emission at $\lambda \lesssim 1.3\, \mu m$ (dominated by the central star) decays with age, since the stellar luminosity decreases as the age increases. In addition, when the disk surface intercepts less stellar irradiation, its density decreases, affecting the disk efficiency at absorbing and emitting radiation, which results in a decay with age in the emission at $20\, \mu m \lesssim \lambda \lesssim 200\, \mu m$. Varying ϵ from 0.01 (solid lines) to 0.0001 (dashed lines) affects the SED at $8\, \mu m \lesssim \lambda \lesssim 200\, \mu m$, since the irradiation surface of a highly settled disk ($\epsilon = 0.0001$) is located at lower heights than the irradiation surface of a disk with low degree of settling ($\epsilon = 0.01$). As a consequence, the disk with $\epsilon = 0.0001$ is geometrically thinner and, thus, its emission in the mid and far IR decreases with respect to the disk with $\epsilon = 0.01$. The second effect is related to the wall, since for a disk of a given $\dot{M}$, ϵ, and age, increasing the height of the wall also increases the near-IR emission ($3\, \mu m \lesssim \lambda \lesssim 20\, \mu m$). The third effect appears when we consider a disk with a fixed $z_{\rm wall}/H$ and ϵ; decreasing $\dot{M}$ induces a decay in the accretion shocks emission, and simultaneously the release of energy by viscous dissipation decreases for lower mass accretion rates, making the inner disk cooler. Finally, Figure 4.2 shows how the global emission from the system decreases with age at all wavelengths, for a given $\dot{M}$ and $z_{\rm wall}/H$.

Once the grids of models for each age bin are calculated, we have DCEs for a large number of models. In our study we compare the values of the different DCEs of the models with the DCEs from the observational sample (see §4.3). In Figure 4.3 we plot the $\mathrm{DCE}_{J-[4.5]}$ versus $\mathrm{DCE}_{J-[24]}$ from the corresponding grid of disk models used in each age bin (empty circles), showing in different colors various values of ϵ: 0.1 (blue), 0.01 (red), 0.001 (green), and 0.0001 (magenta). In addition, we plot the observational sample in each bin (black solid triangles) for reference. Figure 4.4 shows the $\mathrm{DCE}_{J-[5.8]}$ versus $\mathrm{DCE}_{J-[8.0]}$ (see also Figure 2.3), adopting the same color code. In both figures, the observational data and the models' DCEs are located in the same region. Moreover, in Figure 4.3 the models with the largest DCEs (e.g. $\mathrm{DCE}_{J-[4.5]} \gtrsim 3.5$ and $\mathrm{DCE}_{J-[24]} \gtrsim 8$) correspond to models of highly inclined disks, which are more difficult to detect and observe, since the star is hidden by the disk and the disk IR excess above the photosphere is difficult to measure. Notice also in Figure 4.3 that, as the age of the bin increases, the observed disks move towards the smallest values of ϵ, which is in agreement with the results we find using Approximate Bayesian Computation (see §4.3).

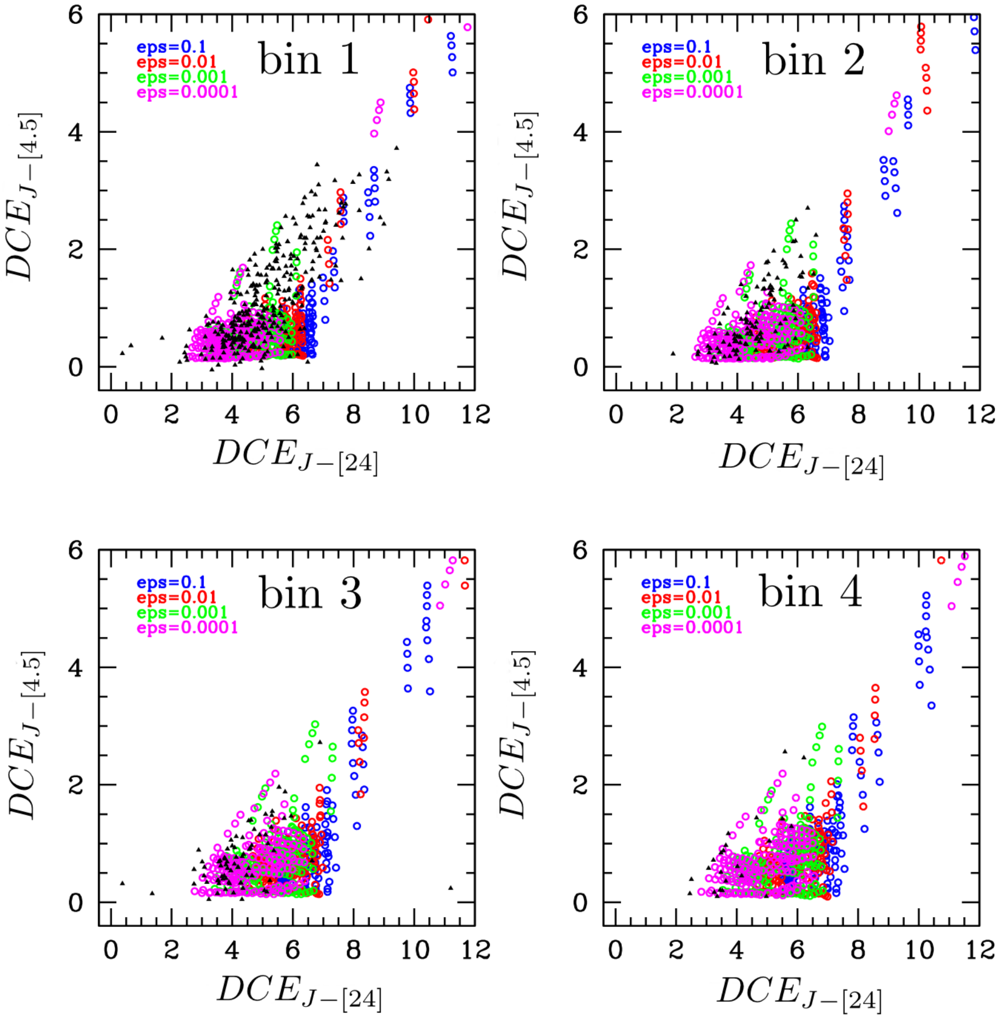

Figure 4.3: Synthetic DCEs obtained from the grid of models for bin 1 (upper left), bin 2 (upper right), bin 3 (lower left), and bin 4 (lower right). Various ϵ are shown in different colors: 0.1 (blue), 0.01 (red), 0.001 (green), and 0.0001 (magenta). The observational sample in each age bin (black triangles) is shown for comparison.

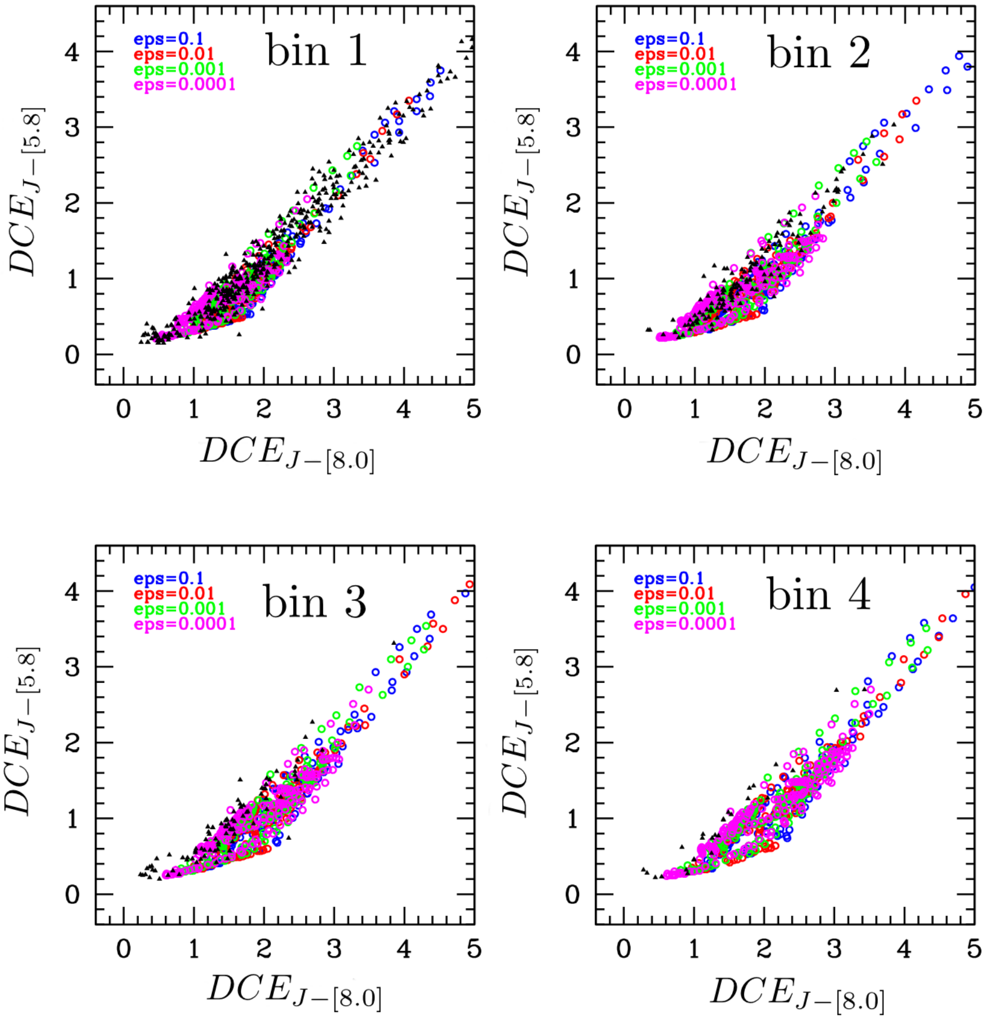

Figure 4.4: Synthetic DCEs obtained from the grid of models for bin 1 (upper left), bin 2 (upper right), bin 3 (lower left), and bin 4 (lower right). Various ϵ are shown in different colors: 0.1 (blue), 0.01 (red), 0.001 (green), and 0.0001 (magenta). The observational sample in each age bin (black triangles) is shown for comparison.

4.2 Bayesian statistics

We now explain some central aspects of Bayesian statistics in order to make clearer for the reader the statistical method used in this work. The data obtained from an experiment can be represented by $Y = \{y_1, y_2, ...y_n\}$, and it depends on a set of parameters θ. The goal of statistical inference is to find information about the distribution of the parameters θ, that allow one to reproduce the observed data.

In Bayesian statistics, the parameters are treated as random quantities together with the data. Information about the parameters is obtained from the *posterior distributions* $\pi(\theta|Y)$ of the parameters, which are the probability distributions after taking into account the observed data. In order to compute the posterior distributions: (1) the *likelihood* of the data must be computed and (2) a *prior* distribution for θ must be supplied. The likelihood, or likelihood function $L(\theta|Y)$, measures the goodness of the fit of a statistical model to a set of observed data and its peak can be interpreted as the combination of model parameters that give the maximum probability of drawing the distribution of the observed sample. The prior for θ can be based on previous observations and/or estimates of this parameter, before the actual observations are taken into account. In this thesis, our prior is given by the observed distributions of mass accretion rates at each age bin (cf. §4.3).

Instead of calculating the likelihood function, Approximate Bayesian Computation (cf. §4.3) uses a simulation of the model that produces an artificial data set X. Then, a comparison between the simulated data X and the observed data Y is performed (Turner & Van Zandt, 2012). The Bayesian approach allows to sample θ-values repeatedly from a prior distribution, which leads to the *accept/reject* algorithm, in which the sampled values θ' produce the artificial data X, and if $X = Y$, θ' is accepted, else, θ' is rejected. The set of accepted θ' forms a sample from the posterior distribution ($\pi(\theta|Y)$); the powerful advantage in these studies is the fact that the explicit calculation of the likelihood function is not required, and the method can be applied to large data sets (Marjoram, Hamblin, & Foley, 2015).

In reality, the accept/reject algorithm will never produce an exact data set such that $X = Y$, due to the complexity of the observed data, thus, an additional assumption must be introduced. In some cases a metric that measures the distance D between the data sets, and a tolerance ϵ are used, such that if $D(Y, X) < \epsilon$, θ' is accepted. In this thesis, we apply the acceptance/rejection policy in which we randomly sample from the cumulative distributions of the parameters θ, until we reproduce the observed data Y (Marjoram, Hamblin, & Foley, 2015), repeating this process 100 times, or *realizations*. This generates 100 distributions for each of the parameters θ that reproduce the observed data Y. Then, we use all the resulting distributions to calculate a mean distribution and the standard deviation for each bin of these distributions (see §4.3).

4.3 Approximate Bayesian Computation: forward modeling

In §4.1 we use a model to obtain DCEs for different disk models, for each age bin. The observed data comprise distributions of DCEs, which are shown in Figure 2.7. Our purpose is then to take our grid of models and determine the underlying parameter values which would recreate the observed DCE histograms (cf. §4.2). We will use Approximate Bayesian Computation (ABC) to quantify the posterior probability distributions for each parameter.

ABC was developed as a way to apply Bayesian statistical methods when an analytical representation of the data likelihood function is replaced with simulation-based models (Turner & Van Zandt, 2012). When using ABC, the forward model grid allows us to sample directly from the posterior by generating simulated datasets that match the observations. ABC requires a forward model, a summary statistic to use on the data and on the simulations, and a rule-set to accept or reject the choice of parameters. The

Bayesian prior is defined by the parameters used in the precalculated grid discussion in §4.1. The summary statistic that we use is the histogram representations of the data presented in §2.5 (cf. Figure 2.7). We use a simple but strict rejection policy where the forward modeled simulation of the data must match our observed histograms precisely (Marjoram, Hamblin, & Foley, 2015).

We search for the distributions of the input parameters $\log(\epsilon)$ and z_{wall}/H (see definition in §4.1) that best reproduce the observations. We create a realization of the observed histograms by randomly sampling from the cumulative distributions of the input parameters $\log \dot{M}$, $\cos(i)$, and either $\log\,\epsilon$ or z_{wall}/H, depending on the color excess we aim to reproduce, and calculating the disk color excess for the given combination of model parameters. Essentially, we use the grid of disk models at each age bin, for which we obtained DCEs in the IRAC and MIPS 24 bands, and randomly generate triads of parameters, either $(\log \dot{M}, \cos(i), \epsilon)$ or $(\log \dot{M}, \cos(i), z_{\text{wall}/H})$. Then, we interpolate in the grid in order to find the DCE associated with the disk model for the given combination of parameters randomly generated: if the corresponding DCE lies in the range of the observed DCE distribution, we accept this value and assign it to its corresponding bin; if the DCE falls out of the range of the observations, it is rejected. We keep randomly generating triads of parameters until the observed DCE distribution is reproduced.

We carry out 100 such realizations, each resulting on a distribution of input parameters that fit the observations. We use the distributions for all realizations to calculate a mean value and standard deviation at each bin of the distribution for each of our parameters of interest. To calculate the cumulative distributions of input parameters, we use as prior the observed mass accretion rate distributions in each age bin (§2.6) and assume a uniform distribution of inclinations, degrees of settling and wall heights, since we do not have any information *a priori* concerning the shape of these distributions.

Depending on the DCE we want to study and reproduce, we use different free parameters. Since the inner wall emission dominates at 4.5 μm in the SEDs (cf. Figure 4.1), we use (z_{wall}/H, $\log(\dot{M})$, $\cos(i)$) as the input parameters when we attempt to reproduce the DCEs in the IRAC bands (J-[4.5], J-[5.8] and J-[8.0]). On the other hand, the degree of dust settling is better traced by 24 μm, where the disk dominates the emission (cf. Figure 4.1), hence, we use ($\log \epsilon$, $\log(\dot{M})$, $\cos(i)$) as input parameters when we attempt to reproduce the DCEs in the MIPS 24 band (J-[24]).

5

Results and implications

In this Chapter we show and discuss our results, as well as their implications, obtained when we reproduce the observed DCEs histograms at each age bin, using approximate Bayesian modeling. In §5.1 we show the distributions of the parameters ϵ and z_{wall}/H obtained from our statistical analysis, and in §5.1.1 and §5.1.2 we put our results in context of the disks' evolution, and give constraints of the values of these parameters at each age bin. In §5.2 we present a brief discussion about two of the disks' evolutionary pathways. In §5.3 we use a simple model to estimate the wind mass-loss rate from a photoevaporative wind that allows to explain the decay of the disk and accretors fraction with age. Finally, in §5.4 we use mean models at each age bin to determine the shape and location of the CO and H_2O snowlines, and how they evolve.

5.1 Implications for disk evolution

Following the method outlined in §4.3, we inferred the distribution of z_{wall}/H from the color excesses J-[4.5], J-[5.8], and J-[8.0], and the distribution of the dust settling parameter log (ϵ) from the $\mathrm{DCE}_{J-[24]}$, at each age bin. Figure 5.1 shows the z_{wall}/H distributions inferred from $\mathrm{DCE}_{J-[4.5]}$ (left column) and

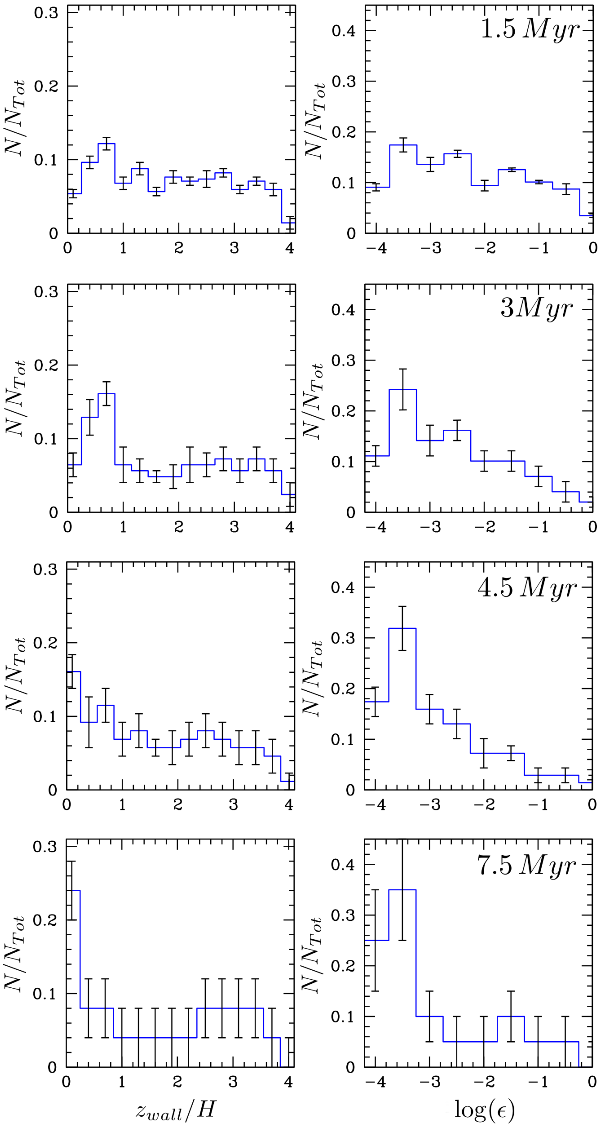

Figure 5.1: Mean distributions for $z_{\rm wall}/H$ (left column) and $\log(\epsilon)$ (right column), for each age bin, with the youngest bin on the top row. The distribution of $z_{\rm wall}/H$ has been calculated from the color excess $J-[4.5]$ with $\epsilon = 0.001$ for bins 1, 2, 3, and 4. The distribution of $\log(\epsilon)$ has been calculated from the color excess J-[24], with $z_{\rm wall} = 1.5$ H. The vertical lines are the standard deviations of each bin.

the distributions of log (ϵ) (right column), for each age bin, the youngest located at the top row. We only show the distribution for the $\mathrm{DCE}_{J-[4.5]}$, since

4.5 μm is the best band to probe the wall height, as discussed in §4.1 and Figure 4.1, where we notice that the other IRAC bands ([5.8] and [8.0]) might contain contribution from the disk emission, while [3.6] is contaminated by the stellar photosphere. It can be seen that the distributions for log(ϵ) move towards lower values as the age of the bin increases (from top to bottom), similarly to what is observed for the mass accretion rates (Figure 2.10) and DCEs (Figure 2.7). In addition, the number of stars with low values of log(ϵ) increases with age, indicating that, although there is a fraction of disks with low values of ϵ in the first age bins, this fraction increases significantly in the oldest bins. For the parameter $z_{\rm wall}/H$, the resulting distributions are flatter, thus, no obvious evolution can be seen in the different age bins.

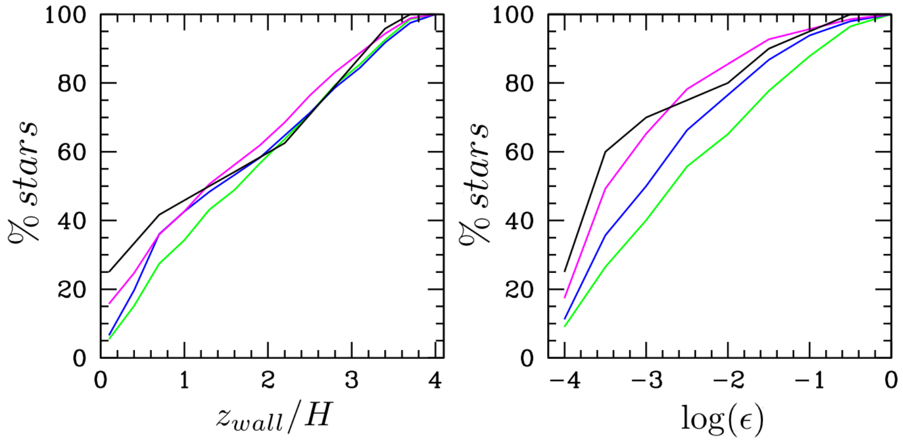

Figure 5.2: Cumulative distributions for $z_{\rm wall}/H$ (left panel) and log(ϵ) (right panel), for bin 1 (green), bin 2 (blue), bin 3 (magenta), and bin 4 (black).

Figure 5.2 shows the cumulative distributions for $z_{\rm wall}/H$ and log(ϵ), that correspond to the distributions shown in Figure 5.1, for the different ages bins: 1.5 Myr (green), 3 Myr (blue), 4.5 Myr (magenta), and 7.5 Myr (black). The left panel shows that for $z_{\rm wall}/H \lesssim 0.6$, the fraction of objects, given a fixed value of $z_{\rm wall}/H$, increases with the age of the bin. For $z_{\rm wall}/H \gtrsim 0.6$ the cumulative distributions show no difference in the different age bins, confirming that we cannot constrain or find an obvious evolution in this parameter. In the right panel, for $\log(\epsilon) \lesssim -3.2$, the cumulative distributions show that the fraction of disks increases with age, for a given value of $\log(\epsilon)$; for disks with $\log(\epsilon) \gtrsim -3.2$ the same behaviour is observed, except in bin 4, in which the cumulative distribution flattens out, with respect to the distribution in bin 3. The results in this plot show that the evolution of the parameter ϵ can be better constrained from the observations than the parameter $z_{\text{wall}/H}$.

Recall that we use a central star in each age bin with the corresponding stellar properties $(T_{\text{eff}}, R_*, L_*)$ associated to the age of that bin, thus, the gas scale height H at a fixed radius is different from one bin to the other. The gas scale height is $H \propto M_*^{-1/2} R^{3/2}$, where M_* is fixed to 0.30 $M_\odot$ (see §2.2 and §4.1) for all bins, but the dust destruction radius, R_{in_i} for the lower ($i = 1$) and the upper wall ($i = 2$), moves inwards with age since $R_{in_i} \propto (L_* + L_{\text{acc}})^{1/2}(T_{w_i})^{-2}$, and the luminosity of the star is decreasing. This means that the gas scale height, and thus the wall, is physically lower as the age bin increases, since it is measured in units of H, which decreases with age. Finally, we explored the effects of increasing the number of realizations in the ABC analysis (see §4.3), in order to test the robustness of the method, and no changes in our results were found.

By reproducing the observed distributions of DCEs (§2.5) using an extensive grid of disk models (§4.1) and taking into account the observed evolution of mass accretion rates (§2.6), we have inferred how the distributions of the disk parameters $\log(\epsilon)$ and z_{wall}/H change with age (Figure 5.1), comparing results for the different age bins. Figure 5.3 shows the results of the dust evolution analysis shown in Figure 5.1 in a different way. This Figure shows the median of the parameters z_{wall}/H and $\log(\epsilon)$ versus the age of the bin, and the quartiles of the corresponding mean distributions. In §5.1.1 and §5.1.2 we discuss these results.

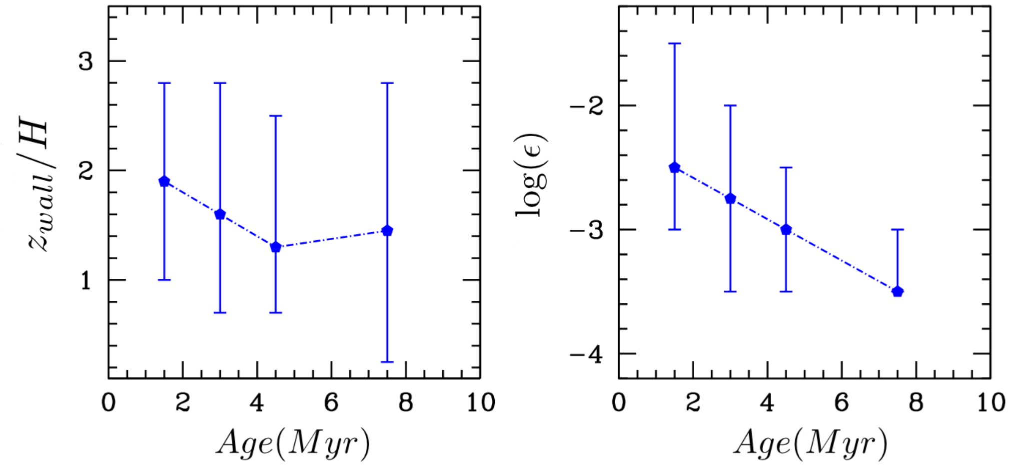

Figure 5.3: Median of $z_{\rm wall}/H$ (left panel) obtained from $\mathrm{DCE}_{J-[4.5]}$ and median of $log(\epsilon)$ (right panel) obtained from $\mathrm{DCE}_{J-[24]}$ versus the age of the bin. The error bars represent the interquartile range, where 50% of the disks lie. In the $z_{\rm wall}/H$ panel, we show the results for a fixed ϵ: 0.001, and in the $\log(\epsilon)$ panel we show the results for a fixed $z_{\rm wall}/H$: 1.5

5.1.1 Degree of dust settling: ϵ

In the right panel of Figure 5.3 we see a decrease of the median of $\log(\epsilon)$ with age. This Figure, as well as Figures 5.2 and 5.1, indicate that dust depletion increases with age in the inner disk regions. Notice that the disk region probed by the flux at 24 μm changes as the dust gets increasingly depleted (D'Alessio et al., 2006). This means that for a highly settled disk, the emission at 24 μm arises from dust radii located at smaller radii than in the case of models with lower degree of settling. To illustrate this effect, we show in Figure 5.4 the contribution to the total flux from the disk region inside radius R as a function of R, at 8 μm (blue line) and 24 μm (green line), for disks calculated with the median $\dot{M}$ (Table 2.4 and Figure 2.11) and the median $\log(\epsilon)$ (left panel in Figure 5.3), in age bins 1 and 4.

It can be seen that $\sim 90\%$ of the flux at 24 μm arises from the inner ~ 10 au of the disk at age bin 1 (left panel) with $\epsilon = 0.003$, while the same flux fraction arises from the inner ~ 1 au of the disk for age bin 4 (right panel), with $\epsilon = 0.0003$. In both cases, our study is probing the inner few au of the disk ($\sim 1-10$ au), which is relevant since in this region terrestrial planets have been found (e.g. Cabrera et al., 2014; Gillon et al., 2017).

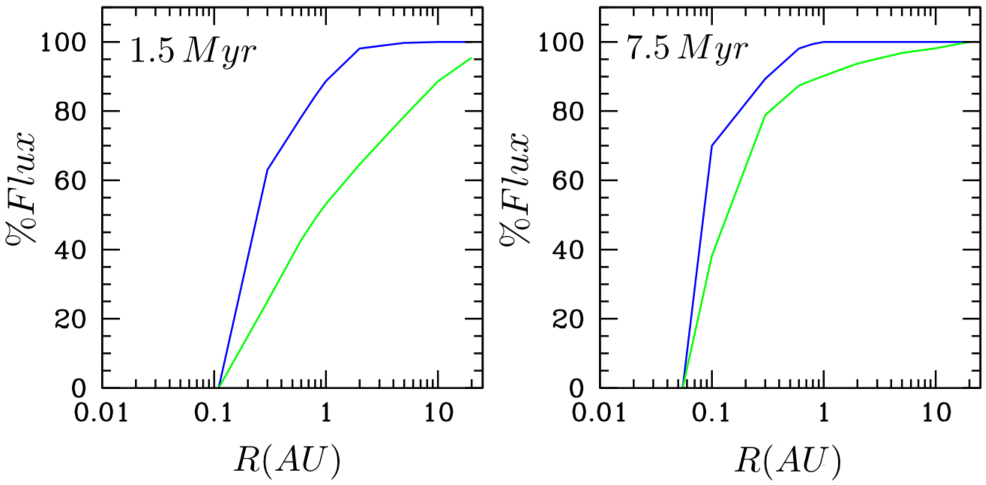

Figure 5.4: Emergent flux at 8 μm (blue line) and 24 μm (green line), at different disk radii, for a disk with $\log(\dot{M}) = -8.49\, M_{\odot}/yr$ with $\epsilon = 0.003$ (left panel) and $\log(\dot{M}) = -9.29\, M_{\odot}/yr$ with $\epsilon = 0.0003$ (right panel), for a 1.5 (bin 1, left panel) and 7.5 Myr old (bin 4, right panel) star, respectively.

Although the median values of $\log(\epsilon)$ shown in the right panel of Figure 5.3, as well as the cumulative distributions shown in the right panel of Figure 5.2, show that the settling increases in the disks as they become older, Figure 5.1 also provides important information, in particular, the low values of $\log(\epsilon)$ (right panels) indicate that even for the youngest groups, disks already show significant dust settling, suggesting that the settling process starts at very early evolutionary stages (~ 1 Myr), as studies of the disk around the young star HL Tau seem to support (see Pinte et al., 2016; Liu et al., 2017; Tapia et al., 2019). At 3 Myr the mode of the distributions of $\log(\epsilon)$ in Figure 5.1 is already highly concentrated around the lowest values of $\log(\epsilon)$.

Our results support the conclusions derived from analysis of IRS spectra in Taurus (Furlan et al., 2006, 2009), Ophiuchus (McClure et al., 2010), and Chamaeleon (Manoj et al., 2011). Furlan et al. (2009) find values of $\log(\epsilon) \sim -2$ to -3 in Taurus, Chamaeleon I (2 Myr; Luhman, 2004) and Ophiuchus ($<$ 1Myr; Luhman & Rieke, 1999). These values are consistent with the median of $\log(\epsilon)$ shown in Figure 5.3 for bin 1 and 2, indicating a large degree of settling in disks. Similarly, our results are consistent with the results of the analysis of Herschel/PACS data of disks in the (1.5 Myr) Lynds 1641 region by Grant et al. (2018) and in the (3 Myr) σ Ori cluster by Maucó et al. (2016), who found a significant fraction of disks with $-2.8 \lesssim \log(\epsilon) \lesssim -1.8$.

5.1.2 The height of the disk wall: $z_{\rm wall}$

The other important parameter we have considered is $z_{\rm wall}/H$, which is related to the height of the disk wall $Z_{\rm wall}$ or dust sublimation front, located at the radius where the disk reaches the temperature above which silicates sublimate (§4.1.) We have used the excess $\mathrm{DCE}_{J-[4.5]}$ as a probe of the wall height. As mentioned before, this is the best band for this purpose since, as can be seen in Figure 4.1 where the flux at 4.5 μm is indicated, the flux at longer wavelengths (5.8 μm or 8.0 μm) includes contributions from the disk, while at 3.6 μm the color excess might be more contaminated by the star.

The results shown in Figure 5.3, together with Figures 5.2 and 5.1, indicate that in this work no clear evolutionary trend is found for $z_{\rm wall}/H$; however, the left panel of Figure 5.2 shows that for $z_{\rm wall}/H \lesssim 0.6$, the fraction of disks given a fixed $z_{\rm wall}/H$ increases with age. Figure 5.1 also provides important information. It shows that at all age bins there is a wide range of values of $z_{\rm wall}/H$, however a concentration of disks towards the low $z_{\rm wall}/H$ barely appears at 1.5 Myr; in contrast, at 7.5 Myr this peak becomes pronounced, indicating a larger number of disks with low walls in the last bin. As noticed before, this is only evident for $z_{\rm wall}/H \lesssim 0.6$, and no conclusive evolutionary trend can be found for this parameter.

Table 5.1: Range of values and mode of $z_{\rm wall}/H$, in each age bin

Age Myr	mode($z_{\rm wall}/H$)	$Z_{{\rm wall}_{\rm min}}$ au	$Z_{{\rm wall}_{\rm max}}$ au	Age Bin
1.5	0.6	3.0×10^{-3}	5.85×10^{-3}	1
3	0.6	2.02×10^{-3}	5.85×10^{-3}	2
4.5	0.2	5.1×10^{-4}	2×10^{-3}	3
7.5	0.2	4.22×10^{-4}	2×10^{-3}	4

In Table 5.1 we show the mode of the distributions of $z_{\rm wall}/H$ shown in Figure 5.1, and the corresponding range of values, in astronomical units, of the total height $Z_{\rm wall}$ in each age bin, given by $Z_{{\rm wall}_{\rm min}}$ and $Z_{{\rm wall}_{\rm max}}$. The values of $Z_{{\rm wall}_{\rm min}}$ and $Z_{{\rm wall}_{\rm max}}$ are determined from the disk models with the lowest and highest values of $\dot{M}$ and ϵ, respectively. As can be seen, even if the distributions for $z_{\rm wall}/H$ show no clear evolution, the physical height of the wall decreases with age (see Table 5.1). This is because the scale height $H \propto R_{in_i}^{3/2}$, and the sublimation radius R_{in_i} for the lower ($i = 1$) and upper ($i = 2$) wall depends on the total luminosity, that is $R_{in_i} \propto (L_* + L_{\rm acc})^{1/2}$, and both the stellar and accretion luminosity decrease with age.

5.2 Evolved disks scenario

In §2.3 we detail the methodology adopted to separate the disk-bearing stars from the rest in our initial sample. The criteria we apply allows us to eliminate transitional disks with large cavities devoid of optically thin dust, i.e., disks with only photospheric near-IR emission. However, we may have included in our analysis a few transitional disks with inner cavities filled with sufficient optically thin material to produce an excess at 5.8 μm and 8 μm that satisfies our observational selection criteria (see §2.3). This is particularly relevant for the oldest bins, since the number of stars that constitute the sample of those bins is much smaller than the number of stars in the youngest ones. According to Espaillat et al. (2014), transitional disks represent $\sim 10-20\%$ of the total population of disks in different stellar groups an this fraction reduces when considering only transitional disks with optically thin material inside their cavities, thus, this issue should not be relevant. In addition, disks with inner clearings have relatively high fluxes at 24 μm, comparable to that of the Taurus median (Maucó et al., 2016), arising in the frontally illuminated edge of the cavity (Grant et al., 2018). In contrast, our statistical analysis indicates that the flux at 24 μm is sufficiently low to be consistent with disks with very high degrees of settling. We conclude that a scenario in which the disk flux decreases at all bands due to increased dust settling and growth is more consistent with our evolutionary results.

Although our analysis does not allow us to determine the conditions under which the disks follow the evolved disks scenario versus inner disk clearing, we find that from the initially compiled sample - that contains diskless as well as disk-bearing stars in all the stellar groups -, before applying the selection criteria described in §2.3 to define our disk-bearing stars sample, $\sim 35\%$ of them were classified as full-disk-bearing stars. These disks have undergone the evolved disk path and thus, according to their SEDs, they do not have large inner cavities of tens of astronomical units, as transitional disks. The other $\sim 65\%$ of the stars, the ones left out in our study, are either diskless stars, transitional disks or objects at earlier evolutionary stages such as Class I objects. Finally, we examined the sample of stars rejected by our selection criteria from the initial sample, searching for transitional disks -

that is, disks without near-IR excess but with 24 μm comparable to that of the Taurus median (Maucó et al., 2016) - and we found 4, 4, 5 and 2 transitional disks, in the age bins 1, 2, 3, and 4, respectively. These transitional disks represent $\lesssim 1\%$ of the initially compiled sample, which also indicates low occurrence of these disks, as other studies suggest (Espaillat et al., 2014).

5.3 Disk frequency

Observations of disk frequency in stellar groups/clusters of different ages (Hernández et al., 2007a; Briceño et al., 2019), indicate that $\sim 70-80\%$ of the stars in young ($\sim$ 1 Myr) stellar groups are disk-bearing stars, while at 5 Myr this fraction drops to $\sim$ 15%. For groups older than $\sim$ 8 Myr, only about $\sim$ 8% of the disk-bearing stars have survived.

We show in Figure 3.2 that the observed decay of the mass accretion rate is consistent with viscously evolving disks; however, viscous evolution cannot explain the decrease of disk frequency, since it only predicts that the disk will expand while decreasing its surface density with age, and a fraction of the disk material will be accreted onto the star. Another agent driving disk evolution is photoevaporation. The upper layers of the disk are heated by high energy radiation from the star and accretion shocks, so that the sound speed becomes higher than the escape velocity. The gas leaves the disk in a photoevaporative wind at radii larger than the gravitational radius, defined as the radius where the Keplerian orbital velocity equals the gas sound speed. The rate at which the wind leaves the disk depends on the radiation field considered to be more effective in driving the wind, either X-rays, FUV or EUV radiation (Alexander et al., 2014, and references therein). Since the mass accretion rate decreases with time as a consequence of disk evolution, it eventually becomes comparable to the mass loss rate in the wind; when this happens, matter from the outer disk flows away instead of reaching the star, while the inner disk quickly drains out onto the star (Clarke et al., 2001). Models of photoevaporative winds predict after this time is reached, the rest of the disk dissipates in time scales smaller than the viscous time scale (Alexander & Armitage, 2007; Alexander et al., 2014).

We have attempted to incorporate the effects of photoevaporation in our study of disk evolution in a simple way. Essentially, we allow the disks around the stars in the first age bin to evolve viscously, and assume that they dissipate instantaneously once their mass accretion rate reaches a given limiting value, which would correspond to the photoevaporation mass loss rate. To do this we take the observed distribution of mass accretion rates at bin 1 (upper left panel in Figure 2.10), and assume a disk fraction of 70% at bin 1 (1.5 Myr) (Briceño et al., 2019). Then, we set a limit for the photoevaporation rate $\dot{M}_{\mathrm{phot,lim}}$ such that if $\dot{M} < \dot{M}_{\mathrm{phot,lim}}$, the disk stops accreting and essentially disappears. We let each bin from the initial distribution of $\dot{M}$ viscously evolve following Equation (3.14), with α=0.01, R_1=10 au, and $M_d(0)$=0.07 $M_\odot$, for a 0.30 $M_\odot$ star, which are the values used in constructing the green solid line in Figure 3.2. At each age bin we eliminate the disks with mass accretion rates below $\dot{M}_{\mathrm{phot,lim}}$ and recalculate the disk fraction. We vary $\dot{M}_{\mathrm{phot,lim}}$ to achieve a good fit to the observed disk fractions. We find that values of $\dot{M}_{\mathrm{phot,lim}}$ between $\sim 1 \times 10^{-9} M_\odot/yr$ and $\sim 3 \times 10^{-9} M_\odot/yr$ give a reasonable fit to the observations, as shown in Figure 5.5, in which we plot the disk fraction and the accretors fraction for different stellar groups as a function of age from Briceño et al. (2019). A higher value of $\dot{M}_{\mathrm{phot,lim}}$ would result in a more rapid decay of the disk frequency because disks would disappear much sooner. Accordingly, much lower values of $\dot{M}_{\mathrm{phot,lim}}$ would predict higher disk fractions than the observed ones.

As shown in Figure 5.5 the predicted disk fraction as a function of age follows the observations reasonably well. Our simple treatment predicts no inner disks beyond 7 Myr, possibly because we did not include other mech-

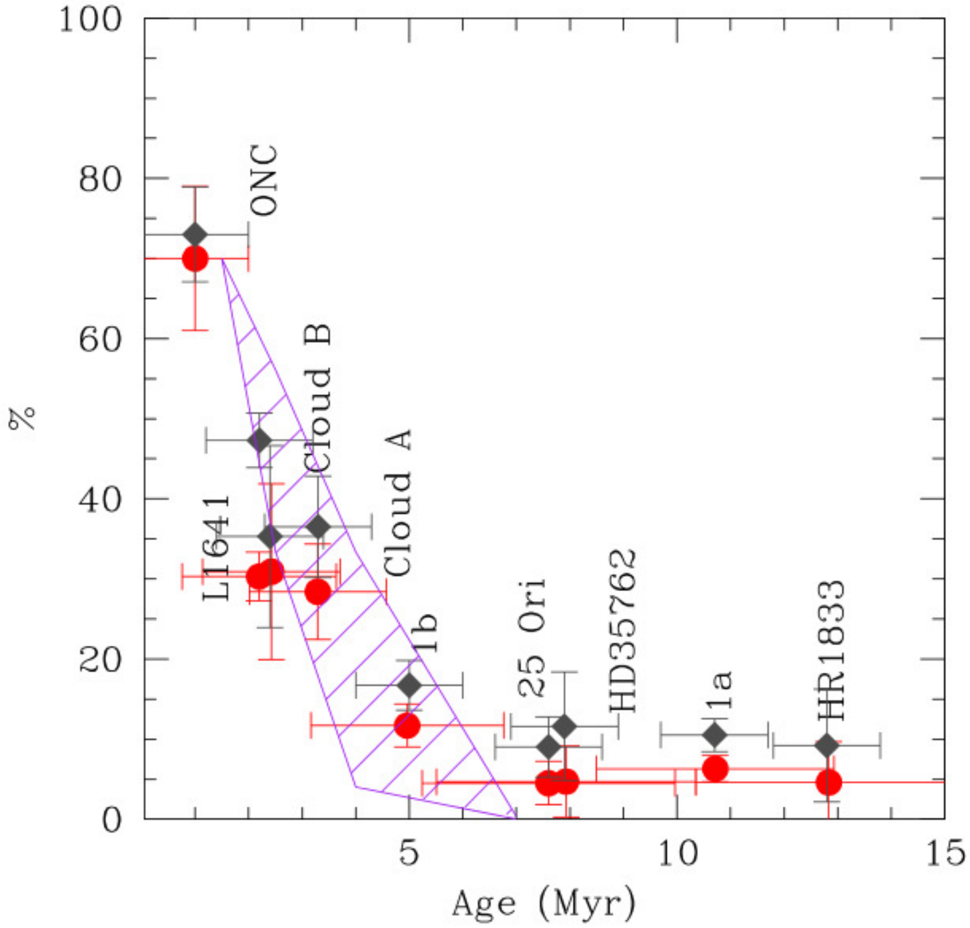

Figure 5.5: Predicted disk frequency as a function of age for disks following viscous evolution and photoevaporation. The purple region shows predictions for $\dot{M}_{\rm phot,lim} \sim 3 \times 10^{-9}\, M_{\odot}/yr$ (lower boundary) and $\dot{M}_{\rm phot,lim} \sim 10^{-9}\, M_{\odot}/yr$ (upper boundary). The fraction of accretors (red dots) and the disk fraction (dark gray diamonds) as a function of age for different stellar groups taken from Briceño et al. (2019) are shown for comparison.

anisms that may allow the existence of inner disk at these older ages. Disks surviving at ages > 7 Myr may be those that started with higher masses, but detailed calculations including the actual evolution of stars in the presence of photoevaporation are required for a better comparison with observations.

A more detailed estimate of the disk frequency needs to be made in order to obtain a disk fraction more consistent with the observed values, in particular in the oldest groups. In any case, our results together with Figure 3.2, suggest that the main agents driving evolution of the gas in the disk are viscous evolution and photoevaporation, at least for the evolved disks studied here.

5.4 Snowlines

Another aspect of this thesis is the study of the location and evolution of different snowlines, in particular the H_2O and CO, under the assumption that the gas and the dust in the disk follow the same temperature distribution.

For each model in our grid we calculate self consistently the vertical and radial structure of the disk (see §3.2), which allows us to find the shape and location of the H_2O and CO snowlines. For this purpose we use disk models, which we refer to as mean models, that were calculated using the median observed values of the mass accretion rate (from Table 2.4 and Figure 2.11) and the median ϵ parameter found in this work (right panel in Figure 5.3), at the different age bins. For H_2O, we take the density-dependent sublimation temperature for water ice reported in Table 3 from Pollack et al. (1994); and for CO we adopt a temperature of 20 K following Öberg et al. (2011) and Qi et al. (2011, 2013, 2015).

In Figure 5.6 we show the shape and location of the H_2O and CO snowlines for our mean models. Notice that the snowlines are not vertical sublimation fronts, instead they curve towards large radii as the height above the midplane increases, which is a consequence of the vertical temperature gradient in irradiated disks in which the temperature increases towards the disk surface

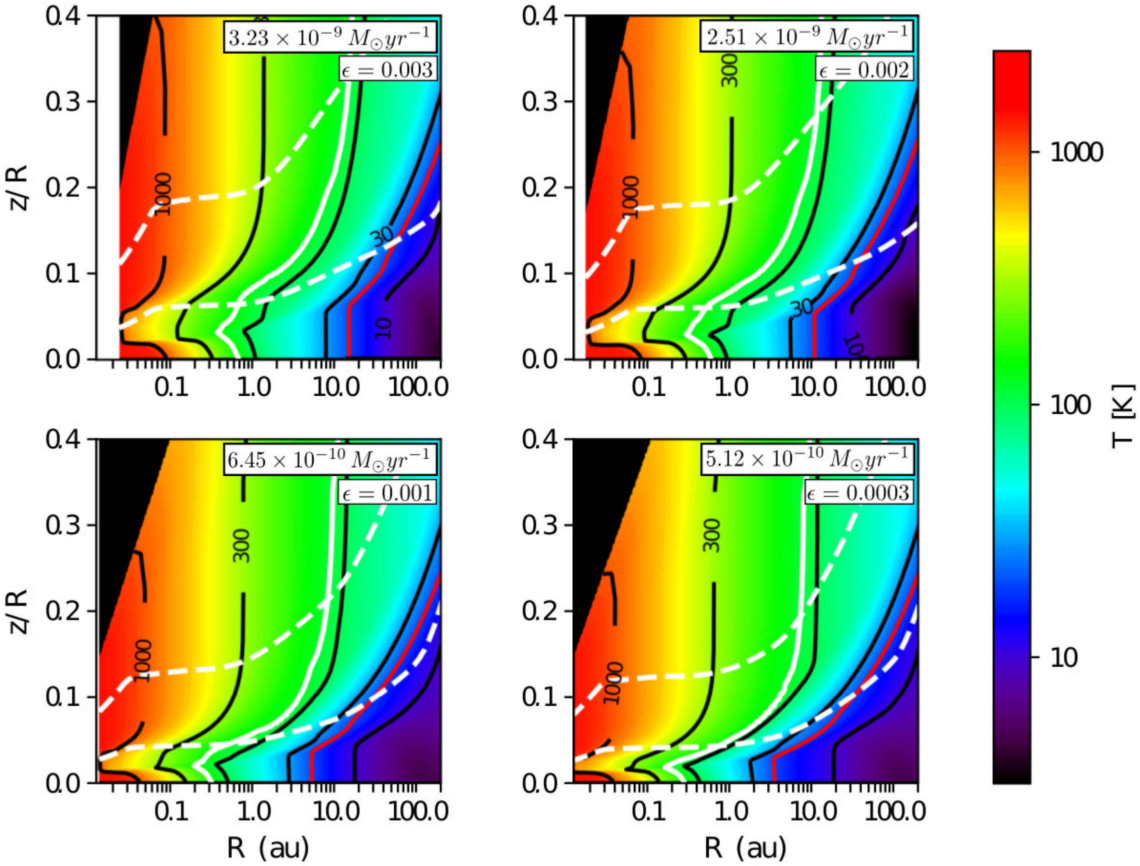

Figure 5.6: Location and shape of the H_2O (white solid line) and CO (red solid line) snowlines for disk models calculated for the median mass accretion rate $\dot{M}$ and median settling parameter ϵ at each age bin, with bin 1 (upper left), bin 2 (upper right), bin 3 (lower left), and bin 4 (lower right). The color scale shows the temperature distribution with temperature iso-contours for 10, 30, 100, 300, and 1000 K (black lines). The white dashed lines show the location of 1 and of 3 scale heights at each radius.

(D'Alessio et al., 1998, 2006). As disks become older, the midplane snowline moves inwards because the stellar and the accretion luminosity decrease (Figure 2.5) and the inner disk becomes colder, allowing certain volatiles to remain frozen closer to the star. There is an additional effect in the H_2O snowline which is more accentuated in the disk models with the highest mass accretion rates (e.g. at bin 1), in which the snowline moves inwards as z/R decreases from the disk surface to the midplane, but at $0 \lesssim z/R \lesssim 0.03$ it is pushed outwards, from ~ 0.4 au at $z/R \sim 0.03$ to ~ 0.7 au at the very midplane ($z/R = 0$). At bin 4 the midplane snowline is pushed from ~ 0.17 au at $z/R \sim 0.02$ up to 0.29 au at $z/R = 0$. This effect is stronger in the first two age bins and it is a consequence of viscous dissipation, since the higher the mass accretion rate, the more efficient the viscous heating in this region (D'Alessio et al., 1998, 2001, 2006; Drążkowska & Alibert, 2017; Huang et al., 2017; Pinte et al., 2018). Figure 5.6 also shows the location of 1 and of 3 scale heights H (white dashed lines), evaluated at the midplane temperature; it can be seen that the scale height decreases with age.

Figure 5.7 shows the location of the H_2O and CO snowlines; this value depends on z/R as already noticed, thus we show the location for different values of z/R: 0 (blue), 0.25 (black), and 0.4 (magenta). The snowline location decreases with age, except for the case $z/R = 0.25$ for the CO snowline, where it remains approximately constant (~ 200 au). For $z/R = 0.4$, the disk temperature exceeds the CO sublimation temperature and no CO is frozen-out in these upper layers. Table 5.2 shows the midplane snowline location for H_2O and CO at the different age bins. At 1.5, 3, 4.5, and 7.5 Myr the water snowline is located at ~ 0.7, 0.6, 0.31, and 0.29 au, respectively, while the CO snowline is located at ~ 15, 7, 5, and 3.5 au. Qi et al. (2013) reported a $R_{\rm sub,CO} \sim 30$ au for the ~ 10 Myr old disk around TW Hya, whereas Schwarz et al. (2016) located the CO midplane snowline at $\sim 17-23$ au, using ALMA observations of CO isotopologues, for the same source. Notice that the disk around TW Hya is a transitional disk, with an inner hole of ~ 4 au (see Espaillat et al., 2014), which should be hotter than the disks from our mean models, since TW Hya has a 0.8 $M_\odot$ star which irradiates directly the disk wall, while our calculations were made for a 0.3 $M_\odot$ star surrounded by a full disk; and this might explain the difference in the locations we find for the CO snowline. The location of the snowlines, determined with observations,

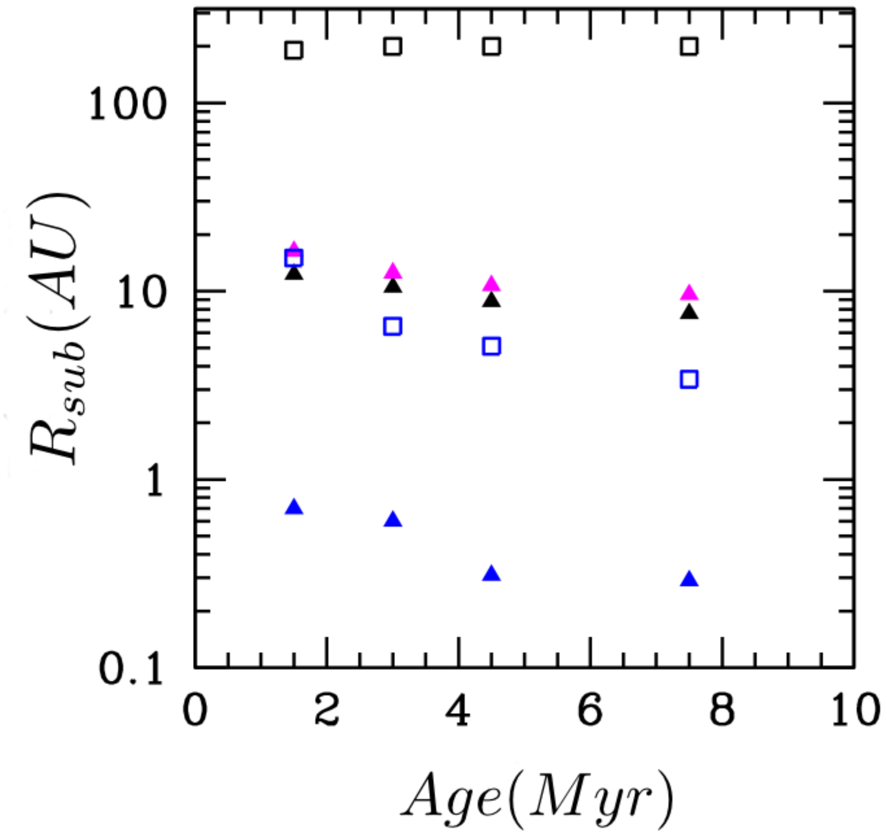

Figure 5.7: Location of the H_2O (solid triangles) and CO (empty squares) snowlines, for different values of z/R : 0 (blue), 0.25 (black) and 0.4 (magenta).

is sensitive to the disk depth at which the emission of the volatiles is being detected; our models show that at $z/R \sim 0.06$ au, $R_{\rm sub,CO} \sim 13$ au while at $z/R \sim 0.12$ au, $R_{\rm sub,CO} \sim 40$ au at bin 4 (7.5 Myr). Mulders et al. (2015) calculate the H_2O snowline for disks with different dust grain sizes, and find an analytical expression for two regimes of the maximun grain sizes: ISM-like and cm-sized grains. The values they find range from 0.28-0.60 au (1.5Myr), 0.22-0.49 au (3 Myr), 0.11-0.23 au (4.5 Myr) and 0.07-0.16 au (7.5 Myr) for a 0.30 $M_\odot$ star, which are similar to our results (Table 5.2). In addition to explaining the chemical composition of some exoplanetary atmospheres and asteroids in the Solar System, the snowlines can also influence the efficiency of dust grains in their process of building larger rocky bodies: dust grains located outside the snowlines have an icy layer in their surface, which increases their stickiness, allowing these dust grains to coagulate more efficiently into larger dust aggregates. These rocky bodies with ices can favour the formation of planets, with respect to the rocks with no ices. The location of the snowlines at the different age bins may also put constraints on the timescale for the formation of planets within the inner au in the disk.

Table 5.2: Midplane location of the H_2O and CO snowlines

Age Myr	$R_{sub,\mathrm{H_2O}}$ au	$R_{sub,\mathrm{CO}}$ au
1.5	0.7	15
3	0.6	7
4.5	0.31	5
7.5	0.29	3.5

6

Summary and conclusions

In this Chapter, we summarize and present a list of the central aspects developed in this thesis (§6.1). Finally, we mention some aspects to be developed in the near future to continue contributing to a better understanding of disk evolution (§6.2).

6.1 Summary of this thesis

- We performed a statistical study focused on the global evolution of protoplanetary disks around T Tauri stars, that includes observed mass accretion rates as a constraint to infer the inner disk properties. The observational sample includes various stellar groups observed with IRAC and MIPS 24 photometry, as well as PANSTARRS $[g-i]$ color (used to calculate $A_{\rm V}$ uniformly for most stars), with ages from 1 to 11 Myr, and located at distances $\lesssim 500$ pc.

- By introducing the disk color excess (DCE) as an indicator of infrared excess, we study the evolution of the observed IR emission from the disk-bearing stars in the stellar groups, separated into different age bins (1.5, 3, 4.5, and 7.5 Myr) to make a more robust statistical study at each age. The median of the different DCEs decreases, and the disks with the highest excesses disappear, as the age of the bin increases.

- We use a different sample of TTSs with significant overlap with the DCEs sample, and with additional GAIA DR2 distances, to determine mass accretion rates using the EW of the Hα line, which was either available from previous works, or determined by us. The observed decay of $\dot{M}$ with age is consistent with viscously evolving disks; in particular we find a good fit to the observed data for a viscosity coefficient α =0.01, an initial disk mass $M_d(0) = 0.07\,M_\odot$, and a characteristic radius R_1 =10 au, inside which 60% of the initial disk mass is located. In addition, although different combinations of the triad $(R_1, M_d(0), \alpha)$ can also provide a good match as determined from the χ^2 value in Figure 3.1, we find that triads with $\alpha = 0.01$ yield disk parameters that are more physically consistent with the observations.

- Using the D'Alessio irradiated accretion disk (DIAD) models, we computed, for each age bin, a grid of disk models varying the degree of dust settling ϵ, the mass accretion rate $\dot{M}$, the parameter $z_{\rm wall}/H$ related to the height of the wall, and the cosine of the inclination angle cos(i). We incorporated a two-layered wall to emulate the wall curvature, as well as an exponential tapering at the outer edge of the disk. Using this grid we computed synthetic DCEs in order to forward model the observed DCEs distributions. The observed $\dot{M}$ distributions at the different age bins are used as constraints in the method.

- The distributions of the parameter ϵ, which measures the dust depletion in the upper disk layers, show that even at 1.5 Myr (bin 1) a fraction of the disks are highly settled (log(ϵ) $\lesssim$ -3.0). In addition, we find that the fraction of highly settled disks increases with age, which is more evident for disks with $\log(\epsilon) \lesssim -3.2$ In contrast, we find no clear evolutionary trend for z_{wall}/H, which measures the height of the wall at the dust destruction radius, however, the fraction of disks with $z_{\mathrm{wall}}/H \lesssim 0.6$ increases with age. These results show that the ϵ parameter can be better constrained from the observations than the parameter z_{wall}.

- We make a first attempt to test photoevaporation by letting the observed distribution of $\dot{M}$ from bin 1 viscously evolve, and we set a photoevaporation mass loss rate $\dot{M}_{\mathrm{phot,lim}}$; stars with $\dot{M} < \dot{M}_{\mathrm{phot,lim}}$ stop accreting mass from the disk, while stars with $\dot{M} > \dot{M}_{\mathrm{phot,lim}}$ are still accreting. We find that $\dot{M}_{\mathrm{phot,lim}} \sim 1 \times 10^{-9} - 3 \times 10^{-9}\, M_{\odot} yr^{-1}$ fits reasonably well the observed decay of the disk and accretors fractions with age.

- We find that the H_2O and CO snowlines curve towards larger radii as the height over the disk midplane increases because of the vertical temperature gradient. At $0 \lesssim z/R \lesssim 0.02$, the H_2O snowline is pushed outwards due to viscous dissipation. The snowlines migrate inwards as the disk evolves, as a consequence of the decrease in the stellar and accretion shocks luminosity with age. The H_2O midplane snowline starts at ~ 0.7 au at 1.5 Myr and ends up at ~ 0.29 au at 7.5 Myr; the CO midplane snowline starts at ~ 15 au at 1.5 Myr and ends up at ~ 3.5 au at 7.5 Myr for the models with the median mass accretion rate $\dot{M}$ and median degree of settling $\log(\epsilon)$ at each age bin.

6.2 Future work

In this thesis we have studied the global evolution of disks in various stellar clusters/groups, finding that an advanced degree of settling can be found in disks of the youngest populations, and the amount of dust settling increases with age. This is important, since dust settling towards the midplane represents one the first steps in the formation of planetesimals and rocky planets. Also important are the radial gradients in the dust size distribution and, thus, one of the next immediate steps is to adapt the D'Alessio models to include these radial gradients in the dust spatial distribution. In addition, the models used in this thesis, as well as new models that include a modified radial distribution of dust grains, can be used to obtain synthetic images of disks using ALMA, the VLA, among others, in order to constrain more parameters of the disks such as their sizes, masses, inner holes, maximum dust grains sizes at different disk radii, etc. Also, predictions concerning the emission from different molecular lines can be made.

In addition, so far we have treated the disk inner wall independently of the disk structure calculation, however, a detailed self-consistent determination of the wall's surface and emission needs to be performed, in order to compare the models with the available and forthcoming observations in different wavelengths. We have started working in this project, which should be finished soon. Also, new determinations of the disk frequency will be made in a future work in order to obtain disk fractions that reproduce better the observed fractions in the oldest stellar clusters/groups.

Finally, further statistical studies using large samples of disks, as well as detailed modeling of these sources, are important in other stellar regimes, e.g., disks around Herbig Ae stars and brown dwarfs, in order to understand the differences in the processes dominating the evolution of the disks around such stars. The D'Alessio models are already adapted to study disks around brown dwarfs, thus, an important effort towards this direction should be done.

Appendix A

Sample selection

Here we present two tables that list the number of stars in each group, when each selection criteria is applied (cf. §2.1). Table A.1 shows the information related to the sample used to study the dust component, and contains: the name of the group (first column), the number of stars without IRAC photometry (second column), the number of stars with IRAC photometry (third column), the number of stars with PANSTARRS and IRAC photometry (fourth column), and the stars classified as disk-bearing stars according to §2.3 (fifth column). Table A.2 shows the information related to the sample used to study the evolution of the mass accretion rates in §2.6, and contains: the name of the group (first column), the number of T Tauri stars with EW Hα (second column), the number of stars with EW Hα and PANSTARRS photometry (third column), the number of stars with EW Hα, PANSTARRS photometry, as well as GAIA DR2 parallaxes (fourth column), and the number of accretors (fifth column); these stars have good determinations of stellar masses, using the evolutionary tracks from Siess, Dufour & Forestini (2000).

Table A.1: IR Sources

Group	Stars without IRAC	Stars with IRAC	Stars with PANSTARRS	Disk-bearing stars
ONC	543	670	508	305
Taurus	*	414	260	87
IC 348	*	307	163	59
σ Ori	*	221	185	73
λ Ori	*	181	142	24
Ori OB1b	234	317	278	45
Upper Sco	216	90	59	19
γ Vel	*	125	**	14
Ori OB1a	997	214	189	13

* The photometric measurements in all IRAC bands was the initial selection criteria in these groups.
** The γ Vel cluster was not observed by the PANSTARRS survey, instead we used the color $[\mathrm{V} - \mathrm{I_c}]$ to calculate A_{V}.

Table A.2: Sources with EW Hα

Group	T Tauri Stars with EW Hα	Stars with PANSTARRS	Stars with GAIA DR2	Accretors
ONC	825	646	592	228
Taurus	100	23	18	16
σ Ori	175	137	125	40
Ori OB1b	551	464	411	59
Ori OB1a	1211	1057	976	77

The second column shows T Tauri stars in the K0-M6 spectral range, with measurements of EW Hα.
The third column shows T Tauri stars with EW Hα and PANSTARRS photometry.
The fourth column shows T Tauri stars with EW Hα, PANSTARRS photometry, and GAIA DR2 parallaxes with relative errors $< 20\,\%$.
The fifth column shows the stars for which $\dot{M}$ could be determined.

Appendix B

Stellar properties

Here we present a table that contains the stellar properties of the complete sample used in this thesis, which includes the stars selected to study the DCEs (§2.3 and §2.5), as well as the stars used to study the evolution of $\dot{M}$ (§2.6).

Table B.1 contains the following columns: the 2MASS identifier, the spectral type (SpT), the extinction ($A_{\rm V}$), the effective temperature ($T_{\rm eff}$), the reference for the spectral type (Ref), the stellar luminosity ($L_*/L_\odot$), the stellar mass ($M_*/M_\odot$), the stellar radius ($R_*/R_\odot$), the distance in parsecs (dist), the equivalent width of the Hα line (EW Hα), the $DCE_{J-[4.5]}$, the $DCE_{J-[5.8]}$, the $DCE_{J-[8.0]}$, the $DCE_{J-[24]}$, and the mass accretion rate ($\dot{M}$). The stars are listed according to the stellar cluster/group they belong to.

Notice that the errors associated with the different DCEs in Table B.1 are underestimated, since they are calculated only with the photometric errors. As discussed in §2.6, this does not affect our results, since we do not use these errors in any way as a weight to determine the disk parameters.

Table B.1. Stellar properties

2MASS	SpT	$A_{\rm V}$	$T_{\rm eff}$(K)	Ref	$L_*/L_\odot$	$M_*/M_\odot$	$R*/R_\odot$	dist(pc)	EW Hα(Å)	$DCE_{J-[4.5]}$	$DCE_{J-[5.8]}$	$DCE_{J-[8.0]}$	$DCE_{J-[24]}$	$\dot{M}(M_\odot yr^{-1})$
ONC														
05362691-0455061	M5.5	0.0	2740	1	0.04			383	-140.1	0.74 ± 0.03	0.95 ± 0.04	1.76 ± 0.04	3.97 ± 0.12	
05354205-0512595	M6.0	0.0	2600	1	0.06			372	-22.7					
05341189-0506162	M5.5	0.55	2740	1	0.03			416	-105.8	0.49 ± 0.04	0.88 ± 0.05	1.69 ± 0.05	4.2 ± 0.09	
05341377-0500041	M6.0	0.15	2600	1	0.02			378	-30.8	0.37 ± 0.08	0.57 ± 0.09	1.28 ± 0.08	3.97 ± 0.15	
05342125-0450326	M3.5	1.4	3260	1	0.03	0.18	0.58	245	-15.0	0.21 ± 0.03	0.55 ± 0.04	1.61 ± 0.04	6.16 ± 0.04	1.06×10^{-10}
05351487-0538055	M0.5	0.0	3700	1	0.15	0.45	0.95	393	-9.5	1.43 ± 0.03	1.65 ± 0.03	2.18 ± 0.04	5.11 ± 0.05	2.46×10^{-10}
05372601-0534013	K3.5	0.6	4440	2	0.81	1.14	1.52	382	-3.0					2.91×10^{-10}
05334954-0536208	K5.5	1.0	4080	1	0.43	0.81	1.31	404	-5.8	1.73 ± 0.02	2.19 ± 0.02	2.87 ± 0.02	4.77 ± 0.03	3.30×10^{-10}
05355894-0532538	M3.5	0.0	3260	1	0.03	0.18	0.62	406	-43.9	2.2 ± 0.06	2.47 ± 0.06	3.29 ± 0.07	6.91 ± 0.07	3.73×10^{-10}
05331344-0451328	M0.0	0.35	3770	2	0.26	0.50	1.21	333	-7.3					3.81×10^{-10}
05335946-0443045	M0.0	0.05	3770	2	0.29	0.50	1.27	386	-6.6					3.90×10^{-10}
05333021-0604096	M0.0	0.07	3770	2	0.27	0.50	1.22	360	-7.4					3.94×10^{-10}
05350357-0529262	M2.5	0.0	3425	1	0.04	0.26	0.58	157	-64.0	2.03 ± 0.03	2.36 ± 0.04	2.86 ± 0.04		4.09×10^{-10}
05344830-0537228	K7.3	0.0	3995	3	0.48	0.65	1.49	361	-5.2	0.06 ± 0.03	0.09 ± 0.03	0.09 ± 0.04		4.17×10^{-10}
05352284-0446414	M3.0	0.12	3360	1	0.13	0.27	1.08	377	-11.4	0.89 ± 0.02	1.18 ± 0.02	1.8 ± 0.03	4.87 ± 0.05	4.18×10^{-10}
05340799-0407170	M0.0	0.0	3770	2	0.27	0.50	1.23	357	-8.2					4.44×10^{-10}
05342960-0547247	M1.5	0.26	3560	1	0.21	0.37	1.21	383	-8.9	0.16 ± 0.02	0.43 ± 0.02	1.53 ± 0.02	5.03 ± 0.03	4.48×10^{-10}
05342743-0500263	M4.5	0.2	3020	1	0.03	0.09	0.66	376	-36.7	0.41 ± 0.03	0.6 ± 0.04	1.29 ± 0.05	3.7 ± 0.16	4.50×10^{-10}
05345662-0511125	M2.5	2.11	3425	1	0.15	0.30	1.10	403	-12.0	1.03 ± 0.03	1.37 ± 0.04	2.09 ± 0.06	5.34 ± 0.04	4.57×10^{-10}
05342034-0458564	M3.0	0.21	3360	1	0.14	0.27	1.11	389	-12.5	-0.0 ± 0.02	0.03 ± 0.03	-0.04 ± 0.05		4.91×10^{-10}
05340731-0513454	K2.0	0.0	4760	2	1.24	1.30	1.64	410	-3.4					5.21×10^{-10}
05344881-0533330	M4.5	0.0	3020	1	0.07	0.12	1.02	406	-16.0	1.04 ± 0.04	1.14 ± 0.04	1.68 ± 0.04	4.97 ± 0.06	5.31×10^{-10}
05332510-0403301	M0.5	0.45	3700	2	0.32	0.46	1.38	360	-7.3					5.52×10^{-10}
05351331-0509195	K7.5	0.65	3910	4	0.46	0.62	1.48	395	-6.5					6.01×10^{-10}
05341202-0524196	M3.5	1.05	3260	1	0.14	0.23	1.18	345	-13.8					6.30×10^{-10}
05342926-0514397	K5.0	0.56	4140	1	0.81	0.85	1.75	304	-4.8	1.67 ± 0.03	1.86 ± 0.03	2.54 ± 0.03	5.35 ± 0.03	6.69×10^{-10}
05353552-0558190	M3.0	1.84	3360	1	0.13	0.27	1.07	397	-18.8	0.36 ± 0.05	0.55 ± 0.05	1.25 ± 0.05	4.67 ± 0.06	6.71×10^{-10}
05342986-0504053	M3.5	0.0	3260	1	0.14	0.23	1.18	375	-14.9	-0.01 ± 0.02	0.05 ± 0.02	0.05 ± 0.04		6.78×10^{-10}
05352088-0607174	M4.5	0.0	3020	1	0.05	0.10	0.82	367	-34.2	0.47 ± 0.03	0.83 ± 0.03	1.76 ± 0.03	4.12 ± 0.09	6.93×10^{-10}
05353852-0459411	M0.0	2.43	3770	1	0.12	0.50	0.82	159	-43.6	1.06 ± 0.05	1.26 ± 0.05	2.06 ± 0.05	4.79 ± 0.06	7.13×10^{-10}
05353914-0558065	M5.0	0.0	2880	1	0.06	0.06	0.98	394	-18.5	0.37 ± 0.04	0.61 ± 0.04	1.17 ± 0.04	3.71 ± 0.1	7.64×10^{-10}
05350167-0432529	M2.0	0.07	3490	1	0.18	0.34	1.17	391	-17.0	0.85 ± 0.03	1.15 ± 0.03	1.87 ± 0.03	4.09 ± 0.08	7.77×10^{-10}
05350137-0603556	M5.0	0.0	2880	1	0.04	0.05	0.89	382	-22.9	0.45 ± 0.03	0.79 ± 0.04	1.52 ± 0.04	4.1 ± 0.08	8.22×10^{-10}
05330206-0408465	K7.5	0.39	3910	2	0.52	0.62	1.57	403	-7.5					8.33×10^{-10}
05341160-0555219	M3.5	0.0	3260	1	0.16	0.24	1.25	304	-16.3	0.89 ± 0.03	1.0 ± 0.04	1.42 ± 0.04	4.51 ± 0.05	8.58×10^{-10}
05344244-0543255	M4.5	0.42	3020	1	0.11	0.14	1.24	429	-18.1	0.64 ± 0.02	0.86 ± 0.03	1.23 ± 0.04	4.75 ± 0.05	9.21×10^{-10}
05353768-0506321	M2.5	0.29	3425	1	0.15	0.30	1.11	392	-24.0	0.56 ± 0.03	1.08 ± 0.03	1.6 ± 0.04		9.37×10^{-10}

2MASS	SpT	$A_{\rm V}$	$T_{\rm eff}$(K)	Ref	$L_*/L_\odot$	$M_*/M_\odot$	$R*/R_\odot$	dist(pc)	EW Hα(Å)	$DCE_{J-[4.5]}$	$DCE_{J-[5.8]}$	$DCE_{J-[8.0]}$	$DCE_{J-[24]}$	$\dot{M}(M_\odot yr^{-1})$
05375023-0426167	M0.0	0.48	3770	2	0.19	0.50	1.04	286	-29.6					9.64×10^{-10}
05351579-0533123	M1.0	0.0	3910	4	0.53	0.41	1.77	401	-8.4	0.94 ± 0.03	1.08 ± 0.04	1.96 ± 0.04	4.45 ± 0.05	9.73×10^{-10}
05342893-0508384	M3.5	1.36	3260	1	0.03	0.18	0.55	339	-163.4	0.53 ± 0.03	0.71 ± 0.04	1.49 ± 0.04	3.89 ± 0.13	9.87×10^{-10}
05351438-0455226	M3.0	0.33	3360	1	0.16	0.28	1.18	376	-21.6					9.88×10^{-10}
05351080-0444106	M3.0	0.0	3360	1	0.10	0.25	0.94	394	-40.7	0.92 ± 0.04	1.25 ± 0.05	2.25 ± 0.06		1.01×10^{-9}
05344351-0451364	M3.5	0.43	3260	1	0.16	0.24	1.28	378	-18.8	-0.03 ± 0.02	0.24 ± 0.05	0.79 ± 0.12	4.98 ± 0.05	1.04×10^{-9}
05344268-0442148	K3.0	2.2	4550	2	2.38	1.44	2.48	397	-2.8					1.06×10^{-9}
05345386-0456222	M0.0	2.26	3770	1	0.55	0.50	1.75	406	-7.0	0.5 ± 0.02	1.0 ± 0.02	1.45 ± 0.03	5.86 ± 0.05	1.09×10^{-9}
05344863-0447499	M4.5	0.0	3020	1	0.11	0.15	1.25	393	-21.1	0.89 ± 0.05	0.97 ± 0.06	1.77 ± 0.06	4.83 ± 0.08	1.10×10^{-9}
05352095-0604004	M5.0	0.0	2880	1	0.05	0.05	0.89	379	-31.4	0.03 ± 0.04	0.31 ± 0.05	1.1 ± 0.05	3.54 ± 0.1	1.11×10^{-9}
05355462-0527075	M1.5	0.0	3560	1	0.30	0.37	1.44	400	-13.2	0.34 ± 0.03	0.7 ± 0.04	1.75 ± 0.04		1.11×10^{-9}
05333443-0514177	M3.0	0.48	3360	1	0.26	0.29	1.50	395	-12.5	0.74 ± 0.02	1.15 ± 0.02	2.15 ± 0.03	5.35 ± 0.03	1.12×10^{-9}
05343276-0458467	M4.5	0.14	3020	1	0.04	0.10	0.79	335	-62.2	0.45 ± 0.03	0.8 ± 0.04	1.6 ± 0.04	4.4 ± 0.09	1.16×10^{-9}
05365186-0508358	M0.5	0.0	3700	1	0.35	0.46	1.45	400	-13.4	1.65 ± 0.02	1.91 ± 0.02	2.53 ± 0.02	4.01 ± 0.03	1.17×10^{-9}
05342554-0537022	M5.0	0.0	2880	1	0.07	0.07	1.12	407	-23.3	0.5 ± 0.03	0.77 ± 0.03	1.47 ± 0.03	4.85 ± 0.05	1.19×10^{-9}
05343575-0540094	M3.0	0.69	3360	1	0.23	0.29	1.41	410	-15.9	1.31 ± 0.03	1.64 ± 0.03	2.29 ± 0.04	5.54 ± 0.04	1.21×10^{-9}
05341387-0536353	M4.5	0.0	3020	1	0.14	0.15	1.38	387	-18.5	-0.03 ± 0.02	-0.04 ± 0.04	0.12 ± 0.06		1.22×10^{-9}
05351491-0536391	M3.5	0.35	3260	1	0.21	0.25	1.44	394	-15.7	0.31 ± 0.03	0.5 ± 0.04	1.1 ± 0.07	4.42 ± 0.06	1.22×10^{-9}
05352275-0443258	M4.5	0.05	3020	1	0.11	0.14	1.23	410	-25.6	1.1 ± 0.04	1.24 ± 0.04	2.4 ± 0.04	5.99 ± 0.05	1.26×10^{-9}
05350460-0458289	M0.0	3.9	3770	1	0.25	0.50	1.17	364	-26.9	1.89 ± 0.04	2.12 ± 0.04	2.79 ± 0.04	5.69 ± 0.05	1.26×10^{-9}
05341705-0448037	M0.0	4.69	3770	1	0.33	0.50	1.36	402	-17.4	1.92 ± 0.05	1.99 ± 0.06	2.49 ± 0.06	4.74 ± 0.07	1.27×10^{-9}
05342857-0530325	M4.0	2.02	3160	1	0.03	0.15	0.65	383	-129.8	0.8 ± 0.11	0.99 ± 0.12	1.62 ± 0.12		1.31×10^{-9}
05344178-0453462	M2.0	0.34	3490	1	0.33	0.34	1.57	411	-12.6	0.91 ± 0.03	1.19 ± 0.04	2.18 ± 0.04	5.57 ± 0.04	1.33×10^{-9}
05342572-0456554	K7.5	0.26	3910	1	0.57	0.62	1.65	390	-10.5	0.87 ± 0.05	1.09 ± 0.05	2.05 ± 0.05	5.41 ± 0.06	1.35×10^{-9}
05355077-0516291	K4.5	0.0	4235	2	0.85	0.96	1.71	398	-10.6					1.36×10^{-9}
05324674-0558020	M0.0	0.0	3770	2	0.26	0.50	1.21	354	-26.6					1.38×10^{-9}
05375990-0413402	K7.5	0.06	3910	2	0.54	0.62	1.61	409	-12.0					1.42×10^{-9}
05345120-0516549	M2.0	0.0	3490	1	0.18	0.34	1.17	338	-32.0	2.16 ± 0.02	2.66 ± 0.02	3.52 ± 0.04		1.42×10^{-9}
05345962-0525399	M0.5	0.0	3700	1	0.40	0.46	1.54	419	-13.6	1.65 ± 0.02	2.07 ± 0.02	2.7 ± 0.02		1.44×10^{-9}
05353901-0521017	K7.5	2.17	3910	1	0.47	0.62	1.50	433	-15.5					1.48×10^{-9}
05342978-0451477	M0.5	2.45	3700	1	0.21	0.45	1.12	369	-36.2	2.57 ± 0.04	3.02 ± 0.04	3.75 ± 0.04	6.65 ± 0.05	1.49×10^{-9}
05320621-0456099	M0.5	0.53	3700	2	0.27	0.46	1.27	420	-25.5					1.49×10^{-9}
05353560-0539081	M2.0	0.0	3490	1	0.07	0.30	0.74	407	-117.4	2.08 ± 0.03	2.33 ± 0.04	2.95 ± 0.05	5.54 ± 0.07	1.50×10^{-9}
05352157-0509497	M4.0	0.0	3160	1	0.11	0.18	1.10	385	-39.3	1.57 ± 0.02	1.9 ± 0.03	2.78 ± 0.05	5.94 ± 0.04	1.54×10^{-9}
05344146-0547561	K7.5	0.87	3910	2	0.79	0.61	1.94	330	-7.4					1.56×10^{-9}
05344476-0456408	M1.0	0.45	3630	1	0.09	0.39	0.79	399	-106.2	1.41 ± 0.04	1.62 ± 0.05	2.13 ± 0.07	4.69 ± 0.08	1.61×10^{-9}
05365979-0523408	K7.0	0.14	3970	2	0.61	0.67	1.66	359	-13.3					1.63×10^{-9}
05342949-0513551	K5.0	1.12	4140	1	0.33	0.84	1.12	376	-44.9	2.47 ± 0.02	2.82 ± 0.03	3.64 ± 0.04	7.08 ± 0.03	1.65×10^{-9}
05353149-0505016	M2.0	0.0	3490	1	0.06	0.30	0.72	181	-143.1	1.91 ± 0.02	2.07 ± 0.03	3.12 ± 0.03	5.94 ± 0.03	1.68×10^{-9}

2MASS	SpT	A_{V}	T_{eff}(K)	Ref	$L_*/L_\odot$	$M_*/M_\odot$	$R*/R_\odot$	dist(pc)	EW Hα(Å)	$DCE_{J-[4.5]}$	$DCE_{J-[5.8]}$	$DCE_{J-[8.0]}$	$DCE_{J-[24]}$	$\dot{M}(M_\odot yr^{-1})$
05350506-0536438	M4.5	0.4	3020	1	0.19	0.16	1.63	414	-16.4	1.3 ± 0.02	1.67 ± 0.02	2.58 ± 0.03	5.85 ± 0.03	1.69×10^{-9}
05360808-0441205	M0.5	0.14	3700	1	0.36	0.46	1.47	378	-18.7	1.14 ± 0.02	1.55 ± 0.02	2.46 ± 0.03	5.74 ± 0.03	1.71×10^{-9}
05354229-0515079	M1.0	1.95	3630	1	0.12	0.39	0.90	394	-77.8	2.1 ± 0.06	2.43 ± 0.07	3.0 ± 0.1		1.73×10^{-9}
05343614-0605346	K7.0	0.0	3970	2	0.31	0.71	1.19	377	-40.7					1.75×10^{-9}
05353333-0451113	M3.0	0.64	3360	1	0.21	0.29	1.37	392	-25.4	0.76 ± 0.02	0.96 ± 0.02	1.47 ± 0.03		1.79×10^{-9}
05324731-0539426	M0.0	0.13	3770	2	0.28	0.50	1.24	380	-34.1			nodata		1.89×10^{-9}
05354413-0448048	M0.0	0.0	3770	1	0.42	0.50	1.52	413	-18.5	1.4 ± 0.02	1.49 ± 0.02	1.89 ± 0.02	5.52 ± 0.03	1.91×10^{-9}
05351317-0536179	M5.0	0.39	2880	1	0.06	0.07	1.06	393	-42.2					1.92×10^{-9}
05362557-0518419	M5.5	0.0	2740	1	0.08	0.04	1.25	396	-20.3					1.97×10^{-9}
05354306-0503075	M5.0	0.18	2880	1	0.08	0.08	1.15	371	-37.5	0.42 ± 0.02	0.75 ± 0.02	1.33 ± 0.05	4.36 ± 0.05	2.01×10^{-9}
05333120-0529576	M4.0	0.3	3160	1	0.10	0.18	1.06	409	-57.0	0.38 ± 0.03	0.52 ± 0.04	1.58 ± 0.06	4.7 ± 0.05	2.01×10^{-9}
05350585-0448432	M0.0	0.0	3770	1	0.30	0.50	1.30	378	-31.6	1.73 ± 0.02	1.88 ± 0.02	2.63 ± 0.02	5.23 ± 0.04	2.02×10^{-9}
05342189-0515305	M5.0	0.0	2880	1	0.05	0.06	0.96	470	-51.8	1.66 ± 0.06	2.11 ± 0.07	3.0 ± 0.07	6.64 ± 0.07	2.06×10^{-9}
05355118-0456276	M2.5	0.8	3425	1	0.13	0.29	1.04	399	-66.5	1.53 ± 0.03	2.2 ± 0.03	3.36 ± 0.04	6.88 ± 0.03	2.17×10^{-9}
05332852-0517262	M0.0	0.0	3770	1	0.40	0.50	1.49	380	-22.5	0.74 ± 0.03	0.85 ± 0.03	1.65 ± 0.03	5.04 ± 0.03	2.18×10^{-9}
05351596-0516575	M3.0	0.49	3360	1	0.24	0.29	1.46	402	-26.5	1.11 ± 0.08	1.31 ± 0.08	1.85 ± 0.11		2.22×10^{-9}
05355730-0615377	M0.0	0.08	3770	2	0.22	0.50	1.11	386	-55.9					2.24×10^{-9}
05334167-0524042	M2.0	0.28	3490	1	0.21	0.34	1.25	378	-41.1	0.63 ± 0.02	1.02 ± 0.02	1.91 ± 0.03	4.87 ± 0.03	2.24×10^{-9}
05352162-0534583	M2.5	0.22	3425	1	0.35	0.31	1.70	428	-17.1	0.95 ± 0.02	1.13 ± 0.02	2.0 ± 0.02	5.36 ± 0.04	2.27×10^{-9}
05360386-0530188	M4.5	0.0	3020	1	0.06	0.11	0.90	351	-91.6	0.71 ± 0.04	1.08 ± 0.05	2.06 ± 0.06		2.31×10^{-9}
05361987-0513064	M5.0	0.0	2880	1	0.07	0.07	1.07	407	-49.8	0.84 ± 0.03	1.2 ± 0.03	2.07 ± 0.04	4.95 ± 0.04	2.35×10^{-9}
05351885-0444100	M5.0	0.0	2880	1	0.12	0.1	1.40	400	-30.0	0.52 ± 0.02	0.79 ± 0.03	1.49 ± 0.05	3.84 ± 0.08	2.37×10^{-9}
05355469-0506278	M5.5	0.39	2740	1	0.08	0.04	1.28	399	-24.1					2.39×10^{-9}
05345085-0529250	M4.5	2.29	3020	1	0.27	0.17	1.91	389	-15.7					2.43×10^{-9}
05343395-0534512	M0.0	0.99	3770	1	0.70	0.50	1.96	423	-11.1	0.88 ± 0.02	1.34 ± 0.02	2.15 ± 0.02	5.35 ± 0.03	2.45×10^{-9}
05345490-0547089	M5.5	0.0	2740	1	0.05	0.02	1.05	467	-22.9					2.49×10^{-9}
05332136-0521347	K3.0	0.64	4550	2	1.26	1.25	1.80	402	-14.9					2.49×10^{-9}
05352074-0537536	M5.5	0.45	2740	1	0.06	0.02	1.10	384	-24.5	0.84 ± 0.05	1.17 ± 0.05	1.94 ± 0.06		2.51×10^{-9}
05354355-0505414	M0.0	0.0	3770	1	0.40	0.50	1.49	411	-27.9	2.55 ± 0.05	2.91 ± 0.05	3.79 ± 0.05	6.55 ± 0.06	2.67×10^{-9}
05354764-0519145	M1.5	1.78	3560	1	0.27	0.37	1.38	414	-36.9	1.79 ± 0.05	2.16 ± 0.05	3.21 ± 0.07		2.73×10^{-9}
05340595-0522435	K7.5	2.92	3910	1	0.48	0.62	1.51	370	-28.3	2.57 ± 0.03	2.94 ± 0.04	3.78 ± 0.04	6.48 ± 0.04	2.76×10^{-9}
05352831-0559132	M3.5	0.0	3260	1	0.23	0.25	1.52	378	-30.8	0.87 ± 0.03	1.34 ± 0.03	2.33 ± 0.04	5.63 ± 0.03	2.76×10^{-9}
05353044-0605007	M5.0	0.57	2880	1	0.03	0.03	0.70	357	-107.5	0.41 ± 0.05	0.77 ± 0.05	1.58 ± 0.05	4.05 ± 0.12	2.78×10^{-9}
05344172-0536488	M5.5	0.0	2740	1	0.06	0.03	1.14	452	-28.9	0.93 ± 0.03	1.17 ± 0.04	1.78 ± 0.06		2.79×10^{-9}
05354049-0452260	M3.5	0.01	3260	1	0.14	0.23	1.18	377	-61.3	0.73 ± 0.04	0.91 ± 0.04	1.57 ± 0.05	4.39 ± 0.07	2.80×10^{-9}
05351303-0534035	M4.5	0.47	3020	1	0.16	0.16	1.46	418	-35.9	1.47 ± 0.05	1.78 ± 0.06	2.43 ± 0.05	5.15 ± 0.06	2.80×10^{-9}
05345343-0510279	M4.5	0.22	3020	1	0.25	0.17	1.83	371	-20.2	-0.13 ± 0.02	-0.15 ± 0.02	-0.32 ± 0.05		2.81×10^{-9}
05344828-0532351	M5.0	1.48	2880	1	0.23	0.12	1.95	421	-17.1	0.11 ± 0.04	0.18 ± 0.05	0.48 ± 0.05		2.81×10^{-9}
05364039-0613334	M0.0	0.09	3770	2	0.34	0.51	1.36	389	-39.1					2.87×10^{-9}

2MASS	SpT	$A_{\rm V}$	$T_{\rm eff}$(K)	Ref	$L_*/L_\odot$	$M_*/M_\odot$	$R*/R_\odot$	dist(pc)	EW Hα(Å)	$DCE_{J-[4.5]}$	$DCE_{J-[5.8]}$	$DCE_{J-[8.0]}$	$DCE_{J-[24]}$	$\dot{M}(M_\odot yr^{-1})$
05344656-0523256	M3.0	0.0	3360	1	0.21	0.29	1.36	407	-42.6	1.84 ± 0.03	2.39 ± 0.04	3.41 ± 0.05	6.15 ± 0.05	2.88×10^{-9}
05350801-0532442	K7.0	0.0	3970	1	0.45	0.69	1.42	413	-37.6	1.72 ± 0.03	2.06 ± 0.03	3.03 ± 0.03	5.95 ± 0.04	2.90×10^{-9}
05350249-0533099	M2.0	0.0	3490	1	0.34	0.34	1.61	399	-25.2	1.21 ± 0.03	1.7 ± 0.05	2.37 ± 0.06	5.12 ± 0.05	2.90×10^{-9}
05360868-0521021	M3.5	0.49	3260	1	0.31	0.26	1.75	409	-22.3					2.97×10^{-9}
05340383-0436062	M2.5	0.0	3425	1	0.20	0.31	1.27	408	-52.9	0.01 ± 0.02	-0.0 ± 0.02	0.2 ± 0.03	5.26 ± 0.03	3.02×10^{-9}
05344204-0504317	M5.0	0.68	2880	1	0.02	0.02	0.58	228	-147.0	0.94 ± 0.05	1.22 ± 0.05	1.94 ± 0.05	4.33 ± 0.07	3.10×10^{-9}
05333304-0511555	M3.5	0.0	3260	1	0.19	0.25	1.37	383	-47.1	0.95 ± 0.02	1.31 ± 0.03	1.96 ± 0.03	5.03 ± 0.03	3.17×10^{-9}
05354987-0518308	M1.5	0.36	3560	1	0.21	0.37	1.23	405	-60.5	2.45 ± 0.14	2.79 ± 0.15	3.79 ± 0.14	7.07 ± 0.15	3.19×10^{-9}
05342767-0537192	M1.5	1.78	3560	1	0.18	0.37	1.12	398	-80.3	4.82 ± 0.08	5.13 ± 0.08	6.12 ± 0.08	8.26 ± 0.08	3.28×10^{-9}
05352845-0451549	M5.5	0.0	2740	1	0.05	0.02	1.06	375	-30.4	0.49 ± 0.03	0.78 ± 0.04	1.47 ± 0.06		3.29×10^{-9}
05342753-0528284	M4.5	0.03	3020	1	0.34	0.18	2.15	461	-15.7	0.01 ± 0.02	0.04 ± 0.03	0.28 ± 0.07		3.32×10^{-9}
05360086-0442588	M5.0	0.0	2880	1	0.07	0.07	1.07	353	-70.6	0.54 ± 0.03	0.88 ± 0.04	1.71 ± 0.05	3.81 ± 0.08	3.32×10^{-9}
05345304-0503271	K7.0	0.0	3970	2	0.41	0.69	1.36	381	-50.8					3.36×10^{-9}
05353447-0440207	K7.0	1.69	3970	1	0.52	0.68	1.53	375	-35.4	0.64 ± 0.02	0.84 ± 0.03	1.27 ± 0.06	6.24 ± 0.03	3.41×10^{-9}
05342792-0526346	K7.0	2.78	3970	1	0.71	0.67	1.79	390	-22.3	2.19 ± 0.04	2.83 ± 0.04	3.8 ± 0.04	6.44 ± 0.04	3.44×10^{-9}
05344117-0546116	M3.5	0.0	3260	1	0.27	0.25	1.64	394	-31.2	1.33 ± 0.03	1.6 ± 0.03	2.52 ± 0.03	6.28 ± 0.03	3.48×10^{-9}
05355433-0526444	M0.5	0.0	3700	1	0.42	0.46	1.59	402	-30.0	2.0 ± 0.03	2.11 ± 0.04	3.03 ± 0.05	6.39 ± 0.04	3.49×10^{-9}
05350052-0601235	M2.0	0.0	3490	1	0.13	0.33	1.02	375	-115.9	0.78 ± 0.03	0.76 ± 0.04	1.45 ± 0.04	4.06 ± 0.05	3.54×10^{-9}
05351630-0618431	M5.5	0.16	2740	1	0.12	0.06	1.59	385	-28.8	-0.11 ± 0.03	-0.09 ± 0.03	-0.06 ± 0.05		3.56×10^{-9}
05350753-0511145	K5.5	3.76	4080	1	0.94	0.79	1.94	408	-19.0	0.43 ± 0.05	0.58 ± 0.05	1.33 ± 0.08	5.07 ± 0.06	3.57×10^{-9}
05333855-0513125	M4.0	0.0	3160	1	0.14	0.2	1.25	373	-66.6	0.79 ± 0.02	1.17 ± 0.02	1.91 ± 0.02	4.64 ± 0.03	3.59×10^{-9}
05340594-0522387	M0.5	3.35	3700	1	1.04	0.46	2.49	356	-8.2					3.63×10^{-9}
05360926-0531096	M4.0	0.12	3160	1	0.05	0.15	0.74	389	-256.3	1.33 ± 0.03	1.58 ± 0.05	2.47 ± 0.08	5.87 ± 0.06	3.68×10^{-9}
05350947-0459413	M5.5	1.02	2740	1	0.17	0.08	1.84	402	-23.9	-0.04 ± 0.02	0.03 ± 0.03	0.31 ± 0.16		3.77×10^{-9}
05362516-0519133	M5.5	0.11	2740	1	0.12	0.06	1.59	428	-30.4	0.0 ± 0.02	0.03 ± 0.03	0.1 ± 0.05		3.79×10^{-9}
05341811-0528335	M2.5	1.74	3425	1	0.20	0.31	1.29	371	-65.2	1.0 ± 0.02	1.29 ± 0.03	2.1 ± 0.05	5.38 ± 0.04	3.82×10^{-9}
05353217-0511579	M5.0	0.0	2880	1	0.18	0.11	1.71	409	-31.3					3.82×10^{-9}
05343064-0435526	M1.0	1.12	3630	1	0.32	0.41	1.44	395	-45.5	0.7 ± 0.02	1.17 ± 0.02	1.95 ± 0.02	4.3 ± 0.04	3.86×10^{-9}
05341566-0532241	M2.0	0.0	3490	1	0.25	0.34	1.39	409	-52.9	2.67 ± 0.03	3.48 ± 0.03	4.33 ± 0.03	7.06 ± 0.03	3.88×10^{-9}
05344927-0600113	M4.5	0.0	3020	1	0.23	0.17	1.77	396	-30.7	0.06 ± 0.04	0.1 ± 0.04	0.14 ± 0.05		3.90×10^{-9}
05360729-0540222	K6.0	2.32	4020	2	1.80	0.69	2.76	403	-6.9					3.96×10^{-9}
05345833-0554288	M0.0	0.0	3770	1	0.37	0.51	1.44	404	-46.1	1.56 ± 0.03	2.0 ± 0.03	2.77 ± 0.03	4.95 ± 0.04	3.97×10^{-9}
05352279-0531372	M1.5	0.0	3560	1	0.36	0.38	1.58	424	-36.5	1.28 ± 0.1	1.53 ± 0.11	2.38 ± 0.11	4.82 ± 0.13	4.01×10^{-9}
05344892-0531315	M5.0	0.0	2880	1	0.07	0.07	1.06	433	-93.2					4.27×10^{-9}
05345045-0516296	M5.0	0.86	2880	1	0.04	0.05	0.89	391	-120.5					4.31×10^{-9}
05344506-0506202	M4.0	1.19	3160	1	0.11	0.19	1.13	413	-103.0	0.91 ± 0.03	1.2 ± 0.03	1.76 ± 0.05	4.5 ± 0.05	4.32×10^{-9}
05352523-0533210	M5.5	0.0	2740	1	0.14	0.07	1.69	421	-31.3	0.07 ± 0.04	0.02 ± 0.05	-0.32 ± 0.12		4.34×10^{-9}
05344587-0541097	M4.0	1.26	3160	1	0.41	0.23	2.14	414	-19.5	0.26 ± 0.02	0.6 ± 0.03	1.98 ± 0.02	5.16 ± 0.03	4.42×10^{-9}
05352288-0437406	M2.5	0.82	3425	1	0.18	0.31	1.20	404	-91.0	0.69 ± 0.02	0.85 ± 0.02	1.89 ± 0.03	5.49 ± 0.03	4.43×10^{-9}

2MASS	SpT	$A_{\rm V}$	$T_{\rm eff}$(K)	Ref	$L_*/L_\odot$	$M_*/M_\odot$	$R*/R_\odot$	dist(pc)	EW Hα(Å)	$DCE_{J-[4.5]}$	$DCE_{J-[5.8]}$	$DCE_{J-[8.0]}$	$DCE_{J-[24]}$	$\dot{M}(M_\odot yr^{-1})$
05352746-0517099	K7.0	0.0	3970	1	0.79	0.66	1.89	390	-24.4	2.39 ± 0.04	2.85 ± 0.04	3.35 ± 0.05		4.47×10^{-9}
05360416-0504088	M4.5	1.7	3020	1	0.23	0.17	1.75	411	-35.7	0.24 ± 0.03	0.46 ± 0.03	0.95 ± 0.04	3.72 ± 0.06	4.48×10^{-9}
05344048-0457396	M4.0	0.0	3160	1	0.13	0.19	1.21	361	-93.3	0.69 ± 0.03	0.77 ± 0.03	1.44 ± 0.03	4.99 ± 0.04	4.57×10^{-9}
05341525-0504517	M5.5	0.6	2740	1	0.18	0.08	1.91	402	-27.4	0.15 ± 0.02	0.33 ± 0.02	0.72 ± 0.03	3.36 ± 0.05	4.67×10^{-9}
05334822-0513262	M1.5	1.55	3560	1	0.21	0.37	1.21	379	-93.0	0.85 ± 0.04	1.26 ± 0.04	2.01 ± 0.04	4.99 ± 0.04	4.74×10^{-9}
05354986-0446323	M4.5	0.11	3020	1	0.17	0.16	1.53	361	-54.5	0.46 ± 0.02	0.82 ± 0.02	1.55 ± 0.03	4.26 ± 0.04	4.74×10^{-9}
05351979-0514053	M4.5	0.0	3020	1	0.08	0.13	1.08	407	-124.9					4.75×10^{-9}
05363720-0526253	K7.5	0.35	3910	2	0.23	0.65	1.04	234	-154.8					4.79×10^{-9}
05361584-0614507	M2.5	0.03	3425	1	0.13	0.29	1.04	383	-148.8	0.1 ± 0.02	0.27 ± 0.02	1.17 ± 0.02	4.95 ± 0.03	4.88×10^{-9}
05353672-0510004	M4.5	0.0	3020	1	0.09	0.13	1.10	385	-127.5	1.54 ± 0.03	1.97 ± 0.05	2.83 ± 0.07	5.71 ± 0.06	4.99×10^{-9}
05345156-0525129	K7.5	0.0	3910	1	0.90	0.60	2.07	403	-19.3	2.19 ± 0.02	2.48 ± 0.02	3.46 ± 0.02	6.38 ± 0.03	5.00×10^{-9}
05353170-0441077	M4.0	0.39	3160	1	0.10	0.18	1.08	388	-136.2	0.34 ± 0.04	0.4 ± 0.04	0.78 ± 0.06	5.69 ± 0.06	5.04×10^{-9}
05344844-0450514	M2.0	0.79	3490	1	0.13	0.32	0.98	406	-184.1	0.79 ± 0.06	1.12 ± 0.06	1.99 ± 0.08	5.24 ± 0.08	5.18×10^{-9}
05341420-0542210	M1.0	0.46	3630	1	0.33	0.41	1.46	394	-58.1	1.03 ± 0.02	1.05 ± 0.02	1.53 ± 0.04	5.59 ± 0.03	5.22×10^{-9}
05342298-0441392	M0.5	0.0	3700	1	0.50	0.46	1.72	408	-36.0	1.37 ± 0.02	1.87 ± 0.02	2.51 ± 0.02	4.62 ± 0.03	5.24×10^{-9}
05355018-0521169	M2.5	0.66	3425	1	0.16	0.30	1.16	394	-126.8	0.81 ± 0.02	1.48 ± 0.05	2.86 ± 0.05		5.54×10^{-9}
05352372-0448166	M4.5	0.0	3020	1	0.10	0.14	1.17	369	-127.9	0.75 ± 0.03	1.25 ± 0.04	2.5 ± 0.04	5.38 ± 0.06	5.67×10^{-9}
05363616-0555288	K7.0	0.85	3970	2	0.80	0.66	1.89	402	-31.8					5.88×10^{-9}
05351609-0429303	M5.0	0.0	2880	1	0.12	0.10	1.43	462	-71.2	0.71 ± 0.04	0.93 ± 0.04	1.3 ± 0.05	3.17 ± 0.13	5.89×10^{-9}
05343654-0536171	M3.0	0.62	3770	4	1.25	0.29	2.84	482	-11.4	0.15 ± 0.05	0.28 ± 0.05	0.76 ± 0.05	3.6 ± 0.06	6.06×10^{-9}
05345932-0505300	M1.5	0.78	3560	1	0.81	0.38	2.38	628	-16.4	0.33 ± 0.03	0.46 ± 0.03	0.73 ± 0.04		6.07×10^{-9}
05354537-0528107	M0.5	0.0	3700	1	0.54	0.46	1.80	408	-36.3	1.72 ± 0.02	2.3 ± 0.02	3.6 ± 0.03	7.41 ± 0.04	6.09×10^{-9}
05342587-0456274	M0.5	0.0	3700	1	0.33	0.46	1.41	394	-81.1	1.24 ± 0.15	1.76 ± 0.15	2.93 ± 0.15	6.16 ± 0.16	6.57×10^{-9}
05345654-0501071	M5.0	1.57	2880	1	0.05	0.06	0.94	382	-170.7	0.33 ± 0.03	0.8 ± 0.04	1.77 ± 0.06	4.89 ± 0.08	6.67×10^{-9}
05333148-0609541	M5.5	0.0	2740	1	0.22	0.09	2.10	490	-33.8	0.63 ± 0.03	1.01 ± 0.03	1.86 ± 0.03	4.07 ± 0.04	6.79×10^{-9}
05355225-0443048	K6.0	0.0	4020	2	0.51	0.74	1.47	398	-83.6					6.82×10^{-9}
05353369-0446237	M0.5	0.05	3700	1	0.39	0.46	1.53	405	-66.5	0.76 ± 0.03	0.86 ± 0.03	1.42 ± 0.03	5.71 ± 0.04	6.87×10^{-9}
05334192-0506148	M5.0	0.0	2880	1	0.02	0.03	0.65	416	-302.6	0.61 ± 0.04	0.99 ± 0.05	1.85 ± 0.05	4.7 ± 0.1	6.94×10^{-9}
05355405-0447193	M2.0	0.16	3490	1	0.26	0.34	1.39	387	-94.1	1.67 ± 0.06	1.9 ± 0.06	2.57 ± 0.06	5.34 ± 0.07	6.97×10^{-9}
05354838-0501287	M0.5	0.0	3700	1	0.33	0.46	1.40	385	-89.3	2.11 ± 0.04	2.35 ± 0.04	3.04 ± 0.04	6.69 ± 0.04	7.09×10^{-9}
05344845-0531072	M4.5	0.0	3020	1	0.07	0.12	1.03	461	-213.2					7.21×10^{-9}
05341320-0533535	M1.5	0.0	3560	1	0.18	0.37	1.14	379	-170.0	1.44 ± 0.04	1.56 ± 0.04	2.57 ± 0.04	5.11 ± 0.05	7.29×10^{-9}
05344188-0453382	M4.0	0.11	3160	1	0.30	0.22	1.84	409	-49.1	0.57 ± 0.03	0.73 ± 0.03	1.59 ± 0.04	5.24 ± 0.04	7.41×10^{-9}
05350822-0537047	M3.0	0.43	3360	1	0.51	0.29	2.11	405	-31.4	1.57 ± 0.02	2.14 ± 0.02	2.48 ± 0.02	4.84 ± 0.04	7.60×10^{-9}
05343371-0540227	M5.5	0.0	2740	1	0.15	0.07	1.75	406	-52.4	0.49 ± 0.02	0.78 ± 0.02	1.53 ± 0.03	4.09 ± 0.05	7.69×10^{-9}
05354040-0455439	M4.5	0.0	3020	1	0.08	0.13	1.09	376	-200.0	0.5 ± 0.02	0.6 ± 0.04	1.38 ± 0.05	5.3 ± 0.05	7.73×10^{-9}
05350133-0520221	M1.0	2.94	3630	1	0.84	0.42	2.33	432	-22.0	1.19 ± 0.07	1.8 ± 0.07	3.1 ± 0.07		7.83×10^{-9}
05350873-0504407	M4.5	0.91	3020	1	0.25	0.17	1.84	370	-56.6	0.54 ± 0.02	0.74 ± 0.02	1.48 ± 0.02	3.8 ± 0.03	7.98×10^{-9}
05355765-0557183	M0.0	0.0	3770	1	0.34	0.51	1.38	380	-106.0	1.36 ± 0.02	1.69 ± 0.02	2.56 ± 0.02	6.31 ± 0.02	8.02×10^{-9}

2MASS	SpT	A_{V}	T_{eff}(K)	Ref	$L_*/L_\odot$	$M_*/M_\odot$	$R*/R_\odot$	dist(pc)	EW Hα(Å)	$DCE_{J-[4.5]}$	$DCE_{J-[5.8]}$	$DCE_{J-[8.0]}$	$DCE_{J-[24]}$	$\dot{M}(M_\odot yr^{-1})$
05352277-0428510	M1.5	0.0	3560	1	0.33	0.38	1.52	395	-81.3	1.05 ± 0.02	1.07 ± 0.02	1.74 ± 0.02	4.67 ± 0.04	8.10×10^{-9}
05351627-0532021	M5.0	0.53	2880	1	0.14	0.10	1.51	394	-90.2	0.81 ± 0.04	1.19 ± 0.04	1.87 ± 0.04		8.24×10^{-9}
05352138-0509422	M5.5	0.0	2740	1	0.05	0.01	1.00	353	-67.9					8.32×10^{-9}
05351487-0507476	M5.5	0.21	2740	1	0.05	0.02	1.05	418	-79.3	1.1 ± 0.03	1.63 ± 0.06	2.8 ± 0.09		8.73×10^{-9}
05340797-0536170	M4.0	0.11	3160	1	0.18	0.21	1.43	382	-116.2	2.1 ± 0.02	2.66 ± 0.02	3.64 ± 0.02	6.41 ± 0.03	8.76×10^{-9}
05343024-0511481	K6.5	0.41	3995	1	0.66	0.69	1.7	386	-67.6	1.84 ± 0.02	2.06 ± 0.02	2.96 ± 0.02	5.92 ± 0.03	8.86×10^{-9}
05353644-0534111	M1.0	0.0	3630	1	0.46	0.41	1.72	389	-63.6	1.82 ± 0.02	2.05 ± 0.02	2.79 ± 0.03	4.58 ± 0.03	9.26×10^{-9}
05344314-0544400	M4.5	0.0	3020	1	0.14	0.15	1.37	302	-145.9	1.47 ± 0.02	1.82 ± 0.03	2.61 ± 0.03	5.46 ± 0.03	9.50×10^{-9}
05343519-0534322	M5.0	0.0	2880	1	0.14	0.11	1.55	391	-101.0	1.21 ± 0.03	1.68 ± 0.03	2.8 ± 0.03	6.08 ± 0.04	9.62×10^{-9}
05345292-0528591	M4.0	0.0	3160	1	0.12	0.19	1.19	401	-204.7	0.96 ± 0.03	1.61 ± 0.04	2.93 ± 0.04		9.67×10^{-9}
05355861-0429241	M3.0	0.0	3360	1	0.31	0.29	1.66	417	-84.4	1.06 ± 0.02	1.38 ± 0.02	2.1 ± 0.02	4.78 ± 0.03	1.01×10^{-8}
05343822-0524236	M4.0	2.76	3160	1	0.34	0.22	1.96	390	-57.8					1.03×10^{-8}
05343911-0534023	M5.5	3.07	2740	1	0.16	0.07	1.81	433	-70.7	0.2 ± 0.13	0.47 ± 0.14	1.01 ± 0.14		1.08×10^{-8}
05353089-0455178	K7.0	0.0	3970	2	0.49	0.68	1.49	397	-126.1					1.10×10^{-8}
05352864-0447265	M4.5	0.0	3020	1	0.19	0.16	1.62	396	-108.2	0.99 ± 0.04	1.49 ± 0.04	2.34 ± 0.04	5.06 ± 0.05	1.11×10^{-8}
05345275-0527545	K7.5	4.11	3910	1	2.89	0.61	3.71	410	-7.8	0.34 ± 0.05	0.55 ± 0.05	1.17 ± 0.05	3.76 ± 0.06	1.14×10^{-8}
05344794-0504550	M1.0	0.12	3630	1	0.74	0.42	2.17	535	-40.0	1.15 ± 0.03	1.31 ± 0.03	2.11 ± 0.03	5.88 ± 0.03	1.17×10^{-8}
05352551-0451205	M0.0	0.0	3770	1	0.29	0.50	1.26	381	-205.0	1.88 ± 0.04	2.07 ± 0.04	3.12 ± 0.04	6.88 ± 0.05	1.20×10^{-8}
05360512-0511137	M5.5	0.41	2740	1	0.06	0.03	1.16	451	-125.9	0.78 ± 0.04	1.14 ± 0.05	1.88 ± 0.05	4.26 ± 0.07	1.22×10^{-8}
05345559-0555293	M3.5	1.41	3260	1	0.22	0.25	1.47	419	-151.7	1.08 ± 0.03	1.65 ± 0.03	2.89 ± 0.03	6.01 ± 0.03	1.24×10^{-8}
05344518-0510476	M1.0	0.31	3630	1	0.35	0.41	1.50	393	-128.4	1.32 ± 0.03	1.45 ± 0.03	1.92 ± 0.04	4.75 ± 0.04	1.25×10^{-8}
05353668-0504145	M1.5	0.0	3560	1	0.85	0.38	2.42	545	-32.1	0.83 ± 0.02	1.02 ± 0.02	1.51 ± 0.03	5.03 ± 0.03	1.26×10^{-8}
05341138-0451229	M0.0	0.0	3770	2	0.29	0.50	1.26	391	-216.2					1.27×10^{-8}
05355676-0519579	M5.0	0.11	2880	1	0.10	0.09	1.30	465	-187.6					1.29×10^{-8}
05354764-0537388	M4.0	0.87	3160	1	0.19	0.21	1.47	417	-171.6	1.56 ± 0.04	1.73 ± 0.05	2.3 ± 0.05	4.53 ± 0.06	1.36×10^{-8}
05352459-0511296	K7.5	3.65	3910	1	0.72	0.61	1.84	362	-76.2	1.48 ± 0.02	1.85 ± 0.03	2.81 ± 0.04	6.63 ± 0.03	1.39×10^{-8}
05352253-0452369	M4.0	0.16	3160	1	0.28	0.22	1.77	407	-104.1	1.98 ± 0.02	2.62 ± 0.02	3.82 ± 0.02	6.78 ± 0.03	1.40×10^{-8}
05353635-0531378	M2.5	0.0	3425	1	0.23	0.31	1.38	401	-210.9	1.88 ± 0.04	2.17 ± 0.05	2.84 ± 0.05	6.03 ± 0.05	1.50×10^{-8}
05352523-0515358	K7.5	0.0	3910	1	0.50	0.62	1.54	389	-145.8	2.91 ± 0.04	3.66 ± 0.04	4.73 ± 0.07		1.52×10^{-8}
05343005-0449506	M0.0	0.0	3770	1	0.42	0.50	1.53	405	-146.4	0.72 ± 0.02	0.73 ± 0.03	0.99 ± 0.03	4.05 ± 0.06	1.53×10^{-8}
05352980-0516064	M4.0	0.0	3160	1	0.31	0.22	1.87	387	-99.9					1.56×10^{-8}
05355965-0529435	K2.5	2.26	4655	2	3.38	1.65	2.83	439	-28.6					1.58×10^{-8}
05360704-0534182	M3.5	0.0	3260	1	0.30	0.26	1.73	434	-129.6	2.67 ± 0.08	3.26 ± 0.08	4.08 ± 0.08	6.86 ± 0.08	1.67×10^{-8}
05352240-0508051	K7.0	3.46	3970	1	1.83	0.65	2.86	340	-28.5	2.62 ± 0.05	3.15 ± 0.05	4.28 ± 0.05	7.52 ± 0.06	1.84×10^{-8}
05350576-0533558	M4.5	0.73	3020	1	0.40	0.18	2.32	398	-107.1	1.79 ± 0.06	2.2 ± 0.06	3.0 ± 0.06	6.66 ± 0.07	2.81×10^{-8}
05352262-0514112	M3.5	0.55	3260	1	0.60	0.26	2.43	412	-83.8					2.91×10^{-8}
05352463-0519096	M3.0	2.23	3360	1	0.72	0.3	2.51	430	-81.0					3.32×10^{-8}
05351852-0513383	M0.0	2.66	3770	1	1.43	0.49	2.80	402	-54.7	2.77 ± 0.02	3.6 ± 0.02	4.52 ± 0.02	7.74 ± 0.02	3.55×10^{-8}
05352461-0511582	M0.0	0.0	3770	4	1.34	0.49	2.71	581	-90.2					5.33×10^{-8}

2MASS	SpT	$A_{\rm V}$	$T_{\rm eff}$(K)	Ref	$L_*/L_\odot$	$M_*/M_\odot$	$R*/R_\odot$	dist(pc)	EW Hα(Å)	$DCE_{J-[4.5]}$	$DCE_{J-[5.8]}$	$DCE_{J-[8.0]}$	$DCE_{J-[24]}$	$\dot{M}(M_\odot yr^{-1})$
05334545-0536323	M5.5	0.36	2740	1	0.29			395	-33.3	0.64 ± 0.03	1.15 ± 0.03	2.44 ± 0.03	5.62 ± 0.03	
05350450-0523565	K2.0	0.0	4760	3	0.96	1.22	1.44	389		2.24 ± 0.02	2.45 ± 0.02	2.7 ± 0.03		
05341954-0530198	K5.0	0.48	4140	3	1.29	0.83	2.21	400		2.01 ± 0.02	2.33 ± 0.02	3.46 ± 0.02	6.77 ± 0.02	
05353287-0530214	K6.0	0.37	4020	4	0.91	0.72	1.97	408		1.6 ± 0.02	1.74 ± 0.02	2.47 ± 0.03	5.8 ± 0.04	
05344295-0520069	K6.0	0.52	4020	3	2.10	0.72	2.99	548		0.27 ± 0.02	0.37 ± 0.03	0.62 ± 0.09		
05343796-0451089	K7.5	1.19	3910	1	0.28	0.64	1.15	415		0.25 ± 0.02	0.21 ± 0.03	0.4 ± 0.05		
05344693-0459127	K7.5	0.37	3910	1	0.37	0.63	1.33	392		0.2 ± 0.02	0.25 ± 0.02	0.28 ± 0.03		
05345879-0521176	K7.5	0.0	3910	1	0.44	0.62	1.46	401		2.02 ± 0.02	2.14 ± 0.03	2.59 ± 0.15		
05351282-0539077	K7.5	1.38	3910	1	0.29	0.64	1.18	414		0.14 ± 0.02	0.23 ± 0.03	0.59 ± 0.07		
05355355-0502345	K7.5	2.76	3910	1	0.32	0.64	1.23	400		0.05 ± 0.03	0.15 ± 0.04	0.49 ± 0.07		
05360021-0603295	K7.5	1.79	3910	1	1.23	0.60	2.42	413		0.26 ± 0.03	0.26 ± 0.03	0.35 ± 0.03		
05341687-0504210	M0.0	2.83	3770	1	3.15	0.50	4.16	611		0.6 ± 0.04	0.9 ± 0.04	2.05 ± 0.04	4.77 ± 0.04	
05344340-0530070	M0.0	0.92	3770	1	0.43	0.50	1.55	398		0.23 ± 0.02	0.26 ± 0.03	0.46 ± 0.05		
05351822-0513068	M0.0	2.4	3770	1	0.29	0.50	1.26	190		1.71 ± 0.03	2.02 ± 0.04	2.73 ± 0.04	5.77 ± 0.04	
05355105-0515090	M0.0	0.0	3770	1	0.34	0.51	1.38	359		0.63 ± 0.02	0.87 ± 0.02	1.01 ± 0.09		
05350082-0538079	M0.0	0.14	3770	3	0.46	0.50	1.60	394		2.31 ± 0.07	2.93 ± 0.07	3.94 ± 0.07	7.01 ± 0.08	
05350532-0534285	M0.0	0.0	3770	3	0.37	0.51	1.43	382		2.07 ± 0.07	2.41 ± 0.07	2.79 ± 0.07		
05343753-0541173	M0.5	1.3	3700	1	1.03	0.46	2.47	461		0.44 ± 0.03	0.6 ± 0.03	1.23 ± 0.03	4.04 ± 0.04	
05344061-0443315	M0.5	2.4	3700	1	0.20	0.45	1.10	297		0.27 ± 0.02	0.28 ± 0.02	0.46 ± 0.05		
05361975-0514386	M0.5	0.0	3700	1	0.33	0.46	1.41	406		1.08 ± 0.02	1.37 ± 0.02	2.14 ± 0.02	4.72 ± 0.03	
05365720-0506049	M0.5	0.33	3700	1	0.46	0.46	1.65	408		1.16 ± 0.05	1.43 ± 0.05	2.0 ± 0.05	3.95 ± 0.06	
05345555-0536061	M0.5	3.23	3700	3	0.52	0.46	1.76	416		1.66 ± 0.04	2.11 ± 0.04	3.16 ± 0.04	6.09 ± 0.05	
05350333-0456430	M1.0	0.35	3630	1	0.30	0.41	1.39	387		0.66 ± 0.02	0.88 ± 0.03	1.75 ± 0.04	5.04 ± 0.04	
05354339-0532441	M1.0	0.64	3630	1	0.36	0.41	1.52	358		0.97 ± 0.02	1.31 ± 0.02	1.91 ± 0.03		
05351357-0535080	M1.0	1.74	3630	3	0.29	0.41	1.37	512		3.44 ± 0.05	3.81 ± 0.06	4.49 ± 0.06	6.8 ± 0.06	
05352290-0532290	M1.0	0.91	3630	3	1.74	0.41	3.34	746		0.6 ± 0.02	0.62 ± 0.02	1.47 ± 0.02	5.76 ± 0.04	
05350959-0528228	M1.0	0.01	3630	3	0.46	0.41	1.73	420		2.18 ± 0.02	2.81 ± 0.03	3.95 ± 0.04		
05362974-0520068	M1.5	0.02	3560	1	0.35	0.38	1.56	412		0.38 ± 0.03	0.4 ± 0.03	0.33 ± 0.04		
05342679-0528321	M1.5	0.0	3560	4	0.26	0.37	1.34	401		0.18 ± 0.02	0.18 ± 0.03	0.5 ± 0.08	5.9 ± 0.03	
05342674-0450456	M2.0	0.75	3490	1	0.26	0.34	1.40	389		0.24 ± 0.02	0.27 ± 0.02	0.31 ± 0.04		
05343168-0528269	M2.0	0.45	3490	1	0.22	0.34	1.30	408		0.92 ± 0.02	1.02 ± 0.02	1.59 ± 0.03		
05343756-0543106	M2.0	0.79	3490	1	0.29	0.34	1.49	390		0.76 ± 0.02	1.01 ± 0.02	1.45 ± 0.02	3.37 ± 0.06	
05351009-0451080	M2.0	0.45	3490	1	0.21	0.34	1.26	396		0.15 ± 0.03	0.25 ± 0.05	0.58 ± 0.13		
05344692-0535078	M2.0	0.3	3490	4	0.70	0.35	2.29	398		0.24 ± 0.03	0.28 ± 0.03	0.43 ± 0.04		
05352746-0509441	M2.0	3.42	3490	4	1.57	0.35	3.43	465		1.53 ± 0.07	1.96 ± 0.05	3.13 ± 0.04		
05351113-0536511	M2.0	0.48	3490	3	0.87	0.35	2.55	379		0.05 ± 0.02	0.2 ± 0.02	0.51 ± 0.07		
05352121-0533175	M2.0	0.83	3490	3	0.09	0.31	0.85	466		0.62 ± 0.03	1.03 ± 0.05	1.66 ± 0.08		
05355003-0517181	M2.0	1.25	3490	3	0.02	0.28	0.39	320		1.48 ± 0.14	1.88 ± 0.15	2.77 ± 0.16	7.26 ± 0.15	
05345566-0456117	M2.5	3.4	3425	1	0.46	0.32	1.94	354		1.67 ± 0.03	1.95 ± 0.03	2.7 ± 0.03	5.54 ± 0.04	

2MASS	SpT	$A_{\rm V}$	$T_{\rm eff}$(K)	Ref	$L_*/L_\odot$	$M_*/M_\odot$	$R*/R_\odot$	dist(pc)	EW Hα(Å)	$DCE_{J-[4.5]}$	$DCE_{J-[5.8]}$	$DCE_{J-[8.0]}$	$DCE_{J-[24]}$	$\dot{M}(M_\odot yr^{-1})$
05350284-0551031	M2.5	0.03	3425	1	0.17	0.31	1.20	395		0.01 ± 0.02	0.32 ± 0.04	1.14 ± 0.05		
05345009-0517121	M2.5	0.0	3425	3	0.12	0.29	1.02	433		1.26 ± 0.03	1.47 ± 0.04	2.16 ± 0.09		
05352617-0530181	M2.5	0.36	3425	3	0.28	0.31	1.52	411		1.79 ± 0.07	2.14 ± 0.07	3.12 ± 0.07	5.46 ± 0.14	
05342381-0508159	M3.0	0.76	3360	1	0.29	0.29	1.59	408		0.08 ± 0.04	0.16 ± 0.04	0.25 ± 0.09		
05343416-0448279	M3.0	0.0	3360	1	0.19	0.28	1.31	403		0.33 ± 0.02	0.53 ± 0.03	1.35 ± 0.06	4.74 ± 0.05	
05350312-0509170	M3.0	1.06	3360	1	0.16	0.28	1.18	389		0.35 ± 0.02	0.67 ± 0.03	1.39 ± 0.04	4.24 ± 0.05	
05351319-0441544	M3.0	0.75	3360	1	0.18	0.28	1.27	400		0.73 ± 0.02	1.09 ± 0.02	1.88 ± 0.03	4.56 ± 0.05	
05351837-0450309	M3.0	0.08	3360	1	0.15	0.27	1.16	439		0.19 ± 0.03	0.16 ± 0.04	0.35 ± 0.08		
05352564-0507573	M3.0	2.11	3360	1	0.73	0.3	2.53	374		1.5 ± 0.03	2.27 ± 0.03	3.25 ± 0.04	8.25 ± 0.03	
05352658-0456067	M3.0	0.0	3360	1	0.41	0.29	1.90	399		0.09 ± 0.05	0.19 ± 0.06	0.55 ± 0.14		
05353522-0447396	M3.0	0.03	3360	1	0.26	0.29	1.51	397		0.65 ± 0.02	1.08 ± 0.03	2.36 ± 0.03	6.38 ± 0.04	
05353716-0510295	M3.0	0.03	3360	1	0.78	0.29	2.60	728		0.55 ± 0.02	0.56 ± 0.04	1.08 ± 0.08		
05354898-0501394	M3.0	0.0	3360	1	0.23	0.29	1.42	413		0.67 ± 0.03	0.95 ± 0.03	1.54 ± 0.04	3.63 ± 0.22	
05360680-0506156	M3.0	0.16	3360	1	0.13	0.27	1.08	378		0.28 ± 0.02	0.49 ± 0.03	1.2 ± 0.03	3.32 ± 0.06	
05345597-0531130	M3.0	0.0	3360	4	0.37	0.29	1.80	404		0.13 ± 0.06	0.24 ± 0.07	0.46 ± 0.07		
05351444-0532464	M3.0	0.91	3360	4	0.41	0.29	1.89	790		2.19 ± 0.05	2.74 ± 0.05	3.69 ± 0.05	7.64 ± 0.05	
05344793-0523403	M3.0	0.0	3360	3	0.08	0.25	0.88	410		0.75 ± 0.02	1.18 ± 0.04	2.15 ± 0.05		
05350161-0533380	M3.0	2.49	3360	3	0.41	0.29	1.90	501		0.87 ± 0.1	1.03 ± 0.11	1.46 ± 0.11		
05351795-0535157	M3.0	0.0	3360	3	0.09	0.25	0.93	344		1.84 ± 0.02	2.03 ± 0.03	2.77 ± 0.03	5.46 ± 0.04	
05352889-0535067	M3.0	0.05	3360	3	0.21	0.29	1.38	404		0.15 ± 0.02	0.51 ± 0.04	1.4 ± 0.05		
05351475-0534167	M3.0	2.16	3360	3	0.34	0.29	1.73	531		2.56 ± 0.07	3.12 ± 0.07	3.66 ± 0.07	5.76 ± 0.07	
05335074-0500394	M3.5	0.19	3260	1	0.10	0.21	1.02	368		0.14 ± 0.03	0.25 ± 0.04	0.68 ± 0.04	4.34 ± 0.07	
05342675-0541573	M3.5	0.13	3260	1	0.17	0.24	1.30	406		0.44 ± 0.02	0.83 ± 0.02	1.77 ± 0.03	3.77 ± 0.06	
05344142-0439138	M3.5	0.18	3260	1	0.11	0.22	1.08	405		0.63 ± 0.03	0.87 ± 0.04	1.32 ± 0.04	3.63 ± 0.1	
05345935-0450117	M3.5	0.05	3260	1	0.40	0.26	1.98	380		0.24 ± 0.02	0.47 ± 0.04	1.24 ± 0.1		
05364965-0504094	M3.5	0.03	3260	1	0.32	0.26	1.78	409		1.34 ± 0.05	1.68 ± 0.05	2.51 ± 0.05	5.4 ± 0.05	
05343710-0531089	M3.5	0.61	3260	4	0.26	0.25	1.60	403		1.29 ± 0.03	1.54 ± 0.04	2.19 ± 0.04	5.72 ± 0.04	
05342068-0435019	M4.0	0.02	3160	1	0.12	0.19	1.2	408		0.34 ± 0.02	0.59 ± 0.02	1.2 ± 0.04	3.34 ± 0.07	
05343417-0505170	M4.0	0.12	3160	1	0.08	0.17	0.98	369		0.47 ± 0.02	1.08 ± 0.03	1.53 ± 0.03	3.89 ± 0.06	
05343996-0450476	M4.0	1.05	3160	1	0.05	0.16	0.80	368		0.79 ± 0.03	1.01 ± 0.05	1.76 ± 0.08		
05350768-0536587	M4.0	2.0	3160	1	0.58	0.23	2.54	347		0.54 ± 0.03	0.79 ± 0.03	1.48 ± 0.03		
05352019-0441342	M4.0	0.0	3160	1	0.13	0.19	1.23	384		1.39 ± 0.02	1.63 ± 0.03	2.28 ± 0.03	4.9 ± 0.04	
05353595-0538426	M4.0	0.04	3160	1	0.42	0.23	2.16	671		0.96 ± 0.02	1.16 ± 0.03	1.56 ± 0.04	4.55 ± 0.05	
05354923-0559142	M4.0	0.19	3160	1	0.07	0.17	0.94	397		-0.06 ± 0.03	0.18 ± 0.05	0.52 ± 0.1		
05362928-0453510	M4.0	0.0	3160	1	0.04	0.15	0.72	201		0.08 ± 0.02	0.15 ± 0.02	0.57 ± 0.03	2.27 ± 0.14	
05335414-0503401	M4.5	0.04	3020	1	0.11	0.14	1.22	334		0.1 ± 0.02	0.16 ± 0.03	0.34 ± 0.05		
05342073-0532351	M4.5	0.0	3020	1	0.10	0.14	1.17	401		-0.03 ± 0.03	0.23 ± 0.04	1.09 ± 0.09		
05343597-0452180	M4.5	0.0	3020	1	0.05	0.11	0.84	378		0.84 ± 0.03	1.13 ± 0.04	1.55 ± 0.08		
05345343-0457328	M4.5	0.42	3020	1	0.08	0.13	1.07	354		0.48 ± 0.02	0.85 ± 0.02	1.51 ± 0.04	3.99 ± 0.05	

2MASS	SpT	A_{V}	T_{eff}(K)	Ref	$L_*/L_\odot$	$M_*/M_\odot$	$R*/R_\odot$	dist(pc)	EW Hα(Å)	$DCE_{J-[4.5]}$	$DCE_{J-[5.8]}$	$DCE_{J-[8.0]}$	$DCE_{J-[24]}$	$\dot{M}(M_\odot yr^{-1})$
05345714-0533294	M4.5	1.07	3020	1	0.26	0.17	1.87	450		0.65 ± 0.03	1.07 ± 0.03	1.96 ± 0.03	4.83 ± 0.04	
05350524-0448027	M4.5	0.0	3020	1	0.21	0.16	1.71	346		0.17 ± 0.03	0.25 ± 0.03	0.48 ± 0.04		
05354859-0605257	M4.5	0.0	3020	1	0.05	0.11	0.86	311		0.1 ± 0.02	0.22 ± 0.03	0.64 ± 0.05		
05355831-0455365	M4.5	0.0	3020	1	0.05	0.11	0.88	384		-0.06 ± 0.03	0.26 ± 0.07	1.65 ± 0.1		
05355948-0537096	M4.5	0.52	3020	1	0.19	0.16	1.60	410		0.57 ± 0.03	0.98 ± 0.04	2.04 ± 0.06	5.18 ± 0.04	
05361901-0518286	M4.5	0.52	3020	1	0.05	0.10	0.83	401		0.08 ± 0.03	0.25 ± 0.06	0.81 ± 0.08	4.26 ± 0.09	
05342807-0505218	M5.0	0.73	2880	1	0.04	0.05	0.88	375		0.33 ± 0.04	0.59 ± 0.04	1.44 ± 0.06	4.23 ± 0.07	
05343894-0557536	M5.0	0.08	2880	1	0.06	0.07	1.04	365		0.51 ± 0.03	0.83 ± 0.04	1.42 ± 0.03	3.11 ± 0.12	
05350039-0509441	M5.0	0.3	2880	1	0.07	0.07	1.11	414		0.08 ± 0.04	0.46 ± 0.06	1.28 ± 0.11	6.49 ± 0.05	
05350504-0432334	M5.0	0.0	2880	1	0.10	0.09	1.32	372		0.24 ± 0.02	0.39 ± 0.03	0.68 ± 0.04	2.43 ± 0.18	
05351887-0444277	M5.0	0.0	2880	1	0.11	0.09	1.38	397		0.22 ± 0.03	0.4 ± 0.04	1.0 ± 0.07	4.08 ± 0.07	
05355132-0613533	M5.0	0.12	2880	1	0.08	0.08	1.20	367		0.78 ± 0.03	1.11 ± 0.03	1.89 ± 0.03	4.21 ± 0.04	
05360629-0603155	M5.0	0.3	2880	1	0.02	0.03	0.62	372		0.51 ± 0.05	0.82 ± 0.06	1.36 ± 0.08	4.22 ± 0.15	
05362627-0518301	M5.0	0.0	2880	1	0.10	0.09	1.27	433		0.65 ± 0.03	0.91 ± 0.04	1.71 ± 0.04	5.12 ± 0.04	
05344698-0535035	M5.0	0.0	2880	1	0.05	0.06	0.92	399		0.99 ± 0.04	1.22 ± 0.06	2.0 ± 0.07	5.15 ± 0.07	
05361456-0533238	M5.0	0.0	2880	4	0.05	0.06	0.93	388		-0.03 ± 0.04	0.15 ± 0.05	0.5 ± 0.1		
05341634-0449271	M5.5	0.0	2740	1	0.11	0.05	1.47	393		0.13 ± 0.03	0.26 ± 0.03	0.64 ± 0.05	3.12 ± 0.09	
05342207-0501342	M5.5	0.0	2740	1	0.09	0.04	1.34	372		0.21 ± 0.03	0.47 ± 0.03	1.3 ± 0.04	5.07 ± 0.05	
05350085-0531058	M5.5	0.0	2740	1	0.04	0.01	0.98	315		1.18 ± 0.03	1.74 ± 0.05	2.67 ± 0.05		
05351268-0601101	M5.5	0.15	2740	1	0.03			375		0.06 ± 0.05	0.23 ± 0.07	0.45 ± 0.14		
05354379-0509588	M5.5	0.0	2740	1	0.06	0.03	1.16	410		0.41 ± 0.03	0.79 ± 0.05	1.86 ± 0.09		
05360282-0532543	M5.5	0.45	2740	1	0.06	0.02	1.11	387		0.43 ± 0.04	0.49 ± 0.05	1.11 ± 0.1		
05352828-0537195	M5.5	0.0	2740	4	0.09	0.04	1.33	460		0.53 ± 0.03	0.8 ± 0.04	1.64 ± 0.05	4.65 ± 0.06	
05354562-0513361	M5.5	1.06	2740	4	0.13	0.06	1.63	445		1.46 ± 0.02	1.78 ± 0.03	2.25 ± 0.11	6.6 ± 0.05	
05342396-0528347	M6.0	0.0	2600	4	0.04			416		0.41 ± 0.04	0.69 ± 0.05	1.51 ± 0.07		
05352157-0509389	K5.0	0.0	4140	3						3.19 ± 0.05	3.91 ± 0.05	4.89 ± 0.05	9.16 ± 0.05	
05353885-0512419	K5.5	2.34	4080	1						1.67 ± 0.02	2.24 ± 0.02	2.99 ± 0.03	5.31 ± 0.03	
05344474-0533421	K6.5	1.94	3995	1						2.13 ± 0.04	2.58 ± 0.04	3.43 ± 0.04	5.82 ± 0.05	
05354201-0510115	K6.5	4.22	3995	1						1.21 ± 0.02	1.53 ± 0.02	2.15 ± 0.02	4.75 ± 0.02	
05342616-0526304	K7.5	9.07	3910	1				384		0.75 ± 0.15	1.05 ± 0.16	1.89 ± 0.15	4.88 ± 0.16	
05352814-0510138	M0.0	2.98	3770	1						1.04 ± 0.03	1.24 ± 0.03	1.72 ± 0.04		
05350644-0533351	M0.5	0.0	3700	3						3.32 ± 0.03	4.05 ± 0.03	5.16 ± 0.03	9.1 ± 0.03	
05353428-0533215	M1.0	1.97	3630	3						1.47 ± 0.05	1.96 ± 0.05	2.96 ± 0.06		
05345203-0524429	M1.5	0.0	3560	1						1.8 ± 0.04	2.13 ± 0.04	2.89 ± 0.04	5.41 ± 0.07	
05354624-0515398	M2.0	2.78	3490	1						1.12 ± 0.04	1.33 ± 0.04	1.73 ± 0.08		
05362753-0530555	M2.5	0.0	3425	1						0.71 ± 0.02	1.0 ± 0.02	1.67 ± 0.02	3.69 ± 0.03	
05341346-0555417	M3.0	0.01	3360	1						0.75 ± 0.02	0.96 ± 0.02	1.4 ± 0.02	3.54 ± 0.05	
05350196-0441145	M3.0	1.67	3360	1						0.43 ± 0.02	0.53 ± 0.03	1.02 ± 0.06		
05350167-0526363	M3.0	0.0	3360	4						2.91 ± 0.05	3.34 ± 0.06	4.04 ± 0.06		

2MASS	SpT	$A_{\rm V}$	$T_{\rm eff}$(K)	Ref	$L_*/L_\odot$	$M_*/M_\odot$	$R*/R_\odot$	dist(pc)	EW Hα(Å)	$DCE_{J-[4.5]}$	$DCE_{J-[5.8]}$	$DCE_{J-[8.0]}$	$DCE_{J-[24]}$	$\dot{M}(M_\odot yr^{-1})$
05333390-0533264	M3.5	0.11	3260	1						0.88 ± 0.02	1.2 ± 0.02	1.75 ± 0.02	4.37 ± 0.04	
05342541-0456550	M3.5	0.0	3260	1						0.65 ± 0.02	0.86 ± 0.02	1.47 ± 0.02		
05344909-0546050	M3.5	0.0	3260	1						0.71 ± 0.04	1.03 ± 0.04	1.84 ± 0.04	4.12 ± 0.05	
05345072-0458368	M3.5	0.85	3260	1						0.86 ± 0.02	1.1 ± 0.02	1.56 ± 0.02	3.14 ± 0.06	
05345175-0539241	M3.5	0.49	3260	1						0.32 ± 0.02	0.48 ± 0.02	0.75 ± 0.03	3.1 ± 0.05	
05345793-0553216	M3.5	0.14	3260	1						0.11 ± 0.02	0.19 ± 0.03	0.64 ± 0.06	2.51 ± 0.08	
05361493-0515336	M3.5	0.1	3260	1						0.49 ± 0.02	0.67 ± 0.02	0.93 ± 0.03	1.69 ± 0.11	
05360641-0441538	M4.0	0.0	3160	1						0.35 ± 0.21	0.61 ± 0.21	1.56 ± 0.21	4.74 ± 0.22	
05360928-0450008	M4.0	0.0	3160	1						0.68 ± 0.02	0.89 ± 0.02	1.61 ± 0.02	4.0 ± 0.05	
05352232-0533559	M4.0	0.7	3160	4						0.13 ± 0.08	0.23 ± 0.09	0.6 ± 0.09		
05361519-0534030	M4.0	4.26	3160	3						0.23 ± 0.03	0.34 ± 0.03	0.43 ± 0.03	0.38 ± 0.04	
05334765-0525485	M4.5	0.0	3020	1						0.32 ± 0.02	0.65 ± 0.05	1.69 ± 0.05		
05335732-0459157	M4.5	0.78	3020	1						0.55 ± 0.02	1.04 ± 0.03	2.04 ± 0.02	4.62 ± 0.04	
05343396-0548249	M4.5	0.0	3020	1						0.4 ± 0.03	0.75 ± 0.04	1.55 ± 0.05		
05350093-0448188	M4.5	0.3	3020	1						0.58 ± 0.02	0.9 ± 0.03	1.71 ± 0.03	4.04 ± 0.05	
05341867-0537081	M5.0	0.0	2880	1						0.83 ± 0.02	0.99 ± 0.02	1.36 ± 0.04	4.19 ± 0.06	
05345939-0607229	M5.0	0.0	2880	1						0.27 ± 0.02	0.56 ± 0.02	1.29 ± 0.02	4.54 ± 0.04	
05353392-0614327	M5.0	0.0	2880	1						0.51 ± 0.03	0.86 ± 0.03	1.65 ± 0.03	4.27 ± 0.04	
05361723-0617245	M5.0	0.0	2880	1						0.23 ± 0.02	0.4 ± 0.02	1.12 ± 0.02	4.17 ± 0.03	
05352568-0530381	M5.0	2.76	2880	4	0.44			394		0.48 ± 0.06	0.83 ± 0.07	1.49 ± 0.07		
05352720-0530247	M5.0	1.69	2880	4	0.44			415		0.23 ± 0.05	0.58 ± 0.05	1.43 ± 0.05		
05354416-0536397	M5.5	1.05	2740	1						-0.05 ± 0.03	0.22 ± 0.03	0.91 ± 0.03	3.33 ± 0.07	
Taurus														
04205273+1746415	M5.5	0.0	2740	5	0.03			117	-20.7	-0.09 ± 0.03	-0.09 ± 0.04	-0.06 ± 0.04		
04270469+2606163	K6.0	0.0	4020	5		0.72	1.92	121	-42.8					8.02×10^{-9}
04324303+2552311	M1.0	0.0	3630	5		0.41	1.96	131	-70.1					1.51×10^{-8}
04141700+2810578	K3.0	2.36	4550	5	1.03	1.21	1.63	132	-90.7	2.98 ± 0.07	3.32 ± 0.07	3.88 ± 0.07	6.61 ± 0.08	1.15×10^{-8}
04333935+1751523	M0.5	0.0	3700	5	0.15	0.45	0.97	136	-134.4	3.49 ± 0.05	4.05 ± 0.06	4.97 ± 0.06		3.59×10^{-9}
04295156+2606448	M0.5	0.0	3700	5	0.47	0.46	1.68	131	-9.7	2.02 ± 0.08	2.31 ± 0.08	2.87 ± 0.08	5.43 ± 0.09	1.33×10^{-9}
04352020+2232146	M0.5	0.0	3700	5	0.14	0.45	0.90	161	-126.1	1.68 ± 0.08	1.76 ± 0.08	2.4 ± 0.08	5.14 ± 0.09	2.78×10^{-9}
04183112+2816290	M3.5	0.0	3260	5	0.24	0.25	1.56	123	-240.8	2.93 ± 0.05	3.43 ± 0.05	4.22 ± 0.05	6.74 ± 0.06	2.30×10^{-8}
04323058+2419572	K6.0	2.59	4020	5	0.61	0.73	1.61	130	-83.7	1.65 ± 0.04	1.89 ± 0.05	2.38 ± 0.05	4.51 ± 0.05	9.04×10^{-9}
04315056+2424180	M0.5	1.99	3700	5	0.32	0.46	1.38	133	-66.5	1.61 ± 0.03	1.83 ± 0.04	2.35 ± 0.04	6.42 ± 0.05	5.02×10^{-9}
04420777+2523118	K7.0	1.64	3970	5	0.82	0.66	1.92	160	-21.8	1.96 ± 0.19	2.36 ± 0.2	3.08 ± 0.2	5.48 ± 0.21	4.21×10^{-9}
04333678+2609492	M0.0	2.59	3770	5	0.43	0.50	1.54	133	-37.6	1.38 ± 0.04	1.74 ± 0.05	2.64 ± 0.05	4.79 ± 0.05	4.05×10^{-9}
04323176+2420029	M0.0	1.83	3770	5	0.50	0.50	1.65	130	-212.5	2.78 ± 0.04	3.17 ± 0.04	3.93 ± 0.04	6.33 ± 0.05	2.82×10^{-8}
05044139+2509544	M3.5	0.35	3260	5	0.19	0.25	1.37	170	-117.6	0.8 ± 0.06	1.0 ± 0.07	1.65 ± 0.07	4.25 ± 0.08	7.96×10^{-9}
04324911+2253027	K6.0	2.92	4020	5	0.84	0.72	1.89	164	-16.8	1.48 ± 0.04	1.68 ± 0.04	2.69 ± 0.04	5.9 ± 0.05	2.96×10^{-9}
04174965+2829362	M4.0	2.11	3160	5	0.15	0.20	1.31	129	-15.3	1.56 ± 0.1	1.92 ± 0.1	2.84 ± 0.1	5.12 ± 0.11	9.07×10^{-10}

2MASS	SpT	A_V	$T_{\rm eff}$(K)	Ref	$L_*/L_\odot$	$M_*/M_\odot$	$R*/R_\odot$	dist(pc)	EW Hα(Å)	$DCE_{J-[4.5]}$	$DCE_{J-[5.8]}$	$DCE_{J-[8.0]}$	$DCE_{J-[24]}$	$\dot{M}(M_\odot yr^{-1})$
04141760+2806096	M5.5	0.0	2740	5	0.04	0.01	0.93	135	-180.3	2.37 ± 0.03	2.82 ± 0.04	3.78 ± 0.04	6.57 ± 0.05	3.01×10^{-8}
04270280+2542223	M2.0	1.48	3490	5				124	-48.4	1.23 ± 0.07	1.59 ± 0.07	2.15 ± 0.07	4.28 ± 0.08	
04355277+2254231	K3.0	0.0	4550	5	0.99	1.21	1.60	177		2.79 ± 0.1	3.23 ± 0.1	4.13 ± 0.1	7.6 ± 0.11	
04181078+2519574	M1.5	0.0	3560	5	0.13	0.36	0.96	131		2.0 ± 0.04	2.41 ± 0.05	3.36 ± 0.05	5.01 ± 0.05	
05075496+2500156	M3.5	0.31	3260	5	0.11	0.22	1.05	164		0.35 ± 0.03	0.63 ± 0.04	1.43 ± 0.04		
04560118+3026348	M3.5	0.3	3260	5	0.10	0.21	1.03	158		1.09 ± 0.03	1.41 ± 0.04	2.06 ± 0.04	4.07 ± 0.05	
04244457+2610141	M2.5	0.52	3425	5	0.20	0.31	1.29	159		2.13 ± 0.1	2.56 ± 0.11	3.39 ± 0.11	5.83 ± 0.12	
04135737+2918193	M3.0	0.0	3360	5	0.06	0.24	0.75	123		3.1 ± 0.06	3.61 ± 0.07	4.35 ± 0.07	6.85 ± 0.07	
04153916+2818586	M3.7	1.55	3210	5	0.21	0.23	1.50	131		0.58 ± 0.03	0.71 ± 0.04	1.42 ± 0.04	4.48 ± 0.05	
04334171+1750402	M4.0	0.82	3160	5	0.11	0.18	1.11	146		0.09 ± 0.03	0.28 ± 0.04	0.77 ± 0.04		
04554535+3019389	M4.7	0.13	2950	5	0.08	0.10	1.10	154		0.59 ± 0.03	0.79 ± 0.04	1.4 ± 0.04	3.44 ± 0.05	
04193545+2827218	M5.2	0.04	2810	5	0.07	0.05	1.13	119		0.77 ± 0.03	1.31 ± 0.04	2.33 ± 0.04	4.54 ± 0.05	
05052286+2531312	M2.0	0.08	3490	5	0.03	0.28	0.50	171		3.16 ± 0.08	3.73 ± 0.08	4.66 ± 0.08		
04393364+2359212	M5.0	0.0	2880	5	0.04	0.05	0.87	127		1.14 ± 0.03	1.43 ± 0.04	2.35 ± 0.04	4.8 ± 0.05	
04214323+1934133	M0.0	3.26	3770	5	0.73	0.50	2.00	148		2.1 ± 0.03	2.8 ± 0.04	3.99 ± 0.04		
04293606+2435556	M3.0	2.17	3360	5	0.21	0.28	1.35	129		1.39 ± 0.04	1.63 ± 0.05	2.05 ± 0.05	4.71 ± 0.05	
04323028+1731303	M5.5	0.29	2740	5	0.10	0.05	1.45	150		0.84 ± 0.04	1.19 ± 0.04	1.99 ± 0.04		
04322210+1827426	M4.7	0.55	2950	5	0.06	0.09	0.94	141		0.59 ± 0.04	0.7 ± 0.04	1.22 ± 0.04	3.69 ± 0.05	
04322415+2251083	M4.5	1.16	3020	5	0.09	0.13	1.13	155		0.46 ± 0.03	0.73 ± 0.04	1.58 ± 0.04	3.7 ± 0.05	
04321540+2428597	M0.0	2.81	3770	5	0.19	0.50	1.02	130		3.81 ± 0.04	4.13 ± 0.05	4.82 ± 0.05		
04321606+1812464	M6.0	0.5	2600	5	0.1	0.02	1.56	144		0.55 ± 0.03	0.9 ± 0.04	1.61 ± 0.04	3.54 ± 0.05	
04422101+2520343	M4.7	1.28	2950	5	0.09	0.11	1.15	136		0.68 ± 0.03	1.12 ± 0.04	1.98 ± 0.04	5.3 ± 0.05	
04265440+2606510	M2.5	3.07	3425	5	0.31	0.31	1.58	139		1.33 ± 0.03	1.8 ± 0.04	2.59 ± 0.04		
04413882+2556267	M0.0	2.45	3770	5	0.14	0.50	0.90	159		2.66 ± 0.04	3.22 ± 0.04	4.26 ± 0.04	8.19 ± 0.05	
04155799+2746175	M5.5	0.48	2740	5	0.04	0.01	0.98	135		0.9 ± 0.03	1.18 ± 0.04	1.87 ± 0.04	4.2 ± 0.05	
04315968+1821305	M1.5	0.39	3560	5	0.05	0.33	0.59	155		2.88 ± 0.03	3.25 ± 0.04	3.77 ± 0.04	6.39 ± 0.05	
04354093+2411087	M1.0	3.09	3630	5	0.28	0.41	1.35	125		2.09 ± 0.05	2.48 ± 0.06	3.31 ± 0.06	5.45 ± 0.06	
04284263+2714039	M5.2	0.34	2810	5	0.03	0.01	0.77	133		1.26 ± 0.03	1.48 ± 0.04	1.84 ± 0.04	4.18 ± 0.05	
04265732+2606284	M5.0	1.87	2880	5	0.11	0.09	1.33	133		1.27 ± 0.03	1.63 ± 0.04	2.25 ± 0.04	3.95 ± 0.05	
04394488+2601527	M5.0	3.01	2880	5	0.28	0.13	2.14	136		0.48 ± 0.04	0.83 ± 0.04	1.46 ± 0.04	4.34 ± 0.05	
04221675+2654570	M1.5	3.48	3560	5	0.22	0.37	1.24	157		2.43 ± 0.07	2.78 ± 0.07	3.42 ± 0.07	6.09 ± 0.08	
04230607+2801194	M6.0	0.32	2600	5	0.02			133		0.5 ± 0.03	0.73 ± 0.04	1.33 ± 0.04	4.01 ± 0.05	
04400067+2358211	M6.0	0.06	2600	5	0.01			120		0.36 ± 0.03	0.58 ± 0.04	1.24 ± 0.04	4.31 ± 0.06	
04224786+2645530	M1.0	3.39	3630	5	0.22	0.41	1.19	157		2.2 ± 0.1	2.58 ± 0.1	3.42 ± 0.1	6.24 ± 0.11	
04362151+2351165	M5.2	0.22	2810	5	0.01			115		0.33 ± 0.03	0.63 ± 0.04	1.21 ± 0.04	3.69 ± 0.07	
04174955+2813318	M5.0	1.12	2880	5	0.05	0.06	0.94	137		0.03 ± 0.03	0.44 ± 0.04	1.46 ± 0.04	4.09 ± 0.05	
04554969+3019400	M6.0	0.0	2600	5	0.02			156		0.21 ± 0.03	0.38 ± 0.04	0.69 ± 0.04	2.98 ± 0.06	
04161210+2756385	M4.7	1.79	2950	5	0.04	0.08	0.83	137		1.58 ± 0.05	1.82 ± 0.06	2.23 ± 0.06	4.85 ± 0.07	
04324938+2253082	M4.2	2.5	3090	5	0.25	0.19	1.75	164		1.09 ± 0.09	1.44 ± 0.1	2.18 ± 0.09		

2MASS	SpT	$A_{\rm V}$	$T_{\rm eff}$(K)	Ref	$L_*/L_\odot$	$M_*/M_\odot$	$R*/R_\odot$	dist(pc)	EW Hα(Å)	$DCE_{J-[4.5]}$	$DCE_{J-[5.8]}$	$DCE_{J-[8.0]}$	$DCE_{J-[24]}$	$\dot{M}(M_\odot yr^{-1})$
04382134+2609137	M6.0	0.54	2600	5	0.01			138		2.37 ± 0.11	2.64 ± 0.12	3.28 ± 0.12	5.61 ± 0.13	
04143054+2805147	K7.0	4.83	3970	5	1.25	0.65	2.36	242		2.34 ± 0.04	2.85 ± 0.04	4.03 ± 0.04		
04410826+2556074	M3.0	1.31	3360	5	0.01	0.22	0.33	140		3.17 ± 0.04	3.68 ± 0.04	4.49 ± 0.04	7.38 ± 0.05	
04554801+3028050	M5.6	0.68	2712	5	0.02			164		0.59 ± 0.04	0.85 ± 0.04	1.54 ± 0.04	4.28 ± 0.06	
04213459+2701388	M5.5	2.3	2740	5	0.10	0.05	1.44	167		0.35 ± 0.03	0.55 ± 0.04	0.93 ± 0.04	2.49 ± 0.05	
04242646+2649503	M5.7	1.46	2670	5	0.02			155		0.32 ± 0.03	0.58 ± 0.04	1.22 ± 0.04	4.01 ± 0.05	
04202555+2700355	M5.2	2.02	2810	5	0.04	0.02	0.87	170		0.34 ± 0.04	0.53 ± 0.05	1.25 ± 0.05	4.63 ± 0.06	
04163911+2858491	M5.5	2.2	2740	5	0.04	0.01	0.93	160		0.73 ± 0.04	0.91 ± 0.05	1.34 ± 0.05	3.23 ± 0.06	
04295950+2433078	M5.0	3.72	2880	5	0.12	0.09	1.39	131		0.91 ± 0.05	1.09 ± 0.06	1.62 ± 0.06	4.24 ± 0.07	
04262939+2624137	M6.0	0.96	2600	5	0.01			155		0.7 ± 0.04	1.11 ± 0.04	1.92 ± 0.04	4.48 ± 0.05	
04334465+2615005	M4.7	4.3	2950	5	0.26	0.15	1.96	173		1.06 ± 0.05	1.42 ± 0.06	2.08 ± 0.06	4.41 ± 0.07	
04190197+2822332	M5.5	2.9	2740	5	0.07	0.03	1.20	135		0.36 ± 0.04	0.35 ± 0.04	0.41 ± 0.04	0.66 ± 0.07	
04411078+2555116	M5.5	0.8	2740	5	0.01			156		1.38 ± 0.06	1.69 ± 0.07	2.4 ± 0.07	4.82 ± 0.08	
04330945+2246487	M6.0	2.13	2600	5	0.02			149		0.63 ± 0.09	0.81 ± 0.1	1.23 ± 0.1	2.59 ± 0.11	
04184250+2818498	M0.7	6.32	3665	5	0.23	0.43	1.18	125		0.76 ± 0.06	0.85 ± 0.06	1.2 ± 0.06		
04330622+2409339	M2.0	0.36	3490	5						1.27 ± 0.04	1.39 ± 0.05	1.95 ± 0.05	4.49 ± 0.05	
04324282+2552314	M2.0	0.0	3490	5						0.89 ± 0.08	1.17 ± 0.08	1.85 ± 0.08		
04423769+2515374	M0.5	0.0	3700	5						3.14 ± 0.03	3.64 ± 0.04	4.62 ± 0.04	7.98 ± 0.05	
04390525+2337450	K5.0	0.0	4140	5						2.43 ± 0.03	2.8 ± 0.04	3.51 ± 0.04	9.0 ± 0.05	
04392090+2545021	M2.5	2.02	3425	5						2.03 ± 0.04	2.27 ± 0.05	3.04 ± 0.05	5.5 ± 0.05	
04220217+2657304	M0.0	2.62	3770	5						2.72 ± 0.05	3.15 ± 0.05	3.99 ± 0.05	7.66 ± 0.06	
04210934+2750368	M5.2	0.09	2810	5						0.17 ± 0.03	0.27 ± 0.04	0.65 ± 0.04	2.47 ± 0.05	
04265352+2606543	K5.0	4.73	4140	5						2.24 ± 0.03	2.75 ± 0.04	3.56 ± 0.04	6.27 ± 0.05	
04355684+2254360	M3.0	2.18	3360	5						1.27 ± 0.03	1.57 ± 0.04	2.27 ± 0.04	4.79 ± 0.05	
04333905+2227207	M1.7	0.65	3560	5						2.19 ± 0.03	2.32 ± 0.04	2.69 ± 0.04	6.8 ± 0.05	
04221568+2657060	M1.0	1.14	3630	5						2.01 ± 0.03	2.25 ± 0.04	2.73 ± 0.04	8.51 ± 0.05	
04313747+1812244	M0.0	0.0	3770	5						2.41 ± 0.08	2.54 ± 0.09	2.93 ± 0.09	7.42 ± 0.09	
04355949+2238291	M1.0	1.57	3630	5				140		1.47 ± 0.05	2.22 ± 0.05	3.46 ± 0.05	7.59 ± 0.06	
04313613+1813432	K7.5	3.4	3910	5				102		3.27 ± 0.17	3.79 ± 0.17	4.5 ± 0.17	8.19 ± 0.18	
04202144+2813491	M1.0	0.0	3630	5						2.53 ± 0.08	2.69 ± 0.09	3.22 ± 0.09	6.01 ± 0.11	
04292165+2701259	M5.2	4.45	2810	5						0.72 ± 0.03	1.0 ± 0.04	1.67 ± 0.04	4.58 ± 0.05	
04290498+2649073	K5.5	2.95	4080	5						3.72 ± 0.05	4.16 ± 0.05	4.97 ± 0.05	9.42 ± 0.06	
04275730+2619183	M4.5	2.31	3020	5						2.54 ± 0.09	3.24 ± 0.1	4.38 ± 0.09	8.88 ± 0.1	
04355760+2253574	M4.5	1.04	3020	5						1.04 ± 0.1	1.32 ± 0.1	1.46 ± 0.1	6.3 ± 0.11	
04231822+2641156	M3.5	4.4	3260	5						1.24 ± 0.1	1.55 ± 0.1	2.22 ± 0.1	5.5 ± 0.11	
IC 348														
03443798+3203296	K6	1.44	4020	6	0.71	0.72	1.73	321.0		1.38 ± 0.03	1.73 ± 0.04	2.51 ± 0.03	5.09 ± 0.04	
03443845+3207356	K6	2.32	4020	6	1.3	0.70	2.35	341.0		0.49 ± 0.03	1.05 ± 0.03	2.09 ± 0.02	4.79 ± 0.04	
03434461+3208177	M0.75	1.39	3665	6	0.36	0.43	1.50	324.0		0.48 ± 0.03	0.55 ± 0.05	1.07 ± 0.04	5.91 ± 0.04	

2MASS	SpT	$A_{\rm V}$	$T_{\rm eff}$(K)	Ref	$L_*/L_\odot$	$M_*/M_\odot$	$R*/R_\odot$	dist(pc)	EW Hα(Å)	$DCE_{J-[4.5]}$	$DCE_{J-[5.8]}$	$DCE_{J-[8.0]}$	$DCE_{J-[24]}$	$\dot{M}(M_\odot yr^{-1})$
03452046+3206344	M1	2.28	3630	6	0.99	0.41	2.51	309.0		1.32 ± 0.03	1.49 ± 0.05	2.2 ± 0.03	5.43 ± 0.04	
03435890+3211270	M1.75	1.15	3525	6	0.25	0.36	1.36	300.0		1.58 ± 0.05	2.13 ± 0.05	2.72 ± 0.05	6.51 ± 0.05	
03443330+3209396	M2	1.22	3490	6	0.31	0.34	1.53	360.0		0.86 ± 0.05	1.03 ± 0.05	1.13 ± 0.1		
03442972+3210398	K8	2.72	3940	6	0.54	0.65	1.58	299.0		1.05 ± 0.02	1.21 ± 0.04	1.88 ± 0.04	5.84 ± 0.05	
03443788+3208041	K7	2.97	3970	6	0.82	0.66	1.91	317.0		1.48 ± 0.03	1.73 ± 0.03	2.32 ± 0.03	4.88 ± 0.04	
03443854+3208006	M1.25	2.48	3595	6	0.48	0.39	1.80	310.0		0.73 ± 0.02	0.98 ± 0.05	1.78 ± 0.03	5.42 ± 0.04	
03443537+3207362	M0	2.69	3770	6	0.44	0.50	1.56	298.0		0.96 ± 0.05	1.45 ± 0.07	2.14 ± 0.09	4.77 ± 0.04	
03442228+3205427	K8	2.2	3940	6	0.29	0.68	1.15	310.0		1.34 ± 0.03	1.6 ± 0.04	2.65 ± 0.04	6.33 ± 0.04	
03443741+3209009	M1	2.29	3630	6	0.28	0.41	1.35	310.0		0.82 ± 0.05	1.05 ± 0.07	1.99 ± 0.08		
03442232+3212007	M1	2.44	3630	6	0.31	0.41	1.40	328.0		0.74 ± 0.03	1.13 ± 0.05	1.95 ± 0.04	4.43 ± 0.04	
03452514+3209301	M3.75	1.94	3210	6	0.42	0.24	2.09	347.0		0.81 ± 0.03	1.13 ± 0.03	2.19 ± 0.04	5.58 ± 0.04	
03442129+3211563	M2	2.37	3490	6	0.22	0.34	1.30	307.0		0.51 ± 0.04	0.67 ± 0.11	1.65 ± 0.05	4.06 ± 0.04	
03442017+3208565	M2	2.23	3490	6	0.22	0.34	1.29	316.0		0.35 ± 0.02	0.6 ± 0.05	1.23 ± 0.05	3.03 ± 0.05	
03443919+3209448	M2	2.28	3490	6	0.28	0.34	1.46	316.0		0.49 ± 0.04	0.79 ± 0.04	1.51 ± 0.09		
03443979+3218041	M3.75	2.26	3210	6	0.16	0.22	1.29	223.0		0.48 ± 0.02	0.67 ± 0.04	1.24 ± 0.04	3.9 ± 0.04	
03444458+3208125	M2	1.79	3490	6	0.17	0.33	1.14	320.0		1.77 ± 0.04	2.16 ± 0.05	2.89 ± 0.05	4.95 ± 0.06	
03442161+3210376	K7	3.86	3970	6	0.60	0.67	1.64	351.0		1.79 ± 0.06	1.87 ± 0.08	2.35 ± 0.09	5.01 ± 0.07	
03442555+3211307	M0	3.42	3770	6	0.40	0.50	1.49	312.0		1.54 ± 0.05	1.94 ± 0.04	2.84 ± 0.04	6.06 ± 0.04	
03443918+3220089	M4.5	1.9	3020	6	0.26	0.17	1.88	377.0		0.21 ± 0.03	0.39 ± 0.04	0.91 ± 0.04	2.69 ± 0.05	
03442530+3210128	M4.75	0.8	2950	6	0.11	0.11	1.29	320.0		0.75 ± 0.04	1.18 ± 0.05	1.86 ± 0.05	4.29 ± 0.06	
03440678+3207540	M4.25	1.72	3090	6	0.14	0.18	1.31	332.0		0.65 ± 0.04	0.88 ± 0.04	1.59 ± 0.04	4.33 ± 0.04	
03443800+3211370	M4	2.05	3160	6	0.11	0.18	1.12	323.0		0.39 ± 0.07	0.72 ± 0.06	1.4 ± 0.07		
03440750+3204088	M4.75	1.49	2950	6	0.07	0.10	1.07	310.0		0.13 ± 0.03	0.43 ± 0.04	1.01 ± 0.07	4.05 ± 0.05	
03442356+3209338	M5	1.04	2880	6	0.07	0.07	1.10	341.0		0.27 ± 0.04	0.51 ± 0.05	1.0 ± 0.13	5.07 ± 0.08	
03443698+3208342	M4.75	1.7	2950	6	0.11	0.11	1.28	307.0		0.59 ± 0.03	0.81 ± 0.09	1.4 ± 0.15		
03444276+3208337	M4.75	1.54	2950	6	0.08	0.10	1.11	295.0		0.92 ± 0.05	1.15 ± 0.08	1.8 ± 0.13	4.32 ± 0.07	
03442668+3208203	M0.5	2.94	3700	6	0.28	0.46	1.29	353.0		1.7 ± 0.04	1.85 ± 0.05	2.5 ± 0.06	5.61 ± 0.05	
03441022+3207344	M5.75	0.0	2670	6	0.01			322.0		0.9 ± 0.06	1.13 ± 0.07	1.42 ± 0.15		
03443896+3203196	M5	0.51	2880	6	0.02	0.03	0.63	281.0		0.79 ± 0.04	1.12 ± 0.05	1.67 ± 0.08		
03443412+3216357	M4.25	0.59	3090	6	0.03	0.11	0.60	305.0		1.34 ± 0.13	1.44 ± 0.11	2.21 ± 0.08	5.05 ± 0.09	
03435602+3202132	K7	4.83	3970	6	0.81	0.66	1.91	326.0		2.13 ± 0.03	2.45 ± 0.03	3.12 ± 0.03	5.84 ± 0.04	
03443814+3210215	M6	0.0	2600	6	0.02			374.0		0.36 ± 0.09	0.29 ± 0.11	0.72 ± 0.26		
03443134+3210469	M4.25	2.17	3090	6	0.07	0.14	0.95	279.0		1.02 ± 0.04	1.39 ± 0.05	1.96 ± 0.04		
03443568+3203035	M3.25	3.01	3310	6	0.06	0.22	0.8	313.0		1.76 ± 0.03	2.16 ± 0.03	3.0 ± 0.04	5.57 ± 0.05	
03442127+3212372	M4.75	2.06	2950	6	0.07	0.10	1.07	331.0		0.31 ± 0.05	0.45 ± 0.07	0.93 ± 0.08	3.1 ± 0.06	
03442554+3206171	M2.25	3.85	3457	6	0.13	0.31	1.01	223.0		0.5 ± 0.03	0.61 ± 0.14	1.32 ± 0.09	4.65 ± 0.04	
03435526+3207533	M5.75	1.2	2670	6	0.08	0.02	1.33	390.0		0.43 ± 0.04	0.8 ± 0.04	1.61 ± 0.05	3.91 ± 0.04	
03443739+3212241	M2	4.17	3490	6	0.33	0.34	1.58	352.0		0.33 ± 0.05	0.6 ± 0.07	1.5 ± 0.05	5.55 ± 0.05	
03445983+3213319	M4.5	2.61	3020	6	0.08	0.12	1.05	321.0		0.26 ± 0.04	0.46 ± 0.05	1.04 ± 0.08	2.71 ± 0.07	

2MASS	SpT	$A_{\rm V}$	$T_{\rm eff}$(K)	Ref	$L_*/L_\odot$	$M_*/M_\odot$	$R*/R_\odot$	dist(pc)	EW Hα(Å)	$DCE_{J-[4.5]}$	$DCE_{J-[5.8]}$	$DCE_{J-[8.0]}$	$DCE_{J-[24]}$	$\dot{M}(M_\odot yr^{-1})$
03441857+3212530	M2.75	2.01	3392	6	0.06	0.26	0.75	302.0		2.5 ± 0.07	2.88 ± 0.08	3.53 ± 0.09	5.93 ± 0.08	
03441297+3213156	M5.25	1.26	2810	6	0.03	0.01	0.78	364.0		0.44 ± 0.06	0.72 ± 0.08	1.08 ± 0.29		
03444116+3210100	M3	3.26	3360	6	0.1	0.25	0.93	292.0		0.88 ± 0.08	1.13 ± 0.14	1.46 ± 0.14		
03444121+3206271	M5.75	1.15	2670	6	0.05	0.01	1.10	443.0		0.58 ± 0.08	0.93 ± 0.09	1.6 ± 0.2		
03450100+3212222	M5.5	1.76	2740	6	0.03			303.0		0.06 ± 0.08	0.32 ± 0.06	1.25 ± 0.07	3.3 ± 0.09	
03442666+3202363	M5.75	1.12	2670	6	0.02			284.0		0.18 ± 0.05	0.38 ± 0.05	0.86 ± 0.14		
03444464+3207301	M5.25	1.75	2810	6	0.06	0.04	1.06	328.0		0.32 ± 0.04	0.45 ± 0.08	0.69 ± 0.1		
03435987+3204414	M5.75	1.56	2670	6	0.05			367.0		0.28 ± 0.06	0.61 ± 0.08	1.38 ± 0.07	4.61 ± 0.07	
03444173+3212022	M5	3.52	2880	6	0.13	0.10	1.45	288.0		0.26 ± 0.05	0.4 ± 0.06	0.97 ± 0.1	5.37 ± 0.06	
03444522+3210557	M5.75	0.9	2670	6	0.01			253.0		0.61 ± 0.09	0.95 ± 0.13	1.74 ± 0.26		
03445614+3209152	K0	3.2	5030	6				332.0		0.82 ± 0.02	0.84 ± 0.07	1.42 ± 0.1	5.92 ± 0.04	
03444472+3204024	M0.5	2.27	3700	6				563.0		1.3 ± 0.04	1.59 ± 0.04	2.25 ± 0.03	5.13 ± 0.04	
03442851+3159539	M3.5	2.17	3260	6				-1.0		0.25 ± 0.04	0.39 ± 0.05	0.97 ± 0.04	3.41 ± 0.04	
03444024+3209331	M4.5	1.15	3020	6				-1.0		1.06 ± 0.05	1.37 ± 0.13	2.52 ± 0.15		
03441012+3204045	M5.75	1.52	2670	6				-1.0		0.55 ± 0.04	0.86 ± 0.05	1.52 ± 0.07	4.46 ± 0.06	
03442724+3210373	M4.75	2.58	2950	6				-1.0		0.6 ± 0.05	0.77 ± 0.06	1.19 ± 0.08	4.42 ± 0.07	
03442980+3200545	M6	1.85	2600	6				490.0		0.56 ± 0.06	0.99 ± 0.07	1.79 ± 0.06	4.33 ± 0.07	
σ Ori														
05394017-0220480	K5.0	0.0	4140	7	0.73	0.85	1.66	397	-25.9	0.95 ± 0.05	1.09 ± 0.05	1.71 ± 0.05	5.86 ± 0.06	3.05×10^{-9}
05382725-0245096	K6.0	0.0	4020	7	0.46	0.75	1.40	397	-56.9	2.7 ± 0.06	3.03 ± 0.06	3.84 ± 0.06	6.32 ± 0.06	4.00×10^{-9}
05382915-0216156	K6.5	0.0	3995	7	0.63	0.7	1.66	414	-50.5	0.37 ± 0.04	0.48 ± 0.04	1.32 ± 0.04	5.66 ± 0.05	6.18×10^{-9}
05392519-0238220	K7.5	0.0	3910	7	0.76	0.61	1.90	383	-55.2	1.51 ± 0.05	1.77 ± 0.05	2.37 ± 0.05	5.32 ± 0.05	1.10×10^{-8}
05400889-0233336	K7.5	0.0	3910	7	0.70	0.61	1.82	403	-77.7	1.84 ± 0.06	2.19 ± 0.06	3.02 ± 0.06		1.37×10^{-8}
05385831-0216101	M0.0	0.0	3770	7	0.30	0.50	1.29	398	-8.2	1.01 ± 0.04	1.17 ± 0.04	1.28 ± 0.04	4.82 ± 0.04	5.16×10^{-10}
05380674-0230227	M0.0	0.45	3770	7	0.66	0.50	1.91	424	-13.0	1.22 ± 0.06	1.44 ± 0.06	2.22 ± 0.06	5.11 ± 0.06	2.64×10^{-9}
05391151-0231065	M0.0	0.5	3770	7	0.50	0.50	1.67	410	-12.1	1.88 ± 0.05	2.51 ± 0.05	3.68 ± 0.05	6.09 ± 0.05	1.64×10^{-9}
05393938-0217045	M0.0	1.0	3770	7	0.75	0.50	2.03	392	-12.7	1.4 ± 0.08	1.75 ± 0.08	2.2 ± 0.08	4.12 ± 0.08	3.13×10^{-9}
05390458-0241493	M0.0	1.45	3770	7	0.12	0.50	0.83	449	-11.9	1.97 ± 0.06	2.31 ± 0.06	3.02 ± 0.06	5.2 ± 0.06	2.05×10^{-10}
05392935-0227209	M0.0	0.0	3770	7	0.18	0.50	0.99	387	-138.8	1.6 ± 0.04	2.17 ± 0.04	3.05 ± 0.04	6.15 ± 0.04	4.00×10^{-9}
05390136-0218274	M0.5	0.35	3700	7	0.63	0.46	1.94	420	-50.8	2.14 ± 0.04	2.41 ± 0.04	3.09 ± 0.04	5.92 ± 0.04	1.07×10^{-8}
05384746-0235252	M0.5	0.0	3700	7	0.53	0.46	1.77	403	-23.0	0.83 ± 0.08	1.18 ± 0.09	2.06 ± 0.08		3.69×10^{-9}
05384791-0237192	M1.0	0.0	3630	7	0.43	0.41	1.66	418	-11.5	1.57 ± 0.05	2.02 ± 0.05	2.98 ± 0.05	5.03 ± 0.05	1.50×10^{-9}
05384301-0236145	M1.0	0.0	3630	7	0.46	0.41	1.72	411	-17.3	1.08 ± 0.06	1.28 ± 0.07	1.96 ± 0.06	5.04 ± 0.07	2.51×10^{-9}
05381315-0245509	M1.5	0.18	3560	7	0.37	0.38	1.61	397	-120.8	1.32 ± 0.04	1.49 ± 0.04	2.06 ± 0.04	4.85 ± 0.04	1.42×10^{-8}
05384537-0241594	M1.5	0.0	3560	7	0.11	0.35	0.87	212	-15.0	0.67 ± 0.05	0.96 ± 0.05	2.0 ± 0.05	4.6 ± 0.05	3.01×10^{-10}
05373094-0223427	M2.0	0.0	3490	7	0.12	0.32	0.95	366	-112.3	1.53 ± 0.04	1.88 ± 0.05	2.82 ± 0.05	6.12 ± 0.05	2.88×10^{-9}
05382333-0225345	M2.0	0.98	3490	7	0.09	0.31	0.83	377	-74.5	0.79 ± 0.04	1.1 ± 0.04	1.79 ± 0.04	4.31 ± 0.04	1.29×10^{-9}
05380826-0235562	M2.5	0.14	3425	7	0.33	0.31	1.64	396	-20.9	0.55 ± 0.04	0.85 ± 0.04	1.88 ± 0.04	4.74 ± 0.04	2.50×10^{-9}
05390297-0241272	M2.5	0.0	3425	7	0.26	0.31	1.45	410	-47.9	1.36 ± 0.04	1.6 ± 0.04	2.18 ± 0.04	4.65 ± 0.04	4.00×10^{-9}

2MASS	SpT	A_V	T_{eff}(K)	Ref	$L_*/L_\odot$	$M_*/M_\odot$	$R*/R_\odot$	dist(pc)	EW Hα(Å)	$DCE_{J-[4.5]}$	$DCE_{J-[5.8]}$	$DCE_{J-[8.0]}$	$DCE_{J-[24]}$	$\dot{M}(M_\odot yr^{-1})$
05385922-0233514	M2.5	0.3	3425	7	0.17	0.31	1.18	396	-53.0	1.25 ± 0.08	1.58 ± 0.08	2.4 ± 0.08	5.07 ± 0.08	2.45×10^{-9}
05381886-0251388	M2.5	0.48	3425	7	0.19	0.31	1.25	392	-10.7	0.81 ± 0.04	1.19 ± 0.04	1.83 ± 0.04	4.12 ± 0.04	5.69×10^{-10}
05395362-0233426	M2.5	0.0	3425	7	0.16	0.30	1.15	387	-97.5	1.34 ± 0.05	1.56 ± 0.05	2.47 ± 0.05	5.15 ± 0.05	4.14×10^{-9}
05383902-0245321	M2.5	0.24	3425	7	0.19	0.31	1.26	428	-28.2	0.9 ± 0.04	1.21 ± 0.04	1.8 ± 0.04	3.55 ± 0.04	1.53×10^{-9}
05383405-0236375	M3.0	0.52	3360	7	0.39	0.29	1.85	384	-16.6	0.17 ± 0.04	0.25 ± 0.04	0.83 ± 0.04	3.57 ± 0.04	2.77×10^{-9}
05390878-0231115	M3.0	0.0	3360	7	0.09	0.25	0.93	335	-19.8	1.01 ± 0.05	1.07 ± 0.05	1.53 ± 0.05	4.97 ± 0.05	4.78×10^{-10}
05382750-0235041	M3.5	0.35	3260	7	0.18	0.24	1.34	403	-28.4	0.43 ± 0.04	0.86 ± 0.04	1.82 ± 0.04	4.72 ± 0.04	1.80×10^{-9}
05390357-0246269	M3.5	0.0	3260	7	0.13	0.23	1.17	370	-50.2	0.47 ± 0.04	0.75 ± 0.04	1.53 ± 0.04	4.62 ± 0.04	2.22×10^{-9}
05382050-0234089	M4.0	0.96	3160	7	0.17	0.21	1.41	342	-22.0	0.6 ± 0.06	1.04 ± 0.07	2.22 ± 0.06	5.26 ± 0.07	1.56×10^{-9}
05384718-0234368	M4.0	0.0	3160	7	0.19	0.21	1.49	395	-77.8	1.14 ± 0.06	1.36 ± 0.06	2.02 ± 0.06		6.40×10^{-9}
05380107-0245379	M4.5	0.6	3020	7	0.09	0.13	1.10	236	-92.6	1.33 ± 0.04	1.7 ± 0.04	2.35 ± 0.04	4.89 ± 0.04	3.67×10^{-9}
05382543-0242412	M4.5	0.75	3020	7	0.02	0.08	0.52	338	-181.6	1.09 ± 0.05	1.41 ± 0.05	2.05 ± 0.05	4.6 ± 0.06	1.24×10^{-9}
05380552-0235571	M4.5	0.85	3020	7	0.01	0.07	0.45	354	-79.0	0.39 ± 0.08	0.67 ± 0.09	1.41 ± 0.09		3.95×10^{-10}
05400195-0221325	M4.5	0.0	3020	7	0.20	0.16	1.66	372	-31.3	0.76 ± 0.04	0.85 ± 0.04	1.4 ± 0.04	4.63 ± 0.05	3.43×10^{-9}
05375486-0241092	M5.0	0.03	2880	7	0.07	0.07	1.11	393	-24.1	0.42 ± 0.04	0.73 ± 0.04	1.36 ± 0.04	3.54 ± 0.04	1.21×10^{-9}
05390853-0251465	M0.5	0.05	3700	7	0.50	0.46	1.72	429		0.22 ± 0.04	0.26 ± 0.04	0.55 ± 0.04	1.88 ± 0.05	
05384227-0237147	M0.5	0.0	3700	7	0.52	0.46	1.76	406		0.55 ± 0.05	0.92 ± 0.05	1.56 ± 0.05	3.9 ± 0.05	
05384143-0217016	M2.0	0.0	3490	7	0.05	0.29	0.62	296		0.27 ± 0.05	0.32 ± 0.06	0.33 ± 0.06		
05383460-0241087	M2.0	0.7	3490	7	0.16	0.33	1.11	401		0.24 ± 0.04	0.33 ± 0.04	0.93 ± 0.04	3.07 ± 0.04	
05390193-0235029	M3.0	0.19	3360	7	0.02	0.22	0.49	335		2.24 ± 0.05	2.64 ± 0.05	3.4 ± 0.05	6.59 ± 0.05	
05382684-0238460	M3.5	1.66	3260	7	0.06	0.19	0.77	352		0.27 ± 0.05	0.49 ± 0.05	1.2 ± 0.05	3.96 ± 0.05	
05383388-0245078	M4.0	1.17	3160	7	0.04	0.15	0.70	350		0.18 ± 0.05	0.39 ± 0.05	1.24 ± 0.05	3.75 ± 0.05	
05391582-0236507	M4.0	0.22	3160	7	0.10	0.18	1.07	381		0.73 ± 0.04	0.88 ± 0.04	1.31 ± 0.04	3.42 ± 0.04	
05390808-0228447	M4.0	0.06	3160	7	0.06	0.16	0.84	461		0.19 ± 0.04	0.32 ± 0.05	0.36 ± 0.05		
05384053-0233275	M4.0	0.44	3160	7	0.16	0.20	1.33	372		0.28 ± 0.04	0.52 ± 0.04	1.12 ± 0.04	3.87 ± 0.05	
05394944-0223459	M4.0	0.61	3160	7	0.13	0.19	1.21	436		0.16 ± 0.04	0.41 ± 0.04	1.04 ± 0.04	3.23 ± 0.04	
05390387-0220081	M4.5	0.0	3020	7	0.04	0.10	0.78	347		0.52 ± 0.04	0.9 ± 0.04	1.63 ± 0.04	4.0 ± 0.04	
05375559-0233053	M4.5	1.08	3020	7	0.02	0.08	0.57	415		0.37 ± 0.07	0.73 ± 0.07	1.36 ± 0.07	3.74 ± 0.08	
05384386-0237068	M4.5	0.0	3020	7	0.13	0.15	1.36	385		0.69 ± 0.05	0.98 ± 0.05	1.74 ± 0.05	4.5 ± 0.05	
05384970-0234526	M4.5	0.0	3020	7	0.14	0.15	1.39	419		0.35 ± 0.04	0.59 ± 0.04	1.17 ± 0.04	nodata	
05395421-0227326	M4.5	0.18	3020	7	0.08	0.12	1.04	381		0.33 ± 0.05	0.76 ± 0.05	2.13 ± 0.05	6.32 ± 0.05	
05384527-0237292	M4.5	0.11	3020	7	0.09	0.13	1.11	394		1.0 ± 0.07	1.28 ± 0.07	1.75 ± 0.07	3.68 ± 0.09	
05384928-0223575	M4.5	0.43	3020	7	0.04	0.10	0.76	411		0.56 ± 0.04	0.97 ± 0.04	1.42 ± 0.05	3.26 ± 0.05	
05385060-0242429	M4.5	0.76	3020	7	0.07	0.12	0.98	398		0.28 ± 0.05	0.67 ± 0.05	1.35 ± 0.05	3.99 ± 0.05	
05400933-0225067	M5.0	0.12	2880	7	0.10	0.09	1.27	379		0.76 ± 0.04	1.15 ± 0.04	1.94 ± 0.04		
05400525-0230522	M5.0	0.27	2880	7	0.04	0.05	0.84	354		0.48 ± 0.04	0.79 ± 0.04	1.33 ± 0.04		
05375745-0238444	M5.0	0.45	2880	7	0.03	0.04	0.8	374		0.08 ± 0.04	0.22 ± 0.05	0.77 ± 0.05	3.16 ± 0.05	
05385542-0241208	M5.0	0.0	2880	7	0.01	0.01	0.37	351		1.81 ± 0.13	2.14 ± 0.13	3.04 ± 0.13	5.5 ± 0.13	
05382119-0254110	M5.5	0.0	2740	7	0.09	0.05	1.35	344		0.58 ± 0.04	0.82 ± 0.04	1.52 ± 0.04	4.77 ± 0.04	

2MASS	SpT	A_V	$T_{\rm eff}$(K)	Ref	$L_*/L_\odot$	$M_*/M_\odot$	$R*/R_\odot$	dist(pc)	EW Hα(Å)	$DCE_{J-[4.5]}$	$DCE_{J-[5.8]}$	$DCE_{J-[8.0]}$	$DCE_{J-[24]}$	$\dot{M}(M_\odot yr^{-1})$
05384809-0228536	M5.5	0.0	2740	7	0.02			363		0.39 ± 0.05	0.71 ± 0.06	1.53 ± 0.05	4.26 ± 0.06	
05395172-0222472	M5.5	0.0	2740	7	0.17	0.08	1.84	400		0.44 ± 0.04	0.86 ± 0.04	1.66 ± 0.04	3.94 ± 0.04	
05394450-0224432	M6.0	0.0	2600	7	0.04			413		0.38 ± 0.04	0.65 ± 0.04	1.4 ± 0.04	4.3 ± 0.04	
05391308-0237509	M6.0	0.0	2600	7	0.01			338		0.27 ± 0.06	0.47 ± 0.07	1.15 ± 0.07		
05382896-0248473	M6.0	0.0	2600	7	0.02			473		0.56 ± 0.06	0.86 ± 0.07	1.41 ± 0.07	3.67 ± 0.07	
05383157-0235148	K7.5	0.28	3910	7						1.2 ± 0.05	1.56 ± 0.05	2.16 ± 0.05	4.28 ± 0.05	
05380994-0251377	M3.0	0.16	3360	7						0.81 ± 0.04	1.02 ± 0.04	1.67 ± 0.04	4.27 ± 0.04	
05383141-0236338	M3.5	0.0	3260	7						1.14 ± 0.04	1.47 ± 0.04	2.48 ± 0.04	5.21 ± 0.04	
05381319-0226088	M4.0	0.12	3160	7						0.31 ± 0.04	0.57 ± 0.04	1.25 ± 0.04	3.34 ± 0.04	
05382358-0220475	M4.0	1.43	3160	7						0.21 ± 0.04	0.57 ± 0.04	1.43 ± 0.04	3.95 ± 0.04	
05381778-0240500	M5.0	0.03	2880	7						0.41 ± 0.04	0.57 ± 0.04	1.22 ± 0.04	4.09 ± 0.04	
05395645-0238034	M5.0	0.0	2880	7						0.43 ± 0.04	0.77 ± 0.04	1.52 ± 0.04	3.97 ± 0.04	
05400453-0236421	M6.0	0.0	2600	7						0.5 ± 0.08	0.88 ± 0.09	1.55 ± 0.09	4.11 ± 0.1	
05380097-0226079	M2.5	0.28	3425	7	0.14	0.30	1.07	349	-60.9	-0.1 ± 0.04	-0.04 ± 0.04	0.29 ± 0.04	4.67 ± 0.04	2.15×10^{-9}
05392883-0217513	M3.5	0.15	3260	7	0.22	0.25	1.47	408	-14.4	-0.01 ± 0.04	-0.01 ± 0.04	0.01 ± 0.04		1.17×10^{-9}
05392639-0215034	K4.5	0.17	4235	7	0.58	0.96	1.41	401	-16.9					1.22×10^{-9}
05382656-0212174	K6.5	2.12	3995	7	0.69	0.69	1.73	350	-7.8					1.08×10^{-9}
λ Ori														
05334791+1001396	M5.5	0.17	2740	9	0.01			414		0.14 ± 0.06	0.46 ± 0.09	1.1 ± 0.08		
05334992+0950367	M3.0	0.04	3360	9	0.17	0.28	1.22	372		0.18 ± 0.04	0.47 ± 0.04	1.48 ± 0.04	5.14 ± 0.1	
05340393+0952122	M2.5	0.99	3425	9	0.17	0.31	1.18	379		1.06 ± 0.06	1.17 ± 0.06	1.71 ± 0.06	3.96 ± 0.14	
05340495+0957038	K6.4	0.81	4000	9	0.35	0.74	1.24	403		0.78 ± 0.04	1.09 ± 0.05	1.77 ± 0.04	4.33 ± 0.1	
05344621+0955376	M5.5	0.0	2740	9	0.01			384		0.28 ± 0.1	0.42 ± 0.12	1.04 ± 0.11		
05345639+0955045	M4.0	0.0	3160	9	0.23	0.22	1.61	494		0.6 ± 0.04	1.12 ± 0.04	2.04 ± 0.04	4.19 ± 0.14	
05350707+0954014	M4.2	0.0	3104	9	0.03	0.12	0.65	445		0.59 ± 0.04	0.85 ± 0.05	1.54 ± 0.05		
05351112+0957195	M5.0	0.0	2880	9	0.03	0.03	0.70	419		0.62 ± 0.05	0.79 ± 0.06	1.22 ± 0.06	3.62 ± 0.56	
05351818+0952241	M2.0	1.12	3490	9	0.13	0.32	1.01	420		0.32 ± 0.03	0.59 ± 0.04	1.34 ± 0.04	3.91 ± 0.23	
05351913+0954424	M4.0	0.14	3160	9	0.07	0.16	0.88	397		1.0 ± 0.05	1.32 ± 0.05	1.96 ± 0.05	5.18 ± 0.15	
05351991+1002364	M1.0	0.57	3630	9	0.30	0.41	1.38	393		1.55 ± 0.03	1.9 ± 0.03	2.83 ± 0.03	5.32 ± 0.05	
05352151+0953291	M1.9	1.84	3504	9	0.08	0.32	0.79	409		0.33 ± 0.04	0.55 ± 0.05	1.02 ± 0.05	4.28 ± 0.25	
05352440+0953519	M5.5	0.45	2740	9	0.01			292		0.54 ± 0.12	0.92 ± 0.12	1.49 ± 0.12	3.95 ± 0.87	
05352536+1008383	M4.2	0.0	3104	8	0.13	0.18	1.25	276		1.15 ± 0.04	1.62 ± 0.04	2.44 ± 0.04	5.1 ± 0.08	
05352846+1002275	M3.5	0.17	3260	9	0.10	0.21	1.02	363		0.46 ± 0.04	0.79 ± 0.04	1.58 ± 0.04	4.47 ± 0.18	
05352877+0954101	M5.5	0.84	2740	9	0.01			319		0.24 ± 0.06	0.57 ± 0.07	1.3 ± 0.07	4.35 ± 0.28	
05355094+0938567	M4.0	0.57	3160	9	0.08	0.17	0.98	469		0.37 ± 0.04	0.48 ± 0.04	0.91 ± 0.04	3.52 ± 0.46	
05355585+0956217	M2.5	0.25	3425	9	0.15	0.30	1.12	401		0.64 ± 0.03	0.89 ± 0.03	1.46 ± 0.03	3.79 ± 0.2	
05362019+0944018	M0.1	0.0	3756	9	0.38	0.49	1.46	412		0.48 ± 0.05	0.47 ± 0.05	0.47 ± 0.05		
05363861+0935052	M1.9	0.14	3504	9	0.31	0.35	1.51	429		0.31 ± 0.04	0.48 ± 0.04	0.84 ± 0.04	2.74 ± 0.32	
05365533+0946479	M3.0	0.5	3360	9	0.13	0.26	1.06	461		0.44 ± 0.04	0.65 ± 0.05	1.35 ± 0.04	3.66 ± 0.33	

2MASS	SpT	A_V	T_{eff}(K)	Ref	$L_*/L_\odot$	$M_*/M_\odot$	$R*/R_\odot$	dist(pc)	EW Hα(Å)	$DCE_{J-[4.5]}$	$DCE_{J-[5.8]}$	$DCE_{J-[8.0]}$	$DCE_{J-[24]}$	$\dot{M}(M_\odot yr^{-1})$
05341129+0944268	M1.9	0.0	3504	8						-0.5 ± 0.21	0.52 ± 0.31	0.65 ± 0.41		
05360981+0942370	M6.0	0.0	2600	9						0.61 ± 0.09	0.89 ± 0.1	1.2 ± 0.11		
05365617+0931227	M1.5	0.62	3560	9						0.45 ± 0.04	0.73 ± 0.04	1.31 ± 0.04	3.73 ± 0.15	
Ori OB1b														
05371885-0020416	K3.0	0.0	4550	2	0.88	1.19	1.51	425	-22.2	1.47 ± 0.03	1.62 ± 0.03	2.18 ± 0.03	5.94 ± 0.03	2.28×10^{-9}
05333982-0038541	K4.0	0.0	4330	2	0.48	0.98	1.24	347	-13.2	1.96 ± 0.03	2.07 ± 0.03	2.59 ± 0.03	5.54 ± 0.03	7.12×10^{-10}
05292326-0125153	K7.0	0.0	3970	2	0.34	0.70	1.24	360	-96.4	1.88 ± 0.05	2.27 ± 0.05	2.69 ± 0.05	5.74 ± 0.05	4.73×10^{-9}
05320040-0140110	M0.5	0.0	3700	2	0.33	0.46	1.39	416	-54.1	0.97 ± 0.04	1.19 ± 0.04	1.66 ± 0.04	4.64 ± 0.04	4.23×10^{-9}
05353178-0023065	M1.0	0.0	3630	2	0.33	0.41	1.47	333	-28.5	0.82 ± 0.03	1.26 ± 0.03	2.03 ± 0.03	4.37 ± 0.03	2.59×10^{-9}
05322569-0157112	K5.5	0.3	4080	2	0.30	0.80	1.11	413	-16.4	1.39 ± 0.05	1.51 ± 0.06	1.66 ± 0.06	4.54 ± 0.06	5.68×10^{-10}
05330196-0020593	M1.5	0.0	3560	2	0.24	0.37	1.29	314	-37.5	1.5 ± 0.07	1.77 ± 0.07	2.48 ± 0.07	5.1 ± 0.07	2.29×10^{-9}
05341714-0109348	M3.0	0.0	3360	2	0.30	0.29	1.63	412	-27.8	0.88 ± 0.03	1.28 ± 0.03	2.24 ± 0.03	5.37 ± 0.03	3.17×10^{-9}
05320641-0126435	M2.0	0.0	3490	2	0.29	0.34	1.48	469	-20.0	0.37 ± 0.05	0.47 ± 0.06	0.98 ± 0.05	3.54 ± 0.06	1.80×10^{-9}
05352000-0016514	M4.0	0.0	3160	2	0.08	0.17	0.95	327	-89.7	1.43 ± 0.03	1.57 ± 0.03	2.44 ± 0.03	5.71 ± 0.03	2.37×10^{-9}
05372168-0040399	M2.5	0.32	3425	2	0.16	0.30	1.16	368	-22.6	0.05 ± 0.02	0.42 ± 0.03	1.32 ± 0.03	4.32 ± 0.02	9.93×10^{-10}
05300324-0138428	M3.0	0.0	3360	2	0.08	0.25	0.85	369	-19.6	1.4 ± 0.04	1.53 ± 0.04	2.04 ± 0.04	4.62 ± 0.04	3.82×10^{-10}
05352244-0040032	M4.0	0.26	3160	2	0.07	0.17	0.90	305	-20.1	0.74 ± 0.02	0.96 ± 0.03	1.58 ± 0.03	3.75 ± 0.02	4.78×10^{-10}
05345443-0144473	M4.0	0.0	3160	2	0.10	0.18	1.06	412	-32.5	1.24 ± 0.04	1.39 ± 0.05	2.02 ± 0.05	4.72 ± 0.05	1.15×10^{-9}
05331130-0037410	M1.5	1.02	3560	2	0.10	0.35	0.84	302	-139.0	0.77 ± 0.03	0.93 ± 0.03	1.39 ± 0.03	4.13 ± 0.03	2.46×10^{-9}
05333513-0055351	M1.0	1.6	3630	2	0.08	0.38	0.73	324	-37.5	0.93 ± 0.06	1.15 ± 0.07	1.67 ± 0.06	4.08 ± 0.07	4.61×10^{-10}
05331776-0041002	M2.0	0.87	3490	2	0.08	0.31	0.78	415	-54.4	0.92 ± 0.03	1.51 ± 0.04	2.47 ± 0.04	4.6 ± 0.03	7.99×10^{-10}
05342701-0054227	M2.0	1.26	3490	2	0.06	0.30	0.69	372	-17.2	0.6 ± 0.03	0.82 ± 0.03	1.21 ± 0.04	3.08 ± 0.03	1.81×10^{-10}
05333251-0112519	M4.0	1.21	3160	2	0.06	0.16	0.87	386	-32.1	0.43 ± 0.03	0.6 ± 0.04	1.03 ± 0.04	12.25 ± 0.03	6.94×10^{-10}
05322578-0036533	K7.0	0.0	3970	2	0.48	0.68	1.46	338		1.28 ± 0.03	1.51 ± 0.03	2.08 ± 0.03	5.29 ± 0.03	
05333609-0128526	K6.0	0.03	4020	2	0.58	0.73	1.58	504		0.15 ± 0.02	0.22 ± 0.03	0.37 ± 0.03	1.36 ± 0.02	
05330623-0042197	M0.0	0.0	3770	2	0.36	0.51	1.41	334		0.2 ± 0.03	0.37 ± 0.03	0.4 ± 0.03	5.06 ± 0.03	
05322711-0022460	M1.0	0.01	3630	2	0.23	0.41	1.22	367		0.24 ± 0.03	0.25 ± 0.03	0.27 ± 0.03	11.2 ± 0.03	
05300369-0155467	K7.5	0.57	3910	2	0.32	0.64	1.23	350		0.71 ± 0.04	0.74 ± 0.04	2.35 ± 0.04	6.63 ± 0.05	
05321009-0151472	M1.0	0.0	3630	2	0.23	0.41	1.23	426		0.18 ± 0.04	0.26 ± 0.04	0.31 ± 0.05		
05352853-0125314	M3.0	0.0	3360	2	0.23	0.29	1.43	411		0.58 ± 0.03	0.93 ± 0.03	1.85 ± 0.03	4.54 ± 0.03	
05291821-0204066	M4.0	0.09	3160	2	0.13	0.19	1.24	331		0.25 ± 0.05	0.31 ± 0.05	0.45 ± 0.05		
05325538-0132511	M4.0	0.0	3160	2	0.17	0.21	1.39	402		0.69 ± 0.06	0.88 ± 0.06	1.27 ± 0.06	3.01 ± 0.06	
05293881-0119179	M3.0	0.57	3360	2	0.06	0.24	0.74	335		1.1 ± 0.04	1.4 ± 0.05	1.97 ± 0.05	4.34 ± 0.04	
05352787-0127287	M4.0	0.21	3160	2	0.10	0.18	1.06	417		0.56 ± 0.03	0.88 ± 0.03	1.27 ± 0.03	2.74 ± 0.03	
05324371-0158109	M3.0	0.61	3360	2	0.07	0.24	0.82	373		0.15 ± 0.04	0.31 ± 0.05	0.7 ± 0.06	3.51 ± 0.05	
05373190-0019168	M2.5	0.8	3425	2	0.13	0.29	1.05	430		0.45 ± 0.03	0.72 ± 0.03	1.17 ± 0.03	3.07 ± 0.03	
05315008-0134383	M1.0	0.0	3630	2	0.02	0.36	0.38	277		0.3 ± 0.05	0.32 ± 0.06	0.41 ± 0.09		
05324392-0125557	M4.0	0.25	3160	2	0.09	0.17	1.00	453		0.21 ± 0.05	0.26 ± 0.05	0.24 ± 0.06		
05292852-0135076	M4.0	0.53	3160	2	0.04	0.15	0.74	380		0.69 ± 0.05	0.98 ± 0.05	1.47 ± 0.05	3.56 ± 0.05	

2MASS	SpT	$A_{\rm V}$	$T_{\rm eff}$(K)	Ref	$L_*/L_\odot$	$M_*/M_\odot$	$R*/R_\odot$	dist(pc)	EW Hα(Å)	$DCE_{J-[4.5]}$	$DCE_{J-[5.8]}$	$DCE_{J-[8.0]}$	$DCE_{J-[24]}$	$\dot{M}(M_\odot yr^{-1})$
05350457-0118017	M5.0	0.0	2880	2	0.04	0.05	0.87	451		0.57 ± 0.03	0.86 ± 0.04	1.56 ± 0.04	12.78 ± 0.03	
05303517-0204051	M3.0	0.58	3360	2	0.01	0.22	0.30	246		-0.05 ± 0.05	0.34 ± 0.07	0.33 ± 0.15		
05383553-0012214	M5.0	0.7	2880	2	0.16	0.11	1.63	672		0.34 ± 0.05	0.58 ± 0.05	1.23 ± 0.05	3.89 ± 0.05	
05374702-0020073	M2.0	0.46	3490	2						0.9 ± 0.04	1.03 ± 0.04	1.7 ± 0.04	4.56 ± 0.04	
05345956-0018598	M4.0	0.0	3160	2						0.96 ± 0.02	1.24 ± 0.02	1.63 ± 0.02	4.0 ± 0.02	
05301105-0206117	M1.0	0.7	3630	2						1.48 ± 0.06	1.68 ± 0.06	2.45 ± 0.06	5.3 ± 0.07	
05335646-0141061	M5.0	0.0	2880	2						0.05 ± 0.03	0.25 ± 0.03	0.63 ± 0.04	3.23 ± 0.03	
05364781-0147087	M5.0	0.1	2880	2						0.34 ± 0.03	0.6 ± 0.03	1.11 ± 0.03	3.16 ± 0.03	
05290925-0121227	M5.0	0.0	2880	2						0.07 ± 0.04	0.2 ± 0.04	0.51 ± 0.05		
05315249-0145461	M5.0	0.0	2880	2						0.58 ± 0.04	0.8 ± 0.04	1.46 ± 0.04	3.84 ± 0.04	
05300606-0154015	M6.0	0.0	2600	2	0.01			282	-37.5	-0.39 ± 0.13	-0.19 ± 0.06	-0.12 ± 0.08		
05315368-0143430	M3.5	0.45	3260	2	0.14	0.23	1.20	422	-18.3	0.07 ± 0.04	0.05 ± 0.04	0.04 ± 0.05		8.58×10^{-10}
05321831-0141205	M2.0	0.57	3490	2	0.09	0.31	0.82	524	-12.7	-0.09 ± 0.03	-0.11 ± 0.04	-0.22 ± 0.07	12.86 ± 0.03	2.16×10^{-10}
05351095-0114149	M2.5	1.67	3425	2	0.20	0.31	1.28	419	-15.1	-0.26 ± 0.03	-0.23 ± 0.03	-0.16 ± 0.04	11.47 ± 0.02	8.72×10^{-10}
05294048-0124433	M5.0	0.0	2880	2	0.04	0.05	0.82	377	-19.4	-0.01 ± 0.04	0.12 ± 0.05	0.1 ± 0.06		6.18×10^{-10}
05332622-0040443	M2.0	1.73	3490	2	0.11	0.32	0.92	348	-11.7	-0.18 ± 0.03	-0.18 ± 0.03	-0.12 ± 0.04	11.75 ± 0.03	2.70×10^{-10}
05325786-0149058	K6.0	0.02	4020	2	0.39	0.75	1.30	434	-4.6	-0.02 ± 0.02	0.03 ± 0.03	0.06 ± 0.03	11.3 ± 0.02	2.53×10^{-10}
05354830-0035496	M4.0	0.05	3160	2	0.04	0.15	0.73	329	-13.8	-0.03 ± 0.03	-0.05 ± 0.04	-0.2 ± 0.06	12.29 ± 0.03	1.85×10^{-10}
05355310-0141570	M2.0	0.46	3490	2	0.11	0.32	0.91	405	-22.8	-0.06 ± 0.02	-0.06 ± 0.03	-0.03 ± 0.05	12.09 ± 0.02	5.09×10^{-10}
05350220-0109594	M2.5	1.79	3425	2	0.09	0.28	0.89	535	-16.5	-0.2 ± 0.04	-0.24 ± 0.06	-0.05 ± 0.15	12.78 ± 0.04	3.55×10^{-10}
05335019-0042397	M2.0	1.64	3490	2	0.11	0.32	0.93	317	-37.4	-0.19 ± 0.03	-0.18 ± 0.03	-0.13 ± 0.04	11.52 ± 0.03	8.96×10^{-10}
05354979-0057421	M0.0	0.0	3770	2	0.30	0.50	1.28	345	-6.0	0.13 ± 0.02	0.13 ± 0.03	0.16 ± 0.03	10.91 ± 0.02	3.70×10^{-10}
05361263-0141296	M2.0	0.62	3490	2	0.19	0.34	1.19	271	-9.8	-0.03 ± 0.03	-0.04 ± 0.03	-0.03 ± 0.03	10.64 ± 0.03	4.61×10^{-10}
05311643-0156055	M2.0	0.66	3490	2	0.15	0.33	1.08	417	-12.4	-0.05 ± 0.04	-0.12 ± 0.04	0.02 ± 0.05		4.47×10^{-10}
05313701-0130415	M3.0	0.38	3360	2	0.01			252	-14.6	-0.22 ± 0.04	-0.33 ± 0.09	-0.51 ± 0.15	13.68 ± 0.04	
05413956-0147020	K5.0	0.0	4140	2	0.16	0.72	0.78	244	-5.0					7.15×10^{-11}
05373338-0002436	M3.0	0.63	3360	2	0.13	0.26	1.06	446	-16.5					5.72×10^{-10}
05352788+0010250	M3.5	0.0	3260	2	0.06	0.19	0.81	432	-31.3					5.50×10^{-10}
05401513-0057266	M2.0	0.14	3490	2	0.16	0.33	1.10	327	-19.9					7.52×10^{-10}
05294664-0053110	M3.5	0.49	3260	2	0.06	0.19	0.82	360	-12.9					2.37×10^{-10}
05392679-0152420	M1.0	0.35	3630	2	0.20	0.40	1.13	361	-10.0					4.27×10^{-10}
05322299-0108331	M1.5	1.64	3560	2	0.08	0.35	0.78	356	-11.1					1.61×10^{-10}
05350356-0015116	M6.0	0.0	2600	2	0.05			336	-61.1					
05305562-0055399	M3.0	0.39	3360	2	0.30	0.29	1.62	386	-15.7					1.78×10^{-9}
05380288-0142369	M4.0	0.78	3160	2	0.12	0.19	1.16	359	-14.0					6.16×10^{-10}
05375904-0046143	M2.0	0.2	3490	2	0.14	0.33	1.04	408	-9.9					3.24×10^{-10}
05400905-0134086	K7.0	0.35	3970	2	0.14	0.67	0.81	344	-6.2					9.10×10^{-11}
05332514-0056370	M1.5	1.07	3560	2	0.09	0.35	0.81	335	-11.8					1.93×10^{-10}
05344045-0012237	K7.5	0.06	3910	2	0.21	0.65	1.01	435	-5.6					1.59×10^{-10}

2MASS	SpT	A_V	$T_{\rm eff}$(K)	Ref	$L_*/L_\odot$	$M_*/M_\odot$	$R*/R_\odot$	dist(pc)	EW Hα(Å)	$DCE_{J-[4.5]}$	$DCE_{J-[5.8]}$	$DCE_{J-[8.0]}$	$DCE_{J-[24]}$	$\dot{M}(M_\odot yr^{-1})$
05313219-0134554	M3.0	0.81	3360	2	0.02	0.21	0.44	387	-15.9					4.87×10^{-11}
05390429-0038099	M4.0	0.37	3160	2	0.11	0.18	1.12	312	-27.2					1.09×10^{-9}
05392030-0118253	M2.5	0.45	3425	2	0.25	0.31	1.42	422	-21.7					1.68×10^{-9}
05380884-0121008	M6.0	0.0	2600	2	0.04			301	-26.7					
05355169-0009559	M4.5	0.26	3020	2	0.11	0.15	1.26	398	-18.5					9.76×10^{-10}
05334246-0007389	M4.0	0.0	3160	2	0.10	0.18	1.07	443	-17.6					6.34×10^{-10}
05375795-0047236	M0.5	0.0	3700	2	0.04	0.42	0.52	338	-400.0					1.77×10^{-9}
05382417-0132226	M5.0	0.16	2880	2	0.04	0.05	0.83	379	-22.2					7.14×10^{-10}
05373853-0124270	M6.0	0.0	2600	2	0.01			324	-24.8					
05380674-0108178	M5.0	0.18	2880	2	0.02	0.03	0.66	319	-17.4					4.09×10^{-10}
05402414-0031213	M3.0	0.0	3360	2	0.26	0.29	1.53	299	-41.4					3.94×10^{-9}
05365983-0120245	M3.0	0.0	3360	2	0.18	0.28	1.27	443	-54.6					3.01×10^{-9}
05372198-0129140	M6.0	0.0	2600	2	0.03			369	-28.9					
05402461-0152309	K6.0	0.9	4020	2	0.50	0.74	1.46	431	-28.7					2.30×10^{-9}
05390532-0135327	M6.0	0.0	2600	2	0.01			409	-140.4					
05372618-0053510	M1.0	0.0	3630	2	0.28	0.41	1.35	365	-9.1					6.40×10^{-10}
05312062-0049197	K7.0	0.0	3970	2	0.30	0.71	1.16	352	-97.0					3.92×10^{-9}
05413275-0157574	M0.0	0.0	3770	2	0.26	0.50	1.20	365	-25.3					1.29×10^{-9}
05391285-0149266	M2.5	0.32	3425	2	0.01			119	-14.6					
05335871-0107526	M2.0	0.68	3490	2	0.01			230	-55.0					
05414141-0143533	K1.0	3.29	4920	2	5.74			389	-19.9					
Upper Scorpius														
16062277-2011243	M5.0	0.06	2880	10	0.04	0.05	0.84	151		0.16 ± 0.03	0.26 ± 0.04	0.79 ± 0.04	4.04 ± 0.05	
16095933-1800090	M5.0	0.0	2880	10	0.06	0.07	1.05	136		0.37 ± 0.03	0.57 ± 0.04	1.51 ± 0.04	5.24 ± 0.04	
16310240-2408431	M5.0	0.75	2880	10	0.04	0.05	0.86	136		0.76 ± 0.03	0.99 ± 0.04	1.47 ± 0.04	3.75 ± 0.05	
16142029-1906481	M0.0	1.39	3770	10	0.38	0.50	1.45	143		2.72 ± 0.03	3.31 ± 0.04	3.85 ± 0.04	6.89 ± 0.05	
16100541-1919362	M5.75	1.71	2670	10	0.01			149		0.71 ± 0.03	0.98 ± 0.04	1.55 ± 0.05	3.6 ± 0.05	
16305349-2424538	M5.5	1.34	2740	10	0.05	0.01	0.99	156		0.41 ± 0.03	0.68 ± 0.04	1.35 ± 0.04	3.79 ± 0.05	
16044068-1946538	M5.5	0.32	2740	10	0.01			157		0.4 ± 0.03	0.58 ± 0.04	1.15 ± 0.04	3.69 ± 0.06	
16302673-2359087	M6.0	1.07	2600	10	0.02			137		0.45 ± 0.03	0.69 ± 0.04	1.55 ± 0.04	4.65 ± 0.05	
16303390-2428062	M4.0	1.94	3160	10	0.11	0.18	1.13	150		0.32 ± 0.03	0.5 ± 0.04	1.15 ± 0.04	3.56 ± 0.05	
16130996-1904269	M4.0	0.91	3160	10	0.06	0.16	0.85	137		0.65 ± 0.03	0.86 ± 0.04	1.52 ± 0.04	4.07 ± 0.05	
16324727-2059375	M6.0	0.34	2600	10	0.01			137		0.33 ± 0.03	0.57 ± 0.04	1.02 ± 0.04	4.28 ± 0.05	
16061144-1935405	M5.0	0.0	2880	10	0.01	0.01	0.49	139		0.91 ± 0.04	1.08 ± 0.05	1.75 ± 0.05	3.84 ± 0.05	
16053215-1933159	M4.75	0.28	2950	10	0.02	0.06	0.66	154		0.89 ± 0.04	1.09 ± 0.05	1.57 ± 0.04	2.89 ± 0.05	
16130235-1904450	M6.0	0.76	2600	10	0.01			185		0.69 ± 0.04	0.97 ± 0.05	1.45 ± 0.05	3.83 ± 0.06	
16101888-2502325	M4.5	0.43	3020	10	0.04	0.10	0.79	155		0.22 ± 0.07	0.45 ± 0.08	0.9 ± 0.08	3.78 ± 0.08	
16103876-1829235	M6.0	0.83	2600	10	0.01			176		0.6 ± 0.05	0.9 ± 0.05	1.45 ± 0.05	4.19 ± 0.08	
16284703-2428138	M6.0	0.0	2600	10	0.01			140		1.12 ± 0.05	1.45 ± 0.06	2.03 ± 0.06	4.13 ± 0.08	

2MASS	SpT	$A_{\rm V}$	$T_{\rm eff}$(K)	Ref	$L_*/L_\odot$	$M_*/M_\odot$	$R*/R_\odot$	dist(pc)	EW Hα(Å)	$DCE_{J-[4.5]}$	$DCE_{J-[5.8]}$	$DCE_{J-[8.0]}$	$DCE_{J-[24]}$	$\dot{M}(M_\odot yr^{-1})$
16263026-2336551	M6.0	1.22	2600	10	0.01			150		1.15 ± 0.08	1.39 ± 0.09	2.0 ± 0.09	4.9 ± 0.1	
16025396-2022480	K6.0	0.09	4020	10						0.32 ± 0.04	0.36 ± 0.04	0.37 ± 0.04	0.38 ± 0.06	
γ Vel														
08074647-4711495	M3.3	0.72	3299	11	0.09	0.23	0.94	394		0.72 ± 0.04	0.99 ± 0.04	1.42 ± 0.04	3.23 ± 0.42	
08082235-4710594	K2.3	1.48	4692	11	0.54	0.95	1.11	381		2.56 ± 0.04	2.69 ± 0.04	3.03 ± 0.04	5.59 ± 0.05	
08105600-4740068	M3.5	0.18	3259	11	0.07	0.2	0.85	386		0.88 ± 0.06	1.08 ± 0.06	1.49 ± 0.06	3.56 ± 0.36	
08074305-4711070	K7.7	0.96	3864	11	0.24	0.59	1.10	376		0.29 ± 0.08	0.28 ± 0.08	0.33 ± 0.08		
08112956-4705036	M2.2	0.12	3455	12	0.37	0.33	1.71	469		0.15 ± 0.04	0.23 ± 0.04	0.54 ± 0.04	2.45 ± 0.34	
08075546-4707460	K3.8	0.08	4363	11	0.79	1.09	1.55	367		1.29 ± 0.04	1.4 ± 0.04	1.79 ± 0.04	5.8 ± 0.06	
08093962-4731102	M3.6	0.81	3244	12	0.05	0.18	0.74	380		0.58 ± 0.05	0.74 ± 0.05	1.12 ± 0.05	3.07 ± 0.63	
08101747-4746136	M3.5	0.82	3260	12	0.07	0.19	0.83	361		0.21 ± 0.04	0.46 ± 0.05	1.0 ± 0.05	3.45 ± 0.23	
08084685-4726446	M3.2	0.63	3324	12	0.02	0.2	0.44	355		0.68 ± 0.05	0.98 ± 0.06	1.42 ± 0.06		
08093328-4739158	M3.7	1.44	3213	12	0.04	0.17	0.71	363		1.04 ± 0.05	1.27 ± 0.06	2.05 ± 0.06	5.07 ± 0.15	
08081914-4714320	M3.8	1.74	3203	12	0.03	0.16	0.64	405		0.02 ± 0.06	0.22 ± 0.09	0.45 ± 0.08		
08100280-4736371	M3.4	0.81	3290	11						0.61 ± 0.04	0.79 ± 0.04	1.13 ± 0.04	4.02 ± 0.22	
08091914-4713570	M3.8	1.31	3211	12						0.39 ± 0.04	0.62 ± 0.05	0.83 ± 0.05	2.5 ± 0.54	
08095790-4721171	M3.8	1.69	3203	12						0.17 ± 0.04	0.54 ± 0.05	1.25 ± 0.04	3.26 ± 0.43	
Ori OB1a														
05253749+0225131	M1.0	1.93	3630	2	0.03	0.37	0.49	359	-7.5	-0.15 ± 0.06	-0.14 ± 0.07	-0.42 ± 0.13	13.14 ± 0.06	2.93×10^{-11}
05252692+0214523	M1.5	1.98	3560	2	0.06	0.34	0.67	386	-13.6	-0.23 ± 0.04	-0.22 ± 0.05	-0.12 ± 0.07	12.66 ± 0.04	1.27×10^{-10}
05291973+0202394	M2.0	2.17	3490	2	0.09	0.31	0.83	372	-9.2	-0.36 ± 0.03	-0.28 ± 0.04	-0.46 ± 0.07	12.12 ± 0.03	1.60×10^{-10}
05251161+0140556	M2.0	1.83	3490	2	0.03	0.28	0.48	330	-11.8	-0.25 ± 0.06	-0.29 ± 0.08	-0.26 ± 0.1		4.38×10^{-11}
05240687+0137001	M2.5	0.36	3425	2	0.10	0.28	0.93	352	-23.3	-0.09 ± 0.04	-0.19 ± 0.05	-0.02 ± 0.05		5.64×10^{-10}
05250755+0134243	M3.0	0.25	3360	2	0.24	0.29	1.44	349	-11.4	-0.13 ± 0.04	0.03 ± 0.04	-0.02 ± 0.04		9.20×10^{-10}
05290186+0142569	M3.5	1.45	3260	2	0.05	0.19	0.70	349	-12.7	-0.26 ± 0.04	-0.28 ± 0.05	-0.29 ± 0.08	12.45 ± 0.04	1.51×10^{-10}
05272108+0215508	M4.0	0.98	3160	2	0.02	0.14	0.57	334	-14.6	-0.16 ± 0.04	-0.13 ± 0.06	-0.17 ± 0.07	12.86 ± 0.04	1.03×10^{-10}
05224654+0134010	M5.0	0.0	2880	2	0.07	0.07	1.12	432	-24.9	-0.22 ± 0.13	0.1 ± 0.05	-0.09 ± 0.05		1.26×10^{-9}
05234784+0138147	M5.0	0.22	2880	2	0.02	0.03	0.68	344	-30.6	-0.2 ± 0.04	0.04 ± 0.05	-0.12 ± 0.08	12.73 ± 0.04	7.39×10^{-10}
05252432+0141073	M5.0	0.24	2880	2	0.08	0.08	1.17	467	-17.0	0.05 ± 0.03	0.12 ± 0.03	0.57 ± 0.04	2.71 ± 0.05	9.37×10^{-10}
05260874-0012574	K0.0	1.79	5030	2	0.42	0.96	0.85	374	-3.4					1.33×10^{-10}
05282697+0048477	K0.0	1.57	5030	2	0.54	0.96	0.97	416	-2.8					1.61×10^{-10}
05273518-0045235	K5.0	0.42	4140	2	0.71	0.86	1.63	335	-20.4					2.29×10^{-9}
05264210-0041088	K6.0	0.0	4020	2	0.64	0.72	1.65	575	-29.9					3.51×10^{-9}
05270686+0327026	M0.0	0.1	3770	2	0.07	0.49	0.65	340	-12.7					1.07×10^{-10}
05264162-0040524	M0.0	0.0	3770	2	0.33	0.50	1.36	422	-10.4					7.57×10^{-10}
05085773-0129161	M0.0	0.15	3770	2	0.25	0.50	1.18	342	-9.8					4.75×10^{-10}
05215741+0011423	M0.0	0.0	3770	2	0.18	0.50	0.99	356	-45.8					1.30×10^{-9}
05290146-0011297	M0.5	0.0	3700	2	0.26	0.46	1.26	351	-7.5					4.35×10^{-10}
05311909+0241562	M1.0	0.09	3630	2	0.21	0.41	1.18	425	-7.8					3.72×10^{-10}

2MASS	SpT	$A_{\rm V}$	$T_{\rm eff}$(K)	Ref	$L_*/L_\odot$	$M_*/M_\odot$	$R*/R_\odot$	dist(pc)	EW Hα(Å)	$DCE_{J-[4.5]}$	$DCE_{J-[5.8]}$	$DCE_{J-[8.0]}$	$DCE_{J-[24]}$	$\dot{M}(M_\odot yr^{-1})$
05415920+0103361	M1.0	0.0	3630	2	0.30	0.41	1.40	405	-20.5					1.63×10^{-9}
05290068+0230291	M1.5	2.21	3560	2	0.02	0.32	0.42	276	-16.1					4.05×10^{-11}
05353482+0227081	M1.5	0.0	3560	2	0.18	0.37	1.12	353	-23.6					9.54×10^{-10}
05400668+0103099	M1.5	0.0	3560	2	0.16	0.36	1.08	338	-86.5					3.15×10^{-9}
05283691+0331344	M2.0	0.24	3490	2	0.12	0.32	0.95	327	-9.1					2.30×10^{-10}
05271385+0346412	M2.0	0.42	3490	2	0.27	0.34	1.44	357	-9.9					8.14×10^{-10}
05141199-0158203	M2.0	0.64	3490	2	0.14	0.33	1.04	357	-10.0					3.23×10^{-10}
05234426+0242432	M2.0	1.24	3490	2	0.06	0.30	0.68	275	-23.8					2.36×10^{-10}
05245740+0028228	M2.0	0.0	3490	2	0.20	0.34	1.24	440	-85.6					4.56×10^{-9}
05270157+0231502	M2.0	1.17	3490	2	0.03	0.28	0.52	365	-20.3					9.48×10^{-11}
05293176+0251217	M2.0	0.95	3490	2	0.11	0.32	0.92	279	-23.0					5.34×10^{-10}
05311793+0252399	M2.0	0.69	3490	2	0.26	0.34	1.41	339	-9.5					7.38×10^{-10}
05175536-0039127	M2.5	0.06	3425	2	0.11	0.29	0.97	343	-16.3					4.39×10^{-10}
05272190+0235360	M2.5	0.74	3425	2	0.15	0.30	1.10	347	-12.1					4.63×10^{-10}
05291517+0222133	M2.5	1.67	3425	2	0.03	0.25	0.52	292	-10.9					5.33×10^{-11}
05273272+0324221	M3.0	0.95	3360	2	0.04	0.23	0.61	336	-14.9					1.14×10^{-10}
05182514-0020031	M3.0	1.5	3360	2	0.02	0.22	0.49	366	-11.2					4.75×10^{-11}
05232173-0147590	M3.0	0.67	3360	2	0.07	0.24	0.81	347	-16.0					2.66×10^{-10}
05280762+0231510	M3.0	0.79	3360	2	0.03	0.22	0.53	351	-31.2					1.66×10^{-10}
05315820+0139383	M3.0	0.27	3360	2	0.04	0.23	0.62	406	-73.5					5.85×10^{-10}
05322510+0320168	M3.0	0.0	3360	2	0.13	0.27	1.08	392	-28.6					1.03×10^{-9}
05231552+0121144	M3.0	0.58	3360	2	0.08	0.25	0.84	357	-12.0					2.20×10^{-10}
05243343+0122433	M3.0	1.49	3360	2	0.04	0.23	0.64	334	-125.0					1.08×10^{-9}
05203346-0015001	M3.5	0.22	3260	2	0.09	0.21	0.98	364	-14.9					4.30×10^{-10}
05254150+0239360	M3.5	1.11	3260	2	0.06	0.19	0.82	426	-12.5					2.28×10^{-10}
05260421-0002210	M3.5	0.77	3260	2	0.05	0.19	0.75	393	-51.9					7.54×10^{-10}
05291980+0217491	M3.5	1.46	3260	2	0.03	0.18	0.57	326	-16.8					1.09×10^{-10}
05274248+0343365	M4.0	1.44	3160	2	0.04	0.15	0.69	324	-14.0					1.65×10^{-10}
05284727+0334339	M4.0	0.99	3160	2	0.03	0.14	0.64	349	-23.6					2.31×10^{-10}
05204275-0043096	M4.0	0.11	3160	2	0.03	0.14	0.62	234	-172.1					1.56×10^{-9}
05351109+0228236	M4.0	0.0	3160	2	0.09	0.18	1.02	265	-22.6					7.34×10^{-10}
05392095+0201036	M4.0	0.23	3160	2	0.01	0.13	0.45	338	-269.6					9.56×10^{-10}
05240726+0115243	M4.0	1.13	3160	2	0.01	0.13	0.31	336	-41.4					5.24×10^{-11}
05290244+0321431	M4.5	0.12	3020	2	0.09	0.13	1.1	386	-42.7					1.67×10^{-9}
05270654-0155307	M4.5	0.0	3020	2	0.06	0.12	0.96	377	-38.8					1.12×10^{-9}
05291313+0056548	M4.5	0.45	3020	2	0.02	0.08	0.61	311	-19.8					1.98×10^{-10}
05302559+0331495	M5.0	0.02	2880	2	0.06	0.06	1.00	415	-18.0					7.62×10^{-10}
05144389-0046094	M5.0	0.16	2880	2	0.16	0.11	1.61	475	-41.7					4.36×10^{-9}
05201555-0019222	M5.0	0.17	2880	2	0.01	0.01	0.49	347	-53.4					9.75×10^{-10}

2MASS	SpT	A_V	$T_{\rm eff}$(K)	Ref	$L_*/L_\odot$	$M_*/M_\odot$	$R*/R_\odot$	dist(pc)	EW Hα(Å)	$DCE_{J-[4.5]}$	$DCE_{J-[5.8]}$	$DCE_{J-[8.0]}$	$DCE_{J-[24]}$	$\dot{M}(M_\odot yr^{-1})$
05202479-0014201	M5.0	0.3	2880	2	0.03	0.04	0.78	277	-22.3					6.55×10^{-10}
05205259-0116447	M5.0	0.0	2880	2	0.04	0.05	0.86	299	-31.2					1.04×10^{-9}
05250571-0030306	M5.0	0.15	2880	2	0.01	0.01	0.48	278	-18.4					3.38×10^{-10}
05252455-0046543	M5.0	0.0	2880	2	0.04	0.05	0.85	294	-31.0					1.03×10^{-9}
05264990-0152393	M5.0	0.0	2880	2	0.08	0.08	1.19	273	-18.5					1.05×10^{-9}
05300605+0033270	M5.0	0.51	2880	2	0.03	0.04	0.78	462	-18.0					5.35×10^{-10}
05370238+0253001	M5.0	0.31	2880	2	0.01	0.01	0.45	300	-26.8					4.81×10^{-10}
05392451+0214299	M5.0	0.25	2880	2	0.04	0.04	0.81	431	-25.8					8.02×10^{-10}
05215430-0007324	M5.5	0.12	2740	2	0.01			369	-23.6					
05255402+0158277	M6.0	0.0	2600	2	0.03			278	-22.4					
05211183-0039035	M6.0	0.0	2600	2	0.03			398	-21.5					
05292893+0114203	M6.0	0.0	2600	2	0.02			355	-25.0					
05375267+0144342	M6.0	0.0	2600	2	0.02			416	-27.5					
05244103+0154386	K5.0	0.71	4140	2	0.25	0.79	0.98	341	-53.5	2.46 ± 0.06	2.7 ± 0.06	3.43 ± 0.06	6.21 ± 0.06	1.40×10^{-9}
05303164+0203051	K7.0	0.0	3970	2	0.40	0.69	1.34	378	-46.5	1.42 ± 0.02	1.63 ± 0.03	2.41 ± 0.03	5.5 ± 0.03	2.97×10^{-9}
05301240+0148214	M2.0	0.0	3490	2	0.06	0.30	0.69	357	-83.9	1.44 ± 0.03	1.71 ± 0.03	2.17 ± 0.03	4.65 ± 0.03	8.72×10^{-10}
05254675+0143303	M3.0	0.34	3360	2	0.10	0.25	0.94	349	-20.3	0.1 ± 0.04	0.27 ± 0.04	0.91 ± 0.04	4.97 ± 0.04	5.10×10^{-10}
05293913+0149156	M2.5	0.78	3425	2	0.07	0.27	0.77	356	-10.9	0.97 ± 0.03	1.26 ± 0.03	1.77 ± 0.03	3.64 ± 0.03	1.57×10^{-10}
05292420+0144547	M3.0	0.12	3360	2	0.02	0.22	0.50	346	-11.9	0.45 ± 0.07	0.78 ± 0.08	1.3 ± 0.08	4.16 ± 0.08	5.19×10^{-11}
05294592+0157317	M5.0	0.0	2880	2	0.04	0.04	0.80	360	-17.7	0.2 ± 0.03	0.45 ± 0.04	1.0 ± 0.04	3.52 ± 0.03	5.36×10^{-10}
05254735+0148320	M4.0	0.86	3160	2	0.03	0.15	0.66	330	-37.6	1.17 ± 0.05	1.43 ± 0.05	1.85 ± 0.05	3.72 ± 0.05	3.91×10^{-10}
05255358+0148033	M6.0	0.0	2600	2	0.02			346	-103.2	0.36 ± 0.05	0.77 ± 0.05	1.35 ± 0.05	3.64 ± 0.05	
05232497+0146085	M2.5	1.88	3425	2	0.03	0.25	0.54	345	-20.4	0.51 ± 0.04	0.74 ± 0.05	1.26 ± 0.05	3.48 ± 0.06	1.06×10^{-10}
05265040+0155037	M2.0	0.0	3490	2	0.16	0.33	1.11	360		0.28 ± 0.06	0.32 ± 0.06	0.28 ± 0.06		
05245885+0125183	M5.0	0.12	2880	2	0.03	0.03	0.70	326		0.1 ± 0.04	0.32 ± 0.05	0.89 ± 0.05	3.35 ± 0.05	
05303829+0146194	M3.0	0.76	3360	2						0.84 ± 0.05	1.05 ± 0.05	1.53 ± 0.06	3.48 ± 0.05	

The errors associated to the DCEs are based only on the photometric errors and thus they are underestimated. References for spectral types (column 5): 1. Hernández et al. (2020a in prep.), 2. Briceño et al. (2019), 3. Hillenbrand (1997), 4. Hillenbrand et al. (2013), 5. Esplin et al. (2014), 6. Lada et al. (2006), 7. Hernández et al. (2014), 8. Bayo et al. (2008), 9. Bayo et al. (2011), 10. Luhman & Mamajek (2012), 11. Spina et al. (2014), 12. This work. The data for the EW Hα comes from: Hernández et al. (2020a in prep.) (ONC), this work (Taurus), Hernández et al. (2014) (σ Ori), and Briceño et al. (2019) (Ori OB1b and Ori OB1a). The extinction A_V, the stellar properties: luminosity L_*, mass M_*, and radius R_*, as well as the color excesses and mass accretion rates $\dot{M}$ are calculated in this work. The distance was obtained here using GAIA DR2 data.

Bibliography

Alcalá, J. M., Natta, A., Manara, C. F., et al. 2014, A&A, 561, A2

Alexander, R. D. & Armitage, P. J. 2007, MNRAS, 375, 500

Alexander, R.; Pascucci, I.; Andrews, S.; et al. Protostars and Planets VI Publisher: University of Arizona press and LPI, 2014. Edited by Henrik Beuther, Ralf S. Klessen, Cornelis P. Dullemond and Thomas Henning.

Ali-Dib, M.; Mousis, O.; Petit, J. M.; Lunine, J. I. 2014, ApJ, 785, 125

ALMA partnership 2015, ApJ, 406, 122

Andre, P., Ward-Thompson, D., & Barsony, M., 1993, ApJ, 820, 40

Protostars and Planets VI. The University of Arizona Press. Edited by Henrik Beuther, Ralf D. Klessen, Cornelis P. Dullemond & Thomas Henning . 2014.

Andrews, S. M. & Williams, J. P. 2005, ApJ, 631, 1134

Andrews, S. M.; Wilner, D. J.; Zhu, Z.; et al. 2016, ApJ, 820, 40

Andrews, Sean M.; Huang, Jane; Pérez, Laura M; et al. 2018, ApJ, 869, 41

Armitage, P. J. Astrophysics of Planet Formation, First Edition. Cambridge University Press, 2010.

Avenhaus, H.; Quanz, S.; Garufi, A.; et al. 2018, ApJ, 863, 44

Bailer-Jones, C. A. L. 2015, PASP, 127, 994

Balbus, S. S., & Hawley, J. F. 1991, ApJ, 374, 214

Baraffe, I.; Chabrier, G.; Allard, F., & Hauschildt, P. H., 1998, A&A, 337, 403

Barrado y Navascués, D., & Martín, E. L. 2003, AJ, 126, 2997

Bayo, A., Rodrigo, C., Barrado Y Navascués, D., et al. 2008, A&A, 492, 277

Bayo, A.; Barrado, D.; Stauffer, J.; et al. 2011, A&A, 536, 63

Birnstiel, T.; Dullemond, C. P.; Brauer, F. 2009, A&A, 503, 5

Birnstiel, T.; Dullemond, C. P. & Brauer, F. 2010, A&A, 513, 79

Birnstiel, T.; Ormel, C. W.; Dullemond, C. P. 2011, A&A, 525, 11

Birnstiel, T.; Klahr, H.; Ercolano, B. 2012, A&A, 539, 148

Bitsch, B., Johansen, A., Lambrechts, M., et al. 2015, , 575, A28

Brauer, F., Dullemond, C. P., Johansen, A., et al. 2007, , 469, 1169

Briceño, C., Hartmann, L. W., Stauffer, J. R., et al. 1997, AJ, 113, 740

Briceño, C.; Calvet, N.; Hernández, J.; et al. 2019, AJ, 157, 85

Cabrera, J., Csizmadia, S., Lehmann, H., et al. 2014, ApJ, 781, 18

Calvet, N.; Patino, A.; Magris, G. C.; D'Alessio, P. 1991, ApJ, 380, 617

Calvet, N.; D'Alessio, P.; Hartmann, L.; Wilner, D.; Walsh, A.; Sitko, M. 2002, ApJ, 568, 1008

Calvet, N.; D'Alessio, P.; Watson, D. M.; Franco-Hernández, R.; Furlan, E., et al. 2005, ApJ, 630, 185

Physical Processes in Circumstellar Disks Around Young Stars. University of Chicago Press. Edited by Paulo J. V. García. 2011.

Calvet, N.; Gullbring, E. 1998, ApJ, 509, 802

Cardelli, J. A.; Clayton, G. C.; Mathis, John S. 1989, ApJ, 345, 245

Carrasco-González, C., Henning, T., Chandler, C. J., et al. 2016, ApJL, 821, L16

Carrasco-González, C., Sierra, A., Flock, M., et al. 2019, ApJ, 883, 71

Chambers, K. C., Magnier, E. A., Metcalfe, N., et al. 2016, arXiv e-prints, arXiv:1612.05560

Chiang, E.; Murray-Clay, R. 2007, Nature, 3, 604

Cieza, L.; Padgett, D. L.; Stapelfeldt, K. R., et al. 2007, ApJ, 667, 308

Cieza, L., Williams, J., Kourkchi, E., et al. 2015, MNRAS, 454, 1909

Cieza, L. A., Casassus, S., Tobin, J., et al. 2016, , 535, 258

Clarke, C. J.; Gendrin, A.; Sotomayor, M. 2001, MNRAS, 328, 485

Allen's astrophysical quantities, 4th ed. Publisher: New York: AIP Press; Springer, 2000. Edited by Arthur N. Cox. Handbook of Star Forming Regions, Volume II: The Southern Sky ASP Monograph Publications, Vol. 5. Edited by Bo Reipurth

Currie, T.; Lada, C. J.; Plavchan, P.; Robitaille, T. P.; Irwin, J.; Kenyon, S. J. 2009, ApJ, 698, 1

Cutri, R. M., Skrutskie, M. F., van Dyk, S., et al. 2003, VizieR Online Data Catalog, 2246.

D'Alessio, P.; Ph.D thesis 1996, Universidad Nacional Autónoma de México

D'Alessio, P.; Cantó, J.; Calvet, N.; Lizano, S. 1998, ApJ, 500, 411

D'Alessio, P.; Calvet, N.; Hartmann, L.; Lizano, S.; Cantó, J., 1999, , 527, 893

D’Alessio, P.; Calvet, N.; Hartmann, L. 2001, ApJ, 553, 321

D’Alessio, P.; Hartmann, L.; Calvet, N.; Franco-Hernández, R.; et al. 2005, , 621, 461

D’Alessio, P.; Calvet, N.; Hartmann, L.; Franco-Hernández, R.; Servín, H. 2006, ApJ, 638, 314

David, T. J.; Hillenbrand, L. A.; Gillen, E.; Cody, A. M.; et al. 2019, ApJ, 872, 161

Da Rio, N., Robberto, M., Soderblom, D. R., et al. 2010, ApJ, 722, 1092

Draine, B. T.; Lee, H. M. 1884, ApJ, 285, 89

Drążkowska, J. & Alibert, Y. 2017, A&A, 608, 92

Dullemond, C. P.; Dominik, C. 2004, ARAA, 48, 205

Dullemond, C. P.; Dominik, C. 2005, A&A, 434, 971

Dullemond, C. P.; Monnier, J. D. 2010, ARA&A, 48, 205

Dutrey, A., Semenov, D., Chapillon, E., et al. 2014, Protostars and Planets VI, 317

Ercolano, B.; Koepferl, C.; Owen, J.; Robitaille, T. 2015, MNRAS, 452, 3689

Espaillat, C.; Calvet, N.; D’Alessio, P.; Hernández, J.; Qi, C.; Hartmann, L.; Furlan, E.; Watson, D. M. 2007, ApJ, 670, 135

Espaillat, C.; D’Alessio, P.; Hernández, J.; Nagel, E.; Luhman, K. L.; Watson, D. M.; Calvet, N.; Muzerolle, J.; McClure, M. 2010, ApJ, 717, 441

Espaillat, C.; Ingleby, L.; Hernández, J.; Furlan, E.; D’Alessio, P.; Calvet, N.; Andrews, S.; Muzerolle, J.; Qi, C.; Wilner, D. 2012, ApJ, 747, 103

Espaillat, C.; Muzerolle, J.; Najita, J.; et al. Protostars and Planets VI Publisher: University of Arizona press and LPI, 2014. Edited by Henrik Beuther, Ralf S. Klessen, Cornelis P. Dullemond and Thomas Henning.

Esplin, T. L.; Luhman, K. L.; Mamajek, E. E. 2014, ApJ, 784, 126

Fairlamb, J. R., Oudmaijer, R. D., Mendigutia, I., et al. 2017, MNRAS, 464, 4721

Fazio, G. G., Hora, J. L., Allen, L. E., et al. 2004, ApJS, 154, 10

Fedele, D.; van den Ancker, M. E.; Henning, T.; Jayawardhana, R.; Oliveira, J. M. 2010, A&A, 510, A72

Flaherty, K. M., Hughes, A. M., Teague, R., et al. 2018, , 856, 117

Franciosini, E., Sacco, G. G., Jeffries, R. D., et al. 2018, A&A, 616, L12

Frasca, A.; Biazzo, K.; Lanzafame, A. C.; Alcalá, et al. 2015, A&A, 575, 4

Furlan, E.; Hartmann, L.; Calvet, N.; D'Alessio, P.; Franco-Hernández, R.; Forrest, W. J.; et al. 2006, ApJS, 165, 568

Furlan, E.; Watson, D. M.; McClure, M. K.; Manoj, P.; Espaillat, C.; D'Alessio, P.; Calvet, N.;et al. 2009, ApJ, 703, 1964

Furlan, E.; Luhman, K. L.; Espaillat, C.; D'Alessio, P.; Adame, L.; et al. 2011, ApJS, 195, 3

Gaia Collaboration, Brown, A. G. A., Vallenari, A., et al. 2018, A&A, 616, A1

Galli, P. A. B., Joncour, I., & Moraux, E. 2018, MNRAS, 477, L50

Galli, P. A. B.; et al. sent to A&A

Goldsmith, P. F. & Langer, W. D. 1978, ApJ, 222, 881

Grant, S. L.; Espaillat, C. C.; Megeath, S. T.; Calvet, N.; Fischer, W. J.; et al. 2018, ApJ, 863, 13

Gillon, M., Triaud, A. H. M. J., Demory, B.-O., et al. 2017, Nature, 542, 456

Guilloteau, S., Dutrey, A., Piétu, V., et al. 2011, A&A, 529, A105

Haffert, S. Y.; Bohn, A. J.; de Boer, J.;et al. 2019, Nature, 3, 749

Hartmann, L., & Kenyon S.J., 1996, ARAA, 34, 207

Hartmann, L.; Calvet, N.; Gullbring, E.; D'Alessio, P. 1998, ApJ, 495, 385

Hartmann, L., Megeath, S. T., Allen, L., Luhman, K., Calvet, N., D'Alessio, P., Franco-Hernández, R., Fazio, G. 2005, ApJ, 629, 881

Hartmann, Lee. Accretion Processes in Star Formation, Second Edition. Cambridge University Press, 2009.

Hartmann, L.; Herczeg, G.; Calvet, N. 2016, ARAA, 54, 135

Herbig, G. H. 1977, ApJ, 217, 693

Herbig, G. H., & Bell, K. R. 1988, Third Catalog of Emission-Line Stars of the Orion Population : 3 : 1988

Herbig, G. H. 1989, in European Southern Observatory Conference and Workshop Proceedings, Vol. 33, European Southern Observatory Conference and Workshop Proceedings, ed. B. Reipurth, 233–246

Herbst, W. 2008, Handbook of Star Forming Regions, Volume I: The Northern Sky ASP Monograph Publications, Vol. 4. Edited by Bo Reipurth)

Hernández, J., Calvet, N., Briceño, C., et al. 2004, , 127, 1682

Hernández, J., Hartmann, L., Megeath, T., et al. 2007a, ApJ, 662, 1067

Hernández, J., Calvet, N., Briceño, C., et al. 2007b, ApJ, 671, 1784

Hernández, J.; Hartmann, L.; Calvet, N.; Jeffries, R. D.; Gutermuth, R.; Muzerolle, J.; Stauffer, J. 2008, ApJ, 686, 1195

Hernández, J.; Morales-Calderon, M.; Calvet, N.; Hartmann, L.; Muzerolle, J.; Gutermuth, R.; Luhman, K. L.; Stauffer, J. 2010, ApJ, 722, 1226

Hernández, J., Calvet, N., Pérez, A., et al. 2014, ApJ, 794, 36

Hernández, J., Briceño, C., Calvet, N., et al. 2017, SpTClass: SPecTral CLASSificator code, ascl:1705.005

Hernández, et al. 2020a in prep.

Hernández, et al. 2020b in prep.

Hillenbrand, L. A. 1997, AJ, 113, 1733

Hillenbrand, L. A.; Hoffer, A. S.; Herczeg, G. J. 2013, AJ, 146, 85

Huang, J.; Öberg, K. I.; Qi, C.; et al. 2017, ApJ, 835, 231

Hughes, A. L. H., & Armitage, P. J. 2010, , 719, 1633

Ingleby, L.; Calvet, N.; Bergin, E.; Herczeg, G.; Brown, A., et al. 2011, ApJ, 743, 1051

Ingleby, L.; Calvet, N.; Herczeg, G.; Blaty, A., et al. 2013, ApJ, 767, 112

Isella, A.; Natta, A. 2005, A&A, 438, 899

Jeffries, R. D., Jackson, R. J., Franciosini, E., et al. 2017, MNRAS, 464, 1456

Keppler, M.; Teague, R.; Bae, J.; Benisty, et al. 2019, A&A, accepted for publication.

Koepferl, C. M.; Ercolano, B.; Dale, J.; Teixeira, P. S.; Ratzka, T.; Spezzi, L. 2013, MNRAS, 428, 3327

Kounkel, M., Covey, K., Suárez, G., et al. 2018, AJ, 156, 84

Krijt, S.; Ciesla, F. J.; Bergin, E. A. 2016, ApJ, 833, 285

Lada, C. J. 1987, Star Forming Regions, ed. M. Peimbert & J. Jugaku, 1

Lada, C. J.; Muench, A. A.; Luhman, K. L.; Allen, L.; Hartmann, L.; Megeath, T.; Myers, P.; Fazio, G.; Wood, K.; Muzerolle, J.; Rieke, G.; Siegler, N.; Young, E. 2006, AJ, 131, 1574

Liu, Y., Henning, T., Carrasco-González, C., et al. 2017, A&A, 607, A74

Long, F.; Pinilla, P.; Herczeg, G. J., et al. 2018, ApJ, 869, 17

Long, F.; Herczeg, G. J.; Harsono, D., et al. 2019, ApJ, 882, 49

Luhman, K. L.; Rieke, G. H. 1999, ApJ, 525, 440

Luhman, K. L. 2004, ApJ, 602, 816

Luhman, K. L.; Allen, P. R.; Espaillat, C.; Hartmann, L.; Calvet, N. 2010, ApJS, 186, 111

Luhman, K. L.; Mamajek, E. E. 2012, ApJ, 758, 31

Luhman, K. L.; Esplin, T. L. 2020 submitted

Lynden-Bell, D.; Pringle, J. E. 1974, MNRAS, 168, 603

Madhusudhan, N., Harrington, J., Stevenson, K. B., et al. 2011, , 469, 64

Madhusudhan, N.; Amin, M. A.; Kennedy, G. M. 2014, ApJ, 794, 12

Manara, C. F., Natta, A., Rosotti, G. P., et al. 2020, arXiv e-prints, arXiv:2004.14232

Manara, C. F., Fedele, D., Herczeg, G. J., et al. 2016, A&A, 585, A136

Manoj, P.; K., K. H.; Furlan, E.; McClure, M. K.; Luhman, K. L.; Watson, et al. 2011, ApJS, 193, 11

Marjoram, P., Hamblin, S., & Foley, B. 2015, Summer Computing Simulation Conference, 47, 10

Maucó, K.; Hernández, J.; Calvet, N., et al. 2016, ApJ, 829, 38

Maucó, K., Briceño, C., Calvet, N., et al. 2018, , 859, 1

McClure, M. K.; Furlan, E.; Manoj, P.; Luhman, K. L.; Watson, D. M.; Forrest, W. J.; Espaillat, C.; Calvet, N.; D'Alessio, P.; Sargent, B.; Tobin, J. J.; Chiang, Hsin-Fang 2010, ApJS, 188, 75

McClure, M. K., Manoj, P., Calvet, N., et al. 2012, ApJL, 759, L10

McClure, M. K.; D'Alessio, P.; Calvet, N.; Espaillat, C.; Hartmann, L.; Sargent, B.; Watson, D. M.; Ingleby, L.; Hernández, J. 2013, ApJ, 775, 114

Megeath, S. T., Gutermuth, R., Muzerolle, J., et al. 2012, AJ, 144, 192

Megeath, S. T., Gutermuth, R., Muzerolle, J., et al. 2016, AJ, 151, 5

Merín, B.; Brown, J. M.; Oliveira, I.; Herczeg, G. J.; et al. 2010, ApJ, 718, 1200

Mohanty, S., Jankovic, M. R., Tan, J. C., et al. 2018, ApJ, 861, 144

Mulders, G. D., & Dominik, C. 2012, A&A, 539, A9

Mulders, G. D.; Ciesla, F. J.; Min, M.; Pascucci, I. 2015, ApJ, 807, 9

Muzerolle, J.; Allen, L. E.; Megeath, S. T.; Hernández, J.; & Gutermuth, R. A. 2010, ApJ, 708, 1107

Nakano, T.; Umebayashi, T. 1986, MNRAS, 218, 663

Öberg, K. I.; Murray-Clay, R.; Bergin, E. A. 2011, ApJ, 743, 16

Oliveira, I., Olofsson, J., Pontoppidan, K. M., et al. 2011, ApJ, 734, 51

Okuzumi, S.; Momose, M.; Sirono, S.; Kobayashi, H.; & Tanaka, H. 2016, ApJ, 821, 82

Ortiz-León, G. N., Loinard, L., Dzib, S. A., et al. 2018, ApJ, 865, 73

Owen, J. E. 2016, PASA, 33,5

Pecaut, M. J.; Mamajek, E. E.; Bubar, E. J. 2012, ApJ, 746, 154

Pecaut, M. J., & Mamajek, E. E. 2013, ApJS, 208, 9

Pérez-Blanco, A., Maucó, K., Hernández, J., et al. 2018, ApJ, 867, 116

Pinilla, P.; Flock, M.; Ovelar, M. de J., & Birnstiel, T. 2016, A&A, 596, 81

Pinte, C., Dent, W. R. F., Ménard, F., et al. 2016, ApJ, 816, 25

Pinte, C.; Ménard, F.; Duchêne, G., et al. 2018, A&A, 609, 47

Piso, A. M. A.; Öberg, K. I.; Birnstiel, T.; Murray-Clay, R. A. 2015, ApJ, 815, 109

Pollack, J. B.; Hollenbach, D.; Beckwith, S.; Simonelli, D. P.; Roush, T.; Fong, W. 1994 ApJ, 421, 615

Pontoppidan, K. M.; Salyk, C.; Bergin, E. A.; Brittain, S.; Marty, B.; Mousis, O.; Öberg, K. I. Protostars and Planets VI Publisher: University of Arizona press and LPI, 2014. Edited by Henrik Beuther, Ralf S. Klessen, Cornelis P. Dullemond and Thomas Henning.

Powell, D.; Murray-Clay, R.; Schlichting, H. E. 2017 ApJ, 840, 93

Preibisch, T.; Brown, A. G. A.; Bridges, T.; Guenther, E.; Zinnecker, H. 2002 AJ, 124, 404

Preibisch, T.; Mamajek, E. 2008, Handbook of Star Forming Regions, Volume II: The Southern Sky ASP Monograph Publications, Vol. 5. Edited by Bo Reipurth

Prisinzano, L., Damiani, F., Micela, G., et al. 2016, A&A, 589, A70

Qi, C.; D'Alessio, P.; Öberg, K. I.; Wilner, D. J.; Hughes, A. M.; Andrews, S. M.; Ayala, S. 2011 ApJ, 740, 84

Qi, C.; Öberg, K. I.; Wilner, D. J.; D'Alessio, P.; et al. 2013 Science, 341, 630

Qi, C.; Öberg, K. I.; Andrews, S. M.; Wilner, D. J.; et al. 2015 ApJ, 813, 128

Rieke, G. H., Young, E. T., ; et al. 2004 ApJS, 154, 25

Rodríguez, L. F., Cantó, J., Torelles, J. M., et al. 1992, ApJ, 393, L29

Rodríguez, L. F., Cantó, J., Torelles, J. M., et al. 1994, ApJ, 427, L103

Sacco, G. G.; Franciosini, E.; Randich, S. & Pallavicini, R. 2008 A&A, 488, 167

Schwarz, K. R.; Bergin, E. A.; Cleeves, L. I.; et al. 2016 ApJ, 824, 91

Shakura, N. I. & Sunyaev, R. A.; 1973 A&A, 24, 337

Shu, F., Adams, F. C., & Lizano, S., 1987, ARAA, 25, 23-81

Shu, F.; Tremaine, F.; Adams, F.; & Ruden, S. P., 1990, ApJ, 358, 495

Siess, L.; Dufour, E.; Forestini, M. 2000, A&A, 358, 593

Smiljanic, R., Romano, D., Bragaglia, A., et al. 2016, A&A, 589, A115

Song, I.; Zuckerman, B. & Bessell, M. S. 2012, AJ, 144, 8

Spina, L.; Randich, S.; Palla, F.; et al. 2014, A&A, 567, 55

Stepinski, T. F. 1992, Icarus, 97, 130

Strom, K. M.; Newton, G.; Strom, S. E.; Seaman, R. L.; et al. 1989, ApJS, 71, 183

Suárez, G.; Downes, J. J.; Román-Zúñiga, C; et al. 2019, MNRAS, 486, 1718

Tannirkulam, A.; Monnier, J. D.; Millan-Gabet, R.; Harries, T. J.; Pedretti, E.; ten Brummelaar, T. A.; McAlister, H.; Turner, N.; Sturmann, J.; Sturmann, L. 2008, ApJ, 677, 51

Tapia, C., Lizano, S., Sierra, A., et al. 2019, ApJ, 887, 244

Testi, L.; Birnstiel, T.; Ricci, L., et al. 2014,Protostars and Planets VI, University of Arizona Press, Tucson. Edited by Henrik Beuther, Ralf S. Klessen, Cornelis P. Dullemond, and Thomas Henning

Tobin, J., Sheehan, P., Megeath, S. T.; et al. 2020, submitted, arXiv:2001.04468

Tognelli E., Prada Moroni P.G., Degl'Innocenti S. 2011, A&A, 533, A109

Tonry, J. L.; Stubbs, C. W.; Lykke, K. R.; et al. 2012, ApJ, 750, 99

Turner, B and VanZandt T 2012, Journal of Mathematical Psychology, 56, 2

Turner, N. J., Fromang, S., Gammie, C., et al. 2014, Protostars and Planets VI, 411

Weidenschilling, S. J. 1997, Icarus, 127, 290

White, R. J., & Basri, G. 2003, ApJ, 582, 1109

Williams, J. P.; Cieza, L. A. 2011, ARAA, 49, 67

Williams, J. P., Cieza, L. A., Andrews, S. M., et al. 2013, , 435, 1671

Zhang, K., Blake, G. A., & Bergin, E. A. 2015, ApJ, 806, L7

Zhang, S.; Zhu, Z; Huang, J.; et al. 2018, ApJ, 869, 47

Zhu, Z.; Nelson, R. P.; Hartmann, L.; Espaillat, C. and Calvet, N. 2011, ApJ, 729, 47

Zhu, Z.; Nelson, R. P.; Dong, R.; Espaillat, C.; Hartmann, L. 2012, ApJ, 755, 62